Enabling the Weak Lensing Science in the 2020s

Tianqing Zhang

Department of Physics
Carnegie Mellon University

Thesis Committee:
Rachel Mandelbaum (Chair)
Scott Dodelson
Jeffrey Newman
Chad Schafer

July 25, 2023

Submitted in partial fulfillment of the requirements
for the degree of Doctor of Philosophy.

Abstract

The 2020s are an exhilarating era for modern cosmology, particularly in the field of weak gravitational lensing science. With the completion of Stage-III imaging surveys such as the Dark Energy Survey (DES), the Subaru Hyper Suprime-Cam (HSC), and the Kilo-Degree Survey (KiDS) in the first half of the decade, weak lensing science has entered the realm of precision observation. These surveys have enabled us to meticulously observe the positions and shapes of hundreds of millions of galaxies, enabling weak gravitational lensing observation with high significance. Combined with other probes such as the cosmic microwave background (CMB), weak lensing allow us to test the standard Λ-CDM model for the universe.

In the latter half of the decade, various survey telescopes, both ground-based like the Vera Rubin Observatory and space-based like the Roman Space Telescope, will become operational. These telescopes will provide datasets with larger coverage areas, deeper optical depths, and higher resolutions. Leveraging the statistical power of these telescopes, we can theoretically achieve higher precision in constraining the large-scale structure and dark energy, thus offering a stress testing to the Λ-CDM model. By measuring the large-scale structure at different redshifts, we can distinguish between models with different parameters w_0 for the dark energy equation of state, including Λ-CDM, which assumes $w_0 = -1$, i.e., a constant dark energy density. These scientific objectives drive the current weak lensing observations and have the potential to reshape modern cosmology.

However, the success of the Stage-IV imaging survey crucially relies on effectively addressing systematic errors in observation and analysis. As the statistical uncertainty decreases with the data volume of these surveys, the tolerance for systematic errors diminishes as well. All sources of systematic uncertainty increase in importance, and even those previously considered subdominant now attain statistical significance. Weak lensing encompasses a wide range of systematic sources, including astrophysical and observational systematics, and systematic effects introduced by analysis and modeling methods.

This thesis will specifically address two of the aforementioned systematics. The first focus is on the systematics arising from the Point Spread Function (PSF). The PSF represents the probability distribution that characterizes the response of an imaging system to a point source in the observed sky scene. Accurate modeling and correction of the PSF are essential in weak lensing observations. While the influence of the second moments of the PSF on weak lensing shear is widely recognized, research on the impact of higher moments of the PSF remains limited. My study initiates and expands the investigation of weak lensing systematics stemming from the higher moments of the PSF. I developed a software suite called PSFHOME, which encompasses image simulation, error propagation, and modeling with regard to the PSF higher moments. Combining with real data from the Hyper-Suprime Cam (HSC), I study the multiplicative and additive bias induced by the PSF higher moments, as well as modeling and propagating such error to the downstream cosmological probes.

Based on this understanding, I further proposed a methodological framework to detect, model, and mitigate the contamination of higher moments on the shear two-point correlation function $\xi_{\pm}$. This framework is applied to investigate the Year-3 shear catalog from the HSC. Using this new framework, I show that previously unidentified systematic biases in weak lensing shear arising from the PSF fourth moments can be effectively modeled and mitigated.

The second topic of focus in this study revolves around systematic errors associated with photometric redshift estimation, commonly referred to as photo-z. To achieve reliable constraints on cosmological parameters in weak lensing shear analyses, it is essential to effectively and accurately marginalize the nuisance parameters of the redshift distribution $n(z)$ of the observed sample. I propose a Bayesian statistical approach, called Bayesian resampling, to fully marginalize the redshift uncertainty in the shear catalog during cosmic shear analysis. This method is compared to existing approaches described in the literature, specifically in the context of a mock cosmic shear analysis for the HSC Year-3 shear catalog. The comparison demonstrates that the new method and the existing approaches yield statistically consistent error bars for the cosmological parameter constraints in the HSC three-year analysis. But the difference will increase for future surveys.

Acknowledgments

This work is made possible by the contribution and support of many.

First and foremost, I want to express my utter appreciation to my advisor, Rachel Mandelbaum. It is such a privilege to be guided by Rachel, an excellent researcher who always pursues the very best and most interesting scientific outcome, a great mentor who truly cares for her student's academic success, physical and mental well-being, and generally, a kind and lovely human. Under five years of her teaching, I learned countless pieces of knowledge about the fundamentals of cosmology, as well as insights into my specific research. She provided me with options to tailor my research project to suit my interests, which means a great deal to me. Apart from academic knowledge, she helped me extend my research network into various collaborations. Her deep commitment to the services of the cosmology community also steers me in this direction to a great extent. She is also a leader by example, her impeccable work ethic, passion for science, and immense self-discipline shape me into a better researcher even without interaction between us.

I would also like to thank my thesis committee members of Scott Dodelson, Jeffrey Newman, and Chad Schafer for giving me constructive suggestions throughout the years. I thank Scott for giving me an earlier advisory in the first year of graduate school and teaching me cosmology in both the class and our group meeting. I thank Jeff and Chad for giving me many superb pieces of advice on my research projects. I am looking forward to working more closely with Jeff in the next stage of my career. I also want to thank the entire thesis committee for providing constructive advice during my yearly review.

I would like to appreciate my senior colleagues and peers at McWilliams Centre for Cosmology at CMU. A special thanks to Xiangchong Li and Markus Michael Rau for providing me with invaluable advice even during their busy early career. I want to thank Rupert Croft, Tiziana Di Matteo, Tina Kahniashvili, Hy Trac, Mohit Bhardwaj, and Alex Malz for working on various events and committees for the center and the department. I would also like to thank a few predecessors that helped me dearly, they are Yueying Ni, Matt Ho, Sukhdeep Singh, Hung-Jin Huang, Husni Almoubayyed, Chien-Hao Lin, and Kuan-Wei Huang. I also want to thank Andresa de Campos, Nianyi Chen, Diptajyoti Mukherjee, Yesukhei Jagvaral, Kuldeep Sharma, Tomas Cabrera, Rachel Buttry, Andy Park, Federico Berlfein, Peikai Li, Yingzhang Chen, Alan Zhou, and Yihao Zhou, Duncan Campbell, Simon Samuroff for all the precious academic discussion and assistance.

The Department of Physics at CMU builds a strong program for us graduate students to be successful, so I thank all the faculties and staff that contributed to this program. I want to thank David Anderson, Jeffrey Peterson, Benjamin Hunt, and Riccardo Penco for helping me with my teaching duty. I want to thank Manfred Paulini, Frederick Gilman, and Markus Deserno for managing the graduate program, and many helpful interactions with me.

I would like to thank my collaborators from different organizations. In the Dark Energy Science Collaboration, I am also honored to work with Joshua Meyers, Morgan Schmitz, Axel Guinot, Bob Armstrong, Claire-Alice Hebert, Pat Burchat, Aaron Roodman, Chris Walter, Chihway Chang, Danielle Leonard, Erin Sheldon, Francois Lanusse, Gary Bernstein,

Pierre-Francois Leget, Douglas Clowe, Henk Hoekstra, Hyeyun Park, Keith Bechtol, Eric Gawiser, Joe Zuntz, Judit Prat, Heather Kelly, Sierra Villarreal, and Mariana Penna-Lima, Camille Avestruz. In the Hyper Suprime-Cam weak lensing working group, I am honored to be working with Arun Kannawadi, Hironao Miyatake, Masahiro Takada, Michael Strauss, Roohi Dalal, Sunao Sugiyama, Surhud More, Andres Plazas Malagon, Andrina Nicola, Divya Rana, Tomomi Sunayama, and Robert Lupton. In the Roman Space Telescope High-Latitude Survey image simulation group, I am pleased to work with Chris Hirata, Masaya Yamamoto, and Michael Troxel. A special shout-out to Mike Jarvis for providing lots of support and comments for my work in multiple collaborations. I also want to thank Ying Zu, Tim Eifler, Elisabeth Krause, Eduardo Rozo, Jeffrey Regier, Anze Slosar, and Frank van den Bosch for their generous help to my career in different aspects.

Three of the five years in my graduate school are the "Covid-era", which is a hard time for many including me. Without my supportive friends, I would not have gone through this as smoothly. I want to thank friends at Pittsburgh, I-Hsuan Kao, Nianyi Chen, Andresa de Campos, Kuldeep Sharma, Yueying Ni, Xiangchong Li, Ryan Muzzio, Beka Modrekiladze and many others for getting through the hardship together and supporting each other. I am extremely grateful for meeting and knowing my roommates Matt Ho, Samuel Foley, and Kahley McBeth, for spending four special years under the same roof in Shadyside. I would like to thank my friends on the internet who spent many hours in the virtual world during the pandemic with me, they are Enze 'Nevermore' Zhang, Yicun 'xxmscat' Liu, Jiaren 'Mapo Tofu' Zou, Guangxin 'Nature Material' Lv, Yuqiu '18' Zhang, Duxin 'pdX' Hao, Xuejian 'MORIsummer' Shen, Fukang 'shikimate' Shi, Ruyang 'Nature Physics' Sun, Lingjie 'Nature Communication' Zhou. I also want to thank all the friends around the world who kept in touch.

I thank Olga Navros for rescuing my pet and my best friend, Tannoudji, and bringing her into my life.

I want to give my biggest shout-out to my parents and my grandma for raising me in an environment that encourages passion, curiosity, and trial. They sacrificed a lot to provide me with a pleasant childhood and adolescence. They are still my biggest supporters to this date. Lastly, I would like to express my deepest gratitude to my beloved partner, Jocelyn Zhang. Her unwavering love, trust, and support have been my greatest source of strength and security throughout my entire graduate school journey. I am eternally thankful for everything she has done for me, and I cherish the beautiful memories we have created together.

I thank the taxpayers from the United States whose hard-earned money has supported and subsidized my graduate school education and research, through the Department of Energy. I thank Simon Foundation for their generous funding that supports my research.

Contents

List of Tables

List of Figures

Chapter 1

Introduction

In this chapter, I am going to describe a few topics that constitute the bedrock of this thesis. Section 1.1 consists of modern physics and cosmological background that motivate this study scientifically. There are also a few key concepts that are crucial to this thesis. Section 1.2 introduce the technique that this thesis focuses on – weak gravitational lensing. The section describes the formalism and challenges of modern weak lensing observation. Most cosmology research requires statistical techniques, so Section 1.3 introduces number of key statistical concepts that are crucial throughout the entire thesis. Section 1.4 lays out the structure of the thesis.

1.1 Contemporary Cosmology

Cosmology is a field of study dedicated to exploring the nature and characteristics of the universe we inhabit. It is an ancient discipline that has existed throughout history, although our current understanding differs significantly from the interpretations held by ancient civilizations (For a read of the evolution of cosmology, see (10)). The development of cosmological theories has historically relied heavily on the observational techniques available to scientists during each era. Modern cosmology follows this pattern, as it is built upon a variety of observational evidence obtained from advanced astronomical instrumentation and techniques.

The first fundamental evidence is the expanding universe, which can be attributed to the pioneering observations of redshift by Vesto M. Slipher (11) and Edwin Hubble (12), as well as the theoretical contributions of Alexander Friedmann (13) and Albert Einstein (14) in the early 20th century, which forms a foundational pillar of modern cosmology. Advancements in the late 20th century further solidified this understanding, particularly with the discovery of the accelerated expansion of the universe through observations of Type-Ia supernovae (15; 16). The former evidence supports the prevailing theory that our universe originated from the "big bang," while the latter evidence points to the existence of a mysterious force referred to as "dark energy" that is responsible for driving the accelerated expansion of space.

The second fundamental evidence is homogeneity and isotropy on a very large scale and the inhomogeneity and structure formation at the small scales. The universe is, at large

scales, homogeneous and isotropic (17), and is in a flat space-time. At small scales, inhomogeneity and anisotropy form because of gravity. Extragalactic surveys reveal significant inhomogeneity and anisotropy in the distribution of galaxies (18) on the small-scales, which is in stark contrast with our observations of an earlier version of the universe through the Cosmic Microwave Background (CMB), which appears predominantly smooth, except for minor fluctuations in the temperature field at a fraction of approximately 10^{-5} (19). For these fluctuations to evolve into the structures we observe in the present-day universe, the existence of "dark matter" is crucial for several reasons. The presence of dark matter is also supported by various observational evidence, including weak gravitational lensing.

1.1.1 The Expanding Universe

In this section, I will provide an overview of the fundamental framework of the modern standard cosmological model. It is widely accepted that our universe is in a state of expansion. According to the standard cosmology model, the universe originated from a singularity called the big bang, where matter and radiation existed in an incredibly dense state. Shortly after the big bang (approximately 10^{-32} seconds), our universe underwent a phase of rapid and exponential expansion known as "inflation." (We will revisit inflation in Section 1.1.3.) Following inflation, the universe has continued to expand, with successive phases driven by radiation, matter, and dark energy.

Edwin Hubble made a significant contribution by confirming the expansion of the universe through his observations of the velocity-distance diagram, commonly referred to as the Hubble diagram (12). Hubble observed that galaxies appeared to be moving away from our own galaxy, and the velocity of recession v_{rec} increased with their distance D from us.

$$v_{\text{rec}}(D) = H_0 D. \tag{1.1}$$

The expansion rate H_0 is known as the Hubble constant. The expansion of the universe can be understood as the expansion of space itself. To illustrate this, imagine two galaxies positioned at opposite ends of an incredibly long ruler, with no relative motion between them. In an expanding universe, these galaxies would still appear to move away from each other because the ruler itself is expanding along with the space it occupies. In cosmology, we employ the scale factor denoted by $a(t)$ to quantify the size of the space. We define the scale factor at the present age of the universe to be 1.

The currently prominent standard cosmology model based on a composite of cold dark matter (CDM), baryons, radiation, and cosmological constant Λ outlined that the universe must expand in a certain manner. During the early stages of the universe, when radiation dominated, the scale factor followed a relationship of $a \propto t^{1/2}$. As time progressed, the universe transitioned into a phase dominated by matter, where the scale factor evolved as $a \propto t^{2/3}$. In the current epoch, we are witnessing a departure from the matter-dominated phase and entering a period of accelerated expansion. This acceleration is suggested by observations of type Ia supernovae(15; 16) , which revitalized Einstein's concept that there

is a dark energy in the universe that act as a cosmological constant, which is later broadly supported by other early and late universe probes.

To quantify the rate of expansion of the universe, we introduce the Hubble rate, defined as the derivative of the scale factor with respect to time divided by the scale factor itself:

$$H(t) = \frac{da/dt}{a}. \tag{1.2}$$

The Hubble rate, denoted as $H(t)$, provides a measure of how rapidly the universe's scale factor changes over time. At the present epoch, $H(t) = H_0$. Determining the value of H_0 requires observations from either the early universe or the late universe. Measurements of H_0 in the early universe predominantly rely on observations of the Cosmic Microwave Background (CMB) (e.g., (20; 21)). In the late universe, the most precise determinations of H_0 involve the observation of distant Cepheid variable stars and Type-Ia supernovae (e.g., (22)). Currently, a tension exists between measurements of H_0 obtained from these two distinct cosmic stages. This tension presents a significant challenge to the standard cosmological model (for a review, see (23)).

1.1.2 Geometry of the Universe

In this section, I will delve into one of the fundamental theories that modern cosmology is built upon, namely general relativity. Specifically, I will direct our attention to the geometry of the universe, exploring the metrics that describe its structure and investigating methods for defining distances within the universe. Additionally, I will introduce a key concept in astronomy, redshift, which serves as a crucial tool for measuring distances on cosmological scales.

A metric establishes a relationship between the coordinates of space-time and the distance between two events. For a four-dimensional space-time, the metric is defined as:

$$ds^2 = \sum_{\mu,\nu=0}^{3} g_{\mu\nu} dx^\mu dx^\nu. \tag{1.3}$$

Building upon the previous section, where we discussed the large-scale homogeneity and isotropy of the universe, our universe has a total density that equals the critical density, and our universe is flat. The flatness means that two parallel lines in space-time will never cross, instead of diverging (in an open universe) or converging (in a closed universe). In this case, a suitable metric that captures these characteristics is the Friedmann-Robertson-Walker (FRW) metric. For the FRW metric in comoving coordinates, we have:

$$g_{\mu\nu} = \begin{pmatrix} -1 & 0 & 0 & 0 \\ 0 & a(t)^2 & 0 & 0 \\ 0 & 0 & a(t)^2 & 0 \\ 0 & 0 & 0 & a(t)^2 \end{pmatrix}. \tag{1.4}$$

Here, $a(t)$ represents the scale factor, which quantifies the expansion of the universe over time. The coordinate χ is fixed within an expanding universe and is referred to as the "comoving distance". Note that we are using the natural units, i.e., $\hbar = c = k_B = 1$. As the universe expands, the physical distance d_p expands in proportion to the scale factor, and it is known as the "proper distance":

$$d_p = a(t)\chi. \tag{1.5}$$

One important concept of a distant object in astronomy is the redshift. Redshift, denoted by z, is quantified as the fractional shift of a specific emission or absorption line's wavelength, relative to its intrinsic wavelength, λ_{int}. Observationally, it is expressed as:

$$z = \frac{\lambda_{obs}}{\lambda_{int}} - 1, \tag{1.6}$$

where λ_{obs} represents the observed wavelength of the emission or absorption line. There are two physical origins to the redshift of a galaxy. The first is the intrinsic motion of a galaxy relative to the reference coordinate system, commonly referred to as the Doppler redshift. The second type arises from cosmic expansion, known as the Hubble flow. When light from a distant galaxy reaches us, it was emitted at a time when the universe had a certain scale factor, denoted by a. The redshift is connected to the scale factor through the relation:

$$z = \frac{1}{a} - 1. \tag{1.7}$$

One classic way to quantify distance in astronomy is to measure the angular size θ of an object with known physical size l, i.e., the standard ruler. The distance to that object is called the "angular distance" d_A,

$$d_A = \frac{l}{\theta}. \tag{1.8}$$

The comoving size of the standard ruler, when the light is emitted, is l/a. In an expanding universe with no curvature, i.e., a Euclidean universe, the angular diameter of that object is $l/(a\chi(z))$. Using 1.7 and 1.8, we get the angular distance as a function of the redshift,

$$d_A = a\chi = \frac{\chi}{1+z}. \tag{1.9}$$

Another important definition of distance in astronomy is the distance measured by the observed flux of an object with known luminosity, i.e., a standard candle. In a static spacetime, the observed flux F of an object with luminosity L at the luminosity distance d_L is

$$F = \frac{L}{4\pi d_L^2}. \tag{1.10}$$

Again, in an expanding Euclidean universe, 1.10 only holds up in the comoving coordinate, or

$$F = \frac{L(\chi)}{4\pi\chi^2}. \tag{1.11}$$

The challenging task in deriving the luminosity distance is to express $L(\chi)$ in terms of the scale factor. For a light source with luminosity L emitted at the age of a, the energy per photon has become a times the original energy. Additionally, the comoving speed of the photon also becomes a times the original comoving speed. Therefore, we have $L(\chi) = La^2$. By equating Equation 1.10 and Equation 1.11, we can derive the luminosity distance as follows:

$$d_L = \frac{\chi}{a}. \tag{1.12}$$

By measuring the flux and using this relation, astronomers can estimate the luminosity distance and thereby determine distances to objects based on their known luminosity. Luminosity distance plays an important role in the conversion of the apparent magnitude $m_{\rm app}$ and the absolute magnitude M,

$$M = m_{\rm app} - 5\log_{10}(\frac{d_L}{10pc}) - K_{\rm corr}. \tag{1.13}$$

Here $K_{\rm corr}$ is a correction term due to the different rest-frame SED for galaxies at different redshifts.

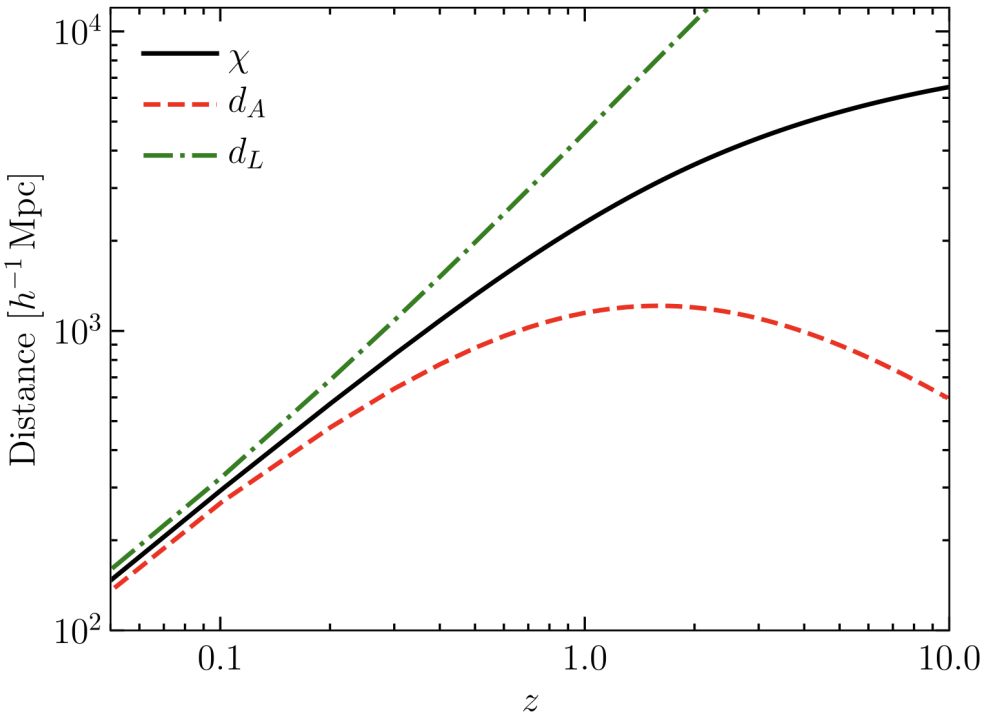

Figure 1.1: Distances in an expanding Euclidean universe as a function of redshift (Image taken from (2)). The comoving distance χ is in the black line, the angular distance d_A in the red dashed line, and the luminosity distance d_L in the green dashed line.

In Fig. 1.1, I show all three distances mentioned here as a function of the redshift(2). It is important to note that when calculating these distances, we make the assumption that

the universe is flat and characterized by a specific $H(z)$ function, which depends on other cosmological parameters.

1.1.3 Structure Formation and Power Spectrum

In this section, I provide a simplified overview of how structures form in the universe and introduce the important concept of the power spectrum. For a more comprehensive understanding, I refer to (24).

While the universe is homogeneous on large scales, it exhibits significant inhomogeneities on smaller scales, with structures ranging from superclusters to globular clusters. Cosmologists focus on studying the large-scale structure (LSS) of the universe. The amplitude of the LSS, which describes the distribution of matter, is quantified using the power spectrum, which is measured through imaging and spectroscopic survey techniques like galaxy clustering and weak lensing.

When discussing structure formation, it is often advantageous to work in Fourier space. Perturbations at different wave numbers k are mathematically independent. This enables the use of perturbation theory for analytical derivations of structure formation in the linear regime.

The amplitude of perturbations on different scales is also characterized in Fourier space through the power spectrum. We define the matter density fluctuation as $\delta_m(\boldsymbol{x}) = (\rho(\boldsymbol{x}) - \bar{\rho})/\bar{\rho}$, where $\rho(\boldsymbol{x})$ is the matter density at position $\boldsymbol{x}$, and $\bar{\rho}$ is the mean matter density. The matter power spectrum $P_m(k)$ is defined as

$$\langle \tilde{\delta}_m(\boldsymbol{k}) \tilde{\delta}_m^*(\boldsymbol{k}') \rangle = (2\pi)^3 \delta_D^{(3)}(\boldsymbol{k} - \boldsymbol{k}') P_m(\boldsymbol{k}), \tag{1.14}$$

where $\tilde{\delta}_m(\boldsymbol{k})$ is the Fourier transform of $\delta_m(\boldsymbol{x})$, the angled bracket denotes an average over an ensemble, and $\delta_D^{(3)}(\boldsymbol{k} - \boldsymbol{k}')$ is the Dirac delta function, which is nonzero only when $\boldsymbol{k} = \boldsymbol{k}'$. In the case of a Gaussian random field, the power spectrum is sufficient to describe the statistics of the field. However, the power spectrum does not capture higher-order statistics or the non-Gaussianity of the matter density field, which occurs after the overdensities grow over the linear regime.

In Fig. 1.2 (3), an example of the growth of a perturbation at a scale equivalent to the size of the Milky Way is shown. The evolution of dark matter and baryonic matter is treated separately due to their distinct physical processes. During the grey area, the perturbation is outside the horizon of the universe, undergoing superhorizon growth due to the difference in expansion rate at different densities. Subsequently, as the perturbation enters the horizon, the universe is in a radiation-dominated era. At this stage, the universe's expansion counteracts the gravitational contraction. Consequently, the amplitude of the dark matter perturbation remains constant, a phenomenon also known as "stagnation". Following the time of matter-radiation equivalence t_{eq}, the universe transitions into a matter-dominated epoch. During this period, gravity becomes more influential than cosmic expansion, leading to a prolonged phase of linear growth for the dark matter perturbation.

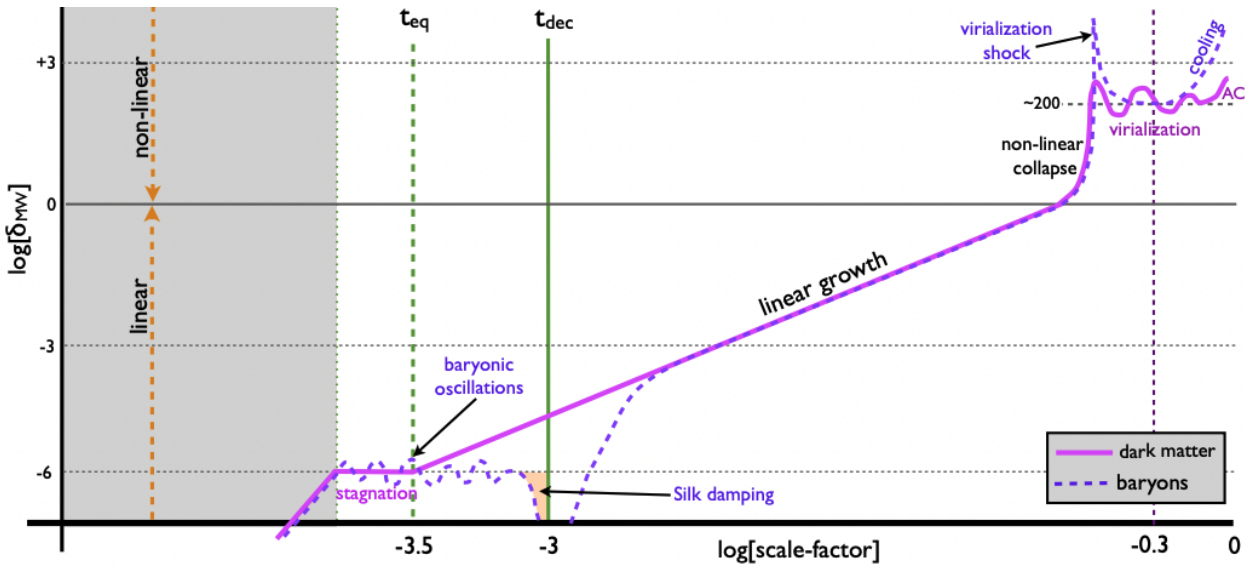

Figure 1.2: The amplitude of the fluctuation with a scale λ_{MW} equal to the size of the Milky Way with the scale factor (Image taken from (3)) in Equation 1.7. The grey area represents the epoch where the perturbation is super-horizon. t_{eq} is the time of matter-radiation equality, t_{dec} is the time of decoupling, otherwise known as recombination. The amplitude is considered linear when $\log(\delta_{MW}) < 1$, and nonlinear otherwise.

The early evolution of baryonic matter is more complex compared to dark matter. Prior to decoupling (t_{dec}), the universe consists of a high-pressure plasma formed by coupled photons and electrons. The pressure of the plasma prevents the growth caused by perturbations, resulting in oscillations of the perturbation amplitude. This phenomenon is known as "Baryonic Acoustic Oscillation" and is observed in both the cosmic microwave background (CMB) (25) and galaxy surveys (26).

As the universe cools down, electrons combine with protons during recombination, causing them to decouple from photons. At this stage, CMB photons begin free streaming. This free streaming process also smoothes out the baryon fluctuations, known as "silk damping". Following recombination, baryons fall back into the gravitational potential wells of dark matter and start their phase of linear growth.

When the perturbation amplitude $\delta_m(\lambda)$ reaches approximately unity, the linear perturbation theory becomes inadequate, and the process of structure formation enters the nonlinear regime. In this regime, dark matter overdensities collapse and undergo virialization, a process where the gravitational potential energy of the system is balanced by the kinetic energy. This leads to the formation of clumps of dark matter known as "dark matter halos".

For baryonic matter, the collapse of structures generates significant heating. However, various cooling processes, such as cooling via radiation and molecular formation, lower the temperature of the baryons. This cooling process enables the formation of stars within the

gas cloud.

The theory of structure formation links the power spectrum at different ages, or redshifts, to a few cosmological parameters in the Λ-CDM model. Probes that are sensitive to the power spectrum in the late universe will have constraining power over the cosmological parameters, such as the ratio of matter in the current universe Ω_m, the mass dispersion of the linear power spectrum on $8Mpc/h$, also known as σ_8. Therefore, probes such as weak lensing that are sensitive to the LSS can be used to constrain the cosmological parameters. Since the same set of cosmological parameters also predict the early universes probes such as CMB, the combination of CMB and weak lensing enables a test to the Λ-CDM model. In the next section, I will introduce the formalism and challenges of weak lensing, a promising probe to constrain cosmology by measuring the power spectrum at the late universe.

1.2 Weak Gravitational Lensing

According to general relativity, the path of light is deflected when it passes near a massive object. This phenomenon is known as gravitational lensing. When a foreground mass, referred to as the lens, has a high mass density, the gravitational lensing effect can be strong and visible, leading to arcs or multiple images of the background galaxy. This is known as strong gravitational lensing. (I refer to (27) and (28) for reviews.) In most cases, however, the lensing effect is relatively weak, resulting in subtle changes in the size and shape of the background galaxies. This is known as weak gravitational lensing, or simply weak lensing (see (29) for a review on weak lensing). Weak lensing provides valuable information about the distribution of matter in the universe and is a powerful tool for studying the large-scale structure and properties of dark matter.

With approximately 80% of the matter content in the universe being dark matter, weak gravitational lensing has emerged as a valuable technique for studying LSS (30). By analyzing the correlation of shapes of background galaxies, known as cosmic shear, we can measure the power spectrum of the large-scale structure, as discussed in Section 1.1.3.

Additionally, by studying the correlation between the shapes of galaxies and the positions of massive galaxies, known as galaxy-galaxy lensing (e.g., (31)(32)), we can infer the mass distribution of dark matter halos. This provides insights into the properties and distribution of dark matter, and can also constrain the halo mass function. These scientific applications, along with the formalism for weak gravitational lensing, are further described in Section 1.2.1.

To ensure accurate cosmological constraints using weak lensing, it is crucial to address and control systematic errors. (For a review, see (33)) Weak lensing relies on imaging surveys that observe millions, if not billions, of galaxies to trace the distortion of their shapes caused by foreground matter. However, various systematics can arise at different stages of the observation and analysis process. Astrophysical systematics such as intrinsic alignment and the effects of baryonic physics can introduce complex and challenging biases to the weak lensing signal, requiring careful modeling. At the observation level, instrumental effects like the Point Spread Function (PSF) of telescopes, survey window effects, and galaxy overlapping can also impact the weak lensing measurements. Furthermore, at the analysis level,

uncertainties in photometric redshift estimation, accuracy of galaxy shape measurement, and statistical inference methods can introduce additional systematic errors.

Given the importance of addressing these systematics, a significant portion of weak lensing research, including this thesis, is devoted to understanding, quantifying, and mitigating such errors. Section 1.2.2 will provide a concise overview of the various systematic effects in weak lensing studies.

1.2.1 Lensing formalism

In this section, I will give a quantitative description of the weak lensing formalism, and how lensing is connected to the standard cosmology we described in the last section. For the general lensing formalism, I refer to (27) for a detailed read.

For the lensing formalism, I will limit the scope of this discussion to the linear region. This means that I will only keep the 0th-order solution of the light deflection of lensing (See (34) for more detail), which is called the Born approximation. In this formalism, we use the Jacobian $\mathbf{A} = \partial\beta/\partial\vartheta$, where ϑ is the 2-d coordinate system of the lensed coordinate, and β is the unlensed coordinate. We parameterize $\mathbf{A}$ by the convergence κ and shear $\gamma = \gamma_1 + i\gamma_2$, as

$$\mathbf{A} = \begin{pmatrix} 1-\kappa-\gamma_1 & -\gamma_2 \\ -\gamma_2 & 1-\kappa+\gamma_1 \end{pmatrix}. \tag{1.15}$$

The cosmological quantity related to the weak lensing signal is the 2D projected gravitational potential $\psi(\vartheta)$, which can be calculated by integrating the 3D gravitational potential ϕ along the line-of-sight,

$$\psi(\vartheta) = \frac{2}{D_S}\int_0^{D_S} dD_L \phi \frac{D_{LS}}{D_L}. \tag{1.16}$$

Here D_S is the distance to the source, D_L is the distance to the lens, D_{LS} is the distance between the lens and source. The convergence and shear are related to the second derivative $\psi(\vartheta)$,

$$\kappa = \frac{1}{2}(\partial_1\partial_1 + \partial_2\partial_2)\psi = \frac{1}{2}\nabla^2\psi \tag{1.17}$$

$$\gamma_1 = \frac{1}{2}(\partial_1\partial_1 - \partial_2\partial_2)\psi \tag{1.18}$$

$$\gamma_2 = \partial_1\partial_2\psi. \tag{1.19}$$

Here, we denote $\partial_1 = \partial/\partial\vartheta_1$ and $\partial_2 = \partial/\partial\vartheta_2$. It is mathematically convenient to express shear by a complex number $\gamma = \gamma_1 + i\gamma_2 = |\gamma|\exp(2i\phi)$, where ϕ is the polar angle between the two components. The shear is a spin-2 quantity, which means that a rotation of π radians restores the shear, and a rotation of $\pi/2$ radians negates it .

Cosmologists utilize the shape of galaxies to probe the weak lensing shear. Assume the galaxy is centered at $\vartheta = (0, 0)$, the galaxy shape is measured using the second moments of

the galaxies, denoted by M_{ij},

$$M_{ij} = \frac{\int \mathrm{d}\vartheta_1 \mathrm{d}\vartheta_2 \, \vartheta_i \vartheta_j \, \omega(\vartheta) I(\vartheta)}{\int \mathrm{d}\vartheta_1 \mathrm{d}\vartheta_2 \, \omega(\vartheta) I(\vartheta)}. \tag{1.20}$$

where $I(\vartheta)$ is the intensity profile of the object in the image coordinates ϑ, and $\omega(\vartheta)$ is a weight function used to suppress pixels with low signal-to-noise ratio. The complex ellipticity of the galaxy is represented by two components, $e = e_1 + ie_2$, and the trace of the second moment, T, is given by

$$T = M_{11} + M_{22} \tag{1.21}$$

$$e_1 = \frac{M_{11} - M_{22}}{M_{11} + M_{22}} \tag{1.22}$$

$$e_2 = \frac{2M_{12}}{M_{11} + M_{22}}. \tag{1.23}$$

After the weak lensing shear, the observed ellipticity of the galaxy, denoted as e^{obs}, can be expressed as

$$e^{\mathrm{obs}} = e^{\mathrm{int}} + \frac{2\gamma}{1-\kappa} \frac{1}{1 + |\gamma|^2/(1-\kappa)} \approx e^{\mathrm{int}} + \frac{2\gamma}{1-\kappa}. \tag{1.24}$$

Here e_i^{int} represents the intrinsic shape of the galaxy before lensing, and $2\gamma_i/(1-\kappa)$ represents the change in shape caused by weak lensing shear. This term is often defined as the reduced shear $g_i = \gamma_i/(1-\kappa)$. Generally, weak lensing makes an assumption that the intrinsic shape of the galaxies is random, and weak lensing signals can be extracted by the average shape of an ensemble of galaxies. However, this assumption is broken by the presence of intrinsic alignment between the galaxies. Despite this, we can infer the shear of a galaxy ensemble g^{inf} in a flat shear field using the average observed ellipticity

$$g_i^{\mathrm{inf}} = \langle e_i^{\mathrm{obs}} \rangle. \tag{1.25}$$

In practice, Eq. 1.25 is not what cosmologists do. Instead, a quantity that weak lensing analyses often use is called the two-point correlation function (TPCF), or two-point function. For cosmic shear measurement, we care about the product of the shapes of the galaxy pairs with a certain angular vector θ with a polar angle ϕ. (For a review of cosmic shear, see (34).) We first define the tangential and the cross term of the shear with regard to θ,

$$\gamma_t = -\mathcal{R}(\gamma e^{-2i\phi}) \tag{1.26}$$

$$\gamma_\times = -\mathcal{I}(\gamma e^{-2i\phi}). \tag{1.27}$$

γ_t correspond to the shear parallel or perpendicular to θ, while $\gamma_\times$ correspond to the shear at a 45 degree angle to θ. The cosmic shear two-point functions are then defined as

$$\xi_+(|\theta|) = \langle \gamma_t \gamma_t^* \rangle_{|\theta|} + \langle \gamma_\times \gamma_\times^* \rangle_{|\theta|} \tag{1.28}$$

$$\xi_-(|\theta|) = \langle \gamma_t \gamma_t^* \rangle_{|\theta|} - \langle \gamma_\times \gamma_\times^* \rangle_{|\theta|}. \tag{1.29}$$

Here the bracket $\langle\cdot\rangle_{|\theta|}$ denotes the average of all galaxy pairs with distance at $|\theta|$. $\xi_\pm(|\theta|)$ are commonly measured in leading wide-field imaging surveys to study the cosmic shear signal. In Fig. 1.3, I show an example of $\xi_\pm$ measured by the HSC Year-3 high-redshift shear catalog (4).

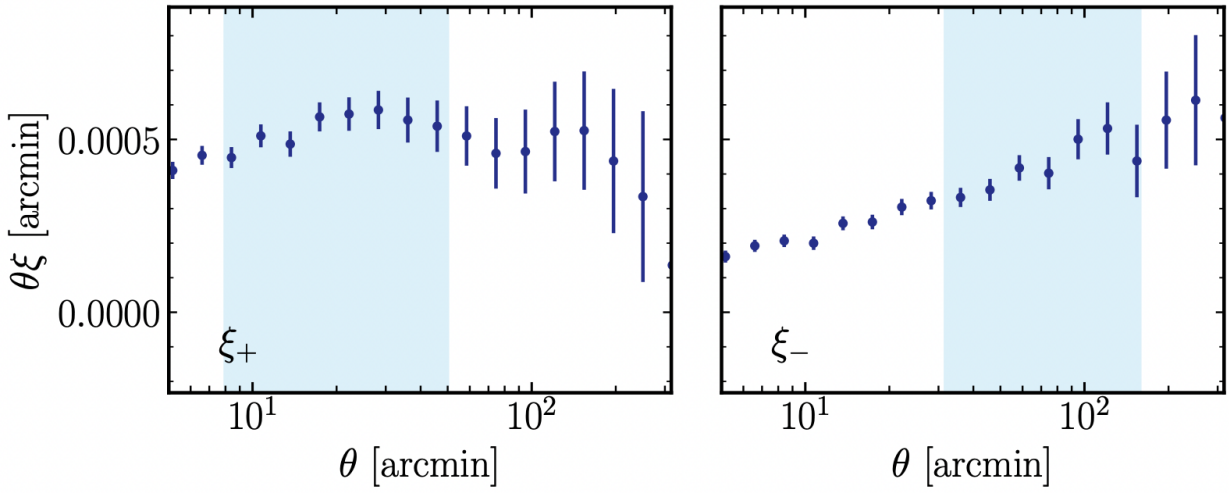

Figure 1.3: The measurement of the cosmic shear correlation function $\xi_\pm$ for the HSC Year-3 high-redshift shear catalog (Image taken from (4)). Data points within the blue region are taken into account in the cosmology analysis. The errorbars of the data points are estimated by 1404 mock shear catalogs.

Cosmic shear provides valuable information about the power spectrum of the universe's large-scale structure. When galaxies are divided into redshift bins, i.e., tomographic bins, the angular power spectrum between bin i and bin j , C_ℓ^{ij} is directly linked to the matter power spectrum (35)(36) in Eq. 1.14 by

$$C_\ell^{ij} = \int \frac{d\chi}{\chi^2} P(\ell/\chi; z(\chi)) q^i(\chi) q^j(\chi). \tag{1.30}$$

Notice that here the wave number is converted to ℓ/χ and the redshift is expressed as a function of the comoving distance. $q^i(\chi)$ and $q^j(\chi)$ are the lensing efficiency function for tomographic bins i and j. They are expressed as

$$q^i(\chi) = \frac{3\Omega_m H_0^2}{2c^2} \frac{\chi}{a(\chi)} \int_\chi^{\chi_h} d\chi' n^i(\chi'(z)) \frac{\chi' - \chi}{\chi'}. \tag{1.31}$$

Here $n^i(\chi(z))$ is the redshift distribution of the tomographic bin i. The shear-shear two-point correlation function can be calculated by the Hankel transform of the angular power spectrum,

$$\xi_\pm^{ij}(\theta) = \frac{1}{2\pi} \int d\ell \ell C_\ell^{ij} J_{2\mp2}(\ell\theta), \tag{1.32}$$

where J_n is the n-th order Bessel function of the first kind. The set of equations explicitly shows that the shear-shear TPCFs are related to the matter power spectrum via the redshift distribution of the ensemble of galaxies. As a result, the uncertainty in the redshift distribution can impact the weak lensing analysis. We will see more on this topic in §5.

In Fig. 1.4, the HSC Year-3 cosmic shear analysis using the TPCF is shown, yielding constraints on Ω_m and S_8, which quantifies the fraction of matter in the universe and the clumpiness of the large scale structure, assuming the universe is governed by the Λ-CDM model. The plot also includes measurements from other surveys like DES-Y3 and KiDS-100, as well as the constraint from Planck 2018. Notably, there appears to be a potential tension between cosmic shear and CMB measurements regarding S_8, posing a challenge to the Λ-CDM model in modern cosmology.

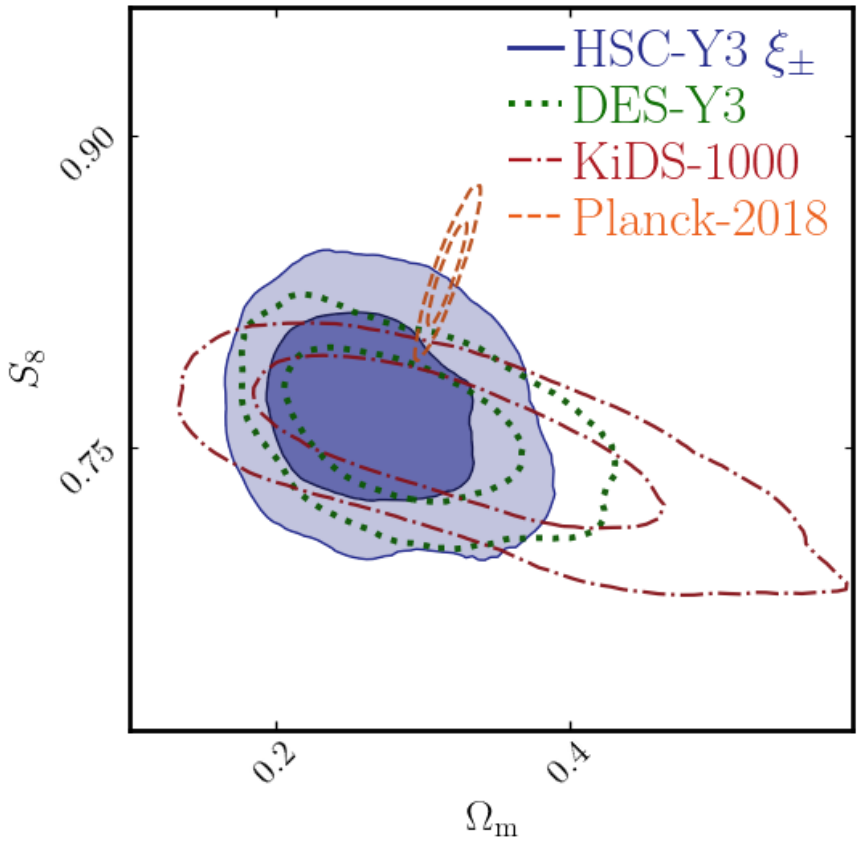

Figure 1.4: The cosmological constraints derived from the cosmic shear two-point correlation functions (2PCFs) (Image taken from (5)) of the HSC-Y3 survey are depicted by the blue solid line. These constraints are compared to the results obtained from the Planck-2018 survey, represented by the orange dashed line. Additionally, the constraints from the DES-Y3 survey are shown in green with a dotted line, while the KiDS-1000 survey results are represented by the red dash-dotted line.

Another important technique in weak lensing is galaxy-galaxy lensing, which involves observing the tangential shear around a galaxy or cluster center. Instead of correlating galaxy shapes with each other as in cosmic shear, galaxy-galaxy lensing correlates the shapes of background galaxies with the positions of lens galaxies. The tangential shear γ_t is directly related to the excess surface mass density $\Delta\Sigma(R)$, which represents the difference between the average surface mass density $\bar{\Sigma}(R)$ within a radius R and the surface mass density $\Sigma(R)$ at that radius

$$\gamma_t(R)\Sigma_{\rm crit}(z_l, z_s) = \Delta\Sigma(R) = \bar{\Sigma}(R) - \Sigma(R). \tag{1.33}$$

Here $\Sigma(R)$ is the surface mass density at R, and $\bar{\Sigma}(R)$ is the average surface mass density within the radius R. $\gamma_t(R)$ is the tangential shear defined in Eq. 1.26. Notice that when the angle θ is pointing from a point mass to a source galaxy, the weak lensing does not generate any $\gamma_\times$. Therefore, $\gamma_\times$ is often used as a signal for the systematics. $\Sigma_{\rm crit}(z_l, z_s)$ is the critical surface density for given redshifts of the lens and source galaxy,

$$\Sigma_{\rm crit}(z_l, z_s) = \frac{c^2}{4\pi G}\frac{d_A(z_s)}{d_A(z_l)d_A(z_l, z_s)(1+z_l^2)}. \tag{1.34}$$

Here $d_A(z)$ is the angular diameter distance from redshift z to the earth, and $d_A(z_l, z_s)$ is the angular diameter distance from z_l to z_s. In Figure 1.5, I show an example of the measurement of excess surface mass density using the HSC Year-3 source galaxies and the BOSS LOWZ lens galaxies (4).

Galaxy-galaxy lensing is a powerful cosmological tool that complements galaxy clustering by providing different sensitivities to galaxy bias (31). By combining galaxy-galaxy lensing, galaxy clustering, and cosmic shear, researchers can break the degeneracies between galaxy bias and the power spectrum amplitude, leading to more robust cosmological constraints. Several studies(e.g., (7; 37; 38)) have already combined these probes to enhance their constraining power. In the 2020s, upcoming surveys like the Vera C. Rubin Observatory and Nancy Grace Roman Space Telescope will provide rich datasets for weak lensing analysis (39; 40), allowing for even tighter constraints on the Λ-CDM model, and explore models beyond that. These advancements have the potential to challenge our current understanding of dark matter and dark energy.

1.2.2 Systematics in Weak Lensing

Understanding and mitigating the systematics in weak lensing measurements is crucial in current research. In this section, we will explore the motivation behind unbiased weak lensing measurements and the increasing challenges associated with them (For a detailed review, see (33)). We will examine various sources of weak lensing systematics and discuss the ongoing efforts to address them.

Motivation

There are two main drivers for studying the systematics of weak lensing. Firstly, the precise measurement of cosmological parameters, particularly the Ω_m-S_8 space, is a key scientific goal

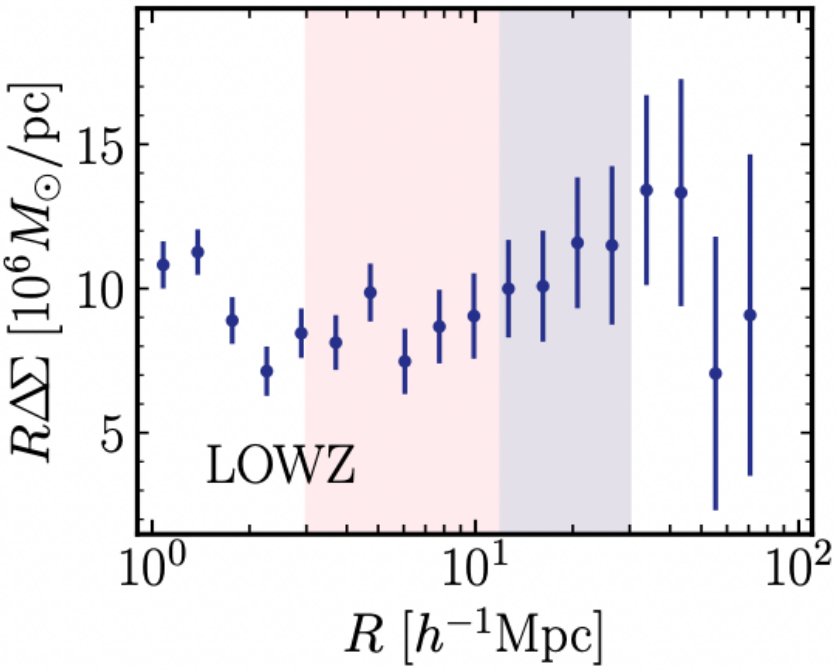

Figure 1.5: Measurement of the excess surface mass density with BOSS LOWZ volume limited lens sample and HSC Year-3 high-redshift source samples (Image taken from (4)). The orange shaded region is the range used for the small-scale analysis (6), the purple shaded region is the range used for the large-scale analysis (7).

of weak lensing. The tension between weak lensing and cosmic microwave background (CMB) measurements in Figure 1.4 challenges the Λ-CDM model, making it crucial to understand and address the systematics of weak lensing.

Secondly, there is a technological driver due to the exponential growth of data volume in weak lensing studies. The number of galaxies observed in cosmic shear surveys has been rapidly increasing, as shown in Figure 1.6. In the early 2000s, cosmic shear generally only involves tens to hundreds of thousands of galaxies (e.g., (41; 42; 43; 44)). In the 2010s, the stage-III surveys push the number to tens to hundreds of millions (e.g., (45; 46; 47)). In the next decade, the emerging Stage-IV surveys will push this number over a billion (e.g., (48; 49; 50)). We can clearly see that the number of galaxies we observe in the galaxy survey is undergoing exponential growth. In fact, the number of galaxies observed doubles every 1.9 years.

This exponential growth leads to a decrease in statistical uncertainties by about $\sim 1/\sqrt{N}$. This has significant implications to the study of systematics for the weak lensing science. First, the budget for mitigating known systematic errors decreases, potentially causing previously effective models to break down. Secondly, previously subdominant systematics may become statistically significant due to the increased statistical precision, motivating the dis-

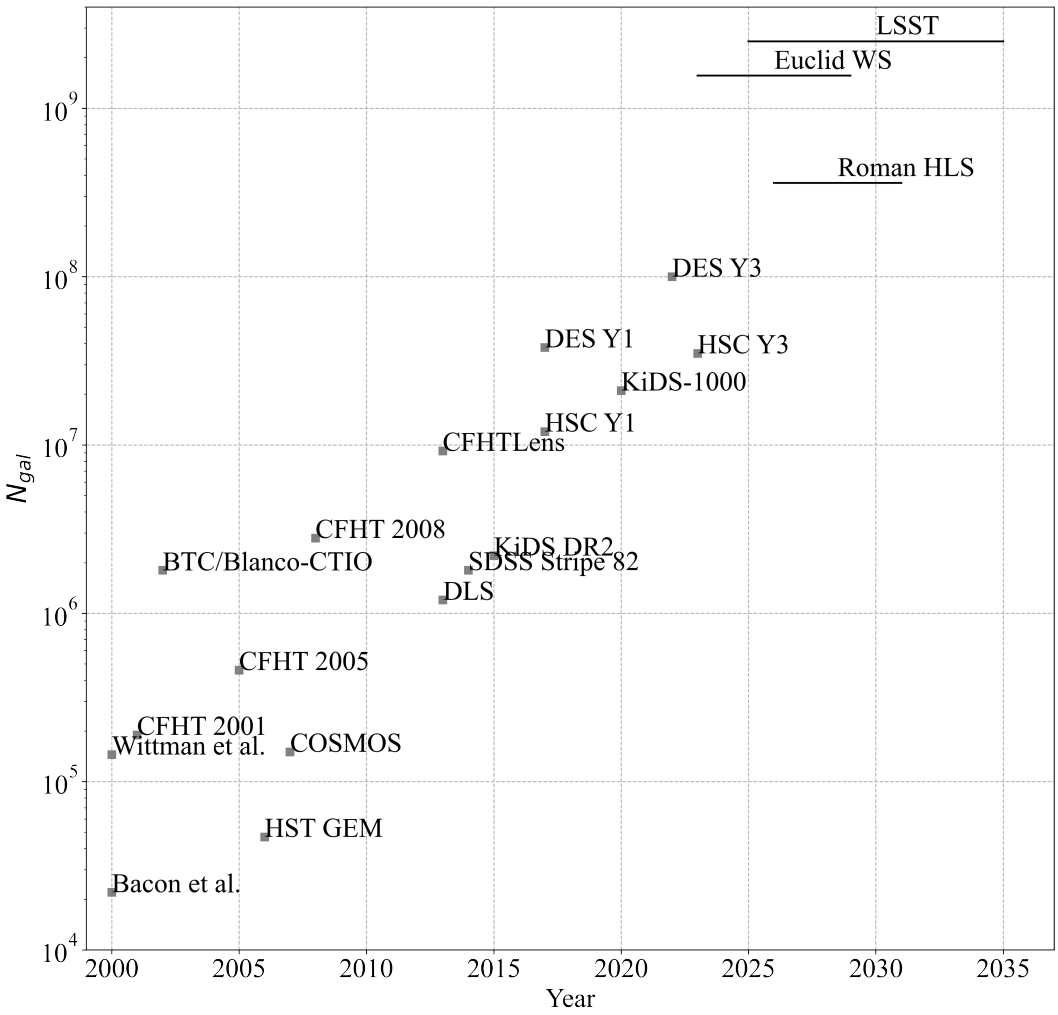

Figure 1.6: The number of galaxies involved in cosmic shear studies in the past, in recent years, and in the future. We can clearly tell that the number follows an exponential increase. The increase in data volume for the weak lensing science decreases the statistical uncertainty of the measurement, making systematics study more important over time.

covery of new systematics.

In summary, understanding and mitigating weak lensing systematics is essential for precise cosmological measurements, given the tension with CMB measurements, as well as the

challenges posed by the exponential growth of data volume.

Sources of systematics

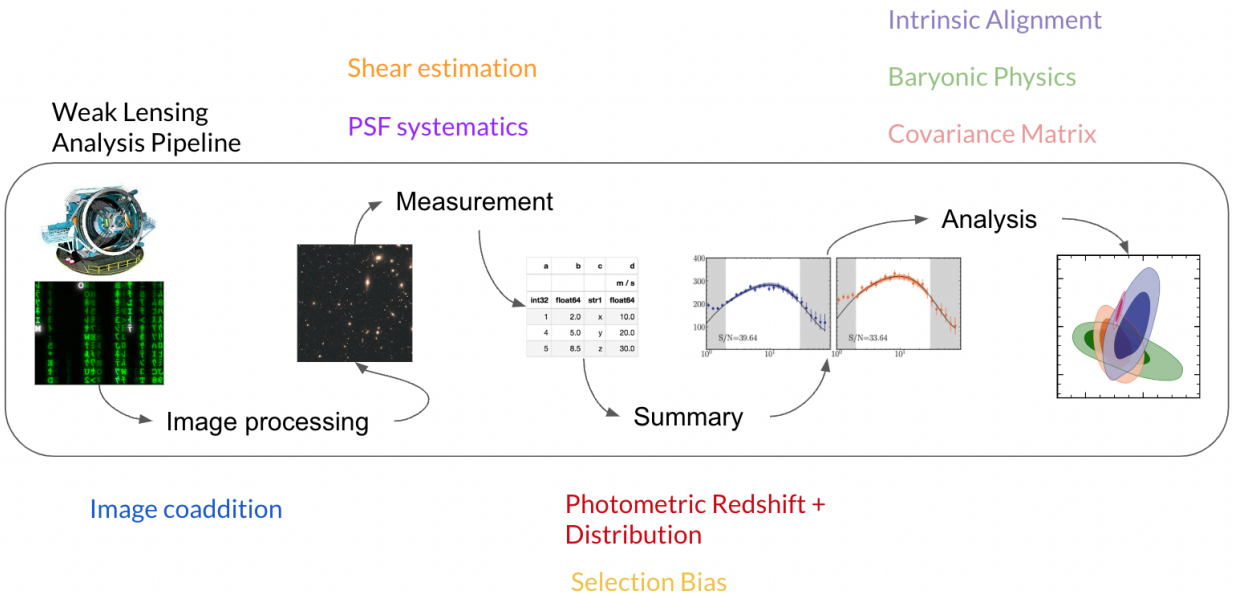

Figure 1.7: A flowchart of the weak lensing analysis pipeline. The data go through the stages of single-exposure images, coadded images, catalogs, summary statistics, and cosmological parameters. Different kinds of systematics error emerge at different stage of the analysis

In this section, I provide a summary of key sources of systematics that need to be considered for precise cosmological analysis using weak lensing measurements. In Figure 1.7, I illustrate the data flow in a typical weak lensing analysis. The data exist in different forms in the pipeline, from single visit exposure to coadded images, to catalog of sources, to summary statistics such as TPCF, and finally to cosmological parameters. In this section, I will summarize systematics that emerges in different stages of the analysis.

At the single exposure or single visit level, detector effects can cause systematics errors. For example, detector effects such as charge transfer inefficiency (CTI), and brighter-fatter effect (51; 52) can cause shear bias. Additionally, the process of stacking exposures into a coadded image also requires careful treatment to avoid shear bias (53).

The process of generating a shear catalog from the coadded images requires detecting the galaxies and estimating their shape and shear. Point Spread Function (PSF) is the response from the imaging system to a point source. The PSF changes the size and shape of the observed galaxies. Therefore, shape correction for PSF is an important part of every shear estimation method. The modeling error of the shape and size, as well as the higher moments of the PSF can also cause shear bias. See § 2-4 for more detail about PSF systematics. Multiplicative bias in shear is a challenging systematics introduced at the shear estimation

process due to its difficulty of detection. One approach to quantifying the multiplicative bias of the galaxy ensemble is through image simulation (e.g., (54; 55)). Other methods construct unbiased estimators during the shear estimation through perturbation-based methods (e.g., (56; 57; 58; 59; 60)).

During the stage of measuring summary statistics from the catalog, Selection bias is a systematic error that can occur due to the dependence of galaxy selection on the shear. When the selection of galaxies is influenced by the shear, it introduces a bias in the measured shear. One example of selection bias is the detection process, where galaxies are typically selected based on their signal-to-noise ratio. Another example is tomographic binning, which involves selecting galaxies based on their photometric redshift.

Another significant systematics in this stage is the inference of the photometric redshift distribution and the proper handling of its uncertainty (61). The redshift distribution, denoted as $n(z)$, plays a crucial role in modeling the cosmic shear signal, particularly due to its strong degeneracy with the amplitude of the power spectrum, as we saw in Section 1.2.1. In order to obtain reliable statistical constraints on the parameters, it is important to properly account for the uncertainty associated with the redshift distribution. This entails marginalizing the uncertainty in the cosmological analysis. For more detailed information on the marginalization of redshift distribution uncertainty in cosmic shear analyses, see §5.

In the analysis level, two significant challenges in modeling astrophysical effects on weak lensing can introduce bias in the cosmological parameters. Firstly, intrinsic alignment refers to the coherence in galaxy shapes that is not caused by lensing effects (62; 63; 64; 65). The weak lensing analysis assumes that galaxy shapes are independent, but intrinsic alignment violates this assumption. Secondly, the modeling of baryonic physics introduces another astrophysical source of systematics. Studying the impact of galaxy formation on the matter power spectrum requires hydrodynamical simulations with high resolution, large box lengths, and realistic galaxy formation models. While challenging, addressing these systematics is feasible in the current era.

1.3 Statistics

Statistics plays a fundamental role in cosmology, providing the mathematical framework for analyzing and interpreting observational data. Many of the physical quantities used to characterize the cosmological model are described in statistical terms, e.g., the power spectrum mentioned in Section 1.1.3 and two-point correlation function mentioned in Section 1.2.1. In cosmological analyses, the likelihood function is employed to determine the most probable values for the cosmological parameters that best fit the data. It is also utilized to account for systematic errors through the process of marginalization.

Accurate formulation of statistical formalism is vital for ensuring the robustness and reliability of weak lensing analyses. Bayesian statistics, in particular, is commonly employed in cosmology. In this section, I will provide a brief overview of statistical formalism, with a focus on Bayesian statistics, to highlight its significance in the field of weak lensing analysis. For a more detailed read about Bayesian statistics and data analytics, see (66; 67).

Let us start by defining the probability of statement X to be true as $P(X)$ and the probability of X being false being $P(\bar{X})$. The constraint on the probabilities will then be

$$P(X) \geq 0 \tag{1.35}$$
$$P(X) + P(\bar{X}) = 1. \tag{1.36}$$

The first equation means that the probability of an event has to be non-negative, and the second equation means that the sum of the probability of all outcomes of an event has to be 1. The scenario can be generalized to the probability of a continuous quantity. Assume x can take any value from $-\infty$ to ∞. Then the constraints on the probability density function $p(x)$ is

$$p(x) \geq 0 \tag{1.37}$$
$$\int_{-\infty}^{\infty} p(x)dx = 1. \tag{1.38}$$

Now let us introduce another variable Y, which can also take true or false as its value. The joint probability of X and Y can be expressed in terms of conditional probability in two different orders,

$$P(X, Y) = P(X|Y)P(Y) = P(Y|X)P(X). \tag{1.39}$$

Here $P(X|Y)$ is the conditional probability, which is the probability of X given the value of Y. The conditional probability gives rise to the most profound equation in Bayesian statistics, the Bayes theorem. For a set of parameter Ω,

$$P(\Omega|D) = \frac{P(D|\Omega)P(\Omega)}{P(D)}, \tag{1.40}$$

which is identical to Eq. 1.39, except we have the quantity Ω that we would like to infer. The left-hand side of Eq. 1.40 is called the posterior on Ω inferred by the data D. On the right-hand side, $P(D|\Omega)$ is called the likelihood function, $P(\Omega)$ is called the prior of Ω, and $P(D)$ is called the evidence of the data.

Let us show a common likelihood function used in cosmological analyses, the Gaussian likelihood. In the weak lensing analysis that uses high dimensional data vector D to infer a set of cosmological parameters Ω, it is often assumed that the observed data vector is drawn from a Gaussian distribution (The Gaussian assumption and cosmological parameter-independent assumption are meticulously studied in (68)). The likelihood function is written as

$$\mathscr{L} = P(D|\Omega) = \frac{1}{(2\pi)^{k/2}\sqrt{\det \Sigma_D}} \exp[-\frac{1}{2}(D - T(\Omega))^T \Sigma_D^{-1}(D - T(\Omega)]. \tag{1.41}$$

Here k is the dimension of the D, Σ_D is the covariance matrix of D, and $\det(\cdot)$ is the determinant of the matrix. $T(\Omega)$ is the theoretical value of the data vector given the cosmological parameters, which involves multiple layers of forward modeling.

An important concept of probability is marginal probability. Consider two continuous random variables x and y. The marginalization rule is

$$p(x) = \int_{-\infty}^{\infty} p(x, y) dy. \tag{1.42}$$

In Bayesian statistics, one important application of the marginalization rule is to compute the evidence. In analyses to get the confidence interval of θ given D, the evidence $P(D)$ is unimportant to the outcome. However, when comparing the likelihood for different Ds, the evidence becomes important. It is calculated by

$$P(D) = \int d\Omega P(D, \Omega) = \int d\Omega P(D|\Omega) P(\Omega). \tag{1.43}$$

An example of the usage of marginalization in cosmology is to incorporate the uncertainty in the nuisance parameters ν, e.g., photometric redshift parameters and multiplicative biases, etc, into the cosmological parameters Ω. To achieve that, we first need the joint distribution $P(\Omega, \nu)$. The marginalized probability of the cosmological parameters are calculated by

$$P(\Omega|D) = \int d\nu P(\nu, \Omega|D) = \int d\nu P(\Omega|\nu, D) P(\nu), \tag{1.44}$$

where $P(\nu)$ is the prior on the nuisance parameters. In §5, we will see that Eq. 1.44 is used to marginalize over the redshift distribution uncertainties under the guidance of Bayesian statistics.

1.4 Structure of the Thesis

Apart from the introductory chapter, this thesis primarily presents the outcomes of four research projects aimed at enhancing our comprehension of weak gravitational lensing systematics for the advancement of weak lensing science in the 2020s. Chapters 2 to 4 form a trilogy that focuses on investigating an essential weak lensing systematic known as the Point Spread Function (PSF). These chapters extend our understanding of PSF systematics beyond second moments, employing techniques like image simulation, Bayesian inference, and forecasting to analyze higher moments. In Chapter 5, I examine a crucial step in weak lensing analysis – the modeling and marginalization of redshift distribution uncertainty. I also propose a statistics-principled method for marginalizing high-dimension redshift distribution uncertainties, called Bayesian resampling.

Chapter 2 serves as the opening part of my PSF systematics trilogy in weak lensing. In this pathfinder investigation, we employ image simulations to demonstrate that inaccuracies in modeling the PSF's radial fourth moments, or kurtosis, result in multiplicative shear bias. To assess the magnitude of this issue, we analyze image data from the HSC Public Data Release 1 (69). We establish the significance of the shear bias caused by modeling errors in the PSF's radial fourth moments, particularly for future stage-IV weak lensing surveys.

This work resulted in the publication of the paper "Impact of point spread function higher moments error on weak gravitational lensing", published in the "Monthly Notices of the Royal Astronomical Society, Volume 510, Page 1978-1993"(70).

Building upon the path-finding study, Chapter 3 presents a more comprehensive study into the impact of PSF higher moments modeling errors. This study expands the analysis beyond kurtosis to include all higher moments M_{pq}. To achieve this, we develop advanced numerical techniques that enable precise generation of specific residuals in higher moments during image simulation. By doing so, we establish a direct connection between shear bias and PSF higher moments modeling residual. Utilizing the HSC PDR1 data, we quantify the realistic modeling errors in PSF higher moments and generate synthetic PSF higher moments residual maps for the LSST DC2. To assess their implications for cosmology, we employ Fisher forecast methods to predict the bias on cosmological parameters. This comprehensive study provides valuable insights into the influence of PSF higher moments modeling errors on weak lensing analyses. This work resulted in the publication of the paper "Impact of point spread function higher moments error on weak gravitational lensing - II. A comprehensive study", published in the "Monthly Notices of the Royal Astronomical Society, Volume 520, Page 2328-2350"(71).

In Chapter 4, a solution is presented to address the issues identified in Chapters 2 and 3. The proposed method expands the traditional null tests, which typically focus on the PSF second moment, to include the PSF fourth moments and other higher-order terms. By applying this extended method to the HSC Year-3 shear catalog, the method revealed that the catalog is affected by PSF fourth moment leakage at a statistically significant level. Importantly, the effectiveness of the proposed method in mitigating this impact on cosmology is demonstrated. The findings of this chapter have played a crucial role in guiding the choice of PSF systematics models in the HSC Year-3 cosmic shear analysis (5; 72). This work resulted in the publication of the paper "A General Framework for Removing Point Spread Function Additive Systematics in Cosmological Weak Lensing Analysis", published in the "Monthly Notices of the Royal Astronomical Society, (*in press*)"(73).

Chapter 5 proposes a statistics-based approach to effectively handle the challenge of marginalizing the uncertainty associated with the redshift distribution in cosmic shear analysis. The high dimensionality of the redshift distribution uncertainty makes its mitigation complicated in a Markov Chain Monte Carlo (MCMC) inference. Conventional analysis typically reduces the dimensionality by only modeling the shift of the distribution. We proposed a novel statistical method that can take the entire high dimensional uncertainty into account, by sampling the probability density of the $n(z)$, analyzing individual samples, and combining the samples. We compare our method to traditional methods and other novel methods. The results indicate that, for the HSC Year-3 cosmic shear analysis, the traditional shift model is sufficient. However, it is demonstrated that as the statistical uncertainty decreases, the bias between the shift model and the proposed method increases. This work resulted in the publication of the paper "Photometric redshift uncertainties in weak gravitational lensing shear analysis: models and marginalization", published in the "Monthly Notices of the Royal Astronomical Society, Volume 518, Page 709-723"(74).

In Chapter 6, I discuss the implication of the work described in this thesis. I specifically focus on the lesson learned in these systematics focusing study, and the path forward for preparing the weak lensing analysis of the stage-IV surveys.

Chapter 2

Impact of point spread function higher moments error on weak gravitational lensing – I. The Path-Finding Study

Tianqing Zhang[1], Rachel Mandelbaum[1], The LSST Dark Energy Science Collaboration.

[1]McWilliams Center for Cosmology, Department of Physics, Carnegie Mellon University, 5000 Forbes Ave, Pittsburgh, PA 15213.

Abstract

Weak gravitational lensing is one of the most powerful tools for cosmology, while subject to challenges in quantifying subtle systematic biases. The Point Spread Function (PSF) can cause biases in weak lensing shear inference when the PSF model does not match the true PSF that is convolved with the galaxy light profile. Although the effect of PSF size and shape errors – i.e., errors in second moments – is well studied, weak lensing systematics associated with errors in higher moments of the PSF model require further investigation. The goal of our study is to estimate their potential impact for LSST weak lensing analysis. We go beyond second moments of the PSF by using image simulations to relate multiplicative bias in shear to errors in the higher moments of the PSF model. We find that the current level of errors in higher moments of the PSF model in data from the Hyper Suprime-Cam (HSC) survey can induce a ~ 0.05 per cent shear bias, making this effect unimportant for ongoing surveys but relevant at the precision of upcoming surveys such as LSST.

2.1 Introduction

Gravitational lensing is the deflection of light from distant objects due to the gravitational effects of more nearby objects on the geometry of the Universe. Weak gravitational lensing,

or weak lensing, is what occurs in the limit that the lensing deflections are sufficiently weak that they only lead to modest changes in the object's observed shape, size, and flux rather than dramatic phenomena such as Einstein rings or multiply-imaged sources. Its sensitivity to the gravitational potential along the line-of-sight makes weak lensing one of the most powerful tools for probing dark matter, dark energy and the growth of large-scale structure of the Universe (75; 76; 77). Among all the effects on the galaxy caused by weak lensing, the change in shape, also called shear, is the most accessible signal up-to-date.

The requirements on removal of systematic biases and control of systematic uncertainties in the measurement become tighter as the statistical errors decrease to sub-percent levels, starting with the ongoing or recently completed "Stage III" cosmological surveys (78) such as the Dark Energy Survey (DES;) (79), the Kilo-Degree Survey (KiDS)(80), the Hyper Suprime-Cam survey (HSC)(81), and the future "Stage IV" ground-based surveys such as the Vera C. Rubin Observatory Legacy Survey of Space and Time (LSST)(48; 82), and space-based surveys such as the *Nancy Grace Roman* Space Telescope (49; 83) and *Euclid* (50).

The Point Spread Function (PSF) is a distribution function that is commonly used to describe the blurring effects of the atmosphere, telescope optics, and pixelization, which convolves the light profiles of the stars and galaxies in the images. The PSF therefore changes the observed shape and size of the galaxy. To measure the true galaxy shape despite the convolution with the PSF, one must model the PSF at the galaxy position, based on the images of stars around it; a variety of methods exist for doing so, e.g., PSFEx (84) and PIFF (PSF in Full FOV; (85)).

Upon obtaining the PSF model at the position of a given galaxy, one can use a variety of methods to measure the shape of the galaxy or its response to weak lensing shear e.g., (56; 57). A mismatch between the PSF model and the true PSF can cause a systematic bias in the weak lensing measurement. Previous work in this field has focused on the impact of the errors in the second moments of the PSF model, i.e., differences between the size and shape of the true and model PSF, on the weak lensing shear measurement (86; 87; 88; 89). Control of residual systematic uncertainties in the shear due to second-moment errors in PSF modeling is considered one of the main systematics in weak lensing shear inference for both previous surveys such as the HSC survey (54) and for upcoming surveys such as LSST (90).

The formalism derived in the aforementioned papers on this topic would predict zero systematic bias in shear inference as long as the second moments of the PSF model completely match those of the true PSF, neglecting any differences between the higher moments of the PSF model and true PSF. When the PSF is unweighted, the weak lensing shear is only associated with the second moments of the galaxy and PSF. However, a weight function is necessary for shear inference in order to reduce the impact of pixel noise. (91) shows how the lensing shear inference is affected by PSF higher moments when weighted PSFs are used. (92) point out that mismatches between the higher moments of the PSF and the true PSF induce additional multiplicative and additive shear biases on top of those predicted by the second moment formalism in (87). In this paper, we investigate the impact of the higher

moments error – later as HME – on the galaxy shear measurement with image simulations generated using GalSim[1] (93) and real data from the HSC Public Data Release 1 (PDR1) (81). We simplify the problem by only investigating round PSFs and only considering their radial fourth moments, and the associated multiplicative biases. The goal of this paper is to investigate whether the HME of the PSF model is a significant contributors to systematic biases and uncertainties in the weak lensing shear measurement for LSST.

The structure of this paper is as follows. In Section 2.2, we describe relevant background material about weak lensing shear estimation and PSF modeling. We introduce the simulation methods and our analysis of real data in Section 2.3. In Section 2.5, we show the results of our analysis of the simulations and real data. Based on the results, we derive conclusions about the significance of shear biases caused by the HME of the PSF model in Section 2.6.

2.2 Background

In this section, we summarize background material related to weak lensing shear (Section 2.2.1), and the impact of the PSF and PSF modeling (Section 2.2.2).

2.2.1 Weak Lensing Shear

Weak gravitational lensing occurs when light from background objects gets mildly deflected by the intervening matter in the Universe (for a review, see 34). The scientific significance of weak lensing is by no means "weak": because of its sensitivity to the gravitational potential of the large-scale structure of the Universe, it is a powerful probe of the dark matter distribution and the growth of cosmic structure with time.

Quantitatively, weak lensing is a local linear transformation between the pre-lensing and post-lensing light-ray. The relation between the post-lensing position (x, y) and the pre-lensing position (x', y') can be expressed as

$$\begin{pmatrix} x' \\ y' \end{pmatrix} = (1-\kappa) \begin{pmatrix} 1-g_1 & -g_2 \\ -g_2 & 1+g_1 \end{pmatrix} \begin{pmatrix} x \\ y \end{pmatrix}, \tag{2.1}$$

where the reduced weak lensing shear $g = g_1 + \mathrm{i}g_2$ is a complex number that describes the anisotropic distortion of the galaxies, i.e. the shape distortion, and the convergence κ is a scalar that describes the isotropic distortion (magnification or contraction) of the observed galaxy. The convergence changes the observed flux and size of the galaxy, while the reduced shear changes the shape of the galaxy, e.g., turning round galaxies into elliptical galaxies. The first component of the reduced shear, g_1, is responsible for the stretch along the x- and y-axes, while the second component, g_2, describes the stretch along the diagonal axes at 45° to the x- and y-axes. In this paper, we will not consider the convergence effect ($\kappa = 0$), so the shear is the same as the reduced shear.

[1] `https://github.com/GalSim-developers/GalSim`

The mild distortions of galaxy shapes induced by weak lensing, i.e., shear, can only be detected through statistical measurements, often including millions of galaxies (54; 94; 95). Typically the coherent shape distortions induced by weak lensing are measured either via cross-correlation with the positions of galaxies in a massive nearby lens sample (galaxy-galaxy lensing), or via auto-correlation of pairs of galaxy shapes (cosmic shear; 1; 47; 96). The statistical and systematic uncertainties in the shear signal are the main obstacles in making precise cosmological measurements using weak lensing (77). There are two primary sources of statistical uncertainty in the shear signal (97): The first one is caused by the dispersion in the galaxy intrinsic shapes, i.e., shape noise. The second source of statistical uncertainty is due to the large-scale structure that causes various weak lensing signal among the Universe, surveys that observe part of the Universe get a sampling uncertainty, also known as the cosmic variance (98).

There are multiple source of systematic biases that affect the measurement of the weak lensing shear (for a review, see 33). A common approach to systematic biases is to estimate and remove them, either by subtraction from the observed measurement or by modeling the physical processes that generate the biases. Since this correction is in general not perfectly known, even after the correction there will still be some residual systematic uncertainty. Generally, we want the systematic uncertainties to be sub-dominant compared to the statistical uncertainties. Upcoming surveys with reduced statistical uncertainties therefore require more stringent control of systematic uncertainty in the weak lensing shear measurement process.

2.2.2 PSF Modeling and Systematics

The Point Spread Function (PSF) describes the blurring of astronomical images due to the atmosphere and telescope optics. In practice, we work with the effective PSF, which also includes the pixel response function of the detector. The effective PSF convolves the light profiles of the stars and galaxies in the image, which changes the observed size and shape of the stars and galaxies.

Inferring the weak lensing shear distortion using information about the pre-PSF galaxy shape given the convolved image and PSF model is a substantial challenge. In the GREAT3 challenge (99), numerous shape measurement methods are tested and compared using simulations. Some of the methods shown there have been used in weak lensing survey science since then, e.g., re-Gaussianization in HSC (54), metacalibration and im3shape in DES (94), and shear calibration using pixel-level simulation (lensfit) in CFHTLenS and KiDS (100; 101; 102). However, several principled shear inference methods have been developed which should work to very high precision by avoiding the sources of bias in earlier methods (57; 58; 103) at least for isolated galaxies – but they do rely on an accurate PSF model.

There are two main categories of PSF modeling methods: empirical approaches that rely on the data in the images, and analytical approaches that simulate the physical processes of the PSF (33). The analytical approach is more commonly used in analysis of the space-based telescopes due to deterministic light propagation, e.g., the *Hubble* Space Telescope (HST)

and its COSMOS weak lensing analysis ((104); see also (105) for methods to assess model fidelity). Analysis of data from ground-based telescopes has tended to utilize empirical PSF models due to the stochastic nature of the atmosphere, e.g., the DES Y1 catalog (94), the KiDS-1000 catalog (95) and the first-year HSC catalog (54). The PSF profiles for space-based and ground-based telescopes are usually very different, because of the existence of the atmospheric PSF for the ground-based telescopes. For the purpose of this paper, we focus on the ground-based telescope PSF. The first step is to measure the effective PSF from a set of stars (typically isolated and with high signal-to-noise ratio) in the image – we refer to these as the PSF stars. Then the PSF at other positions is obtained by interpolation of the PSF model inferred from the PSF stars. Out-of-focus wavefront sensing has been recently developed to model the optical PSF (e.g., 106; 107; 108; 109) and a composite PSF model with wavefront modeling of the optical PSF component is planned to be used in future DES releases (85). The coadded image is a combination of several images at a given point on the sky, which has implications for its PSF. For example, in the HSC pipeline, the coadded PSF is generated in a principled way through weighted averaging of individual exposures, resulting in a well-defined PSF model also based on weighted averages (110).

The limited information on the spatial and temporal variation of the PSF for ground-based telescopes leads to some intrinsic limitations in the PSF model fidelity. Moreover, errors in modeling some detector effects, such as the brighter-fatter effect (51) and the interpixel capacitance of the complementary metal-oxide-semiconductor (CMOS) detectors (111; 112), can also drive errors in PSF models. Most of the commonly-used tests to determine the quality of PSF modeling rely on estimates of PSF and star sizes and shapes, mathematically defined using the observed second moments of the images, e.g., most tests in (110). The weighted second moment Q_{ij} of a light intensity profile $f(x)$ is defined as

$$Q_{ij} = \frac{1}{F^{(0)}} \int \mathrm{d}x_i \mathrm{d}x_j (x_i - x_i^{\mathrm{cen}})(x_j - x_j^{\mathrm{cen}}) f(\boldsymbol{x}) \omega(\boldsymbol{x}). \tag{2.2}$$

Here $\omega(\boldsymbol{x})$ is the adaptive Gaussian weight that has a size and shape matched to that of the light intensity profile, centred at the centroid of the profile (86). The weight is introduced to reduce the effect of noise in real images; however, it is the reason that the PSF higher-moments affect shear measurement (91). $F^{(0)}$, the normalization factor, is the total flux of the light profile weighted by $\omega(\boldsymbol{x})$. x_i^{cen} is the weighted centroid in the i^{th} dimension, calculated as

$$x_i^{\mathrm{cen}} = \frac{1}{F^{(0)}} \int \mathrm{d}x_i \mathrm{d}x_j x_i f(\boldsymbol{x}) \omega(\boldsymbol{x}). \tag{2.3}$$

The weighted second moments radius of the light profile can be defined as $\sigma = \sqrt{(Q_{11} + Q_{22})/2} = \sqrt{T/2}$, where T is the trace of the second moment matrix. The ellipticity can be defined as $e_1 = (Q_{11} - Q_{22})/(Q_{11} + Q_{22}) = (Q_{11} - Q_{22})/T$ and $e_2 = 2Q_{12}/(Q_{11} + Q_{22}) = 2Q_{12}/T$. The e_1 and e_2 are related to the axis ratio and position angle of the galaxy ellipse. Like the reduced shear $g = g_1 + ig_2$, the shape is also a spin-2 quantity. Therefore, for the rest of the paper, we denote shape as $e = e_1 + ie_2$ and the amplitude of the shape as $|e| = \sqrt{e^* e}$.

(87) explored the systematic biases in weak lensing shear measurement associated with errors in modeling the second moments of the PSF. The bias in the measured ellipticity of the galaxy $\delta e^{\rm sys}$ is

$$\delta e^{\rm sys} \simeq (e_{\rm gal} - e_{\rm PSF}) \frac{\delta(R^2_{\rm PSF})}{R^2_{\rm gal}} - \left(\frac{R_{\rm PSF}}{R_{\rm gal}}\right)^2 \delta e_{\rm PSF}, \tag{2.4}$$

where $R_{\rm gal}$ and $R_{\rm PSF}$ are the radius of the pre-PSF galaxy and the PSF, respectively. The two error terms, $\delta(R^2_{\rm PSF})$ and $\delta e_{\rm PSF}$, are typically referred to as the PSF size and shape error, respectively. Eq. (2.4) is usually used to place requirements on the quality of the PSF model, given some requirement on the control of systematic biases in the weak lensing shear $\delta e^{\rm sys}_{\rm PSF}$. Based on the formalism above, requirements can be placed on tolerance for systematic uncertainty in second moments of the PSF model for weak lensing (e.g., Section 3 of 54). This formalism is exactly correct when the weight $\omega(\boldsymbol{x}) \equiv 1$ or when both the galaxy and the PSF are Gaussian with a Gaussian weight. In a realistic scenario, neither of these conditions will be met. Therefore, this formalism cannot be used to predict precise numerical values for the shear biases caused by PSF second moment errors, though it still provides an approximate estimate of their magnitude and trends with galaxy size.

The formalism described above for estimating weak lensing systematic biases and uncertainties induced by PSF modeling errors only considers the PSF second moments, not any of the higher moments of the PSF model.

In this paper, we explore shear biases directly associated with the higher moments modeling error of the PSF, by conducting image simulations with deliberated added HME to the PSF model, and by comparing real PSF model images to star images. In our approach, we focus on PSFs in ground-based observations. We will show that the HME of the PSF modeling (at least given current PSF modeling algorithms) contributes non-negligible systematic error for Stage IV ground-based weak lensing surveys.

In this paper, we demonstrate methodology and project shear biases due to higher moment errors of the PSF using a PSF modeling method called PSFEx (84). This method has been used in practice for weak lensing science in HSC (54; 110) and DES Y1 (47). Although Rubin's LSST science pipelines are unlikely to use PSFEx for LSST itself, assessing the status of algorithms that are currently in use can help us understand the current level of PSF modeling error and its impact on weak lensing science, and place requirements on future performance.

2.3 Methods

In this section, we describe key analysis methods used for this work. The first approach we take to quantifying the relationship between weak lensing shear systematics and the HME of the PSF model uses image simulations. Before diving in the simulation step, we first define the quantities we measure for the higher moments in Section 2.3.1, and explore the shear measurement methods that we are taking in Section 2.3.2. In Section 2.3.3, we introduce the

inputs and steps for producing the image simulations. Section 2.4 describes the approach to inspecting the PSF and its model in real data from the HSC survey. While the simulations enable us to relate the HME of the PSF model to a shear bias, the real data provides an estimate for the current level of HME in PSF models in real data.

2.3.1 Higher Moments

In this subsection, we introduce how the moments of light profiles are defined and computed in practice.

In principle, carrying out our study requires a method for measuring any higher moment of PSF light profiles (beyond second moments), and for introducing a controlled variation in individual higher moments while preserving the second moments. However, for this initial pilot study we consider a simplification, and quantify the impact of deviations only in the weighted radial fourth moment (defined below). In practice, we recognize that other higher moments may be relevant, but we defer a detailed decomposition to future work, focusing here on a rough order-of-magnitude estimate of the importance of the higher moments of the PSF for weak lensing.

In practice, we measure the standardized weighted radial 4^{th} moment, or kurtosis $\rho^{(4)}$, using GalSim (93). For a light profile $f(\mathbf{x})$, this quantity is defined as

$$\rho^{(4)} = \frac{\int (r/\sigma)^4 f(\mathbf{x})\omega(\mathbf{x})\mathrm{d}\mathbf{x}}{\int f(x)\omega(\mathbf{x})\mathrm{d}\mathbf{x}}. \tag{2.5}$$

where $r = |\mathbf{x}|$ and $\omega(\mathbf{x})$ is the adaptive Gaussian weight we used in Eq. (2.2), σ is the second moment radius. The superscript of $\rho^{(4)}$ is a notation for the kurtosis, rather than the 4^{th} power. The denominator is a normalization factor. The weighted radial kurtosis for some common PSF profiles is listed in Table 2.1. The Airy PSF has an undefined second moment σ and kurtosis when calculated without a weight function, and the weighted moments depend strongly on the choice of weight function. The kurtosis value we show in Table 2.1 is calculated with an adaptive Gaussian weight function with $\sigma_{\text{w}} = 0.41\lambda/D$, where D is the diameter of the aperture. This algorithm-generated weight function has the size proportional to the PSF size, and keeps the Airy profile well-sampled for moment measurements. For the rest of the paper, we define the fractional kurtosis bias $B[\rho^{(4)}]$ as

$$B[\rho^{(4)}] = \frac{(\hat{\rho}^{(4)} - \rho^{(4)})}{\rho^{(4)}} \tag{2.6}$$

where $\hat{\rho}^{(4)}$ is the model kurtosis and $\rho^{(4)}$ is the true kurtosis.

Again, to reiterate, while we quantify the impact of higher moments error (HME) of the PSF using the radial weighted kurtosis, in general not only the kurtosis but rather all higher radial moments are perturbed. All higher moments referred to throughout this paper are the scale-independent standardized weighted moments.

[!ht]

Profile	$\rho^{(4)}$
Gaussian	2.00
Kolmogorov	2.09
Moffat, $\beta = 3.5$	2.11
Sérsic, n = 1	2.35
Sérsic, n = 4	2.74
Airy PSF, $\lambda = 750$nm, $D = 8$m	1.91

Table 2.1: The weighted radial kurtosis value $\rho^{(4)}$ for commonly-used light intensity profiles. The kurtosis is measured using images with gradually decreasing pixel scale to the point that the kurtosis value converges to the second decimal place. Note that these are the radial kurtosis values for the named profiles themselves, without any additional pixel response function. The Airy profile is that for an 8-meter aperture telescope at $\lambda = 750$ nm. The kurtosis is calculated with a Gaussian weight function with $\sigma_{\rm w} = 0.41\lambda/D$, proportional to the scale of the Airy profile.

2.3.2 Shape and Shear Measurement

When measuring cosmological weak lensing, there are methods that measure the shape of individual galaxy and then take the average shape to measure shear. There are also methods that directly act on galaxy ensembles to measure shear. For the first category, the shape measurement method is a crucial element in the pipeline. For this reason, we investigate the bias on the outcome of shape measurement, for single galaxies, as a step toward understanding the impact of HME on weak lensing shear. It is important to notice that the shape biases we investigate are not induced by intrinsic limitations of the shape measurement methods, and we are expecting to get different responses from different methods. One commonly used shape measurement method is the re-Gaussianization (86) method implemented in the HSM module (113) in GalSim (93). To test for different responses to errors in the higher moments of the PSF model, we also carried out limited testing with the linear (86; 114) and KSB (115) methods as implemented in GalSim.

To ensure that our results reflect galaxy shape or ensemble shear biases due to errors in the higher moments of the PSF model, rather than reflecting limitations in the shape measurement methods, we perform each measurement twice. The first measurement e or g uses the true effective PSF, and the second measurement $\hat{e}$ or $\hat{g}$ uses the model effective PSF. The difference between the two measurements, $\hat{e} - e$ or $\hat{g} - g$, is the shape or shear bias we are interested in, denoted as δe or δg.

In real weak lensing observations, very large galaxy ensembles are typically measured to beat down the intrinsic shape noise. However, in the image simulations, we can bypass this problem using the approach from (116) of creating a 90-degree rotated counterpart for each galaxy before applying the cosmological lensing shear. We refer to a galaxy and its rotated

counterpart as a 90-degree rotated pair; the galaxies in each pair have opposite values of e_1 and e_2 in the absence of lensing shear, so (especially in simulations without pixel noise added) a very small number of galaxy pairs can be used to efficiently assess the level of ensemble shear estimation bias. The shear bias of the 90-degree rotated pair is calculated by

$$\delta g = \frac{(\hat{e} + \hat{e}_{90}) - (e + e_{90})}{2}, \tag{2.7}$$

where $\hat{e}$ and $\hat{e}_{90}$ are the shape of the original and the rotated galaxy, measured using the model PSF, and e and e_{90} are measured using the true PSF. When we have more than one galaxy and its pair, which we will call a galaxy ensemble, the ensemble shear is the average over different galaxy shear $\langle g \rangle$. The ensemble shears $\langle g \rangle$ and shear biases $\delta\langle g \rangle$ are estimated in an analogous process, with $\hat{e}$ replaced by the average shape $\langle \hat{e} \rangle$ in Eq. (2.7).

While significantly increasing the efficiency of the simulation and decreasing the statistical uncertainty on the ensemble shear, this approach using 90-degree rotated pairs has its limitations. For example, it limits our ability to measure selection bias; however, this is not the focus of this paper.

In addition to these older battle-tested methods whose limitations are well-understood, we also use metacalibration (56; 57), a state-of-the-art method that self-calibrates multiplicative and additive bias in the ensemble shear inference. The goal of doing so is to check how sensitive our results are to the choice of shear inference method. We use the implementation of metacalibration in the publicly-available NGMIX[2] package.

2.3.3 Image Simulation

Here we describe the image simulation procedure used in this paper. The objects we simulate are postage stamp images of PSF-convolved galaxies and PSFs. For each step, we first explain the general settings for all simulations, and then provide details of different simulations. The parameters used in some of the simulations are tabulated in Table 2.2.

For all of the image simulations, we will need to generate two types of postage stamp images with GALSIM objects: the observed image of the isolated galaxy convolved with true PSF, and the image of the PSF, with or without kurtosis error. All images are generated with a pixel scale of 0.2arcsec, similar to the pixel scale of the LSST camera. The images are rendered using the Fourier Transform method in GALSIM, and include the pixel response function. The PSF-convolved galaxy and true PSF images are then used to estimate the single galaxy shape e, 90-degree rotated pair shear g and the ensemble shear $\langle g \rangle$. The PSF-convolved galaxy and model PSF images are used to estimate the single galaxy shape $\hat{e}$, 90-degree rotated pair shear $\hat{g}$ and the ensemble shear $\langle \hat{g} \rangle$. No noise is included in the images.

The galaxy profiles that we simulate as specified in Section 2.3.4, and the PSF profiles specified in Section 2.3.5, exhibit a gradual increase in complexity and realism. We provide a general roadmap to our simulations in Section 2.3.6. There we describe how the simpler

[2] `https://github.com/esheldon/ngmix`

simulations help us develop intuition about the main parameters that determine shear biases for a given PSF kurtosis bias, while the complicated simulations provide a more realistic estimate of ensemble shear biases due to PSF kurtosis bias for LSST.

2.3.4 Galaxy Profile

The first step of the image simulation process is to define the galaxy profiles that we are going to simulate. Our approach is to generate simulations that include galaxy profiles with increasing complexity. First we generate a single (non-round) Gaussian galaxy, then we add complexity to the model to include Sérsic profiles. We generate 90-degree rotated galaxy pairs, as described in Sec. 2.3.2, to certify the results we get from single galaxy experiments. Finally, we generate ensembles of galaxies that include a range of profiles, sizes, and shapes, similar to that found in real data. We also generate 90-degree rotated pairs for the galaxies from the catalog, to eliminate the shape noise. To gain intuition, we start by quantifying shape measurement biases for single galaxy experiments. We later proceed to study ensemble shear biases.

The first and simplest galaxy profile we generate is a 2d Gaussian profile, specified by its size σ and ellipticity e. We alter the parameters of the Gaussian galaxy to see its impact on the kurtosis induced shape/shear bias. The size of the Gaussian galaxies range from FWHM $= 1.2''$ to $12.0''$, and the ellipticity of the Gaussian galaxies are altered between $|e| = 0.0$ to 0.5.

A more realistic and commonly-used (117) galaxy model is the Sérsic profile (118). A round Sérsic profile $f_{\rm Sérsic}(R)$, is given by

$$f_{\rm Sérsic}(R) = \exp\left[-b_n\left(\frac{R}{R_h}\right)^{\frac{1}{n}}\right], \tag{2.8}$$

where R_h is the half light radius of the single Sérsic profile, and n is the Sérsic index. b_n is a scaling factor to make sure the profile has the correct half light radius; its value is pre-determined for a fixed Sérsic n. We first carry out experiments that simulate individual Sérsic galaxies with a chosen value of Sérsic index and R_h, along with their 90-degree rotated pair, to examine the relation between shear bias and Sérsic profile parameters. After that point, we proceed to simulate galaxy ensembles with realistic size, shape, and Sérsic index distributions.

To study the shear biases of galaxies with a realistic distribution of sizes, shapes and Sérsic indices, we use a sample of galaxies from COSMOS with Sérsic fits[3] (99), for which GalSim has a class defined so as to efficiently use the sample for image simulations. The COSMOS parametric galaxy catalog that we use includes Sérsic profile fits to the real galaxy images in the COSMOS HST survey (119) for galaxies down to a limiting magnitude of F814W= 25.3. Without any cut on the galaxy population, we have $\sim 50,000$ galaxies and its 90-degree rotated-pair to work with. We use the fits to single Sérsic profiles with the Sérsic index

[3] `https://github.com/GalSim-developers/GalSim/wiki/RealGalaxy-Data`

Galaxy Type	Galaxy Parameters	PSF Type	PSF Parameters	$B[\rho^{(4)}]$
Gaussian	FWHM = 1.2 arcsec	Gaussian	FWHM = 0.7, 1.2, 1.6 arcsec	-0.01 – 0.01
Gaussian	FWHM = 2.4, 12.0 arcsec	Gaussian	FWHM = 0.9 – 4.7 arcsec	~ 0.005
Gaussian	FWHM = 2.35, 12.0 arcsec	Kolmogorov	FWHM = 0.7 – 3.3 arcsec	~ 0.005
Gaussian	FWHM = 2.35, 12.0 arcsec	Moffat	FWHM = 0.7 – 3.3 arcsec	~ 0.005
Sérsic	$R_h = 1, 5$ arcsec $n = 0.5, 1.5, 3$	Gaussian	FWHM = 0.9 – 4.7 arcsec	~ 0.005
Sérsic	$R_h = 1, 5$ arcsec $n = 0.5, 1.5, 3$	Kolmogorov	FWHM = 0.7 – 3.3 arcsec	~ 0.005

Table 2.2: The specification of the galaxy, PSF and shape measurement methods in the single galaxy simulations described in Section 2.3.3. The commas in the table denote a list of values for which simulations were carried out. The "–" means we make simulations covering a range of values between the two endpoints shown. The kurtosis error is given by Eq. (2.6). The half light radius, or "R_h" in the table, is used to define the size of the Sérsic galaxies. The kurtosis bias $B[\rho^{(4)}]$ changes by a few percent when constructing the model PSF and rescaling to ensure the PSF second moment is preserved; in our analysis we use the actual measured $B[\rho^{(4)}]$ rather than the idealized value in this table.

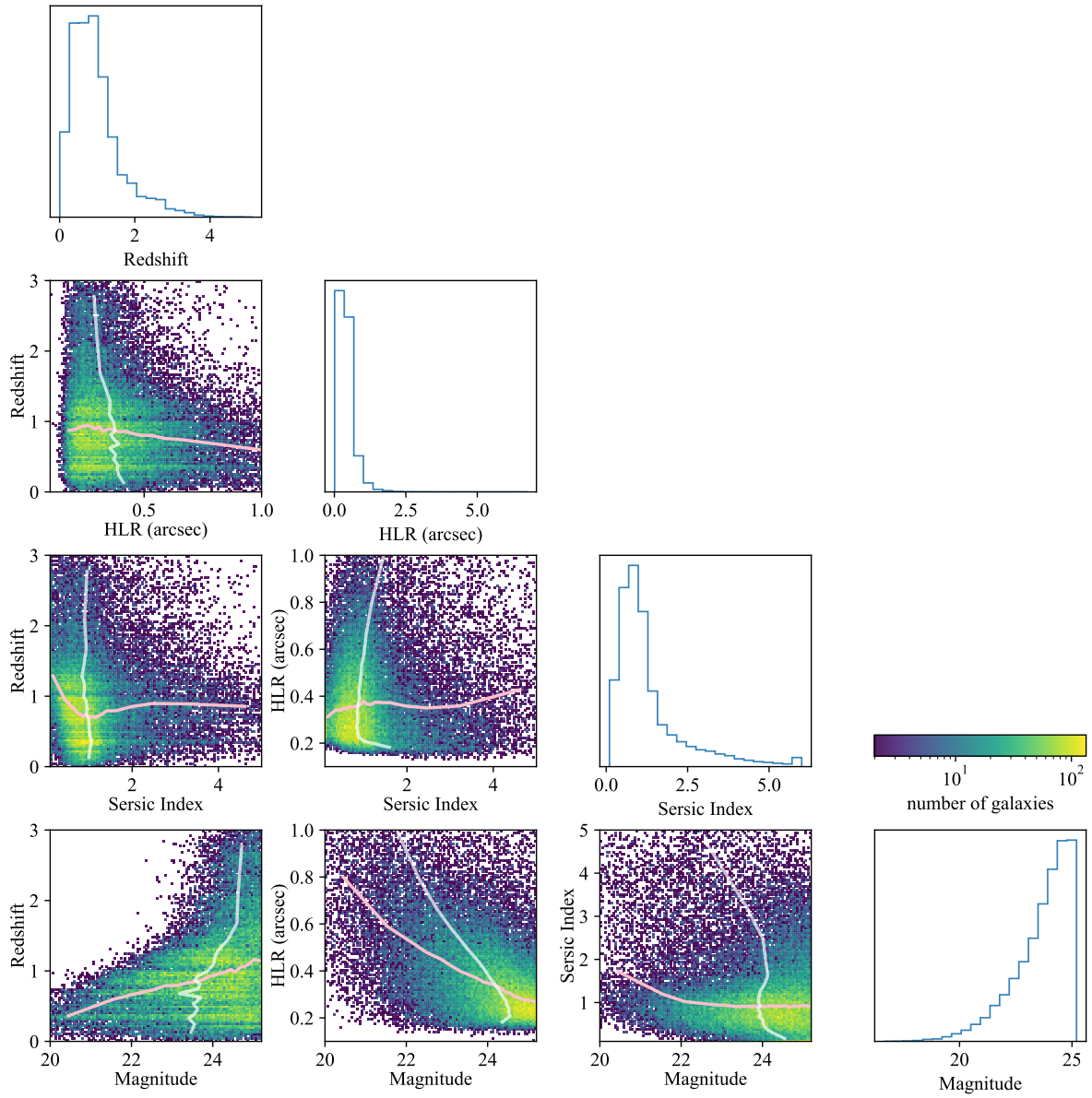

Figure 2.1: One- and two-dimensional histograms of galaxy properties including redshift, half light radius, F814W magnitude and Sérsic index in the COSMOS parametric catalog, with the pink trend-lines on each panel showing the median of the properties on the vertical axis when binned by the properties on the horizontal axis, and white trend-lines showing the median of the horizontal properties binned by the vertical properties. One-dimensional histograms of individual properties are shown on top. The color of the plot represents the number of galaxies on a logarithmic scale. The single Sérsic profile fitted to the COSMOS galaxy is parameterized by the half light radius and the Sérsic index shown. The relationships between parameters can be used to explain the redshift-dependent shear biases.

allowed to vary to generate the Sérsic galaxy samples using the COSMOSCatalog module in GalSim. The centroids of the generated galaxies are randomly displaced (by a uniform distribution) within one pixel from the centre of the images. We have confirmed that this displacement does not affect the overall results. To generate a galaxy population similar to what LSST may use for weak lensing shear inference, we impose a cut on the resolution factor R_2 defined by

$$R_2 = 1 - \frac{T_P}{T_I}, \tag{2.9}$$

where T_P is the second moment trace of the PSF and T_I is the trace of the PSF-convolved image. The galaxy is well-resolved when $R_2 \sim 1$ and poorly-resolved when $R_2 \sim 0$. As suggested by (54), we use galaxies with $R_2 > 0.3$. After the cut, we are left with $\sim 41,000$ galaxies and their 90-degree rotated-pairs. By drawing randomly from this catalog, we hope to mimic the observed galaxy light profiles for a sample of galaxies such as would be used for an LSST cosmology analysis. While Sérsic profiles do not include some of the more complex features of realistic light profiles, we will observe that the simulations with Gaussian versus more general Sérsic light profiles do not exhibit very different behavior with respect to shear biases due to errors in the higher moments of the PSF. For that reason, we consider the omission of more complex light profiles to be acceptable in this pathfinder study. After we create the 90-degree rotated pairs, we apply the same amount of shear to these galaxies as the signal we are measuring.

Since there is statistical uncertainty due to cosmic variance, the COSMOS galaxies are not fully representative of the full distribution of galaxy properties (120). This is particularly an issue when binning the galaxies by redshift, so that an even smaller volume is being sampled than when using the entire COSMOS volume. However, even if they were a representative sample, we would still need to determine how many galaxies we must sample from the COSMOS parametric catalog so as to reduce the statistical uncertainty due to the limited number of samples necessary level. We do this based on the statistical uncertainty in the shear bias measured using subsamples of galaxies from the catalog and their 90-degree rotated pairs in the absence of pixel noise. Since the systematic shear biases that we are interested in constraining are at the 0.1% level, we want shear biases to be measured at least one order of magnitude more precisely than that. We determine the ensemble shear uncertainty by bootstrap resampling the same size of subsamples of galaxies within the ensemble for 10^4 times, and adopt the standard deviation of these re-sampled ensemble shear as the errorbar on the shear. When doing so, we confirm that the statistical uncertainty scales like $n^{-\frac{1}{2}}$, where n is the number of 90-degree rotated pairs in the subsample. To reduce the statistical uncertainty of multiplicative bias m below 10^{-4}, we need at least 10^2 galaxy pairs randomly drawn from the ensemble. The results we show in Section 2.5.2 are derived from galaxy ensembles with at least 250 galaxy pairs, so the statistical uncertainty on the shear bias is well below our requirements.

In Fig. 2.1, we show one- and two-dimentional distributions of galaxy properties for the COSMOS parametric dataset, so as to better understand the population and associated simulation results. The median trend lines in Fig. 2.1 show that with increasing redshift,

the galaxies become smaller in apparent size and fainter in magnitude, as expected for a flux-limited population. There is no strong trend in Sérsic index as a function of redshift.

2.3.5 PSF Profile

To simulate errors in the higher moments of the PSF model, we first need to define a base PSF (which we will refer to as the true PSF). In this work, we generate simulations with three parametric base profiles: Gaussian, Kolmogorov, and Moffat PSF with $\beta = 3.5$. [4] Notice that these are the base PSFs rather than the base effective PSFs, which involve the pixel-response function. We have another non-parametric PSF: the stacked HSC PSF, which helps us validate the results from the parametric simulations.

In each simulation, there are two types of PSFs, the model PSF and the true PSF, which are defined using the base PSF with and without any additional kurtosis error. To generate the final image, the galaxy profile is convolved with the effective true PSF. Both the base true PSF and the base model PSF are round, and have the same weighted second moments, given by Eq. (2.2), The shape/shear of the convolved image is estimated separately using the effective true and model PSF. The shear bias - the difference between these two - is solely caused by the higher moments of the PSF model.

We define model PSFs that differ only in higher moments (not second moments) by perturbing the PSF model differently depending on the original base PSF. For the Gaussian base PSF, we define the model PSF using a Sérsic profile with index n close to (but not precisely) 0.5, since the Sérsic profile reduces to a Gaussian when $n = 0.5$. For the Kolmogorov base PSF, we construct the model PSF by summing (with equal weights) two Kolmogorov functions with slightly different sizes, parameterized by the ratio of the size of second Kolmogorov to the first. For the Moffat PSF with $\beta = 3.5$, we define the model PSF by varying β. We are not expecting the results from different types of PSF to be the same, since the higher-moments other than kurtosis are all perturbed differently.

All three these modifications have two free parameters: one of them (Sérsic index, Kolmogorov size ratio, or *beta*) is adjusted to explore different modifications to the higher moments of the PSF, while the other is a resizing parameter (Sérsic and Moffat R_h, and the size of the first Kolmogorov) that can be adjusted to achieve our goal of matching the second moments of the model PSF to those of the true PSF. The actual process of adjusting the resizing parameter to match the observed second moments of model and true PSF is as follows:

Step 1: Create the base PSF profile and the initial guess for the model PSF profile, without adjusting the size of the model PSF profile.

Step 2: Convolve both PSFs with the pixel response function and render each into an image with the adopted pixel size.

[4] We fit the HSC PSFs with Moffat profiles, and find that the β parameter is typically 3.5. This value is also adopted in (121) on HSC-like simulation.

Step 3: Measure the observed second moment size $\hat{\sigma}$ of the effective true PSF $\hat{\sigma}_{\rm true}$ and of the effective model PSF $\hat{\sigma}_{\rm model}$. Notice that the $\hat{\sigma}_{\rm true}$ will be slightly different from the assigned σ for the base PSF, because of the convolution with the pixel response.

Step 4: Dilate the model PSF base profile by $f'(x') = f'(\hat{\sigma}_{\rm true}x/\hat{\sigma}_{\rm model})$, using the expand transformation in GalSim, and replace the old model PSF profile with it.

Steps 2–4 are repeated until $\hat{\sigma}_{\rm model} - \hat{\sigma}_{\rm true} < 10^{-6}$ arcsec. Note that with a round base PSF and a model PSF that only differ in the radial moments, the shear bias can only be multiplicative. Therefore, in the rest of the paper, we focus on analyzing the multiplicative bias caused by such modeling error, though future analysis should also consider non-round PSFs and change non-radial moments of the PSF to investigate the additive bias. In the case that the pixel size is comparable to the scale of the PSF, the radial kurtosis values are slightly different when we re-scale the PSF size in Step 4, changing by a few percent. As a result, we cannot strictly control the kurtosis of our model PSF, and we re-measure the actual kurtosis of the model PSF $\hat{\rho}^{(4)}$ after the transformation to calculate $B[\rho^{(4)}]$ by Eq. 2.6.

Additionally, we test the shear biases using the stacked HSC PSF directly (these data will be described in Section 2.4). To do so, we interpolate star images and PSFEx models, and stack them with a common centroid, as the true and model PSF respectively. We transform all PSFs so that their shape is round, and they have the same second moment σ as the true PSF. We bin the HSC stars by their kurtosis biases $B[\rho^{(4)}]$, producing a true and model PSF for each bin, and measure the shape biases of Gaussian galaxies with different sizes.

Although the image simulations in this paper do not include noise, an adaptive weight function that matches the size of the PSF is still applied to the PSF when measuring galaxy shape. This is crucial because (a) it matches how weak lensing shear inference is done in real data, (b) the weight function is the reason why PSF higher moment errors can cause weak lensing shear biases (91). The choice of the weight function can affect the connection between PSF higher moment errors and shear biases. Therefore, we use the adaptive Gaussian weight function, which adjust its size and shape depending on the PSF, as it is similar to what is effectively used in many moment-based and model-fitting (e.g., 122) shear measurements. However, we do not explore this nuance in detail as it is beyond the scope of this paper.

2.3.6 Simulation Roadmap

In this section, we describe the flow of the simulations in this paper. We start with simulations with only one galaxy, in order to isolate the primary factors that determine the shear bias caused by higher moments error of PSF model. Then, we simulate galaxy ensembles with realistic distributions of size, shape and Sérsic indices to understand the impact on real galaxy surveys.

The experiments we conduct with single galaxies and parametric PSFs are defined in Table 2.2, and the results are shown in Section 2.5.1. We gradually increase the complexity of both galaxies and PSFs. First, we simulate a Gaussian galaxy and a Gaussian true PSF, while modifying the galaxy shape to see if the shape bias is multiplicative or additive. We also

change the kurtosis biases of the PSF, with several sizes of the galaxies, to check dependency of the galaxy shape biases on the kurtosis biases, described in row 1 of Table 2.2. We then explore the galaxy size-dependence in greater depth, as described in row 2 of Table 2.2. Next, we increase the model fidelity for both the galaxies and the PSFs, and conduct the same tests of galaxy size-dependence. For the PSFs, we change the model to Kolmogorov and Moffat, in row 3 and row 4 of Table 2.2. For the galaxies, we change the model to Sérsic profiles, and experiment with several values of Sérsic indices, in row 5 of Table 2.2. Finally, we conduct experiments with Sérsic galaxies and Kolmogorov PSFs, in row 6 of Table 2.2. For rows 2–6, we also use the 90-degree rotated pair method described in Section 2.3.4, to check whether we can translate the conclusions from shape biases to shear biases. These experiments help us understand the fundamental factors that determine how PSF kurtosis bias translates into galaxy shape and shear bias, which is essential for understanding experiments with higher model fidelity.

Next, we simulate the galaxy ensemble with a realistic distribution of sizes, shapes and Sérsic indices, obtained using the COSMOS catalog described in Section 2.3.4, with results shown in Section 2.5.2. The PSF model we use in this experiment is a Kolmogorov profile, with a fixed FWHM of 0.7 arcsec. We first conduct basic experiments, including changing the kurtosis bias of the PSFs, and the shear of the galaxies, to test the validity of conclusions from the previous, simpler experiments. We also change the size of the galaxy ensembles to understand the errorbars of the shear biases. We investigate the parameter-dependence of the shear bias by creating sub-ensembles binned by particular parameters. We bin the galaxies by their half light radii R_h, grouping with/without Sérsic index. We also explore the redshift-dependence of the induced shear bias by binning the galaxies in redshift bins. We further discuss the consequence of these results for cosmological weak lensing shear measurements in Section 2.5.4.

2.4 HSC Data

In this work, we inspect real data from the Hyper Suprime-Cam (HSC; 81) to understand how the current level of PSF modeling is doing in recovering higher moments, in specific, the radial kurtosis $\rho^{(4)}$. The dataset we are utilizing is the HSC star catalog of the first HSC public data release (PDR1; 69). The HSC pipeline (110) uses a modified version of the PSFEx (84), part of the LSST Data Management (DM; 123) codebase, for PSF modeling. We use the coadded image of the selected bright stars, for which selection criteria will be described in Section 2.4.1, as the true effective PSF. These are compared with the coadded PSF models at the same locations as the stars. The details of the PSF modeling and their coaddition in HSC PDR1 can be found in Section 3.3 of (110).

Below we describe the two key analysis steps applied to HSC data: star selection and kurtosis measurement.

2.4.1 Star Selection

The first step of utilizing the HSC star catalog is to select objects that are suitable for radial kurtosis measurement. First, we apply the first 11 “basic flag cuts" in table 3 of (54), and change the iclassification extendedness to 0 to include only non-extended objects. These flags cuts ensure that the coadded images of the objects in our catalog do not include artifacts such as exposure edges, bad pixels, saturation or cosmic rays. The iclassification extendedness cut is meant to omit extended objects. While our sample may still include small galaxies that are classified as non-extended, (110) showed that the classification works well for objects brighter than $i \sim 24$, which describes the star sample we are using.

We also determine the minimum signal-to-noise ratio (SNR) cut on the stars so as to ensure the measurement of the radial weighted kurtosis has a reasonable statistical precision for our purposes. To set a SNR threshold, we simulate stars with 10^4 noisy realizations of the same profile with a certain SNR with GalSim. We then measure the radial kurtosis of all realizations to estimate the relationship between statistical uncertainty on radial kurtosis and SNR. The results of this exercise suggest that to achieve a statistical uncertainly $\delta B[\rho^{(4)}] \lesssim 0.1\%$ in the radial weighted kurtosis, the SNR should exceed 800. Therefore, we set the minimum SNR to 1000. The 0.1% threshold still leaves us with a reasonably-sized sample while ensuring sufficiently high-precision measurements.

The final step in generating a star catalog is removing objects whose light profiles are contaminated by light from other objects. Given the sensitivity of the radial kurtosis to the outer part of the light profile, this step is particularly important. We do this using two methods: removing double stars and removing blended stars. To remove double stars, we detect them by scanning through the entire catalog of objects flagged as unique detections with the idetect_is_primary flag using a k-d tree structure. With a k-d tree, we can detect any two objects in the entire catalog that are located within some chosen tolerance (here we choose 2 arcsec), and call them “objects with near neighbor(s)". We then remove any stars with such near neighbor(s) detected from our star catalog.

To remove the blended objects, we utilize the parameter iblendedness_abs_flux, which describes how much flux of the object is potentially from other objects, and set an upper limit based on tests to determine when blending may be affecting the image enough to noticably impact the second moments. We use the residuals (difference between PSF model and moments measured from the image) of the second moment σ, e_1 and e_2 for this purpose. In Fig. 2.2, we show the PSF model residuals of stars in our catalog before applying a cut to remove blended objects, binned by the blendedness of the stars. We can see that when the blendedness exceeds 10^{-3}, the second moments of the bright stars measured from the images differ noticeably from the moments of the PSF model. Therefore, we exclude stars with iblendedness_abs_flux $> 10^{-3}$. We also notice a positive bias on second moment σ across all blendedness bins. This is likely connected to the brighter i-band magnitude of the stars we have selected: (110) shows that brighter PSF stars tend to have positive $\delta\sigma/\sigma$.

With these two methods, we remove stars that are too close to other (likely compact) objects, or are contaminated by a potentially extended background light profile. Out of the six fields in the HSC dataset, we chose to analyse a field with better-than-typical seeing,

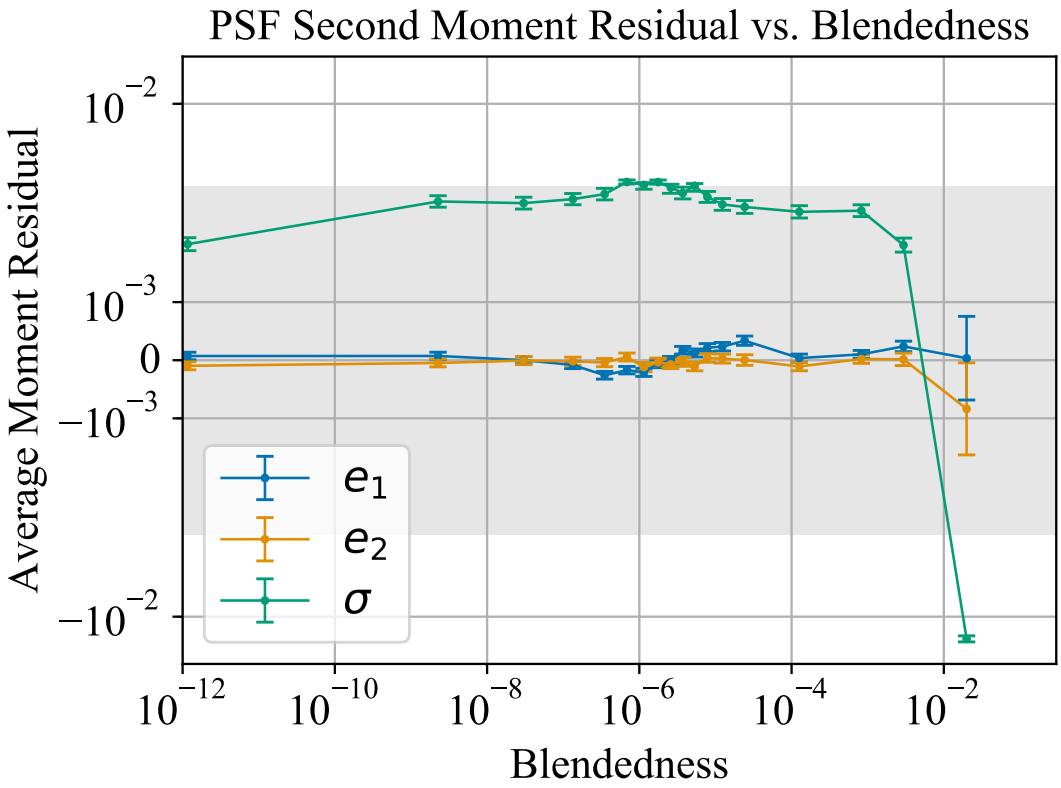

Figure 2.2: Average second moments residual (comparing the moments of the PSF model to those measured in the postage stamp image) for bright stars in the HSC survey, binned by the blendedness of the star. When the blendedness is larger than 0.001, we see significant residuals in the second moments. The y-axis is symmetric-log scaled with a linear threshold = 0.003. The linear region is shaded.

Steps	Criteria	Number of Objects
1	Basic flags cuts	2.7×10^6
2	Signal-to-noise $> 10^3$	8.0×10^4
3	Blendedness $< 10^{-3}$	7.0×10^4
4	Nearby object detection	6.8×10^4

Table 2.3: The number of stars remaining after each operation in our star selection on the HSC GAMA_15H field. The details and reasoning for the cuts are explained in Section 2.4.1.

since the better-seeing fields generally have worse PSF modeling quality (54), and are better samples for testing the PSF model. We choose GAMA_15H, since it has the best seeing among the fields that pass the nominal cuts on PSF modeling quality in (54). The number of stars remaining after each cut is applied to the catalog is shown in Table 2.3. At the end of the selection process, we have $\sim$ 68,000 star samples for investigating the PSF modeling

quality.

We use the same flag cuts for stars as in (54); however, the SNR cut that we add to the flag cuts results in selection of a star population that is brighter than that in (54). Our selected stars have i-band magnitudes ranging from 18–20.5. As a result, the second moment distribution is slightly larger than that in (54), but the dataset can still serve the purpose of this paper.

2.4.2 Analysis of HSC stars

After we select the stars to create the catalog, we retrieve postage stamp images of the stars (which we consider as representing the true PSFs), and the model PSFs reconstructed at the positions of the stars. We are using the coadded images rather than the original individual exposures, to which CCD-level processing was applied. The PSF models are also appropriately weighted coadditions of the individual exposure PSF models. We measure the second moments and radial kurtosis of the stars and model PSFs to obtain a catalog of stars with moments of their true and model PSF, as a function of their position on the sky.

cwrThe magnitude distribution of the selected stars is within but at the brighter side of the i-band magnitude distribution for PSF stars in (54). We also inspect the second moment modeling quality of our selected stars. We use

$$f_{\delta\sigma} = \frac{\sigma_{\rm model} - \sigma_{\rm true}}{\sigma_{\rm true}} \tag{2.10}$$

to measure the size model quality. We bin our selected star by their i-band magnitude into 10 bins, and find that the average $f_{\delta\sigma}$ values for each bin do not exceed the requirement on $f_{\delta\sigma}$ for HSC, 0.004, reproducing the results of Fig. 6 in (54).

This catalog enables us to determine the mean value and standard deviation of the true and residual PSF kurtosis, where the residual PSF kurtosis is defined by Eq. (2.6).

For a given sample of galaxies used to measure the weak lensing shear, the shear field depends on the position on the sky $\mathbf{x}$; so does the kurtosis bias, and therefore the associatd shear multiplicative bias. The observed shear $\hat{g}(\mathbf{x}) = [1 + m(\mathbf{x})]g(\mathbf{x})$, where the $g(\mathbf{x})$ is the true shear. When $|m| \ll 1$, the observed shear correlation function is

$$\langle \hat{g}(\mathbf{x})\hat{g}(\mathbf{x}+\theta)\rangle = (1 + 2\langle m\rangle)\langle g(\mathbf{x})g(\mathbf{x}+\theta)\rangle.$$

The mean multiplicative bias of a galaxy ensemble $\langle m\rangle$ can be calculated by the average multiplicative bias of the galaxies in it, $\langle m\rangle = \langle m(B[\rho^{(4)}])\rangle$, when there is no other source of systematics. Since the shape and shear biases are proportional to the kurtosis bias, as we later find out, we can estimate the shear bias by taking the first term of Taylor expansion

$$m(B[\rho^{(4)}]) \approx \frac{\partial m}{\partial B[\rho^{(4)}]} B[\rho^{(4)}]. \tag{2.11}$$

The first factor in the equation above is determined primarily by the galaxy population and the second factor by the PSF. So, they are independent random variables and the averages

can be separately calculated. We have tested this linear approximation and found it to be accurate at the level of $\sim 0.1\%$ of the measured shear bias, within the $B[\rho^{(4)}]$ range of HSC data.

For a galaxy ensemble, based on the assumption of Eq. 2.11, $\langle m \rangle = \langle \partial m / \partial B[\rho^{(4)}] \rangle \langle B[\rho^{(4)}] \rangle$. Functionally, this means that we can simply calculate the average of $B[\rho^{(4)}]$ over the PSF model across the survey, and average $\partial m / \partial B[\rho^{(4)}]$ over the galaxy population. Those two separate results can be combined to estimate an average weak lensing shear bias for galaxy populations that resemble those that will be used for measurements of weak lensing surveys such as LSST.

2.5 Results

In this section, we show the results of carrying out the measurements described in Sec. 2.3. First, we show the results of the image simulation – simulations with simpler galaxy populations in Section 2.5.1 and using the full COSMOS catalog in Section 2.5.2. Next, we show the results of analyzing the moments of the HSC PDR1 star sample in Section 2.5.3. Finally, we estimate the redshift-dependent weak lensing shear bias caused by errors in the higher moments of the PSF in Section 2.5.4, combining the simulation and HSC results.

2.5.1 Single Galaxy Experiments

Here we show the results of controlled numerical experiments that test the impact of errors in the higher moments of the PSF model on the shape measurement of a single galaxy.

First, we check the behavior of the shape measurement bias $\delta e = \hat{e} - e$ caused by the PSF kurtosis bias. We simulate a Gaussian galaxy convolved with a round Gaussian PSF, which has kurtosis $\rho^{(4)} = 2$, as shown in Table 2.1. The model PSF is generated using a Sérsic profile with index slightly different from $n = 0.5$ (Gaussian case) as mentioned previously in Section 2.3.5. We simulate several galaxies with different ellipticities and find out that the shape error δe is proportional to the galaxy shape e, which means that the shape error caused by kurtosis is a multiplicative bias. We also carried out a test with $e = 0$ to verify that the additive bias on the shape is zero under PSF kurtosis bias, for the round PSF configurations used in this experiment. Since the shape bias is multiplicative, in future experiments regarding shape error, we only simulate one value of $e = (0.28, 0.0)$, i.e. the intrinsic galaxy shape dispersion, and use $\delta e / e$ as the multiplicative bias.

In the second experiment, we simulate Gaussian galaxies with a single value of e and σ, and convolve them with a Gaussian PSF, of which the values are shown in row 1 of Table 2.2. We then measure the shape of the galaxy using the PSF model that has a perturbing Sérsic index around 0.5, and with the same second moments as the true PSF, explained in Section 2.3.5. Compared to the last experiment, we are changing the amount of kurtosis error in our model PSF, to determine the relationship between galaxy shape bias and PSF kurtosis error. In Fig. 2.3, we show that the multiplicative galaxy shape bias for a single galaxy is linearly proportional to the kurtosis bias, for both re-Gaussianization

and Metacalibration. In later image simulations, we focus quantifying $\partial m/\partial B[\rho^{(4)}]$, so that we can predict the shear bias for the HSC dataset by combining the simulation with the measurement of $B[\rho^{(4)}]$, as shown in Eq. (2.11). This constant of proportionality depends on the ratio of the size of the galaxy to the size of the PSF (and, notably, is not monotonic in that ratio). Our next goal is to explore the potentially complex dependency on the ratio of galaxy-to-PSF sizes.

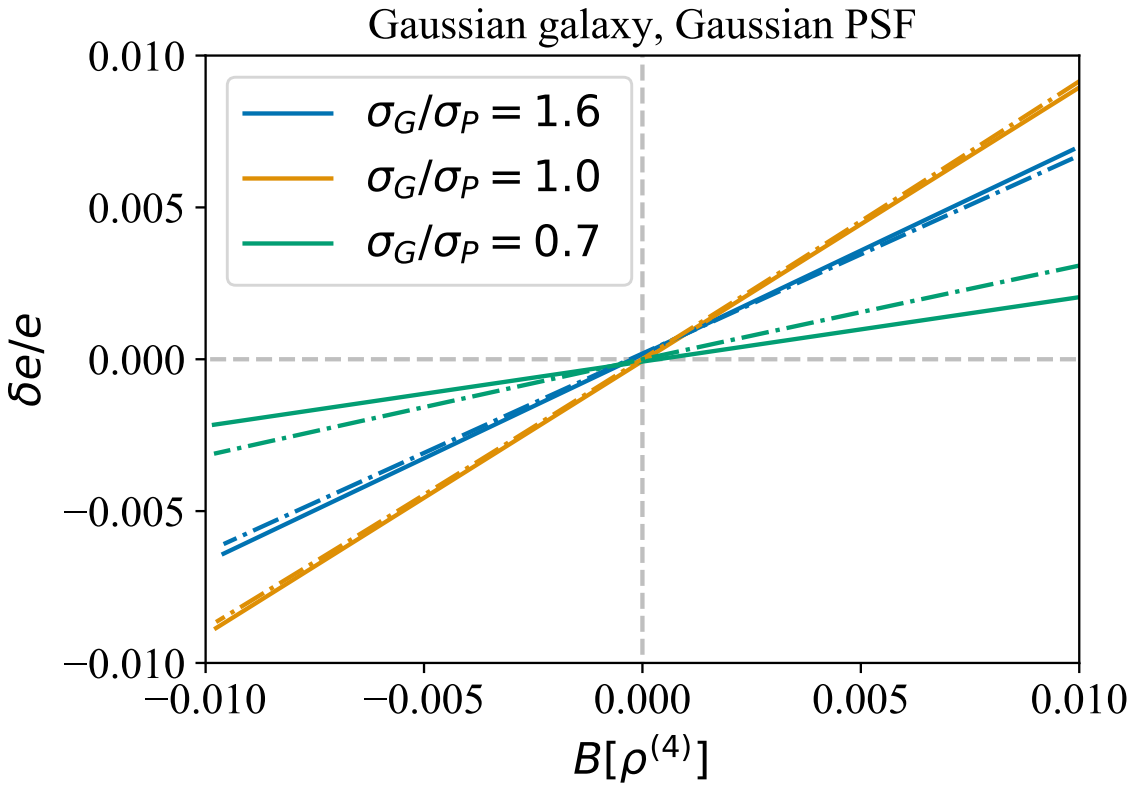

Figure 2.3: Here we show the galaxy shape bias as a function of PSF kurtosis bias for a Gaussian galaxy and Gaussian PSF, with re-Gaussianization (dot-dashed) and metacalibration applied to re-Gaussianization (solid) for three different size ratios of the galaxy and PSF. Dashed lines indicate the zero value for both plotted quantities. As shown, the galaxy shape bias depends linearly on the PSF kurtosis bias, and depends in a more complex way on the galaxy versus PSF size ratio. The kurtosis bias is defined in Eq. (2.6).

The results of exploration of the relationship between the galaxy shape bias and the kurtosis bias, expressed in terms of the derivative $(\partial\hat{e}/e)/(\partial B[\rho^{(4)}])$, are shown in Fig. 2.4. In this test, we simulate Gaussian galaxies cwrwith three parametric PSFs: Gaussian PSFs (blue), Kolmogorov PSFs (orange), Moffat PSFs (green), with shear estimation via re-Gaussianization (solid) and metacalibration (dot-dashed). The main parameters of this experiment are specified in rows 2-4 of Table 2.2. In addtion, we also measure the shear

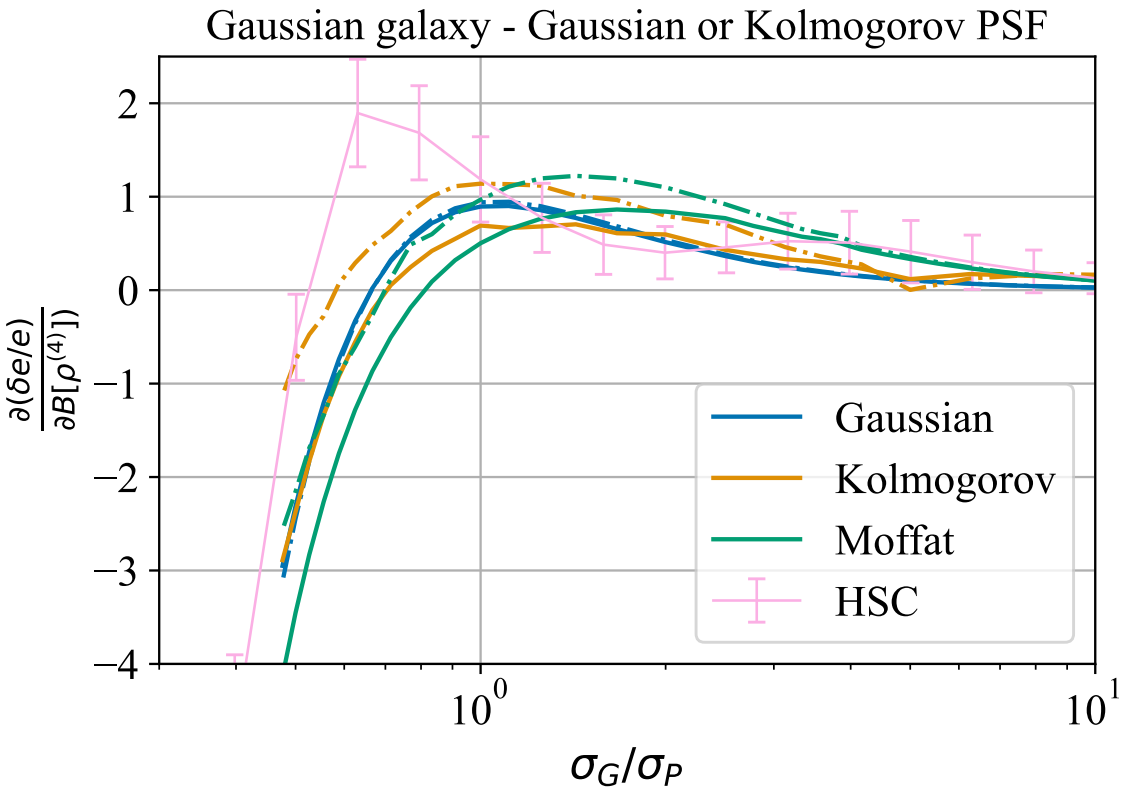

Figure 2.4: This plot illustrates the relationship between the slope of the lines from Fig. 2.3 (ratio of galaxy shape bias to kurtosis bias) and the size ratio between the galaxy and PSF. The colors of the lines indicate the functional form for the true PSF (indicated in the legend). Dot-dashed lines show the results when using metacalibration, and the solid lines show the results for re-Gaussianization. The stacked HSC PSF are only measured in re-Gaussianization. As shown, the trends in the dependence on the galaxy versus PSF size ratio are quite similar for all four PSF models and shape measurement methods.

estimation with a non-parametric PSF: the stacked star images and PSFs from the HSC data. The galaxies have a shape of $e_1 = 0.28$ and $e_2 = 0$. We find that the shape biases respond to different PSFs with a similar trend. We tested other cwrmoment-based shape measurement methods, and we found that cwrthe responses from these shape measurements follow the same trend as a function of the size ratio, though potentially differing in magnitude by a factor up to 2 for small galaxies. cwrIn (92), shape measurement methods seem to have very different responses to the HME. However, there are a few differences between the two studies: (a) the tests in (92) are for a space-based telescope, while we study a ground-based telescope; (b) (92) also explore more complicated PSF model residuals, while we have controlled experiments that only have radial moment residuals; cwrand (c) the shear measurement methods in (92) also have more fundamental differences from each other, while

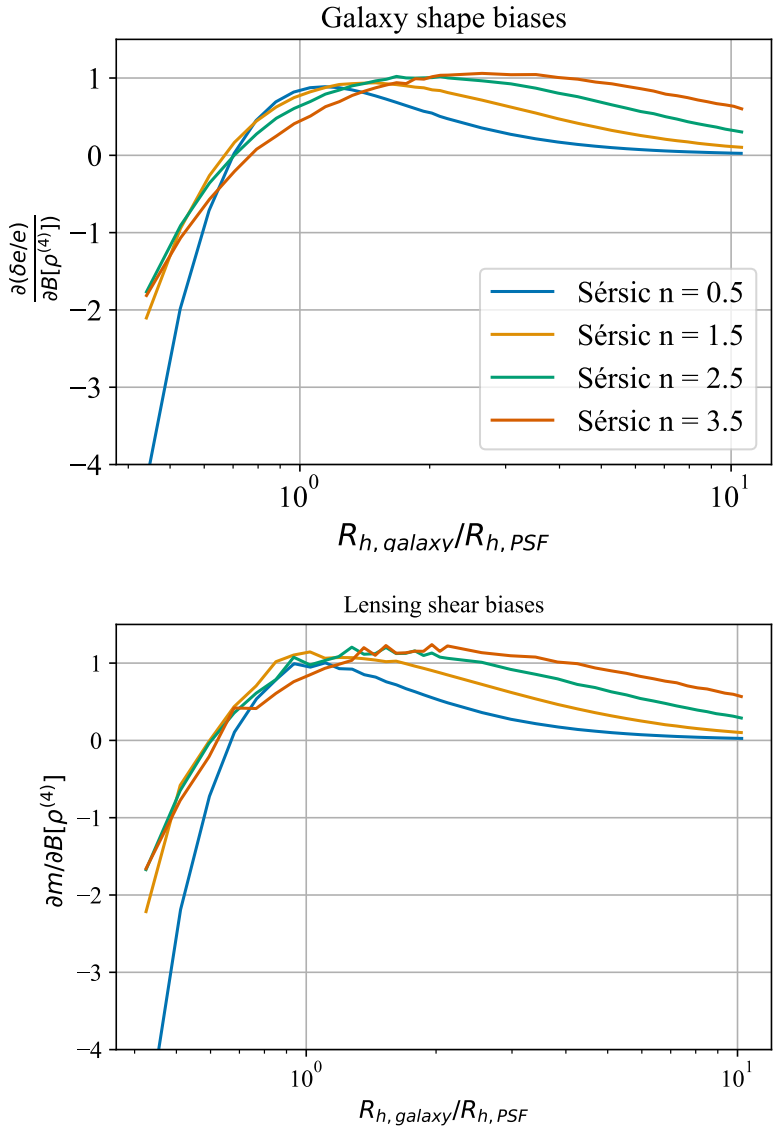

Figure 2.5: **Left:** The relationship between the ratio of galaxy shape bias to PSF kurtosis bias and the galaxy-to-PSF size ratio, simulated with a Sérsic galaxy profile and Gaussian PSF. **Right:** Same as the left panel, but for the ensemble shear bias (rather than galaxy shape bias), measured using 90-degree rotated pairs and a Gaussian PSF. The measurements in both panels are made using re-Gaussianization. As shown, both the galaxy shape and weak lensing shear bias are only mildly dependent on the Sérsic index, with the minor differences between the curves for different Sérsic indices being subdominant to the dependence on galaxy-to-PSF size ratio.

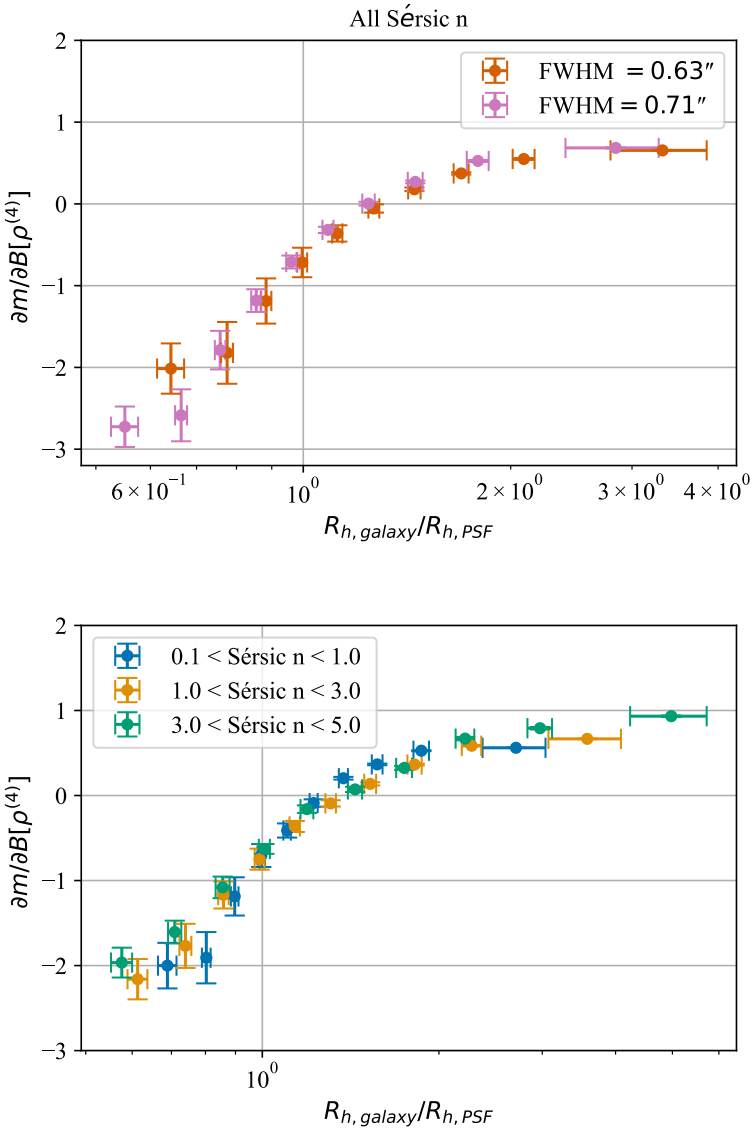

Figure 2.6: **Left:** Multiplicative bias per PSF kurtosis bias for subsamples of galaxies from the COSMOS parametric catalog, binned by the size ratio $R_{h,\mathrm{galaxy}}/R_{h,\mathrm{PSF}}$, including all Sérsic indices, for two runs with PSF FWHM = 0.63 and 0.71. **Right:** The same quantities as on the left, shown separately for three ranges of Sérsic index. The variation between the curves with different Sérsic indices is significantly less than the variation with galaxy size, just as for single galaxy simulations. The horizontal errorbars show the standard deviation within each bin, while the vertical errorbars show the uncertainty on the mean value, generated by bootstrap resampling from the fixed subsample of the COSMOS catalog 10^4 times.

the shape measurement methods compared in this study are relatively similar.

Next, we compare the metacalibration results to those for re-Gaussianization; both are shown in Fig. 2.4. cwrMetacalibration applied to re-Gaussianization has a similar results as re-Gaussianization alone for the Gaussian PSF. However, for the Kolmogorov PSF, we do see differences between the two methods of up to a factor of 2, despite the fact that the qualitative trends with galaxy-to-PSF size ratio are similar.

In Fig. 2.4, we also add complexity to the PSF model in the simulation, specified in row 3 and row 4 of Table 2.2. We use a Kolmogorov profile as the true PSF, and the double-Kolmogorov as a perturbed model PSF, again with preserved second moments. We also use the Moffat PSF with $\beta_0 = 3.5$ as the true PSF, and vary the β as the perturbed PSF. This figure therefore provides a comparison among results with Gaussian, Kolmogorov, Moffat PSF and stacked HSC PSF – in all four cases, with a Gaussian galaxy. We find that compared to a Gaussian PSF, kurtosis residuals in the model for the Kolmogorov PSF and Moffat cause slightly more shape bias given the same kurtosis bias, for larger galaxies. While it may seem that the shape bias in the case of a Kolmogorov and Moffat PSF converges to a positive constant, this is not the case: we have confirmed that the shape bias converges to zero for sufficiently large galaxies with $\sigma_G/\sigma_P > 20$. It is expected that the results from different types of PSF are different by a factor-of-a-few, since a fixed kurtosis bias corresponds to different perturbations of the other higher moments. This is especially true for the real stacked PSF, as kurtosis biases might be correlated with other higher-moments biases in real data. However, the goal of this paper is to provide an initial order-of-magnitude estimate of the impact of errors in the higher order moments of the PSF. At that level, all our results show a consistent magnitude and dependence on galaxy and PSF size ratio, which points to kurtosis bias as the most important higher moment for determining the weak lensing multiplicative shear bias.

Next, we extend our results to greater complexity in the galaxy model by using Sérsic profiles, which have one more parameter than Gaussian profiles. Since the galaxy shape bias is multiplicative and is directly proportional to the PSF kurtosis bias, we present the results in the same form as Fig. 2.4. The parameters of this experiment are specified in row 4 of Table 2.2. The left panel of Fig. 2.5 shows the results of simulating a series of Sérsic profile galaxies with Sérsic indices n ranging from 0.5–3.5, and with galaxy-to-PSF size ratio ranging from 0.5–3. We use the half light radius (R_h) to define the size ratio between the galaxy and PSF in this case. The Sérsic galaxy with $n = 0.5$ is simply a Gaussian galaxy, and the result for that case is the same as in Fig. 2.4. As shown, the Sérsic index plays a relatively minor role in determining the galaxy shape bias for a given level of PSF kurtosis bias. However, this result would not hold if we had plotted the results as a function of second moment size, since galaxies with the same σ and different Sérsic indices have quite different half light radii. If we use the second moment σ as the scale parameter, the different Sérsic index curves would unify at large size ratios ($\sigma_{\rm galaxy}/\sigma_{\rm PSF} > 2$), but would be highly discrepant for small size ratios. Since most of the galaxies that we are interested in have a small size ratio, we choose to use the half light radius R_h as the scale parameter.

Our final step in this section is to switch to measuring the ensemble weak lensing shear

bias (rather than galaxy shape bias) due to errors in the PSF higher moments. We simulate a galaxy with $e_1 = 0.28$ and its 90-degree rotated pair. Again, we check that the additive bias is zero when $g = 0$. We then apply non-zero shear to check the multiplicative biases. In the right panel of Fig. 2.5, we simulate Sérsic galaxy pairs convolved with a Gaussian PSF, with the shear of the 90-degree rotated pair measured as described in Section 2.3.2. The shape measurement method used in this experiment is re-Gaussianization. This plot shows that the ensemble shear bias induced by PSF kurtosis bias is nearly the same as the induced galaxy shape bias, indicating that we can generalize the results from earlier in this section to shear bias. We also test with Kolmogorov PSF, and receiving results cwrwith similar trend to Gaussian PSF. In the rest of this work, we will focus on tests of ensemble shear recovery with galaxy ensembles, using the ensemble shear multiplicative bias m.

2.5.2 Experiments with Realistic Galaxies

Here we extend the results from Section 2.5.1 on weak lensing shear bias due to PSF model kurtosis bias for individual galaxies (as a function of their properties) to consider a galaxy population with a realistic distribution of galaxy sizes, shapes, and Sérsic indices. The galaxy population we use is based on the COSMOS parametric catalog, the galaxy cut is described in Section 2.3.4. For the following tests we use a Kolmogorov PSF, run twice with FWHM = 0.63 arcsec and FWHM = 0.71 arcsec, and the PSF model is a double-Kolmogorov PSF as described in Section 2.3.5. We impose a cut on the resolution factor R_2, according Section 2.3.4. The ensemble shears are measured by Metacalibration.

Before proceeding based on the assumptions from single galaxy experiments, we confirmed the following conclusions from the previous subsection carry over to ensembles of galaxies with varying sizes and shapes: the weak lensing shear bias generated by PSF kurtosis bias is multiplicative (proportional to the shear) and proportional to the kurtosis bias. We test these conclusion for shear $|g| < 0.01$ and for kurtosis bias $|B[\rho^{(4)}]| < 0.004$. This enables us to continue quantifying our results in terms of the multiplicative shear bias per PSF kurtosis bias, or $\partial m/\partial B[\rho^{(4)}]$. In the later simulations, both shear and kurtosis bias are kept constant with $(g_1, g_2) = (0.01, 0.0)$ and $B[\rho^{(4)}] = 0.0015$. The vertical errorbars of the results in this section is determined by the bootstrap resampling method discussed in Section 2.3.4, and the horizontal errorbars are the standard deviation of the binned properties.

We want to confirm that the dependence of the ensemble shear bias on the size ratio of galaxy and PSF still holds for the ensemble. On the left panel of Fig. 2.6, we bin the entire catalog in equal number of galaxies by the half light radius size ratio of the galaxy over PSF, and show the relationship between multiplicative shear bias per kurtosis bias and the size ratio for both FWHM = 0.63 arcsec and FWHM = 0.71 arcsec. We show that the primary determining factor for shear bias induced by PSF kurtosis bias is the size ratio between the galaxies and the PSFs, as previously shown in the simpler experiments in Sec. 2.5.1. We further confirm that the results in Section 2.5.1 can be generalized to galaxy ensemble shear by splitting the galaxies in the COSMOS catalog based on their Sérsic indices, shown in the right panel of Fig. 2.6. For this test, we only plot the results from FWHM = 0.63 arcsec run.

The three sets of galaxies have similar shear biases despite the fact that the Sérsic indices differ significantly for the three groups – a similar conclusion as from Fig. 2.5 (right panel).

Since weak lensing cosmology analyses typically involve tomography, i.e., binning by redshift, we have a strong motivation to investigate what happens to the ratio of shear bias and PSF kurtosis bias when binning the COSMOS parametric galaxies by other properties such as redshift. The results of this experiment are shown in Fig. 2.7. We show that $\partial m/\partial B[\rho^{(4)}]$ becomes more strongly negative at higher redshift. This can be explained in terms of the trend in Fig. 2.1, which showed that galaxy sizes are smaller at higher redshift, and Fig. 2.6, which showed that smaller galaxies have a more negative value of $\partial m/\partial B[\rho^{(4)}]$. As (124) noted, the inferred dark energy equation of state is relatively insensitive to a constant multiplicative bias m_0. Rather, redshift-dependent multiplicative bias $m(z)$ can more directly mimic changes in the dark energy model (105). This means that we need to properly model the redshift-dependent shear bias caused by kurtosis to ensure unbiased cosmological parameter constraints.

2.5.3 HSC PSF Modeling

So far, we have developed an understanding of the weak lensing shear bias for a given level of PSF kurtosis bias, with increasingly complex galaxy populations. In this subsection, we now change direction to assess the typical level of PSF kurtosis bias in one ongoing weak lensing survey, using the HSC star catalog described in Sec. 2.4. Doing so will enable us to assess the resulting level of weak lensing shear bias, and eventually place requirements on PSF model quality for upcoming surveys such as LSST. Our assessment involves measuring the moments of coadded i-band star images and the i-band PSF model at their positions (see Sec. 2.4 for more details).

In Fig. 2.8, we show maps of the true PSF radial kurtosis and the residual kurtosis $B[\rho^{(4)}]$ for one of the six fields in the HSC PDR1. The total range of variation in the truth and model kurtosis is around 5%, with an average around 2.16. According to Table 2.1, the HSC PSF typically has a slightly higher radial kurtosis than Kolmogorov and Moffat PSF, meaning that it has relatively larger tails. There is some spatial structure in the true PSF kurtosis, which is captured well by the PSF model. The kurtosis bias of the PSF model is typically less than 0.5 per cent of the true PSF kurtosis, and also exhibits spatial structure. The average kurtosis bias is $\langle B[\rho^{(4)}]\rangle = 0.0011$. In Sec 2.5.4, we show that the two point statistics of weak lensing shear are only impacted by the mean multiplicative bias. This mean kurtosis bias is the key result we need in order to estimate the mean multiplicative bias in shear. As an aside to understand this result, we discuss the one- and two-point functions of these PSF model moment residuals in Appendix 2.A. In general, the second moment properties of our PSF samples matches what is found in (110) and (54).

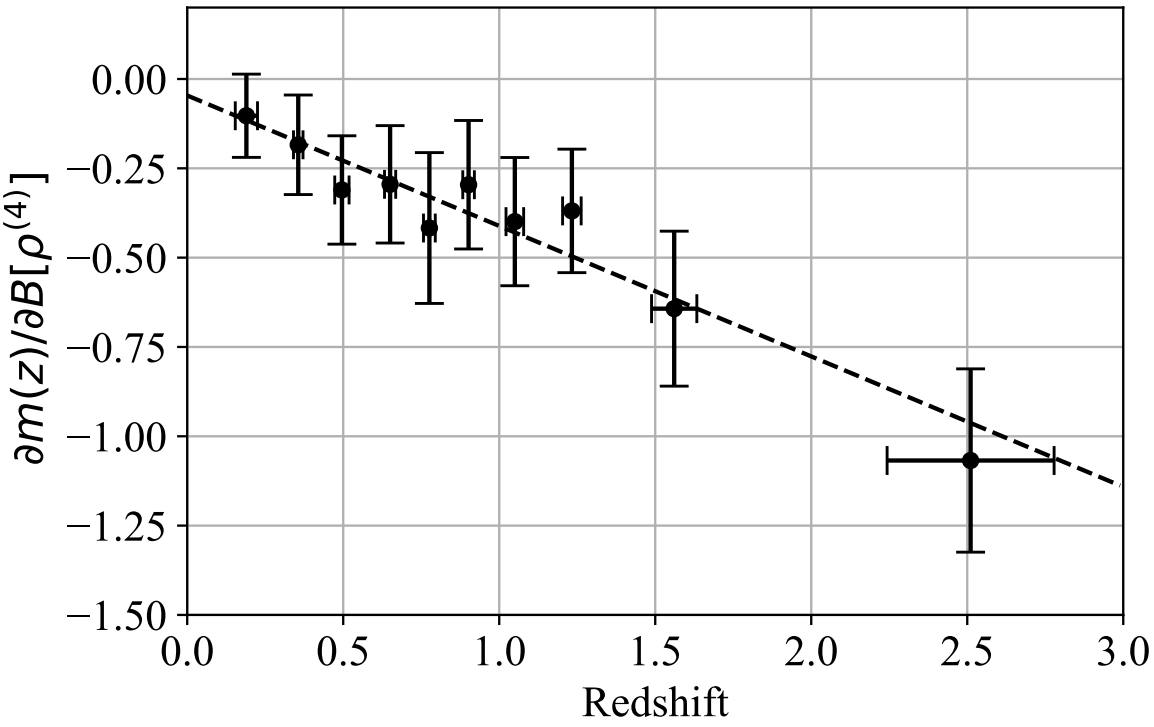

Figure 2.7: Ratio of weak lensing shear bias and PSF kurtosis bias when binning the COSMOS parametric galaxies by their photometric redshift. The effect can by explained by the fact that galaxies at higher redshift tend to be smaller in apparent size, which results in a more negative shear bias for a given value of PSF kurtosis bias. The horizontal error bar shows the standard deviation within each redshift bin, while the vertical errorbar shows the error on the mean value, generated by bootstrap resampling from the redshift bin 10^4 times. The dashed-line shows the linear model specified by Eq. (2.12).

2.5.4 Redshift Dependent Bias

Our final step is to synthesize the results from Subsec. 2.5.2 and 2.5.3 to estimate the level of redshift-dependent shear bias due to errors in the higher moments of the PSF for HSC-like PSF modeling quality. According to The LSST Dark Energy Science Collaboration Science Requirements Document version 1 (hereafter referred to as the DESC SRD; 90), the redshift-dependent multiplicative shear bias should not exceed 0.013 for Y1 or 0.003 for Y10. This requirement is determined based on a quantity m_0 defined by a linear parameterization,

$$m(z) = m_0 \left(\frac{2z - z_{\rm max}}{z_{\rm max}} \right) + \bar{m}, \tag{2.12}$$

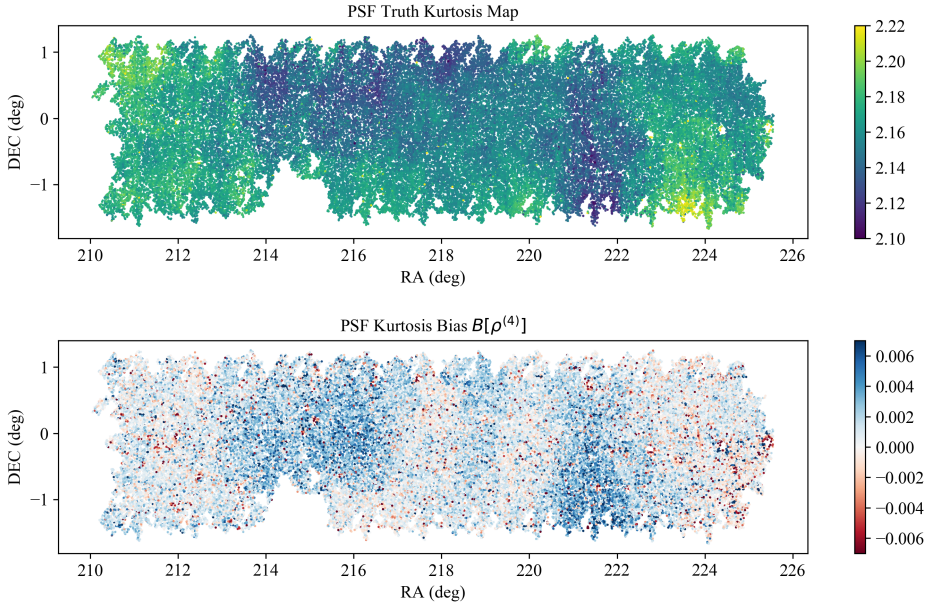

Figure 2.8: HSC PSF kurtosis as a function of position in the GAMA15H field: true kurtosis (top), and residual of the model $B[\rho^{(4)}]$ (bottom). Each point in the plots represents one star we choose to measure kurtosis. The value for the truth and the model is the weighted radial kurtosis $\rho^{(4)}$, and the residual is the fractional error $B[\rho^{(4)}]$. The results in the true PSF kurtosis contain shot noise in the image. However, in Sec. 2.4.1, we show that stars with SNR exceeding 10^3 have $\delta B[\rho^{(4)}] < 0.001$, thus our results here are not heavily affected.

where $\bar{m}$ is a constant multiplicative bias, which is removed beforehand and omitted in the definition of the DESC SRD. Our prediction is based on the image simulation with COSMOS-based Sérsic profile galaxies and a Kolmogorov PSF, and kurtosis bias measured by HSC PSF. Notice that we approximate the impact of the HSC PSF model residuals in simulations with a simple Kolmogorov PSF, which means we expect some uncertainty on the order of tens of per cent for our prediction in this Section, as our previous results show this is the level of difference between results with a Gaussian versus a Kolmogorov PSF. This is an acceptable uncertainty for this initial pathfinder uncertainty to estimate the approximate level of ensemble shear bias from errors in PSF higher moments.

More quantitatively, the multiplicative bias of a tomographic source bin can be estimated by multiplying the average kurtosis bias (Subsec. 2.5.3) by the ratio of shear bias to PSF kurtosis bias at the redshift of the tomographic bin (Fig. 2.7). From this figure, we can approximate m_0 using $\partial m(z)/\partial B[\rho^{(4)}]$ and the average PSF kurtosis bias $\langle B[\rho^{(4)}]\rangle$ in HSC. Setting $z_{\rm max} = 2.4$, $\partial m_0/\partial B[\rho^{(4)}] = -0.46 \pm 0.05$. Adopting $\langle B[\rho^{(4)}]\rangle = 0.0011$ as in Section 2.5.3, we get a redshift-dependent multiplicative bias parameter $m_0 = -0.0005 \pm 0.0001$. However, the requirements on multiplicative shear bias mentioned above are meant to cover all sources of shear biascwr, and there might be multiplicative bias caused by other higher

moments as well. For consistency with the method of allocating the systematic error budget in the DESC SRD, since there are many sources of systematic biases when estimating weak lensing shear, we can only allocate $\sim 1/3$ of the above budget to errors in the PSF-related systematics. Therefore, while this is a factor of four below the goal for Y1 results, it is comparable to the error budget for Y10, motivating further improvements in PSF modeling methodology and incorporation of tests of higher moments of the PSF model during the course of the survey. Notice that this prediction is carried out with PSFEx, which is not the planned PSF modeling algorithm for either LSST Y1 or Y10. Therefore, we expect different modeling quality and shear bias in the actual LSST survey.

Our fitting to the redshift-dependent multiplicative biases is subject to cosmic variance within the COSMOS dataset, as discussed in (120). This source of uncertainty will not be reflected in bootstrap errorbars or other internal uncertainty estimates, which means that the fit residuals may noticeably exceed the errorbars. However, this does not affect the conclusions of this paper. Furthermore, our results are based on the shear response to the Kolmogorov PSF, and can be different for the other PSF models we explored in Fig. 2.4. Based on our run of the COSMOS dataset on the Moffat PSF, we observe a shift and a $\sim 50\%$ change to the slope, compare to the redshift-dependent multiplicative biases $\partial m(z)/\partial B[\rho^{(4)}]$ of the Kolmogorov PSF in Fig. 2.7. Considering that the shear responses to all kinds of PSFs follow the same trend, we do not expect the redshift-dependent multiplicative biases of them to be significantly different in the order-of-magnitude.

Finally, we emphasize that the galaxy population we adopt is not a fully realistic realization of what LSST will observe at full survey depth. This introduces some additional uncertainty on our predictions of shear bias due to PSF higher moments error. However, our results illustrate at the order-of-magnitude level that errors in modeling the higher moments of the PSF modeling are a non-negligible source of systematic uncertainty for weak lensing with LSST.

2.6 Conclusion

In this paper, we carried out an initial exploration of the impact of errors in the higher moments (beyond second moments) of PSF models on weak lensing shear measurement. We used image simulations with parametric galaxies (at various levels of complexity) and PSF models produced using GalSim to study how errors in the higher moments of the PSF impact galaxy shape measurement and ensemble weak lensing shear measurement. We used images of stars and the associated PSF models in the HSC PDR1 data to measure the bias in PSF model kurtosis for real PSFs estimated with PSFEx. Combining the simulation and the HSC results, we found that the current level of errors in the cwrkurtosis of the PSF model in HSC can cause $\sim$0.05% multiplicative bias in shear measurement.

There are a number of simplifications associated with our work. In this paper, we only quantified errors in the radial kurtosis of the PSF model. The resulting galaxy shape and lensing shear systematics are purely multiplicative as a result (shear error proportional to input shear) and are also directly proportional to the kurtosis difference between the model

and true PSF. We found that the derivative of the linear relationship between shear bias and kurtosis bias depends primarily on the size ratio of the galaxy to the PSF; this relationship is not monotonic. We conduct tests of such effect on three different parametric PSFs and a non-parametric PSF, and find similar trends among all results. Dependencies on the galaxy Sérsic index and the galaxy shape measurement method are significantly weaker. cwrComparing to the findings of (92), we did not see significant shape measurement dependence for the shear bias induced by errors in the higher moments of the PSF. Since the PSF higher moment residuals in (92) are more complicated than our radial moments residual, further simulation on other moments is needed to understand the difference. Furthermore, (92) studies the PSF of space-based telescope, while we are focusing on ground-based PSF: the difference between the base PSF might also induce a different response from certain shape measurement methods. cwrLastly, the shape measurement methods compared in this paper are less different than those compared in (92), which could easily explain the different findings.

We used stars with high signal-to-noise ratio in HSC coadded images, together with the PSF model at the star positions, to measure the errors in the radial weighted kurtosis of the HSC PDR1 PSF models. We found that the kurtosis error of the PSF model is on average $\sim$0.1 per cent, but can be as large as $\sim$1 per cent of the true kurtosis value. The PSF model kurtosis tends to be overestimated for smaller PSFs.

Finally, we used the COSMOS parametric catalog to simulate the impact of PSF model kurtosis biases on weak lensing shear measurement with a galaxy population that has a realistic distribution of galaxy sizes, shapes, and Sérsic indices. Our results suggest that the resulting shear biases are redshift-dependent, primarily due to the shear biases depending on the galaxy apparent size (which is redshift-dependent). The redshift-dependent multiplicative bias m_0, defined in Eq. (2.12), which can affect cosmological parameter constraints, is estimated as being roughly 0.05%, at the level of Y10 requirements for LSST.

While our results show that the ensemble weak lensing shear bias caused by errors in PSF higher moments are not a concern for the current generation of ground surveys, e.g. DES, HSC and KiDS, it is large enough that future surveys such as LSST will need to address this challenge. We see several implications from this study. First, the development of future PSF modeling algorithms should include tests of the fidelity of recovering PSF higher moments, rather than just the second moments. Second, future surveys should explicitly test the modeling quality of PSF higher moments as part of their science verification process. Finally, this paper also motivates future work on more detailed and rigorous analysis on the shear bias associated with errors in the higher moments of the PSF model. One limitation of the analysis carried out in this pathfinding work is that we are changing multiple moments at a time, while using the radial kurtosis as a single proxy for the impact of higher moments. A more rigorous future analysis requires consideration of individual higher moment and analysis of their impact to weak lensing, as well as a guidelines for placing requirements on the modeling fidelity for these moments.

2.A Statistics of the HSC PSF

In Fig. 2.A.1, we show the 1D histogram of PSF true $\rho^{(4)}$ and model kurtosis $\hat{\rho}^{(4)}$, and 2D histogram of the true kurtosis $\rho^{(4)}$, its bias $B[\rho^{(4)}]$, and their connection to the PSF size. 0.1% larger than the true PSF kurtosis in panel **(a)**. The width of the true PSF kurtosis distribution is slightly larger than the width of the model PSF kurtosis. A smaller PSF generally has a smaller kurtosis. This is likely caused by a more substantial contribution from the Airy PSF, for smaller PSFs, as Table 2.1 suggests that Airy PSFs have a smaller kurtosis than Kolmogorov PSFs. Also, when the PSF is small, the PSF model tends to overestimate the kurtosis. Note that there is shot noise in the images we measure. However, its impact on this figure is negligible, since our simulation in Sec. 2.4.1 shows that the uncertainty in $B[\rho^{(4)}]$ due to shot noise is < 0.001, and the effect on the average $B[\rho^{(4)}]$ is $< 0.001/\sqrt{n}$, orders of magnitude smaller than our average bias measured.

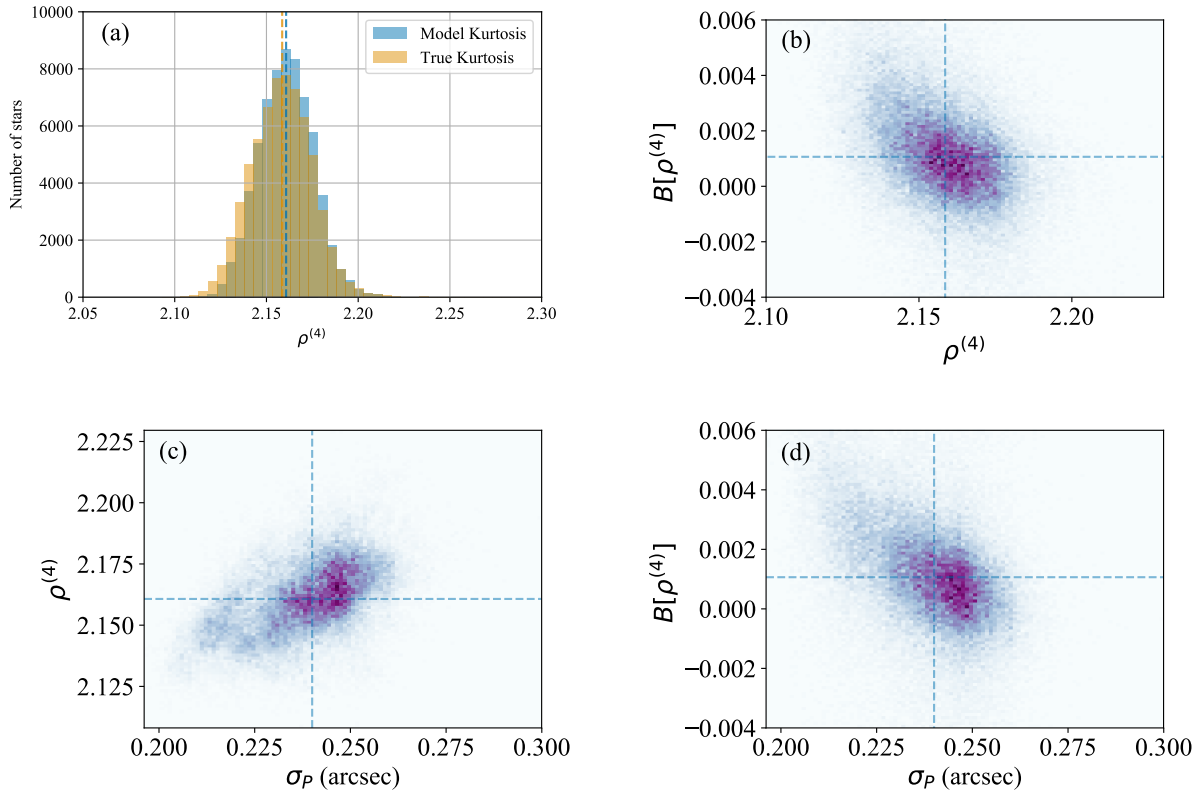

Figure 2.A.1: **(a)**: 1D distributions of the true and model PSF kurtosis. **(b)**: 2D distribution of the kurtosis bias $B[\rho^{(4)}]$ and PSF size σ_P; **(c)**: 2D distribution of the true kurtosis $\rho^{(4)}$ and the PSF size σ_P; **(d)**: 2D distribution of the kurtosis bias $B[\rho^{(4)}]$ and the PSF size σ_P. For the three 2D distribution plots, the median values of the quantities on each axis are shown with dashed lines. The color scales of the distributions are linear in the density.

Chapter 3

Impact of point spread function higher moments error on weak gravitational lensing – II. The Comprehensive Study

Tianqing Zhang[1], Husni Almoubayyed[1], Rachel Mandelbaum[1], Joshua E. Meyers[2], Mike Jarvis[3], Arun Kannawadi[4], Morgan A. Schmitz[5], Axel Guinot[6], The LSST Dark Energy Science Collaboration.

[1] McWilliams Center for Cosmology, Department of Physics, Carnegie Mellon University, 5000 Forbes Ave, Pittsburgh, PA 15213, USA.
[2] Lawrence Livermore National Laboratory, Livermore, CA 94551.
[3] Department of Physics and Astronomy, University of Pennsylvania, Philadelphia, PA 19104, USA.
[4] Department of Astrophysical Sciences, Princeton University, 4 Ivy Lane, Princeton, NJ 08544, USA.
[5] Université Côte d'Azur, Observatoire de la Côte d'Azur, CNRS, Laboratoire Lagrange, Bd de l'Observatoire, CS 34229, 06304 Nice
Cedex 4,France.
[6] Université de Paris, CNRS, Astroparticule et Cosmologie, F-75013 Paris, France.

Abstract

Weak lensing is one of the most powerful probes for dark matter and dark energy science, although it faces increasing challenges in controlling systematic uncertainties as the statistical errors become smaller. The Point Spread Function (PSF) needs to be precisely modeled to avoid systematic error on the weak lensing measurements. The weak lensing biases induced by errors in the PSF model second moments, i.e., its size and shape, are well-studied. However, (70) showed that errors in the higher moments of the PSF may also be a significant source of systematics for upcoming weak lensing surveys. Therefore, this work comprehensively investigate the modeling quality of PSF moments from the $3^{\rm rd}$ to $6^{\rm th}$

order, and propagate the PSFEx higher moments modeling error in the HSC survey dataset to the weak lensing shear-shear correlation functions and their cosmological analyses. The overall multiplicative shear bias associated with errors in PSF higher moments can cause a $\sim 0.1\sigma$ shift on the cosmological parameters for LSST Y10, while the associated additive biases can induce 1σ uncertainties in cosmology parameter inference for LSST Y10, if not accounted. We compare the PSFEx model with PSF in Full FOV (Piff), and find similar performance in modeling the PSF higher moments. We conclude that PSF higher moment errors of the future PSF models should be reduced from those in current methods, otherwise needed to be explicitly modeled in the weak lensing analysis.

3.1 Introduction

Weak gravitational lensing, or weak lensing, is the slight deflection of the light from distant objects by the gravitational effect of nearby objects. Weak lensing leads to a mild change in the object's shape, size and flux, and it is a powerful probe of the dark matter distribution of the Universe due to its sensitivity to the gravitational potential along the line of sight (75; 76; 77). To date, the most promising way of measuring weak lensing is to measure its coherent effects on the galaxy shape, i.e., the weak lensing shear. Weak lensing can be caused by a nearby massive galaxy or cluster, i.e., as measured using galaxy-galaxy lensing (e.g., 32; 45; 125); or by the large-scale structure of the Universe, as measured using cosmic shear (e.g., 1; 126; 127).

The coherent galaxy shape distortions caused by weak lensing are currently measured using millions, in the future even billions, of galaxies in large astronomical surveys. The "Stage III" cosmological surveys (128) that started in the previous decade provided weak lensing observation that moved the field forward substantially; these include the Dark Energy Survey (DES; 79), the Kilo-Degree Survey (KiDS; 80), and the Hyper Suprime-Cam survey (HSC; 81). In the near future, "Stage IV" surveys will begin to observe at greater depth and/or area than the previous generation; the Stage IV surveys include the Vera C. Rubin Observatory Legacy Survey of Space and Time (LSST; 48; 82), the *Nancy Grace Roman* Space Telescope High Latitude Imaging Survey (49; 83) and *Euclid* (50). These new surveys will provide greater statistical precision in the measurements, and therefore demand greater control of systematic uncertainties in weak lensing.

The Point Spread Function (PSF) is the function that describes the atmospheric turbulence, telescope optics, and some detector effects (129; 130) on a point source image. PSF modeling algorithms reconstruct the PSF at the position of the stars, and interpolate the model to arbitrary positions on the image, e.g., PSFEx (84), or to positions on the sky, e.g., Piff (PSF in Full FOV; (85)).

The raw light profile of the galaxies is convolved with the PSF, changing their observed shapes and sizes. Since measuring weak lensing signals relies heavily on measuring the coherent galaxy shape distortions, modeling the PSF correctly is fundamental for controlling weak lensing systematics. Failure of the PSF model to represent the true PSF causes systematic errors in the inferred galaxy shapes and weak lensing shears. Previous studies have

developed a formalism that cleanly describes how the errors in modeling PSF second moments, i.e., the shape and size, affect the galaxy shape measurement and weak lensing shear inference (e.g., 86; 87; 88; 89). There is also a formalism that describes how the PSF second moment errors further propagate to the weak lensing observables (shear-shear correlations), using the "ρ-statistics" (88; 89).

However, the aforementioned formalism, which is commonly used for quantifying the quality of PSF modeling, does not consider the impact on weak lensing shear caused by errors in the higher moments, i.e., moments with order higher than the second, of the PSF model. In (92), excess multiplicative and additive shear bias is found in addition to the predictions of the second moment formalism, for *Euclid*'s PSF. A previous study by (70) (hereafter ZM21) explored this topic by carrying out shape measurement experiments, with the radial kurtosis of the PSF intentionally mis-modeled, while preserving the PSF second moments. They found that errors in the PSF radial kurtosis can induce a multiplicative bias in the inferred weak lensing shear. They also found that for parametric galaxy models based on the COSMOS survey, and for PSF radial kurtosis errors as in the HSC public data release 1 (PDR1; 69) PSF models from PSFEx (84), the PSF radial kurtosis error can cause a redshift-dependent multiplicative shear bias at the level of the LSST Y10 requirement (90), thus motivating further research on this topic.

In this paper, we want to extend the understanding from ZM21 in several ways: (a) include a wider range of PSF higher moments, which might induce both multiplicative and additive shear biases; (b) propagate the biases into the common weak lensing data vector, the two-point correlation function (2PCF) $\xi_{\pm}$, and to cosmological parameter estimates; (c) include Piff, which might provide some estimate of how algorithm-dependent the errors in PSF higher moments are, and might serve as a better example of an algorithm that will be used for LSST.

We introduce background material, including the weak lensing shear, PSF higher moments, and shapelet decomposition in Section 3.2. In Section 3.3, we describe the HSC datasets in this work for measuring the PSF higher moments, and show the results of the PSF modeling quality on the second and higher moments for two PSF models, PSFEx and Piff. In Section 3.4, we describe the methodology of single galaxy simulations, including simulation workflow, galaxy and PSF profiles, and how we change the PSF higher moments with the aid of shapelet decomposition. We also show the results based on these single galaxy simulations. In Section 3.5, we combine the results from Section 3.3 and 3.4 to further propagate the systematics induced by PSF higher moment errors to the weak lensing 2PCF, and its associated cosmology analyses by Fisher forecasting. In Section 3.6, we discuss the implications of our results for weak lensing with future imaging surveys.

3.2 Background

In this section, we describe the background of this paper. In Section 3.2.1, we introduce the formalism to quantify the weak lensing shear. In Section 3.2.2, we introduce the method for

measuring the higher moments of PSFs. We then introduce the radial shapelet decomposition, used as a basis in which we expand any given PSF light profile, in Section 3.2.3.

3.2.1 Weak Lensing

Weak gravitational lensing, or weak lensing, is the coherent gravitational distortion on the background (source) galaxy flux, size, and shape by foreground (lens) objects. The lens can be any massive object, e.g., a galaxy cluster, or a cosmic large-scale structure. Weak lensing is a powerful observable because of its sensitivity to the matter distribution along the line of sight (75; 76; 77). In this paper, we are interested in cosmic shear, which is the coherent distortion of the source galaxy shapes by the large-scale structure of the Universe, resulting in a nonzero two-point correlation function of galaxy shapes. The distortion of the galaxies by the weak lensing shear is determined by the reduced shear $g = g_1 + ig_2$, which is a combination of the shear and the convergence (33). g_1 describes the shear along the x- or y-axes, while g_2 describes the shear along an angle $\pi/4$ defined by growing counterclockwise from the x-axis on the image. Here the x-y axes are aligned with the local (RA, Dec) axes on the sky.

For a cosmological weak lensing analysis, it is useful to measure the weak lensing two-point correlation function (131), also referred to as the 2PCF. We can calculate the shear along a chosen angular vector $\boldsymbol{\theta}$ connecting two galaxies, with polar angle ϕ, by $g_t = -\mathcal{R}(ge^{-2i\phi})$, and $\pi/4$ to $\boldsymbol{\theta}$ by $g_\times = -\mathcal{I}(ge^{-2i\phi})$. The shear 2PCF is computed by

$$\xi_\pm(\theta) = \langle g_t g_t \rangle(\theta) \pm \langle g_\times g_\times \rangle(\theta). \tag{3.1}$$

Since the weak lensing shear is isotropic (statistically speaking), the $\xi_\pm(\theta)$ is integrated over the polar angle ϕ and presented as a function of the angular distance $\theta = |\boldsymbol{\theta}|$.

The weak lensing shear 2PCF as measured through $\xi_\pm$ is sensitive to the coherent change in galaxy shapes due to large-scale structure (97), though it is contaminated by intrinsic alignments (e.g., 62; 63; 64; 65), i.e., the correlated galaxy alignments due to local effects such as tidal fields.

Estimating shear accurately is a key step in any cosmological analysis of weak lensing data. Shear biases are commonly modeled as two terms, the multiplicative bias m and the additive bias c (116; 132), which enter the estimated shear as

$$\hat{g} = (1 + m)g + c, \tag{3.2}$$

where $\hat{g}$ denotes the estimated shear. Systematic biases in the estimated shear must not exceed a certain portion of the statistical error to avoid substantial biases in the reported constraints on the cosmological parameters compared to those that would ideally be recovered. We are particularly interested in a redshift-dependent multiplicative bias; as suggested in (124), a redshift-dependent multiplicative bias can bias the inferred dark energy equation of state parameter from weak lensing. This is motivated since ZM21 found that the shear response to the PSF higher moment errors depends on the galaxy properties, which means

that the galaxy ensemble in each tomographic bin will respond differently to the same PSF higher moment error. In (90), the redshift-dependent multiplicative bias is parameterized by m_0 in

$$m(z) = m_0 \left(\frac{2z - z_{\max}}{z_{\max}} \right) + \bar{m}, \tag{3.3}$$

where $\bar{m}$ is a non-zero average multiplicative bias over redshift. Error budget requirements are placed on the upper bound of the absolute value of multiplicative biases for weak lensing surveys (54; 89). Taking LSST Y10 as an example (90), the requirement on the redshift-dependent multiplicative bias, which is the difference in m across the full source redshift range, is 0.003. This motivates detailed studies on the connection between weak lensing shear systematics and other factors, including the PSF higher-moment modeling error (ZM21 and this work). Note that we only discuss the PSF-induced multiplicative shear biases in this work, without other sources of redshift-dependent multiplicative biases (e.g., 55).

3.2.2 Moment Measurement

In this section, we introduce the methods for measuring higher moments of the PSF. Firstly, we define the adaptive second moment $\mathbf{M}$ for a light profile,

$$M_{pq} = \frac{\int \mathrm{d}x\, \mathrm{d}y\, x^p\, y^q\, \omega(x,y)\, I(x,y)}{\int \mathrm{d}x\, \mathrm{d}y\, \omega(x,y)\, I(x,y)}, \tag{3.4}$$

where $(p,q) = (2,0)$, $(1,1)$, or $(0,2)$. Here $I(x,y)$ is the image intensity, where $\mathbf{x} = (x,y)$ is the image coordinate with origin at the centroid of $I(x,y)$. $\omega(x,y)$ in Eq. (3.4) is the adaptive Gaussian weight, which has the same second moments as the light profile $I(x,y)$ (86), defined by

$$\omega(\mathbf{x}) = \exp[-\mathbf{x}^T \mathbf{M}^{-1} \mathbf{x}]. \tag{3.5}$$

The second moment size σ and shape e_1 and e_2 can then be calculated from the second moments $\mathbf{M}$ using

$$\sigma = [\det(\mathbf{M})]^{\frac{1}{4}} \tag{3.6}$$

$$e_1 = \frac{M_{20} - M_{02}}{M_{20} + M_{02}} \tag{3.7}$$

$$e_2 = \frac{2M_{11}}{M_{20} + M_{02}}. \tag{3.8}$$

Here $\det(\mathbf{M}) = M_{02}M_{20} - M_{11}^2$ is the determinant of the second moment matrix. From Eqs. (3.6)–(3.8), we can solve for the weighted second moments M_{ij} given the weighted shape (e_1, e_2) and size σ, which are measured using the HSM module[1] (86; 113) in GalSim (93).

[1] `https://galsim-developers.github.io/GalSim/_build/html/hsm.html`

Based on the second moments, we also define a standardized coordinate system (u, v) in Eq. (3.9); this is the coordinate system where the profile $I(u, v)$ has zero second moment shape $e_1 = e_2 = 0$, defined in Eqs. (3.7)–(3.8), and second moment size $\sigma = 1$, defined in Eq. (3.6). The standardized coordinate system can be determined via a linear transformation of the image coordinate system as follows:

$$\begin{pmatrix} u \\ v \end{pmatrix} = \mathbf{M}^{-\frac{1}{2}} \begin{pmatrix} x \\ y \end{pmatrix} = \begin{pmatrix} M_{20} & M_{11} \\ M_{11} & M_{02} \end{pmatrix}^{-\frac{1}{2}} \begin{pmatrix} x \\ y \end{pmatrix}. \tag{3.9}$$

The standardized adaptive higher moment, M_{pq}, is then defined by

$$M_{pq} = \frac{\int \mathrm{d}x\, \mathrm{d}y\, [u(x,y)]^p\, [v(x,y)]^q\, \omega(x,y)\, I(x,y)}{\int \mathrm{d}x\, \mathrm{d}y\, \omega(x,y)\, I(x,y)}. \tag{3.10}$$

For the n^{th} moments, p takes any value between 0 to n, and $q = n - p$. We choose to measure PSF higher moments in the standardized coordinate system (u, v) instead of (x, y), as such quantities are scale and shape independent, assuming the PSF is well-sampled. The weight ω is applied to suppress image noise at large radii during the measurement process. The denominator is the normalizing factor, such that the higher moments will not depend on the amplitudes of the weight and the image.

Throughout this paper, we define the biases on the moment M_{pq} as

$$B[M_{pq}] = M_{pq,\mathrm{model}} - M_{pq,\mathrm{true}}, \tag{3.11}$$

where $M_{pq,\mathrm{model}}$ is the moment of the model PSF, and $M_{pq,\mathrm{true}}$ is the moment of the true PSF. Note that we refer to the standardized higher moments as the "higher moments" throughout this paper.

3.2.3 Shapelet Decomposition

The shapelet decomposition is an expansion of a two-dimensional image with the eigenfunctions of the 2D quantum harmonic oscillator as the basis functions. This basis function is also referred to as the Laguerre Function with Gaussian weight. This method was used to expand the galaxy and PSF profile in (133) and used to measure weak lensing shear in (134). For detailed explanations of shapelet expansions, see also (114). In this study, we use the shapelet decomposition implemented in GalSim[2] (93).

The shapelets basis functions are parameterized by a single parameter: the length scale L. After determining the value of L for the image, the image can be decomposed into a series of shapelet coefficients b_{jk}, indexed by j and k. We also defined two more indices, i.e., the order $N = j + k$ and the spin number $m = j - k$. The PSF image $I(r, \theta)$ can be expanded by the basis functions of the shapelet coefficients b_{jk},

$$I(r, \theta) = \frac{1}{L^2} \sum_{jk} b_{jk}\, \psi_{jk} \left(\frac{r}{L}, \theta \right), \tag{3.12}$$

[2] `https://github.com/GalSim-developers/GalSim`

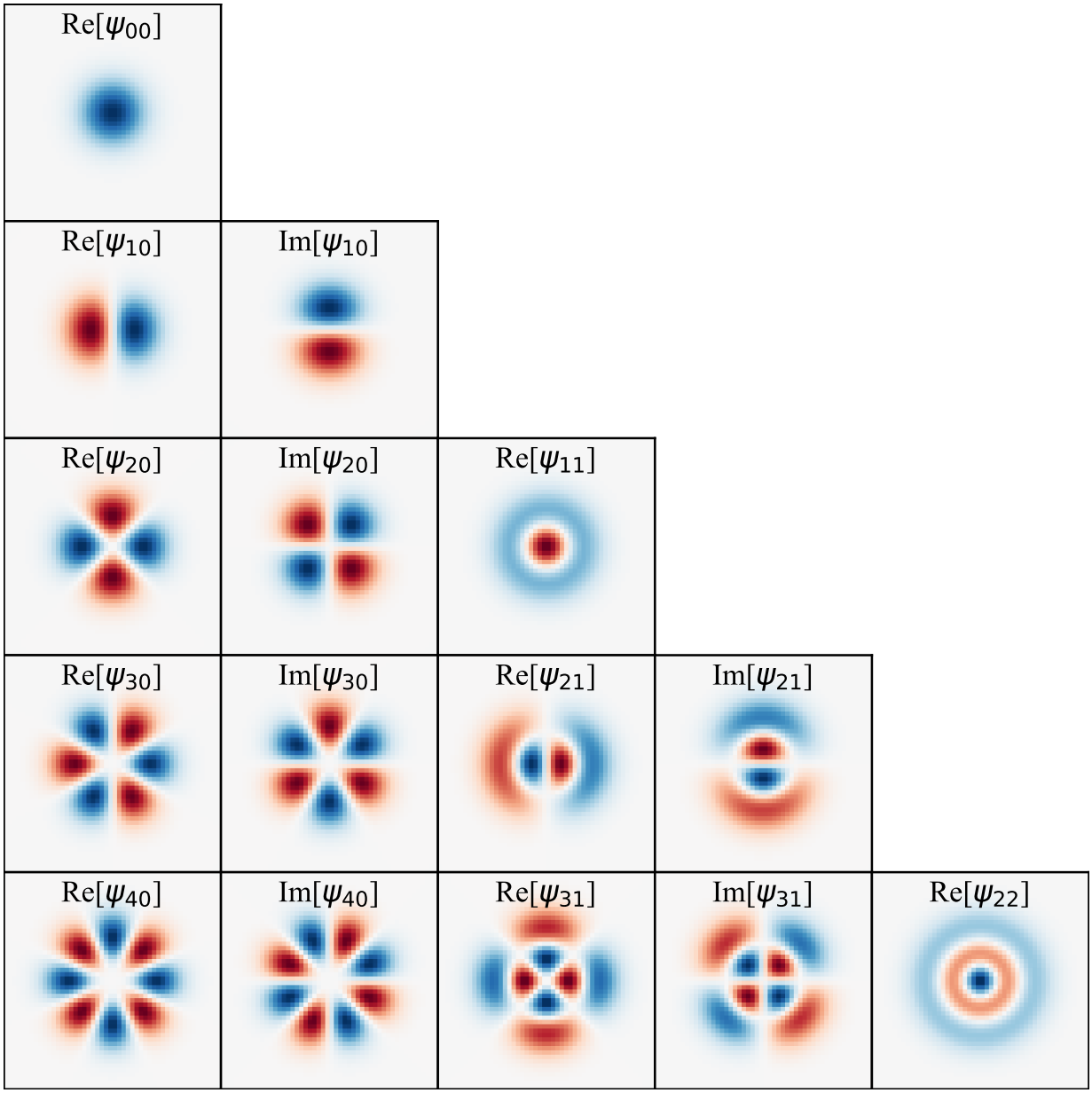

Figure 3.2.1: The first 15 unique real and imaginary parts of the shapelet basis functions in Eq. (3.13). We plot the first 5 orders of this basis, i.e., $p+q=0$ through 4. The color scale for each base covers $[-A, A]$, where A is the maximum of the absolute value of that basis function.

where $\psi_{jk}\left(\frac{r}{L}, \theta\right)$ is the Laguerre Function with Gaussian weight, i.e., the radial shapelet basis in a polar coordinate system with radius r and polar angle θ,

$$\psi_{jk}(r,\theta) = \frac{-1^q}{\sqrt{\pi}} \sqrt{\frac{j!}{k!}}\, r^m\, e^{im\theta}\, e^{-\frac{r^2}{2}}\, \mathbf{L}_j^{(m)}(r^2). \tag{3.13}$$

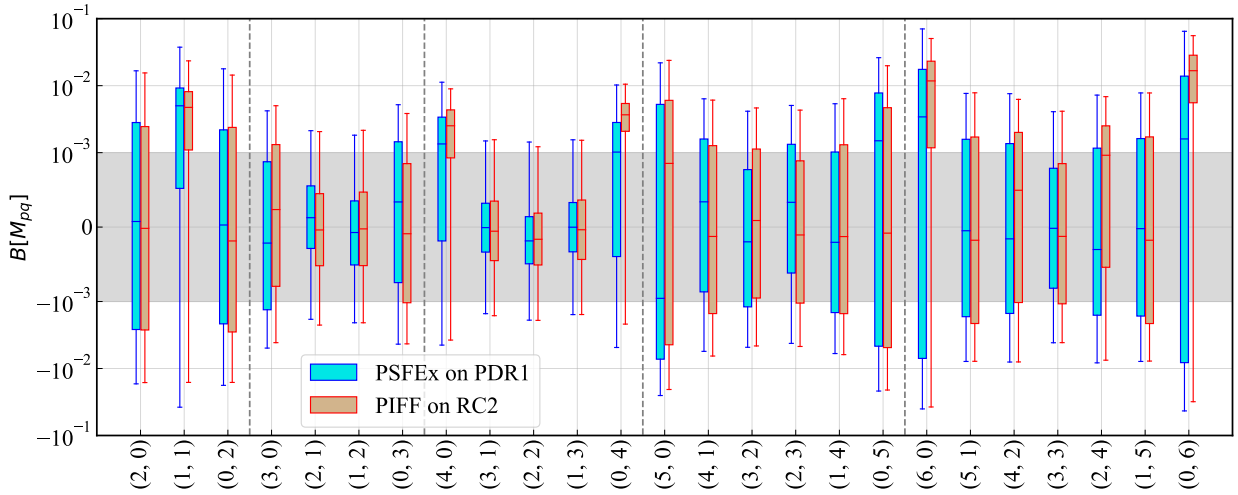

Figure 3.3.1: Box plot showing the PSF moment biases from the 2nd to the 6th moments, with the whiskers showing the 2σ range (from 3rd to 97th percentile), the boxes showing the interquartile range, and the bars showing the median. The PSFEx and Piff results are shown side-by-side. The y-axis is symmetrical log-scaled, with the linear region shown in grey. Although PSFEx and Piff were used to model two different HSC datasets, we observe a comparable order of magnitude in PSF model residuals for the two methods. However, Piff's median residuals on M_{40}, M_{04}, M_{60} and M_{06} are a few times larger than those of PSFEx. These are the main contributing higher moments to the shear biases, thus motivating further development of Piff.

The $\mathbf{L}_k^{(m)}(r^2)$ is the Laguerre Polynomial. Fig. 3.2.1 shows the first 15 basis images of ψ_{pq} that we used to decompose the PSF. For a given order N, there are $2N+1$ shapelet basis functions. Due to conjugate pairings, N of the shapelet coefficients b_{jk} are identical to b_{kj}. Therefore, to expand a real image, we have $N+1$ distinct shapelet basis functions for order N that satisfy $j \geq k$.

To determine the length scale L, we carried out the following experiment: We decomposed the PSF with different length scales L; kept the 40 leading b_{jk}s of the shapelet series; reconstructed the image using the first forty b_{jk}; and measured the residual of this reconstruction. We found that to minimize the absolute value of the residual of the reconstruction, the length scale L should be set to the weighted second moment σ of the PSF defined in Eq. (3.6). This rule was found to be true on both the Gaussian and Kolmogorov profiles. We therefore adopted this approach throughout this work.

3.3 Data

In this section, we introduce the data from the Hyper Suprime-Cam survey (HSC; 81) to study how well current PSF models recover PSF higher moments. We inspected two datasets,

one for PSFEx and one for Piff. For both datasets, we used the coadded images of bright stars as the true effective PSF, and compared them with the PSF model at the bright stars' positions. The PSFEx and Piff star catalogs are described in Sections 3.3.1 and 3.3.2, respectively. We describe the measurement results of the PSF higher moments error in Section 3.3.3.

3.3.1 PSFEx Dataset

The dataset for quantifying the modeling quality of PSFEx is the star catalog of the first HSC public data release (PDR1; 69). The PSFEx model in this study was generated by the HSC pipeline (110) with a modified version of PSFEx (84); see Section 3.3 of (110) for more details. We used all six fields in the PDR1 survey to inspect the PSF higher moments, instead of just the GAMA_15H field as in ZM21. Our star selection process for the PSFEx is detailed in Section 3.4.1 in ZM21, so we only summarize it briefly here.

We adopted the "basic flag cuts" from Table 3 of (54), with iclassification_extendedness set to 0 to identify non-extended objects. These flag cuts eliminate objects that are contaminated or affected by exposure edges, bad pixels, saturation or cosmic rays, and reduce the number of selected stars to 1.1×10^7. We adopted a signal-to-noise ratio (SNR) cut SNR > 1000 to reduce noise in the PSF higher moments measurement, which further reduced the sample size to 3.1×10^5. The SNR cut was determined so that the statistical uncertainty in the PSF radial fourth moments of the star images is $< 0.1\%$ (ZM21), avoiding a scenario where the higher moments are dominated by the image noise. The i-band magnitudes of the selected stars are between 18 to 20, a regime in which the correction for the brighter-fatter effect (110) is highly effective as shown in Section 4.2 of (54). The SNR selections are only done for our PSF modeling inspection, not when running the PSF modeling step.

ZM21 identified the need for a cut iblendedness_abs_flux> 0.001 to address the fact that the moment measurements of blended objects are biased. In this work, that cut reduced the sample size to 2.6×10^5. Finally, we also excluded stars with a close neighbor within 2 arcmin of their centroids using a k-d tree. At the end of the selection process, we had 2.4×10^5 stars, around four times the amount in ZM21 since we used all six HSC fields. The number density of the PSFEx star dataset is 0.62 arcmin^{-2}. Examples of moment residual maps for PSFEx are shown in Appendix 3.A.

3.3.2 Piff Dataset

We measured the performance of Piff (85) on the HSC data in order to compare with PSFEx. Piff was used as the PSF modeling algorithm for the DES Y3 dataset and performed better than previous DES PSF models, especially at modeling continuous trends across multiple detectors. Piff has been run on the HSC Release Candidate 2 (RC2)[3], which consists of two HSC SSP-Wide tracts and one HSC SSP-UltraDeep tract. We used version 1.1.0

[3]Detailed description of the RC2 dataset can be found in `https://dmtn-091.lsst.io/v/DM-15448/`.

of PIFF. It modeled PSFs in the image coordinate system, instead of in the WCS coordinates, with pixel scale equal to the native pixel scale (0.168 arcsec). The model kernel size is 21×21 pixels. The PSF was interpolated with a second order polynomial. We used χ^2 outlier rejection with nsigma= 4.0 and max_remove= 0.05. We refer the readers to (85) for a detailed explanation of these settings. The RC2 dataset is reprocessed biweekly using the latest version of Rubin's LSST science pipelines (123). We inspected the PSF modeling quality on the two wide-field tracts, which correspond to an area of ~ 6 deg^2 (each tract of the HSC data is roughly 3 deg ^{2}).

The star selection differs from that used for the PSFEX dataset: we used the pre-selected PIFF candidate stars with SNR$>$ 1000, without the need for the blending flux and close-neighbor cut. By this criterion, we had in total 11366 stars and PSF models to compare. The number density of the PIFF dataset is 0.55 arcmin^{-1}, about 13 per cent lower than that for PSFEX. Examples of moment residual maps for PIFF are shown in Appendix 3.A.

3.3.3 Measuring PSF Higher Moment Error

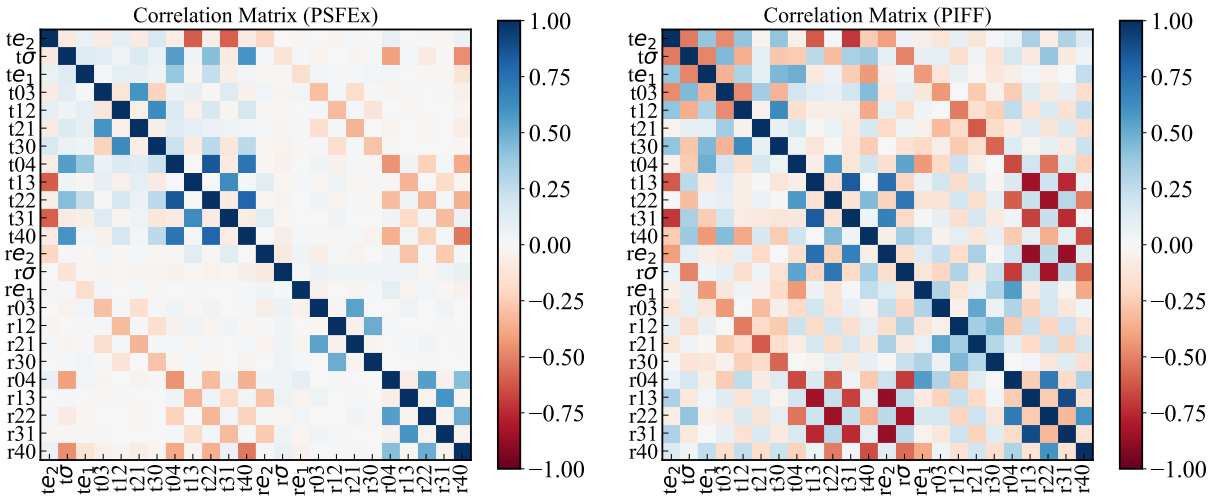

Figure 3.3.2: The correlation matrix of PSFEX (upper) and PIFF (lower) moments from the 2$^{\text{nd}}$ to the 4$^{\text{th}}$ moments, where "t" denotes the true values of the moments and "r" denotes the moment residuals.

We used the postage stamp images of the selected stars as measures of the true PSF. We obtained the PSF models evaluated at the position of the stars, as the model PSF. We used coadded star images, for which the PSF models are a weighted coaddition of the PSF model in each exposure (110). We measured the 22 higher moments, defined in Eq. (3.10), from the 3$^{\text{rd}}$ to the 6$^{\text{th}}$ order with the method described in Section 3.2.2. We also measured the weighted second moments with the HSM (113) module of GALSIM.

We measured the moment biases $B[M_{pq}]$ by subtracting the star PSF moments $M_{pq,\text{true}}$

from the model PSF moments $M_{pq,\mathrm{model}}$, as in Eq. (3.11). In Fig. 3.3.1, combining the measurements of the PSF higher moments for all of the selected stars in these datasets, we show the distributions of the PSFEx and Piff moment errors $B[M_{pq}]$ with box plots side by side. The whiskers of the plot show the 2σ ranges of the distributions, the boxes show the interquartile ranges, and the bars show the median. We can see from the box plots that the two PSF models have similar PSF second moment residuals, and the PSF sizes are positively biased in both models, as observed for PSFEx in (54). We listed the mean of the moment residual $\langle B[M_{pq}]\rangle$ for PSFEx and PIFF in Table 3.4.2.

We calculated the "bias fluctuation" field $\widetilde{B}[M_{pq}](\mathbf{x})$ by

$$\widetilde{B}[M_{pq}](\mathbf{x}) = B[M_{pq}](\mathbf{x}) - \langle B[M_{pq}](\mathbf{x})\rangle. \tag{3.14}$$

We then used the two-point correlation function (2PCF) to measure the cross-correlation of the bias fluctuations $\widetilde{B}[M_{pq}](\mathbf{x})$ and $\widetilde{B}[M_{uv}](\mathbf{x})$,

$$\xi^{pq,uv}(\theta) = \langle \widetilde{B}[M_{pq}](\mathbf{x})\widetilde{B}[M_{uv}](\mathbf{x}+\theta)\rangle. \tag{3.15}$$

When $p = u$ and $q = v$, Eq. (3.15) becomes the auto-correlation function of $\widetilde{B}[M_{pq}](\mathbf{x})$. We measured the 2PCFs of the PSF higher moment errors using TreeCorr[4] (8).

Because of the relatively small area of the Piff dataset, we only measured its one-point statistics (mean, covariance matrix, etc.), not its two-point statistics. Therefore, we can only compare Piff with PSFEx at the early analysis stage, rather than propagating to the weak lensing data vector contamination and biases in cosmological parameter estimates.

The version of Piff used for this work produces similar order-of-magnitude PSF moment residuals as PSFEx from the 2$^{\mathrm{nd}}$ to the 6$^{\mathrm{th}}$ moments. However, its median residuals on M_{40}, M_{04}, M_{60} and M_{06} are several times larger than those for PSFEx, which is important because those are the primary moments contributing to the shear bias. This finding is not surprising because the implementation of Piff integrated with Rubin's LSST Science Pipelines has not been thoroughly tuned, and in particular, none of its testing has focused on its optimization for accurate recovery of PSF higher moments. The results for Piff in Fig. 3.3.1 motivate further algorithm development and tuning, by providing additional metrics toward which to optimize in addition to the 2$^{\mathrm{nd}}$ moments. In Appendix 3.A.2, we show an apples-to-apples comparison between Piff and PSFEx on the RC2 dataset; the results further motivate the optimization of Piff toward minimizing PSF higher moment residuals.

In Fig. 3.3.2, we show the correlation matrix between the true PSF moments and their residuals for PSFEx (upper) and Piff (lower panel). We see a chequered-flag pattern in the correlation matrices. The true moments with the same parity for both p and q are usually positively correlated, and likewise for the residuals. This results in a chequered pattern within the same order $n = p + q$ – the (p, q) and the $(p \pm 2, q \mp 2)$ moments are correlated – as well as a bigger chequered pattern across the orders – between n and $n \pm 2$ orders, though the latter cannot be seen in our plots, since we are only showing $n = 3$ and $n = 4$

[4] `https://github.com/rmjarvis/TreeCorr`

moments. There is an even larger scale pattern: the true moments and residuals for a given (p, q) are typically anti-correlated with each other due to the impact of noise on the true moments. We also observe a significant anti-correlation between "tσ" and "r04"/ "r40" for PSFEx. This indicates that M_{04} and M_{40} are preferentially overestimated in areas of the survey with good seeing. This result is consistent with the findings of ZM21, but it is not seen in the Piff results because it does not perform oversampling for good-seeing images. However, the correlation matrix of Piff shows stronger anti-correlations between the true and the residual moments, which suggests that the model is relatively unresponsive to the true values.

There are some caveats regarding the results presented in this section: (a) Due to the way that HSC PDR1 reserves PSF stars randomly for each exposure, 97% of the stars in the PDR1 dataset were used to generate PSF models in more than one exposure before the coadding process (110), so we are potentially underestimating the systematic uncertainties from the PSF interpolation process. (b) The results in this paper may overestimate $B[M_{04}]$ and $B[M_{40}]$ compared to the real HSC cosmic shear catalog, as the anti-correlation between $B[M_{04}]$ and $B[M_{40}]$ and seeing suggested that PSFEx severely overestimated $B[M_{04}]$ and $B[M_{40}]$ in good-seeing parts of the survey, which were eliminated from the shear catalog (54). Later HSC releases (135) showed that the updated HSC coaddition method using the fifth-order Lanczos kernel did considerably better at modeling the PSF in good-seeing regions than the third-order Lanczos kernel in the first data release. Therefore, the modeling errors in the good-seeing fields are reduced for the later HSC three-year shear catalog (136). Given this resolution, we will not further investigate this particular issue.

3.4 Image simulation

In this section, we introduce the image simulations used in this study. The main purpose of the image simulation is to understand the shear response to the PSF higher moments modeling error, of which the methods and results are presented in this section.

We will briefly cover the parts that are similar to the image simulation process in Section 3.3 of ZM21 and focus on the details that are different from the previous paper. The general simulation workflow is introduced in Section 3.4.1, the galaxy profiles in Section 3.4.2. In Section 3.4.3, we introduce our method of manipulating PSF higher moments by changing the coefficients of the shapelet decomposition, and the PSF profiles used in this work in Section 3.4.4. We show the results of the shear response to the PSF higher moment errors with image simulations in Section 3.4.5.

3.4.1 Simulation Workflows

Fig. 3.4.1 introduces the general image simulation workflow. The top part of the figure shows the steps of the image simulation process for one parametric galaxy and PSF. We started with a galaxy profile and its 90- deg rotated pair (116), an approach we used to reduce simulation volume by nullifying shape noise, for which the parameters will be introduced in

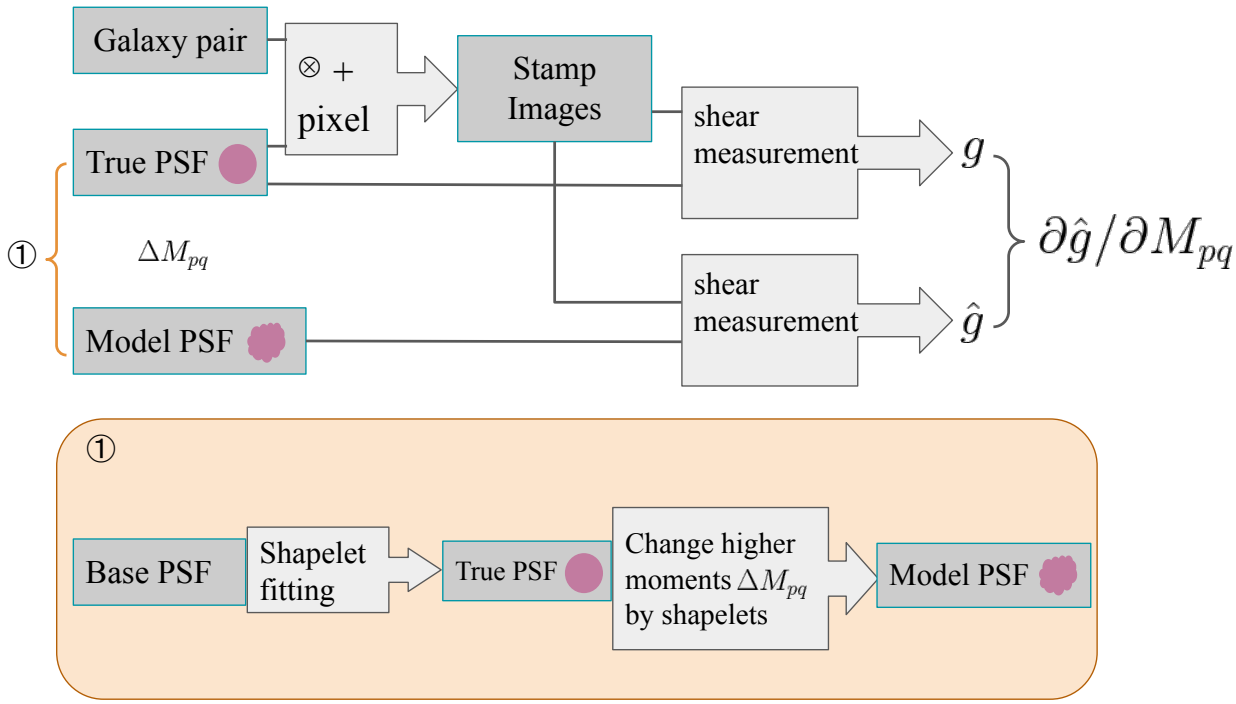

Figure 3.4.1: The workflow of the image simulation for one parametric galaxy and PSF model with one of the higher moment biased compared to the true PSF. The top part shows this workflow, while the bottom orange box shows the process that generates the true and model PSF.

Section 3.4.2. The two galaxy profiles were convolved with the true effective PSF, introduced in detail in Section 3.4.4; it includes the convolution with a pixel response function (0.2 arcsec). The convolved profiles were then sampled at the centers of pixels, generating the postage stamp images. The image set for the rotated galaxy pair was fed into the shear measurement algorithm, which is the re-Gaussianization (86) method implemented in the HSM module (113) in GalSim (93). We do not use Metacalibration (56; 57) as ZM21 showed that systematic biases in shear due to PSF modeling errors do not strongly depend on shear estimation methods. We used the average of the measured shears for the galaxy and its 90- deg rotated pair as the shear estimate for a given PSF. Finally, the difference between the two shear estimates $\Delta\hat{g}$, measured by the true PSF and the model PSF, provides the shear bias associated with the PSF higher moment bias $B[M_{pq}]$.

The additive shear response to the higher moment error M_{pq} was estimated at $g = 0$ by

$$\frac{\partial c_{pq}}{\partial M_{pq}} = \frac{\Delta\hat{g}}{B[M_{pq}]}. \tag{3.16}$$

To estimate the multiplicative shear bias generated by the PSF higher moment errors, we introduced another shear $g' = g + 0.01$. Its estimated values $\hat{g}'$ for the true and model PSF,

and their difference $\Delta\hat{g}'$, were used to estimate the multiplicative biases as

$$\frac{\partial m_{pq}}{\partial M_{pq}} = \frac{\Delta\hat{g}' - \Delta\hat{g}}{0.01B[M_{pq}]}. \tag{3.17}$$

There are some general settings that apply to all of our image simulations: we used GalSim (93) to render the simulated images, all of which are noise-free postage stamp images with a pixel scale of 0.2 arcsec, similar to the pixel scale of the Rubin Observatory LSST Camera (LSSTCam).

3.4.2 Galaxy Profile

Two types of galaxy profiles were used in this study. The simpler galaxies were simulated as elliptical Gaussian light profiles. Gaussian galaxies were used in preliminary tests to develop basic intuition about the shear biases induced by errors in the PSF higher moments. The more complex galaxy model was a bulge+disc galaxy, consisting of a bulge and a disc component. The bulge+disc model was used for more sophisticated tests that attempt to represent a more realistic galaxy population as in the cosmoDC2 catalog (137).

The Gaussian profiles were parameterized by their size σ and ellipticity (e_1, e_2). We used them for initial tests to understand the relationship between shear bias and PSF higher moment bias (linear or non-linear?), the type of induced shear bias (multiplicative or additive?), and to determine which PSF higher moments actually contribute to weak lensing shear biases. The galaxy and PSF parameters for these preliminary single galaxy simulations are shown in Table 3.4.1, with results shown in Section 3.4.5. All base PSFs used in these initial simulations were Gaussian profiles, except for the last row, which is a Kolmogorov PSF.

A more sophisticated galaxy profile we used is the bulge+disc galaxy, a classic model used by many studies (e.g., 138; 139). The bulges and disks in this work have common centroids. The bulge component was a de Vaucouleurs profile (140), a Sérsic profile (118) with $n = 4$, which means the surface brightness is proportional to $\exp(-R^{1/4})$, where R is the distance from the centroid in units of its scale radius. The disk component was an exponential profile, i.e., the surface brightness is proportional to $\exp(-R)$, or the $n = 1$ Sérsic profile. Both components have independent size and shape parameters. The luminosity profile of the components of the bulge+disc galaxy was governed by two parameters: total luminosity and the bulge fraction (B/T). The bulge+disc simulations allowed us to estimate the shear response to error in the PSF higher moments as a function of galaxy properties, which is an important input to the catalog-level simulations later in Section 3.5.3.

3.4.3 Moment-Shapelet Relation

Before introducing the PSF profile, we need a way to generate light profiles that differ in higher moments, introduced in Section 3.2.2, from the base PSF in ways that we can specify. Unfortunately, we do not know an analytical expression for a basis that has a one-to-one mapping with the higher moments. However, since the shapelet basis and the

Index	Galaxy Type	Galaxy Parameters	(g_1, g_2)	PSF Parameters	$B[M_{pq}]$
1	Gaussian	$\sigma_{\rm gal} = 0.17$ arcsec	$(0, 0)$	$\sigma_{\rm PSF} = 0.24$ arcsec	$-0.01 \sim 0.01$
2	Gaussian	$\sigma_{\rm gal} = 0.17$ arcsec	$(0 \sim 0.01, 0 \sim 0.01)$	$\sigma_{\rm PSF} = 0.24$ arcsec	0.005
3	Gaussian	$\sigma_{\rm gal} = 0.1 \sim 0.9$ arcsec	(0.0, 0.0)	$\sigma_{\rm PSF} = 0.3$ arcsec	0.005
4	Sérsic, n=3	$R_{\rm gal} = 0.1 \sim 0.9$ arcsec	(0.0, 0.0)	$\sigma_{\rm PSF} = 0.3$ arcsec	0.005
5	Gaussian	$\sigma_{\rm gal} = 0.1 \sim 0.9$ arcsec	$(0 \sim 0.01, 0 \sim 0.01)$	$\sigma_{\rm PSF} = 0.3$ arcsec	0.005
6	Sérsic, n=3	$R_{\rm gal} = 0.1 \sim 0.9$ arcsec	$(0 \sim 0.01, 0 \sim 0.01)$	$\sigma_{\rm PSF} = 0.3$ arcsec	0.005
7	Bulge+Disc	$R_{h,b}, R_{h,d}, B/T, e_b, e_d$ in Table 3.5.1	$(0 \sim 0.01, 0 \sim 0.01)$	FWHM= 0.6 arcsec	0.005

Table 3.4.1: The specification of galaxies, PSFs, and higher-moments error applied to the PSFs for the single galaxy image simulations in this paper. The M_{pq} in the last column stands for all viable moments from $3^{\rm rd}$ to $6^{\rm th}$ order. All base PSFs in the single galaxy simulations are Gaussian PSFs, except for the last row with Kolmogorov PSFs. Note that the PSF σ values in the table describe the pixel-convolved true and model PSFs, not the base PSFs.

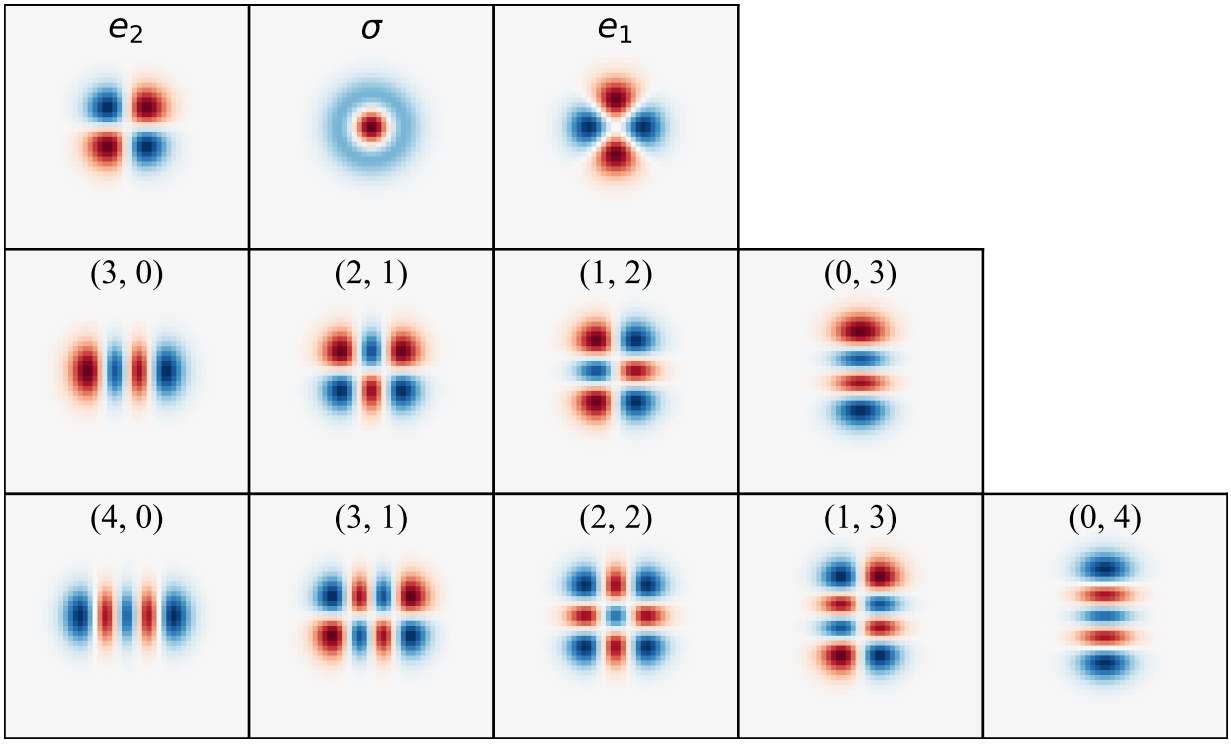

Figure 3.4.2: The moment responses for a Gaussian PSF. We only show the second to fourth moments here, with index (p, q) in Eq. (3.10) labelled in each box. We use e_1, e_2, and σ to represent the second moments. The color scale for each base covers $[-A, A]$, where A is the maximum of the absolute value of the basis function.

unknown moment response can be used to describe the same linear space, we can reconstruct the unknown basis through linear combinations of the known shapelet basis, described in Section 3.2.3.

To do so, we defined the Jacobian matrix

$$T_{pq,jk} := \frac{\partial M_{pq}}{\partial b_{jk}}, \tag{3.18}$$

which is the generalized gradient of the moments M_{pq} with respect to the shapelet coefficients b_{jk} defined in Eq. (3.12). We ranked the shapelet coefficients and PSF higher moments according to the orders in Fig. 3.2.1 and Fig. 3.4.2 We then directly estimated the change in moment ΔM_{pq} given the change in all shapelet coefficients b_{jk},

$$\sum_{j,k} \frac{\partial M_{pq}}{\partial b_{jk}} \Delta b_{jk} = \Delta M_{pq}. \tag{3.19}$$

Since b_{jk} converges to zero at large $j + k$ for Gaussian-like profiles including ground-based PSFs, we were able to truncate the shapelet expansion at some finite order, making Δb_{jk} and $T_{pq,jk}$ finite-sized vectors and matrices.

To numerically measure $T_{pq,jk}$ of the PSF with higher moment M_{pq}, we first decomposed the PSF into a set of shapelet coefficients b_{jk}. Then we perturbed $b'_{jk} = b_{jk} + \Delta b_{jk}$, and measured the higher moment M'_{pq} after the perturbation. The Jacobian element was then estimated by

$$T_{pq,jk} = \frac{M'_{pq} - M_{pq}}{\Delta b_{jk}}. \tag{3.20}$$

In Appendix 3.B, we show a visualization of the Jacobian matrix that describes how PSF moments can be modified through changes in the shapelets coefficients.

In the next section, we introduce the PSF profiles in this paper, and describe how we use the Jacobian $T_{pq,jk}$ defined in this section to precisely change the PSF higher moments.

3.4.4 PSF Profile

In the image simulations, we created the true and model PSF based on a "base PSF". We considered two base PSFs: Gaussian and Kolmogorov. Note that the base PSFs do not include the pixel response function, but the model and true PSFs do include it. The process to create the true and model PSF is shown in the orange box in Fig. 3.4.1.

To change the PSF moments using the technique described above, we first rendered an image of the base PSF including convolution with the pixel response function, and expanded that image by the shapelet decomposition implemented in GalSim (93). We carried out the shapelet decomposition up to order 10, which corresponds to determining 66 shapelet basis coefficients. To test that the shapelets decomposition is effectively representing the higher moments of the PSF profile, we confirmed that the fractional kurtosis error measured using the adaptive moments of the shapelets-reconstructed PSF compared to the original image is 10^{-5} for Kolmogorov and 10^{-9} for Gaussian, which is an acceptable precision for this study. The kurtosis is a good quantity for comparing higher moments, since (a) it is a combination of three moments (M_{04}, M_{22}, and M_{40}); (b) many other higher moments are zeros, and are not suitable for comparing fractional differences.

After representing the true PSF as an order 10 shapelet series, we calculated the Jacobian $\boldsymbol{T}$ that links the 66 shapelet coefficients with the PSF higher moments. The Jacobian is defined by Eq. (3.18) and estimated by Eq. (3.20). In this study, we investigated the higher moments from $3^{\rm rd}$ to $6^{\rm th}$ order, corresponding to 22 moments. Together with the three second moments, the Jacobian is a 25×66 matrix. As an example, the Jacobian for the first 15 moments and first 15 shapelet modes is shown in Fig. 3.B.1.

Before describing how to use $\boldsymbol{T}$ to construct images with precisely modified higher moments, we first define our notation. The true and model PSF are represented as vectors of shapelet expansion coefficients $\mathbf{b}$ and $\mathbf{b}'$. The corresponding moment vectors are $\mathbf{M}$ and $\mathbf{M}'$.

Ideally, we only change one higher moment of the PSF at a time, by solving for $\boldsymbol{\Delta}\mathbf{b}$ in Eq. (3.19). However, because of the non-linearity of the moment-shapelet relationship, the higher moments will not change exactly according to $B[\mathbf{M}]$ when we add $\mathbf{b}$ and $\boldsymbol{\Delta}\mathbf{b}$. Therefore, we introduced multiple iterations until the target moment biases $B[\mathbf{M}]$ are achieved, specified in Algorithm 1. We defined $\boldsymbol{\Delta}\mathbf{M}$ as the difference between our target moment

vector and the current moment vector, which is the quantity we want to minimize. We used the L^2 norm to quantify the magnitude of $\mathbf{\Delta M}$, i.e., $||\mathbf{\Delta M}||_2 = \sqrt{\mathbf{\Delta M}^T \cdot \mathbf{\Delta M}}$.

Algorithm 1: Moment Change

Initialize: $\mathbf{b}$, $\boldsymbol{T}$;
Target moment bias: $B[\mathbf{M}]$;
Target final moment vector: $\mathbf{M}' \leftarrow \mathbf{M} + B[\mathbf{M}]$;
$\mathbf{\Delta M} \leftarrow B[\mathbf{M}]$;
while $||\mathbf{\Delta M}||_2 > t_0$ **do**
  Solve $\boldsymbol{T}\mathbf{\Delta b} = \mathbf{\Delta M}$ for $\mathbf{\Delta b}$;
  Generate new model PSF: $\tilde{\mathbf{b}} = \mathbf{b} + \mathbf{\Delta b}$, measure its moments vector $\widetilde{\mathbf{M}}$;
  Update the $\mathbf{\Delta M}$: $\mathbf{\Delta M} \leftarrow \mathbf{M}' - \widetilde{\mathbf{M}}$;
  Update Jacobian: $\boldsymbol{T} \leftarrow \frac{\partial \widetilde{\mathbf{M}}}{\partial \tilde{\mathbf{b}}}$
end

We used this algorithm to ensure that the moments of the new PSF model approach the target moments $\mathbf{M} + B[\mathbf{M}]$, so the new PSF model has moment biases that differ from those of the true PSF by $B[\mathbf{M}]$. We set the default threshold t_0 for the error in moment change to be 10^{-6}, and the algorithm usually took less than 5 iterations to converge for Gaussian and Kolmogorov PSFs. Note that we included the second moments in the moment bias vector $B[\mathbf{M}]$ and set them to zero. In this way, we actively verified that the model and true effective PSF have the same second moments.

Introducing one component of $B[\mathbf{M}]$ at a time enabled us to inspect the moment response from second to sixth order by taking the difference between the images before and after one moment is slightly biased, in Fig. 3.4.2. This also enabled us to quantify the impact on weak lensing shear associated with errors in the PSF model for a specific moment.

3.4.5 Shear Response to PSF Higher Moments

In this section, we show the results of the image simulation and shear measurement experiments described in Sections 3.4.1 to 3.4.4, using Gaussian PSFs and 90- deg rotated galaxy pairs. Using the single galaxy simulations, we can learn the following: (a) the form of the shear response to PSF higher moment errors – are they linear, quadratic, or even more complicated; and (b) the pattern of shear biases associated with PSF higher moment errors, including magnitude of the biases and symmetry in the response to particular moments. Item (b) is particularly useful as it permits dimensionality reduction to focus on only the key PSF moments in later experiments.

ZM21 found only multiplicative biases associated with the radial kurtosis error of the PSF model. In this study, we cannot assume that all biases will be multiplicative, since we introduced other moment errors. In Fig. 3.4.3, we show the additive shear biases due to $B[M_{pq}]$ in the $3^{\rm rd}$ and $4^{\rm th}$ moments of the PSF model, with (p, q) shown on top of each

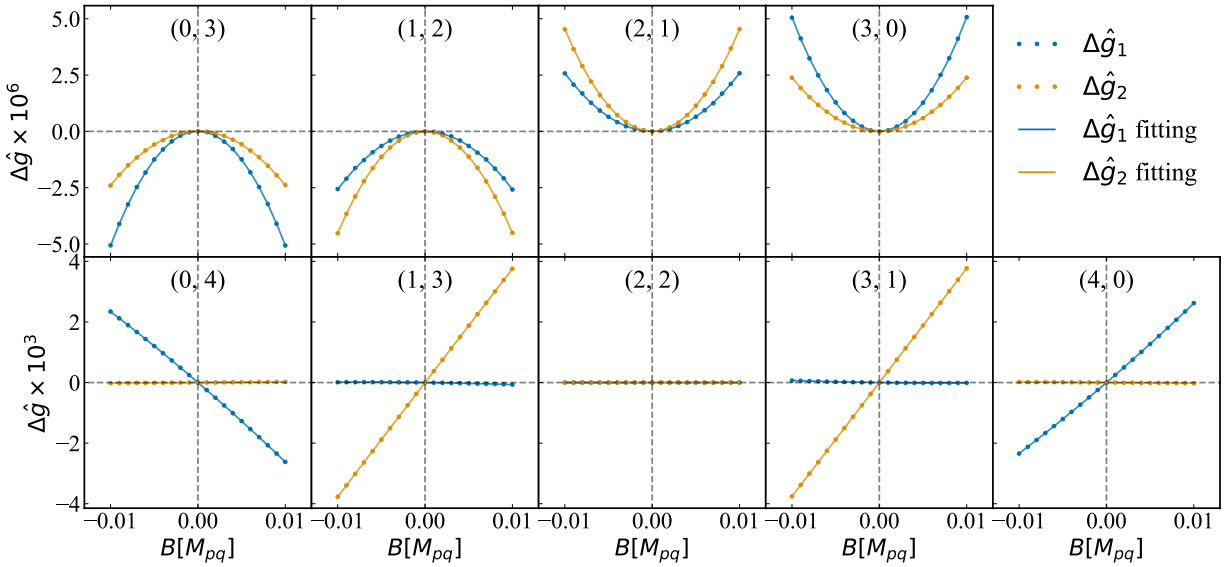

Figure 3.4.3: The additive shear bias generated by errors in the 3$^{\text{rd}}$ and 4$^{\text{th}}$ moments of the PSF. Both the galaxy and PSF have constant sizes. The shear biases for odd moments are well-fitted by a quadratic function, while those for even moments are linear. The quadratic fits are shown as lines, while individual simulation results are shown by dots. The quadratic terms for the 4$^{\text{th}}$ moments are ≈ 0, so the fitting functions appear to be linear. As indicated in the y-axis labels, the order-of-magnitude difference in the additive shear biases between the 3$^{\text{rd}}$ and 4$^{\text{th}}$ moments is 10^3.

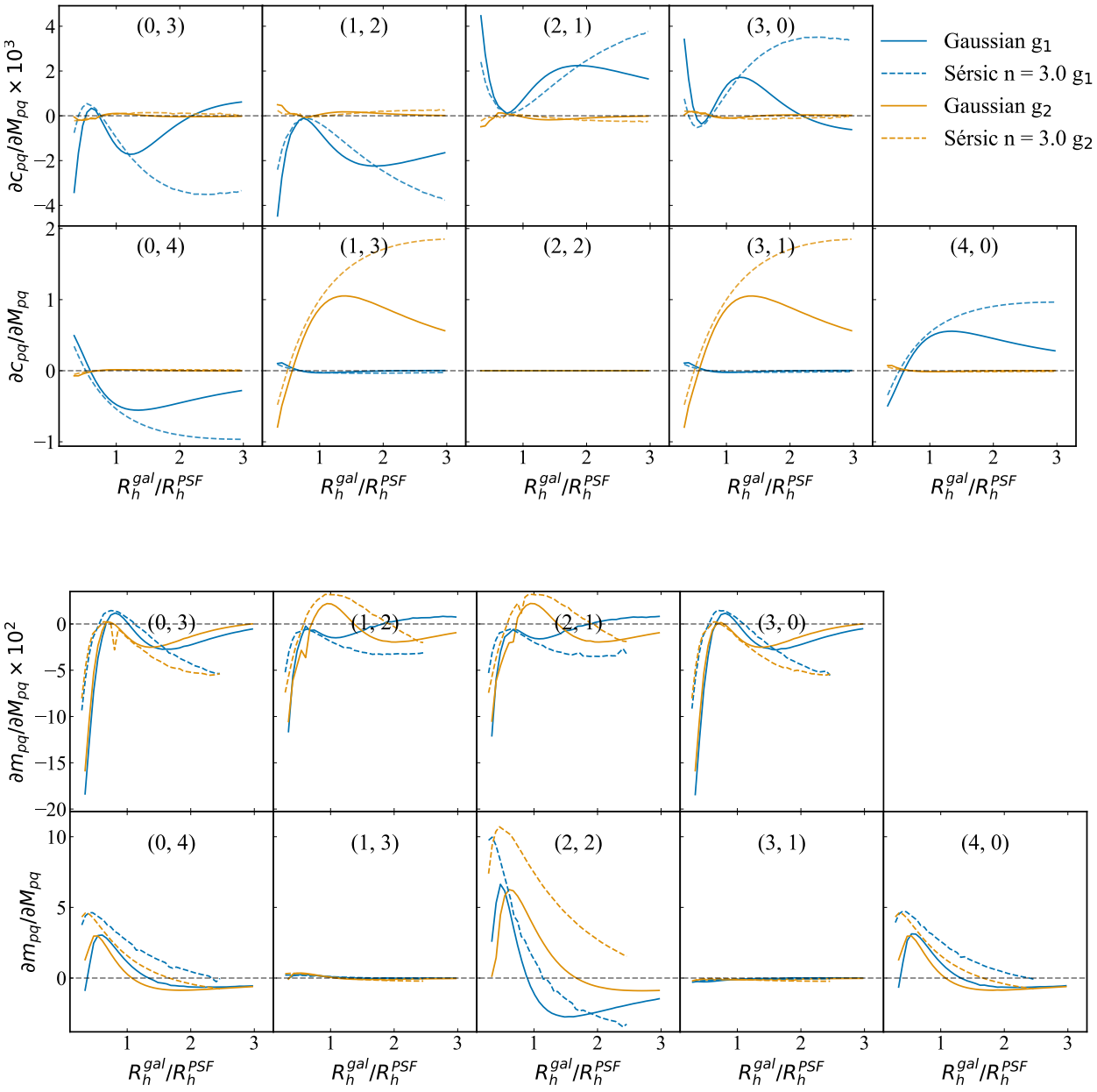

Figure 3.4.4: Additive (top) and multiplicative (bottom) bias responses to errors in the 3$^{\rm rd}$ and 4$^{\rm th}$ PSF moments as a function of the ratio of the galaxy and PSF half light radii $R_h^{\rm gal}/R_h^{\rm PSF}$. We show results for both Gaussian galaxies and Sérsic galaxies with $n = 3.0$, both with a Gaussian PSF. The size ratio is the primary factor determining the response, and the Sérsic index of the galaxy is an important secondary parameter. As indicated in the y-axis labels, the order-of-magnitude differences in the additive (multiplicative) shear biases between the 3$^{\rm rd}$ and 4$^{\rm th}$ moments are 10^3 (10^2).

sub-plot. The galaxy and PSF parameters are given in row 1 of Table 3.4.1. Fig. 3.4.3 shows that the $4^{\rm th}$ moments induce shear biases that are linear in the moment residuals, while $3^{\rm rd}$ moments induce shear biases that are non-linear in the moment residuals across the range of higher moment residuals seen in real data. We found that these curves can fit with a quadratic form. The shear response to the even moments is 2-3 orders of magnitude higher than to the odd moments, at a fixed $B[M_{pq}]$. We also note that the shear responses to conjugate higher moments, such as M_{12} and M_{21}, have opposite signs. This is expected since the two moments are related through a 90- deg rotation, causing an opposite effect on the shear. The symmetries in the shear responses to PSF higher moment errors are further discussed in Appendix 3.C. To reduce the size of the figure, we omitted the $5^{\rm th}$ and $6^{\rm th}$ moments, but they exhibit the same trends as the $3^{\rm rd}$ and $4^{\rm th}$ moments in terms of parity symmetry and different order of magnitude between shear biases for odd and even moments.

Next, to measure both additive and multiplicative shear biases, we used the same galaxy and PSF sizes as in Fig. 3.4.3, but we varied the lensing shear applied to the galaxies (specified in row 2 of Table 3.4.1). In Table 3.4.2, we show the multiplicative and additive shear biases per unit of PSF higher moments biases $m_{pq}/B[M_{pq}]$ and $c_{pq}/B[M_{pq}]$ for the $3^{\rm rd}$ to $6^{\rm th}$ moments, at the average PSF higher moment biases. Similar to Fig. 3.4.3, the shear responses to the odd moments are at least two orders of magnitude smaller than the responses to the even moments. All even moments generate multiplicative shear biases, and they also strongly determine the additive biases. Notice that since the shear responds nonlinearly to the odd moments, the values for those moments in Table 3.4.2 depend on the PSF moment residuals. Based on the results from Section 3.3.3, we can simply estimate the order of magnitude of m and c for a typical galaxy as being on the order of 10^{-3} to 10^{-2}. A more precise estimate of the systematic biases for ensembles of galaxies will be provided in Section 3.5.3.

ZM21 showed that the galaxy-to-PSF size ratio is the most important factor that determines the shear response to the errors in modeling the PSF radial kurtosis. Here we checked the sensitivity of the additive and multiplicative shear biases induced by individual PSF higher moment errors to that size ratio. We explored this relationship by simulating Gaussian and Sérsic galaxies with various sizes, specified in rows 3 to 6 in Table 3.4.1. In Fig. 3.4.4, we show the additive (multiplicative) shear biases in the upper (lower) panel, as a function of the galaxy-to-PSF size ratio measured by the half light radii $R_h^{\rm gal}/R_h^{\rm PSF}$. We can see that the size ratio plays an important role, but the Sérsic index also affects the shear responses significantly, especially for large size ratios. This is consistent with the findings in ZM21. In Fig. 3.4.4, we note that the shear responses of Gaussian galaxies to the PSF third moments are non-monotonic, crossing the 0 reference line multiple times. The simulations in Fig. 3.4.3 corresponded to a galaxy-PSF size ratio of 0.7, for which the third moment responses of g_1 and g_2 happen to have the same sign. As seen in Fig. 3.4.4, the signs of the shear biases for the third moment residuals in Fig. 3.4.3 are not representative of many galaxy-to-PSF size ratios, and should not be over-interpreted. However, the small magnitude of the additive shear biases caused by third moment modeling errors in Fig. 3.4.3 are more generally applicable.

Moment	$\frac{m_{pq}}{B[M_{pq}]}$	$\frac{c_{pq}}{B[M_{pq}]}$	$\langle B[M_{pq}]\rangle \times 10^3$
(0,3)	$(0.009, 0.001)$	$(0.000, 0.000)$	-0.21(0.24)
(1,2)	$(-0.005, 0.000)$	$(0.000, 0.000)$	0.13(-0.04)
(2,1)	$(0.004, 0.005)$	$(0.000, 0.000)$	-0.07(-0.02)
(3,0)	$(0.002, 0.000)$	$(0.000, 0.000)$	0.34(-0.09)
(0,4)	$(2.223, 1.550)$	$(-0.255, 0.002)$	1.35(2.52)
(1,3)	$(-0.216, -0.166)$	$(-0.005, 0.376)$	-0.01(-0.06)
(2,2)	$(1.940, 5.367)$	$(0.000, 0.000)$	-0.19(-0.16)
(3,1)	$(0.193, 0.219)$	$(-0.002, 0.377)$	-0.0(-0.04)
(4,0)	$(2.248, 1.543)$	$(0.255, -0.002)$	1.02(3.67)
(0,5)	$(0.002, 0.000)$	$(0.000, 0.000)$	-0.96(0.86)
(1,4)	$(0.001, 0.000)$	$(0.000, 0.000)$	0.34(-0.13)
(2,3)	$(0.003, 0.005)$	$(0.000, 0.000)$	-0.2(0.09)
(3,2)	$(-0.001, 0.005)$	$(0.000, 0.000)$	0.33(-0.11)
(4,1)	$(0.001, 0.002)$	$(0.000, 0.000)$	-0.2(-0.13)
(5,0)	$(0.000, 0.000)$	$(0.000, 0.000)$	1.5(-0.08)
(6,0)	$(-0.360, -0.078)$	$(0.110, -0.007)$	3.42(11.77)
(5,1)	$(0.477, 0.480)$	$(-0.003, -0.206)$	-0.05(-0.18)
(4,2)	$(0.072, -1.266)$	$(0.105, 0.028)$	-0.16(0.49)
(3,3)	$(0.029, 0.012)$	$(0.064, -0.413)$	-0.02(-0.13)
(2,4)	$(0.060, -1.95)$	$(-0.105, -0.028)$	-0.3(0.96)
(1,5)	$(-0.479, 0.478)$	$(-0.002, -0.206)$	-0.02(-0.18)
(0,6)	$(-0.358, -0.071)$	$(-0.110, 0.008)$	1.6(16.72)

Table 3.4.2: Table of multiplicative and additive shear biases per unit of PSF higher moment residuals, $m_{pq}/B[M_{pq}]$ and $c_{pq}/B[M_{pq}]$, for the 3^{rd} to 6^{th} moments. Since the shear biases respond nonlinearly to the odd moment errors, values in this table are computed with the average PSF higher moment error of PSFEx, shown in Section 3.3.3. We also list the mean of $B[M_{pq}]$ of the PSFEx (PIFF) in the last column for reference.

In the next section, we will combine the findings in this section and in Section 3.3 to estimate the systematic error in weak lensing observable and cosmology analyses associated with PSF higher moment errors.

3.5 Weak Lensing and Cosmology Analyses

In this section, we discuss the propagation of errors in shear to the weak lensing 2PCF, and further into cosmology. We first provide a general derivation of our approach in Section 3.5.1, and then describe an important practical issue – reducing the number of moments – in Section 3.5.2. We introduce the mock galaxy catalog we use for estimating systemat-

ics, the cosmoDC2 catalog (141), in Section 3.5.3. We further propagate the weak lensing shear systematics to cosmological parameter analysis using Fisher forecasts as described in Section 3.5.4.

3.5.1 General Error Propagation

Our discussion of how errors in the PSF higher moments affect the weak lensing 2PCF is based on two assumptions: (a) Each PSF higher moment may produce additive shear biases c_{pq} and multiplicative biases m_{pq} on the observed shear, $\hat{\gamma} = (1 + m_{pq})\gamma + c_{pq}$. (b) The total multiplicative and additive bias $m_{\rm total}$ and $c_{\rm total}$ produced by simultaneous errors in multiple higher moments of the PSF can be expressed as the sum of the individual multiplicative and additive biases m_{pq},

$$m_{\rm total} \approx \sum_p \sum_q m_{pq} \tag{3.21}$$

$$c_{\rm total} \approx \sum_p \sum_q c_{pq}, \tag{3.22}$$

with uncertainties that are negligible for this work. The assumption (a) was illustrated in Section 3.4.5, and (b) was confirmed with an image simulation test, where 100 galaxies sampled from cosmoDC2 were assigned random PSF higher-moments residuals. That test showed that the absolute value of the differences between the two sides of Eqs. (3.21) and (3.22) for individual galaxies are $\leq 10\%$. We have explicitly confirmed that for ensemble shear estimation, the error due to assumptions of linearity is further reduced to $\leq 2\%$. For the multiplicative biases, since $m_{pq} \ll 1$, we can ignore the high-order correlations, and just focus on the first order expansion of the observed 2PCF of weak lensing shear. Additive biases can be written as the sum of their averages and fluctuations, $c_{pq}(\mathbf{x}) = c_{0,pq} + \tilde{c}_{pq}(\mathbf{x})$. Combining the additive and multiplicative terms, we get the full expression for the observed weak lensing 2PCF between bins i and j,

$$\begin{aligned}\langle \hat{\gamma}^i \hat{\gamma}^j \rangle =& (1 + m_{\rm total}(z_i) + m_{\rm total}(z_j))\langle \gamma^i \gamma^j \rangle \\ &+ \sum_{pq}\sum_{uv} \langle \tilde{c}_{pq}\tilde{c}_{uv}\rangle + c_{0,pq}c_{0,uv},\end{aligned} \tag{3.23}$$

where $m_{\rm total}(z_i)$ is the multiplicative bias defined in Eq. (3.3). Throughout this work, we ignored the spatial variation of the multiplicative bias, which as shown by (142) can enter the shear power spectrum at a lower level than the mean multiplicative bias.

As shown in Eq. (3.23), the additive shear bias terms have two effects. First, the observed 2PCF is shifted by a constant $c_{0,pq}c_{0,uv}$. Second, it is also shifted by the scale-dependent auto-correlation function of the zero-mean additive bias field $\langle \tilde{c}(\mathbf{x})\tilde{c}(\mathbf{x}+\theta)\rangle$. We explore the impact of these changes in subsequent sections.

3.5.2 Dimensionality Reduction for PSF Higher Moments

There are 22 correlated PSF moments from 3rd to 6th order, and the high dimensionality of this dataset can pose challenges in understanding the main issues determining the weak lensing systematic biases. Therefore, dimensionality reduction to only the PSF higher moments that induce substantial shear biases is an important first step. Since this task is based on a rough estimate of the importance of individual PSF higher moments, we used simple models for this: both the galaxy and PSF in the dimensionality reduction process are Gaussian profiles.

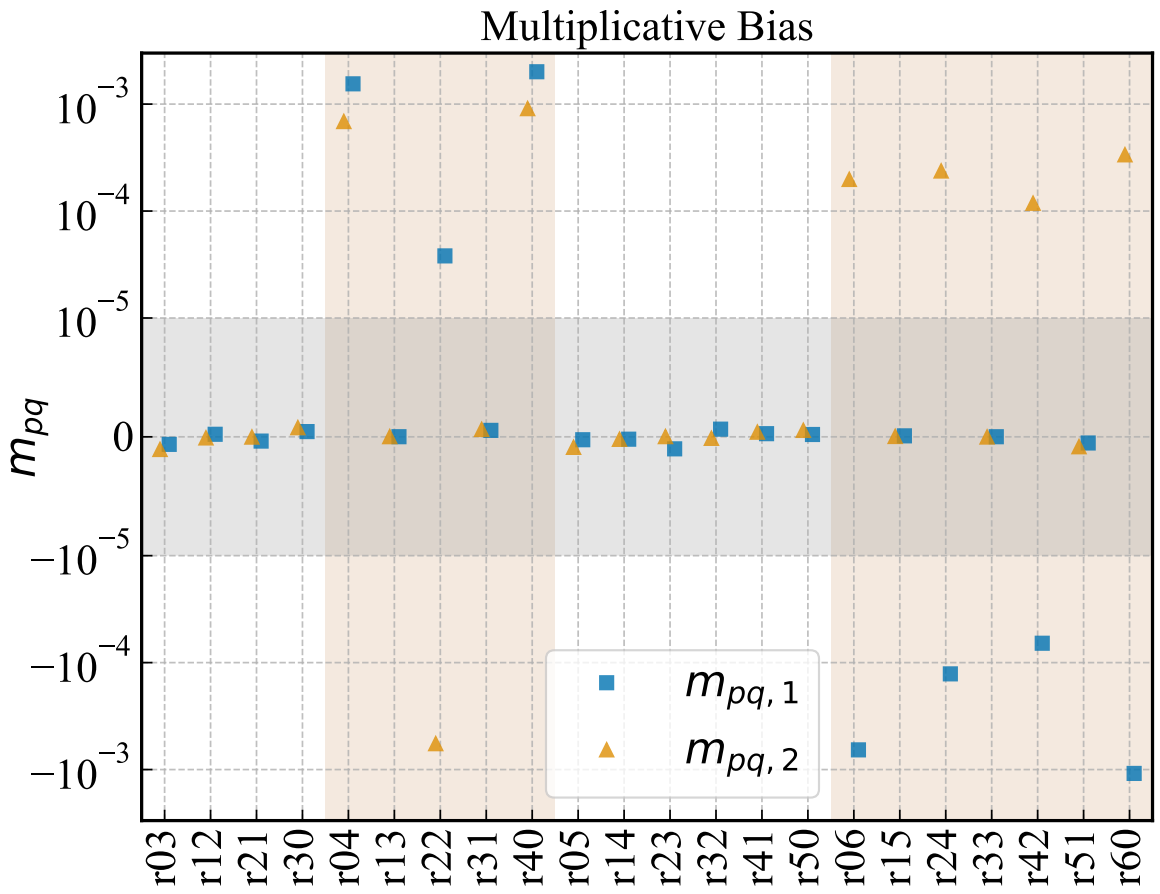

Figure 3.5.1: An estimate of the weak lensing shear multiplicative biases, aimed at understanding which PSF higher moments are most important in generating multiplicative biases. This plot is based on ensemble shear biases for a simulated COSMOS galaxy sample, given the average error on individual higher moments of the PSF model in HSC PDR1. The orange areas are the even moments and the white areas are the odd moments. Both components of the multiplicative bias show the same set of 7 moments that contribute significantly. The y-axis is symmetrical log-scaled, with the grey area being the linear region.

Eq. (3.23) shows that multiplicative bias affects the weak lensing 2PCF through its total $m_{\rm total}$, which is a summation over all m_{pq}. We used the methods described in Section 3.4.1 to calculate $\partial m_{pq}/\partial M_{pq}(\sigma_{\rm gal})$ as a function of the galaxy's second moment $\sigma_{\rm gal}$. To roughly estimate m_{pq}, we used the $\sigma_{\rm gal}$ of 44386 COSMOS galaxies with magnitude < 25.2, and galaxy resolution factor $R_2 > 0.3$ (later defined in Eq. 3.27) as the input galaxy sizes. The second moments were computed after convolving with the Hubble PSF, but before convolving with our Gaussian PSF. The Gaussian PSF size was fixed at a Full Width at Half Maximum (or FWHM) of 0.78 arcsec. Assuming the shear bias is proportional to the PSF moment bias, the multiplicative bias should be proportional to the moment bias as well. Therefore, we estimated the multiplicative bias $\langle m_{pq}\rangle$ associated with $B[M_{pq}]$ as

$$\langle m_{pq}\rangle = \left(\frac{1}{N}\sum_{i=1}^{N}\frac{\partial m_{pq}}{\partial M_{pq}}(\sigma_{{\rm gal},i})\right)\,\langle B[M_{pq}]\rangle, \tag{3.24}$$

where the COSMOS galaxies are indexed by i, and $\langle B[M_{pq}]\rangle$ is the average moment bias of M_{pq} in the HSC data, as described in Section 3.3.3. The method to estimate $\partial m_{pq}/\partial M_{pq}$ was described in Section 3.4.1. We ranked the magnitude of the values of $\langle m_{pq}\rangle$ to estimate the importance of individual PSF moments. The importance is expected to be different for g_1 and g_2, given different spatial patterns are involved in different moments.

The resulting multiplicative biases from this simplified simulation are shown in Fig. 3.5.1. Both the $m_{\rm total,1}$ and $m_{\rm total,2}$ results indicate that PSF higher moments with both p and q even (seven in total) determine the multiplicative shear bias. The total multiplicative biases are $m_{\rm total,1} = 0.0017$ and $m_{\rm total,2} = 0.0019$, dominated by the contributions of 7 PSF higher moments.

The additive biases are more complicated as shown in Eq. (3.23), since we must calculate the weak lensing 2PCF $\xi_{+/-}$ to understand the importance of the moments. We designed the preliminary tests for the additive biases as follows: We used the PSF higher moments and their errors as a function of position in the HSC PDR1 from Section 3.3, and for the positions of bright stars in the PDR1 fields, we simulated a synthetic Gaussian galaxy with the average size and shape of the population from COSMOS catalog. We then measured the shear biases of the Gaussian galaxies with the PSF higher moments biases at these positions. We obtained the biases on the shear 2PCF directly from the shear bias at position $\mathbf{x}$, estimated by

$$c_{pq}(\mathbf{x}) = \frac{\partial c_{pq}}{\partial M_{pq}} B[M_{pq}](\mathbf{x}). \tag{3.25}$$

As shown in Fig. 3.5.2, the additive bias on ξ_+ has a magnitude $\sim 10^{-7}$ on tens of arcmin scales, which corresponds to a ~ 1 per cent additive systematics contribution at small scales, and a few per cent at large scales, which is significant enough to potentially affect cosmological inference. The sharp decrease at $\theta \sim 100$ arcmin suggests that physical effects associated with the HSC field of view (FOV) are the cause of structural PSF systematic biases. However, $\Delta\xi_-$ is effectively zero.

Since each term in the additive biases on the 2PCF is associated with two different PSF moments (Eq. 3.23), the ranking of importance for the PSF moments is more complex in this

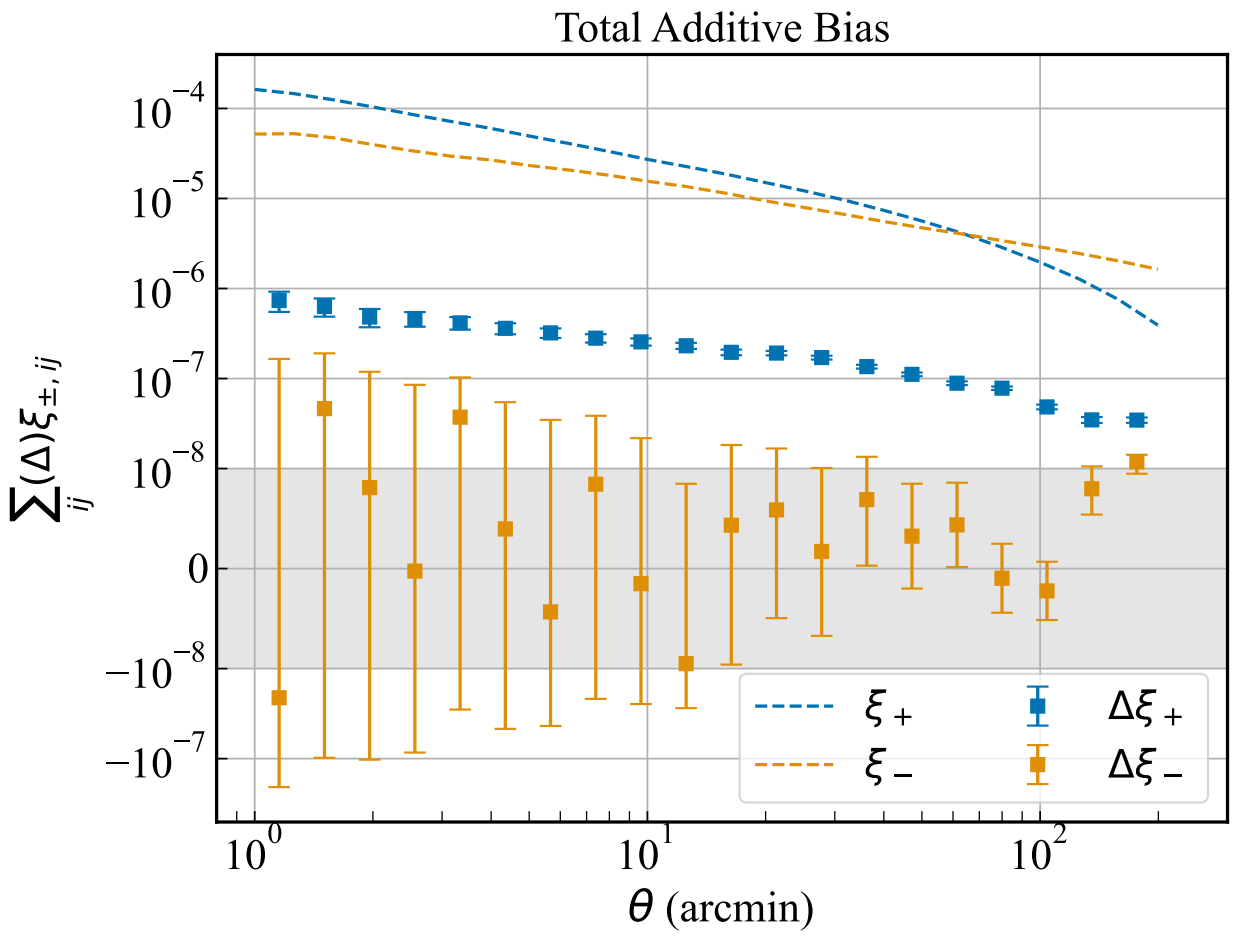

Figure 3.5.2: The total additive bias on the weak lensing 2PCF $\xi_\pm$ for the simulated galaxies used for dimensionality reduction. The expected shear-shear correlation functions $\xi_\pm$ for our fiducial cosmological parameters (across all redshift bins combined) are shown as dashed lines. While $\Delta\xi_+$ is positive on all scales shown, $\Delta\xi_-$ is consistent with zero.

case. We designed two different ranking system: (a) the **front-to-back** approach and (b) the **back-to-front** approach. In the **front-to-back** approach, we calculated the contribution of each $\langle c_{pq}c_{uv}\rangle$ term to the total additive bias $\Delta\langle gg\rangle$, by integrating over θ from 1 to 200 arcmin. We ranked the contribution of a given moment M_{pq} by the total reduction in additive bias if we removed all terms that involve M_{pq}. After removing the highest-contributing PSF moment, we performed the same calculation and removed the next highest-contributing moment, until only one moment remains.

Similarly, for the **back-to-front** approach, we removed the least-contributing PSF moment first, after performing the same contribution calculation described above. We then removed the next least-contributing moment, until we were left with only one moment. These two approaches provided two rankings of the PSF moments that contribute from most to

least to the weak lensing additive shear bias. We expect to obtain a reasonably consistent set of PSF moments from these two approaches. If the two results were to disagree, the conservative approach would be to use the inclusive set of moments considered important by either method.

We ranked the moments separately for $\langle g_1 g_1 \rangle$ and $\langle g_2 g_2 \rangle$. In Fig. 3.5.3, we show the results of executing the dimensionality reduction process for additive shear bias outlined in Section 3.5.2. In the upper and middle panel, we show the ranking of the PSF moments' contribution to $\langle g_1 g_1 \rangle$ and $\langle g_2 g_2 \rangle$. We show both the "front-to-back method" and "back-to-front method", described in Section 3.5.2. The relative rankings given by the two methods are slightly different, but the methods agreed about which moments we should discard. The moments that contribute the most strongly are four of the five 4^{th} moments: (4,0), (3,1), (1,3), (0,4), and all seven 6^{th} moments. We further separated those 11 moments into two groups depending on which shear component they affect (g_1 or g_2). The moments in the g_1 (g_2) group are those with even (odd) values for both p and q. In the bottom panel, we show the additive biases on $\langle g_1 g_1 \rangle$ and $\langle g_2 g_2 \rangle$ contributed by all PSF higher moments, compared to just the contributions of the 'g_1 group' and the 'g_2 group'. The plot shows that the 'g_1 group' and 'g_2 group' moments dominate the total additive shear biases, and therefore we can focus on just these higher moments.

After the dimensionality reduction of PSF higher moments, we only propagate the errors on the reduced moment set to the lensing signal in the analysis in subsequent sections. In other words, from this point on we only consider errors in 7 (11) PSF higher moments for the multiplicative (additive) biases.

3.5.3 Mock Catalog Simulations

To connect PSF higher moment errors with weak lensing systematics, we need a realistic galaxy catalog with galaxy properties and positional information. For this purpose, we used the cosmoDC2 catalog (137), as it is designed to match the galaxy population LSST is going to observe, with multiple validation tests against real datasets (143), and has sufficient area ($\sim$440 deg ^{2}) for our purposes. We accessed the cosmoDC2 catalog using GCRCatalogs[5] (144).

We estimated the multiplicative and additive shear biases for each individual galaxy in cosmoDC2 using two pieces of information: shear response to PSF higher moment errors, and a synthetic catalog of PSF higher moment errors, both described below.

Shear Response

The shear response to errors in PSF higher moments, $\partial \hat{g} / \partial M_{pq}$, depends on the galaxy and PSF properties. We used a bulge+disc decomposition model for the galaxy, and determined the shear response as described in Section 3.4. To reduce the computational expense, we carried out simulations for a grid of bulge+disc model parameters that cover the majority

[5] `https://github.com/LSSTDESC/gcr-catalogs`

of the cosmoDC2 galaxies, discarding $\lesssim 1$ per cent (large galaxies that do not contribute significant shear bias) outside of the grid. The free parameters in the grid are the half-light radius of the bulge $R_{h,b}$, the half-light radius of the disc $R_{h,d}$, and the bulge fraction B/T, and the grid is linear in all three dimensions. We used the same bulge and disc shapes for all galaxies[6]. We set the size and shape of the Kolmogorov PSF to be constant. The pixel size is 0.2 arcsec, like that of the Rubin Observatory LSST Camera. The range of bulge+disc parameters in the image simulation is in Table 3.5.1.

Parameter	Range
Bulge $R_{h,b}$	$0.1 \sim 1.0$ arcsec, interval $= 0.1$ arcsec
Disc $R_{h,d}$	$0.2 \sim 2.0$ arcsec, interval $= 0.2$ arcsec
Bulge-to-total ratio B/T	$0.0 \sim 1.0$, interval $= 0.2$
Bulge shape	$e_1 = \pm 0.05, e_2 = \pm 0.05$
Disc shape	$e_1 = \pm 0.16, e_2 = \pm 0.16$
PSF FWHM	0.6 arcsec

Table 3.5.1: The parameters used in the bulge+disc image simulation. The top three rows define the parameter grid used for the simulation, while the bottom three rows are fixed parameters. We use the average absolute values of ellipticity for the bulges and disks. The $\pm$ signs indicate that the ellipticities of the galaxies in the 90- deg rotated pairs have opposite signs. The PSF FWHM shown is the size for the effective true and model PSFs.

After estimating a multiplicative and additive shear response to PSF higher moment errors $B[M_{pq}]$ at each grid point, we then used multi-dimensional linear interpolation from SciPy[7] to estimate the multiplicative and additive shear biases for galaxies in cosmoDC2 using this grid. The SciPy routine performs a piece-wise interpolation in the 3-D parameter space[8].

PSF Moment Biases

Given the position for each galaxy in cosmoDC2, we need to assign PSF higher moment biases that reflect the average PSF higher moment biases and their correlation functions in the PSFEx dataset. Since cosmoDC2 is larger in area than any of the six HSC fields, it is impossible to directly cover the cosmoDC2 area with HSC fields. Therefore, we generated a synthetic PSF moment residual field $B[M_{pq}](x)$ with the same statistical properties as the PSFEx dataset, specifically the average moment residuals and auto- and cross-correlation functions. The averages of the residuals are important for determining the multiplicative

[6]Our tests showed that using the same ellipticity for all galaxies generates <1 per cent error on the prediction of the ensemble shear biases, while saving tremendous computational time.

[7]`https://www.scipy.org/`

[8]Our tests compared predictions for the ensemble shear bias of a sample of 100 simulated galaxies as estimated with the linear interpolation and with direct image simulations. We found no significant numerical difference between the two methods.

shear biases, and the correlation functions are important for the additive biases (see Section 3.5).

As is described in Section 3.3.3, the biases of PSF moments M_{pq} and M_{uv} are described by the average of the moment biases: $\langle B[M_{pq}]\rangle$, $\langle B[M_{uv}]\rangle$, and the correlation function of the fluctuation $\xi^{pq,uv}(\theta)$. For the PSF moments that are of interest, we fit the correlation functions in the PSFEx dataset to parametric models and Hankel transformed them to get the angular power spectrum using SkyLens[9] (145), by computing

$$C_\ell^{pq,uv} = 2\pi \int \mathrm{d}\theta\, \theta\, \xi^{pq,uv}(\theta)\, J_0(\ell,\theta), \tag{3.26}$$

where $J_0(\ell,\theta)$ is the Bessel function of order 0. Assuming the residual field is a Gaussian field, we generated the n-d correlated Gaussian field using these $n(n+1)/2$ angular power spectra. We used the python package Healpy[10] (146), a python wrapper of the HEALPix software[11] (147), to generate a synthetic spherical harmonic decomposition $a_{\ell m}$ with $\ell_{\rm max} = 3072$ and $-\ell \leq m \leq \ell$. With the $a_{\ell m}$, we generated an n-d Gaussian Random Field (GRF) evaluated at the centers of HEALPix pixels with $N_{\rm side} = 2048$, which corresponds to a pixel size of 1.7 arcmin. The details of the GRF generation process are described in Appendix 3.D. We then added the average moment biases for the PSFEx dataset to the GRF fluctuations to generate the total PSF higher moment bias fields. The PSF moment biases of any cosmoDC2 galaxy are the values for the HEALPix pixel that the galaxy sits in. The disadvantage of this method is that we cannot accurately evaluate $\langle \tilde{c}_{pq}(\mathbf{x})\tilde{c}_{uv}(\mathbf{x}+\theta)\rangle$ for angular bins below the HEALPix pixel size, i.e., $\theta \lesssim 1.7$ arcmin, though those scales make a negligible contribution to biases in cosmological parameters.

Galaxy Selection and Weak Lensing Measurement

The process outlined in the previous sections provided the galaxy responses $\partial\hat{g}/\partial M_{pq}$ and the correlated PSF higher moment biases $B[M_{pq}](\mathbf{x})$ for each galaxy in the cosmoDC2 catalog. However, not all of galaxies in this catalog will be used for lensing science in LSST. Similar to the practice in ZM21, we cut on how well-resolved a galaxy is based on its resolution factor R_2, which is calculated by

$$R_2 = 1 - \frac{T_P}{T_I}, \tag{3.27}$$

where T_P and T_I are the trace of the second moment matrix for the PSF and the galaxy, respectively. The galaxy is well resolved when $R_2 \to 1$, and poorly resolved when $R_2 \to 0$. Consistent with the approach used by the HSC survey (54), we only retained galaxies with $R_2 > 0.3$, eliminating $\sim$9 per cent of the sample[12]. We excluded galaxies fainter than an

[9] `https://github.com/sukhdeep2/Skylens_public/tree/imaster_paper/`

[10] `https://github.com/healpy/healpy`

[11] `http://healpix.sourceforge.net`

[12] Since we did not simulate each cosmoDC2 galaxy, we estimated their resolution factors by interpolation from the galaxies on the grid.

i-band magnitude of 25.3 for similar magnitude distribution as the LSST-'gold' samples (82), and those outside the bounds of our grid of size values in Table 3.5.1. The lower limit of the size cut did not exclude any galaxies after the resolution factor cut, and the upper limit excluded ~ 1 per cent of the galaxies. After the cuts, the total number density of the catalog is 31.8 arcmin^{-1}.

The bias on the 2PCF of the weak lensing shear $\Delta\xi_{+/-}$ was measured by

$$\Delta\xi^{ij}_{+/-}(\theta) = \langle\hat{g}^i(x)\hat{g}^j(x+\theta)\rangle - \langle g^i(x)g^j(x+\theta)\rangle, \tag{3.28}$$

where i and j are the tomographic bin index. In our measurement, we split the galaxies based on their true redshifts into three tomographic bins, centred at 0.5, 1.06, and 1.85. The ensemble biases on the weak lensing 2PCFs $\Delta\xi^{ij}_{+/-}(\theta)$ were measured using TreeCorr (8). In the next section, we use Fisher forecasts to understand the impact of these shear biases on cosmological parameter constraints.

Systematics on Shear 2PCF

In Fig. 3.5.4, we show the total multiplicative biases of the cosmoDC2 galaxies in redshift bins after including all relevant PSF higher moment errors. We used a quadratic function to fit the 10 data points, and overplot the best-fitting curve as the dashed line. As suggested by (124), a linear form for the redshift dependence of the multiplicative biases affects the estimate of the dark energy equation of state using weak lensing. The linear coefficient of our best-fitting $m(z)$ suggests that m_0 in Eq. (3.3) is 0.0015, which is about half of the error budget in the LSST Y10 requirement (90). Since the linear term of $m(z)$ can potentially cause significant cosmological parameter biases, and the impact of the quadratic term is unclear, we carried out a Fisher forecast for the impact of the redshift-dependent multiplicative biases, defined in Eq. (3.3), on the inferred cosmological parameters, using the full quadratic $m(z)$.

For the additive biases, we measured the difference in the weak lensing 2PCF, i.e., $\Delta\xi_+ = \sum_{pq}\sum_{uv}\langle\tilde{c}_{pq}(\mathbf{x})\tilde{c}_{uv}(\mathbf{x}+\theta)\rangle + c_{0,pq}c_{0,uv}$, derived in Eq. (3.23). In Fig. 3.5.5, we show the additive biases $\Delta\xi_\pm$, with galaxies split into three tomographic bins. Similar to the preliminary test, the additive biases on ξ_+ are positive, with magnitudes increasing at higher redshifts. $\Delta\xi_-$ is consistent with zero everywhere. We parameterized $\Delta\xi_+$ as a double-exponential function, $\Delta\xi_+ = a_1 e^{-s_1\theta} + a_2 e^{-s_2\theta}$, as shown in orange.

In the next section, we propagate the estimated multiplicative and additive on the shear 2PCF, parameterized by the double-exponential function, to the cosmological parameter analysis using Fisher forecasts.

3.5.4 Fisher Forecast

The goal of assessing the impact of PSF higher moment errors is to quantify their impact on a cosmological analysis using weak lensing shear, assuming that they are not explicitly accounted for in the analysis through modeling and marginalization. Since we only need an approximate estimate of the magnitude of induced cosmological parameter biases, we carried

out a Fisher forecast on shear-shear data with 5 tomographic bins for the full LSST dataset (Y10).

In practice, we computed the Fisher information matrix elements I_{ij} using the following equation:

$$I_{ij} = \frac{\partial C_\ell}{\partial p_i}^T \mathrm{Cov}^{-1} \frac{\partial C_\ell}{\partial p_j} + \delta_{ij}(\sigma_i \sigma_j)^{-1}, \tag{3.29}$$

where i and j are indices of the vector of parameters $\mathbf{p}$ (including both cosmological and nuisance parameters), C_ℓ is the angular power spectrum of the cosmic shear, and Cov^{-1} is the inverse covariance matrix. The prior on each parameter p_i was added to its diagonal element in the Fisher information matrix as $1/\sigma_i^2$, where σ_i is the standard deviation of the Gaussian prior. We used the DESC Science Requirements Document (SRD) covariance matrix (90).

The forward model in this forecast includes 7 cosmological parameters (Ω_m the matter density, Ω_b the baryonic matter density, h the Hubble parameter, n_s the spectral index, the power spectrum normalization parametrized as σ_8 and the dark energy equation of state parameters w_0 and w_a), 4 intrinsic alignment (IA) parameters of the non-linear alignment model (NLA; 148), i.e., the IA amplitude A_0, redshift-dependent power-law index η_l, redshift-dependent power-law index at redshift $z > 2$ η_h, and luminosity dependent parameter β. The Fisher forecast code and setup was adapted from and explained more thoroughly in Almoubayyed, et al., *in prep.* The fiducial values and priors of all parameters are shown in Table 3.5.2.

Parameter	Value	Prior σ	Parameter	Value	σ
Ω_m	0.3156	0.2	A_0	5.0	2.0
σ_8	0.831	0.14	η_l	0.0	2.0
Ω_b	0.049	0.006	η_h	0.0	2.0
h	0.6727	0.063	β	0.0	2.0
n_s	0.9645	0.9645			
w_a	0.0	2.0			
w_0	-1.0	0.8			

Table 3.5.2: The fiducial values of and priors on the cosmological and intrinsic alignment parameters we use as the baseline of the Fisher forecasting.

Derivatives of the angular power spectrum with respect to these parameters were taken using `numdifftools` (149) with an absolute step-size of 0.01, which was validated to be stable through a convergence test in Almoubayyed, et al., *in prep*, and for the cosmological parameters, was also shown to be stable in (150).

The C_ℓ values were computed in 20 ℓ bins, consistent with the binning used in the DESC SRD, using the Core Cosmology Library (151). The additive shear 2PCF biases for the tomographic weak lensing signal for redshift bins i and j measured in cosmoDC2 were parameterized by

$$\Delta\xi_+^{ij}(\theta) = a_1^{ij} e^{-s_1^{ij}\theta} + a_2^{ij} e^{-s_2^{ij}\theta}, \tag{3.30}$$

where the parameters a_1^{ij}, a_2^{ij}, s_1^{ij}, and s_2^{ij} are linear functions of $z_i + z_j$, the sum of the mean redshifts of the tomographic bins being correlated. This fitting function was empirically selected based upon visual inspection, and all fractional fitting residuals are within 3% of the true values. Using the fitting function in Eq. (3.30) enables us to calculate the 2PCF additive biases for any tomographic binning.

The model for the additive biases associated with PSF higher moment errors has in total 8 parameters. The multiplicative biases were modeled for each tomographic bin, using a quadratic function to fit $m(z)$. Our model for the 2PCF with multiplicative biases is

$$\hat{\xi}_+^{ij} = (1 + m^i(z_i) + m^j(z_j))\xi_+^{ij}, \tag{3.31}$$

where $\hat{\xi}_+^{ij}$ and ξ_+^{ij} are the observed and true cosmic shear 2PCFs. Since the multiplicative shear biases for individual bins were determined from a quadratic fitting formula, only 3 parameters are needed to model the multiplicative biases. The 2PCF additive biases for the 15 tomographic bin-pairs were calculated using the best-fitting parameters for the linear functions of z_i+z_j. Next, they were Hankel transformed to obtain biases in the angular power spectra, ΔC_ℓ. The forecasted biases on the cosmological and intrinsic alignment parameters p_i were calculated using (152)

$$B[p_i] = \sum_j (I^{-1})_{ij} \frac{\partial C_\ell}{\partial p_j}^T \mathrm{Cov}^{-1} \Delta C_\ell. \tag{3.32}$$

We compared the bias $B[p_i]$ on each parameter with its forecasted 1σ uncertainties from the Fisher matrix formalism in order to determine the relative importance of the systematic biases on cosmological parameter constraints due to PSF higher moment errors, if not corrected or removed.

In Fig. 3.5.6, we show the cosmological parameter shifts induced by failure to account for the additive shear biases caused by PSF higher moment residuals when interpreting cosmic shear measurements at the level of LSST Y10 (90). In this forecast, we marginalized over the intrinsic alignment parameters A_0, β, η_l, and η_h. The shifts in cosmological parameters $B[p_i]$ caused by errors in the PSF higher moments correspond to ~ 60 to ~ 100 per cent of their 1σ uncertainties.

Next, we applied redshift-dependent multiplicative biases $m(z)$, shown in Fig. 3.5.4, to the cosmic shear $\xi_\pm$ in the Fisher forecasts. For LSST Y10 (90), we found that these multiplicative biases only shift the cosmological parameters by a few per cent of their 1σ uncertainties. As discussed in Section 3.5.3, the linear coefficient of $m(z)$ suggests that we have $m_0 = 0.0015$ in Eq. (3.3), which corresponds to around 50 per cent of the systematic error budget for this parameter. This prediction overestimates the impact of the redshift-dependent multiplicative biases on the cosmological parameter estimates compared to our Fisher forecasts. The most likely reason for this finding is that our $m(z)$ is dominated by the quadratic term rather than the linear term, and therefore the redshift-dependent multiplicative shear bias is less degenerate with structure growth than the linear shear bias in Eq. (3.3).

We repeated the Fisher forecast analysis for LSST Y1, incorporating differences in its redshift distribution and covariance matrix. The LSST Y1 forecast yielded a larger σ for

all of the parameters p_i. For the additive biases, our analysis predicted that the average $|B[p_i]|/\sigma$ for LSST Y1 is 0.21, compared to 0.73 for LSST Y10, over the parameters that the cosmic shear constrains, i.e., Ω_m, w_0, w_a, and σ_8. For the multiplicative biases, our analysis predicted that this average $|B[p_i]|/\sigma$ for LSST Y1 is 0.039, compared to 0.062 for LSST Y10. In general, the PSF higher moment errors affect the results for LSST Y1 less so than LSST Y10, but they still must be accounted for in the Y1 analysis, if the PSF modeling is not improved.

In summary, our Fisher forecast analysis showed that the PSF higher moment errors of PSFEx as applied to HSC PDR1 (if not reduced in magnitude or marginalized over in the analysis) can cause up to a 1σ shift in the cosmological parameter estimates in an LSST Y10 cosmic shear analysis. This result is dominated by additive biases; the multiplicative biases only shift the estimated cosmological parameters by $\sim 0.1\sigma$ according to the Fisher forecast.

3.6 Conclusions and Future Work

In this paper, we have presented the results of a comprehensive study of the weak lensing shear biases associated with errors in modeling the PSF higher moments (beyond second moments) for ground-based telescopes, following the previous path-finding paper that identified the potential for non-negligible weak lensing systematics due to this effect for LSST (ZM21). We have quantified the additive and multiplicative shear biases due to errors in the $3^{\rm rd}$ to $6^{\rm th}$ moments of the PSF, including 22 moments in total, including estimating the typical magnitude of these errors when using current PSF modeling algorithms, and propagating them to the impact on cosmological parameter estimation.

To carry out this study, we developed an iterative algorithm that uses a shapelet expansion to modify individual PSF moments in our image simulations while preserving the other moments. Using this approach, we measured the multiplicative and additive shear responses, $\partial m_{pq}/\partial M_{pq}$ and $\partial c_{pq}/\partial M_{pq}$, to the individual PSF moment errors. We identified trends in these quantities with the galaxy-to-PSF size ratio and the Sérsic index of the galaxy. The behavior of the shear responses can be summarized as follows:

1. Given the typical magnitude of modeling errors in PSF higher moments, the amplitude of the shear biases due to errors in the odd moments of the PSF is 2-3 magnitude smaller than those caused by the even moments, which means that they can be ignored.

2. For the even moments, the multiplicative and additive shear biases are linear functions of the moment biases $B[M_{pq}]$, and the responses primarily depend on the galaxy-to-PSF size ratio and Sérsic index.

3. Other galaxy parameters, e.g., bulge fraction B/T and galaxy shapes, play a more minor role in determining the shear biases due to PSF higher moment errors.

As an example of the current state of the art, we have measured the modeling quality of the PSF higher moments with two different PSF modeling algorithms (PSFEx and Piff)

applied to the HSC survey dataset. We used high-SNR star images as the true PSF, and the interpolated PSF model at the stars' position as the model PSF. To focus on the impact of errors in the PSF higher moments, we measured the true and model PSF higher moments in a regularized coordinate system, where $e_1 = e_2 = 0$, and the second moment σ values are the same for the model and true PSF. Overall, the PSF modeling quality is comparable for these methods. Our findings suggest there is value in further tuning and optimizing the PSF modeling performance for the $4^{\rm th}$ and $6_{\rm th}$ moments for future versions of PIFF.

To reduce the dimensionality of the higher moment data vector and develop a basic understanding of the impact of the PSF higher moments on weak lensing, we began with preliminary tests. We put an artificial Gaussian galaxy at each HSC bright star position to determine the leading PSF higher moments that affect shear measurement. Through these tests, we put 6 (5) moments into 'g_1 group' ('g_2 group'), which generate additive biases on g_1 (g_2). These 11 moments also include the 7 leading moments that generate multiplicative shear biases.

We then used the mock galaxy catalog cosmoDC2 to propagate PSF modeling errors to the weak lensing shear 2PCF. We used Gaussian Random Field to generate realizations of PSF higher moments error of the 11 aforementioned leading moments, based on their means and correlation functions measured in the HSC PSFEx dataset. We adopted the bulge+disc model that cosmoDC2 provides, and interpolated the shear bias for each galaxy based on their bulge size, disk size, and B/T ratio. We subdivided the cosmoDC2 galaxies into three tomographic bins to measure redshift-dependent shear biases, and found that PSF higher moment errors only generate non-zero biases in ξ_+. Both the multiplicative and additive biases are redshift dependent, as they all depend on the galaxy property distributions at that redshift.

Finally, we have propagated the PSF higher moments error to systematic biases in inferred cosmological parameters using Fisher forecasting. We find that additive shear biases due to PSF higher moment errors can cause a 1σ systematic shift on key cosmological parameters, such as Ω_m, σ_8 and w_0, at the LSST Y10 level – implying that either PSF higher moment errors must be reduced from current levels for LSST Y10, or this effect must be explicitly modeled in the cosmological parameter analysis. In contrast, the multiplicative shear biases only cause cosmological parameter shifts of at most 0.1σ. The forecast shows that the impact of the PSF higher moment errors on LSST Y1 is smaller than that on LSST Y10, but the effect is still not negligible even for Y1.

This work motivates several future studies:

- The results of this paper imply that future surveys, including LSST and the High Latitude Survey of the Roman Space Telescope, need to design null tests to ensure that the additive shear biases due to PSF higher moment errors do not cause an unacceptable level of contamination of the weak lensing shear data vectors. Requirements on PSF higher moment modeling quality, and/or mitigation methods, are needed for these surveys to recover credible cosmological constraints from the weak lensing shear data.

- Modeling the PSF higher moment residuals is needed in the cosmological analyses.

By cross correlating PSF higher moments residual with the estimated shear, one can measure the systematics in 2PCF associated with the PSF higher moments error, and marginalize over it in the cosmological analyses. However, the high dimensionality of this source of systematic uncertainty remains challenging, even though this work has reduced the dimensionality by a factor of 2, encouraging future development.

- This work also motivates the inspection of PSF higher moment modeling quality to drive the further development of new PSF modeling algorithms. This includes inspecting whether the reconstruction, interpolation, as well as the coadding process can generate errors in the PSF higher moments. Careful attention to this issue could greatly simplify the points mentioned above about modeling the impact of this systematic in future surveys. Because of the size dependence we find in both the additive and multiplicative biases, we recommend further development in redshift-dependent additive and multiplicative biases PSF systematics modeling in the cosmological analyses for the cosmic shear.

3.A Moment Residual Maps in HSC

In this appendix, we show the moment residual results that are not included in the main text. In Section 3.A.1, we show two maps of PSF truth and residual in the HSC PDR1 data. In Section 3.A.2, we show the PSF residual distribution in the HSC RC2 dataset comparing Piff and PSFEx.

3.A.1 PSF Residuals by Fields

In Fig. 3.A.1, we show two examples of the PSF moment maps that we measure in the 6 HSC fields. We show maps for the true moments and the residual $B[M_{pq}]$. We can see that the true PSF higher moments and their residuals clearly have real spatial structure, as is found in ZM21 for the radial kurtosis. The residuals are both correlated with the true moments, showing that PSFEx performs differently depending on the true underlying PSF, which suggests that one opportunity for improvement in future algorithms is greater performance stability. Comparing to figure 1 in (54), we observe that the better seeing parts of the area have PSF higher moment biases that are higher than other areas, especially for the 4^{th} and 6^{th} moments. Many of these good-seeing areas are eliminated from the HSC first-year shear catalog, described in section 4 of (54), due to them failing various PSF modeling tests. This is confirmed both visually and by the correlation matrix in Fig. 3.3.2 for PSFEx.

3.A.2 Comparison between Piff and PSFEx in RC2

In Figure 3.A.2, we show an apples-to-apples comparison between Piff and PSFEx on the RC2 dataset. This is in addition to the comparison made in Section 3.3.3. Due to their settings, PSFEx and Piff have opposite signs in many key moments for the weak lensing

systematics. However, PSFEx shows lower moment residuals compared to Piff. This further motivates the development and optimization of Piff, which when properly tuned should improve in performance.

3.B Shapelet-Moment Relation

In Section 3.4.3, we explained that the key to changing the PSF moments through a shapelet decomposition is to compute the Jacobian matrix using Eq. (3.20). In Fig. 3.B.1, we show an example of the Jacobian matrix T for PSF higher moment errors $B[M_{pq}]$ with respect to the shapelet modes b_{jk} for a Kolmogorov PSF. There is a block diagonal structure that shows the PSF second moments depend on the 4^{th} to 5^{th} shapelet modes. The PSF third moments depend on the 6^{th} to 9^{th} shapelet modes. The PSF fourth moments depend not only on the 10^{th} to 14^{th} shapelet modes, but also on the shapelet modes that determine the second moments. This means that the n^{th} PSF higher moments basis can be approximately decomposed into shapelets components with the same order n.

With the Jacobian matrix shown in Fig. 3.B.1 and the Algorithm 1, we modify the individual PSF higher moments with moment error threshold $||\mathbf{\Delta M}||_2 = 10^{-6}$. This precision is sufficient for exploring systematic shear biases associated with errors in the PSF higher moments.

3.C Symmetry in the response to PSF higher moments

In Fig. 3.4.3, it is clear that the shear response to the PSF higher moments exhibits symmetries among the different higher moments. In this section, we explore and explain this symmetry. We start by proposing four lemmas, and derive the symmetry of the shear response based on these four lemmas.

Lemma 1: For any two PSF modeling residual basis functions $B[M_{pq}](x, y)$ and $B[M_{uv}](x, y)$ such that $B[M_{pq}](x, y)$ can be obtained by rotating $B[M_{uv}](x, y)$ by ± 90 deg, the corresponding shear biases $\Delta\hat{g}(B[M_{pq}])$ and $\Delta\hat{g}(B[M_{uv}])$ satisfy the following constraint:

$$\Delta\hat{g}(B[M_{pq}]) = -\Delta\hat{g}(B[M_{uv}]) \tag{3.33}$$

Note that this Lemma is also the basis for the fact that a 90 deg rotated galaxy pair has an average shape of 0, a fact that we use in the single galaxy simulations. We also stress that the $B[M_{pq}](x, y)$ in this section is a functional basis of the higher moments error (see Fig. 3.4.2 for examples), different from the moment biases $B[M_{pq}]$ elsewhere.

Lemma 2: The PSF modeling residual function $B[M_{pq}](x, y)$ has the form

$$B[M_{pq}](x, y) = B[M_{pq}](-x, y) \qquad \text{if p is even} \tag{3.34}$$

$$B[M_{pq}](x, y) = -B[M_{pq}](-x, y) \qquad \text{if p is odd.} \tag{3.35}$$

This is due to the symmetry (asymmetry) in the even (odd) functions used in the moment measurement.

Lemma 3: Similar to Lemma 2, the PSF modeling residual function $B[M_{pq}](x, y)$ has the form:

$$M_{pq}(x, y) = M_{pq}(x, -y) \qquad \text{if q is even} \tag{3.36}$$
$$M_{pq}(x, y) = -M_{pq}(x, -y) \qquad \text{if q is odd.} \tag{3.37}$$

Lemma 4: For any p and q, the PSF modeling residual function satisfies the relationship

$$B[M_{qp}](x, y) = B[M_{pq}](y, x). \tag{3.38}$$

This is easily proved by substituting y for x and vice versa.

With these lemmas, we can identify symmetry relationships between different moments, as long as the moment responses are rotations of each other. But first, we must define the rotation operators $\mathcal{R}$ and $\mathcal{R}'$,

- $\mathcal{R}(B[M_{pq}](x, y)) = B[M_{pq}](y, -x)$ – a function that rotates the moment response by 90 deg clockwise.
- $\mathcal{R}'(B[M_{pq}](x, y)) = B[M_{pq}](-y, x)$ – a function that rotates the moment response by 90 deg counter-clockwise.

Fig. 3.4.3 shows that the symmetry between results for different moments depends on the parity of the moment index p and q. Therefore, we consider four scenarios with different parities.

Case 1: If both p and q are even:

$$\begin{aligned} B[M_{qp}](x, y) &= B[M_{pq}](y, x) \\ &= B[M_{pq}](y, -x) = \mathcal{R}(B[M_{pq}](x, y)) \end{aligned} \tag{3.39}$$

The first two steps use Lemma 4 and Lemma 3, respectively. The last step relies on the definition of $\mathcal{R}$. Using Lemma 1 on the very left-hand-side (LHS) and very right-hand-size (RHS) of this equation, we infer that $\Delta\hat{g}(B[M_{pq}]) = -\Delta\hat{g}(B[M_{qp}])$, which is consistent with the results for $(p, q) = (0, 4)$ in Fig. 3.4.3. This case also implies that for even values of $p = q$, $\Delta\hat{g}$ must be 0, as is seen for the $(p, q) = (2, 2)$ case in Fig. 3.4.3.

Case 2: If p is even and q is odd:

$$\begin{aligned} B[M_{qp}](x, y) &= B[M_{pq}](y, x) \\ &= B[M_{pq}](-y, x) = \mathcal{R}'(B[M_{pq}](x, y)). \end{aligned} \tag{3.40}$$

The first two steps utilize Lemma 4 and Lemma 2, respectively. The last step relies on the definition of $\mathcal{R}'$. With Lemma 1 applied to the very LHS and RHS, we infer that $\Delta\hat{g}B[(M_{pq}]) = -\Delta\hat{g}(B[M_{qp}])$ for this case. This finding is consistent with the results for $(p, q) = (0, 3)$ and $(2, 1)$ in Fig. 3.4.3.

Case 3: If p is odd and q is even, the only difference from Case 2 is to flip x instead of y in the second step:

$$\begin{aligned} B[M_{qp}](x,y) &= B[M_{pq}](y,x) \\ &= B[M_{pq}](y,-x) = \mathcal{R}(B[M_{pq}](x,y)). \end{aligned} \tag{3.41}$$

The first two steps utilize Lemma 4 and Lemma 3. The last step relies on the definition of $\mathcal{R}$. With Lemma 1 applied to the very LHS and RHS, we infer that $\Delta\hat{g}(B[M_{pq}]) = -\Delta\hat{g}(B[M_{qp}])$.

Case 4: If both p and q are odd:

$$\begin{aligned} B[M_{qp}](x,y) &= B[M_{pq}](y,x) \\ &= -B[M_{pq}](y,-x) = -\mathcal{R}(B[M_{pq}](x,y)). \end{aligned} \tag{3.42}$$

The first two steps use Lemma 4 and Lemma 3. The last step relies on the definition of $\mathcal{R}$. Applying Lemma 1 to the very LHS and RHS, we infer that $\Delta\hat{g}(B[M_{pq}]) = \Delta\hat{g}(B[M_{qp}])$. This finding is consistent with the results for $(p,q) = (1,3)$ in Fig. 3.4.3.

In conclusion, only when both p and q are odd will we get $\Delta\hat{g}(B[M_{pq}]) = \Delta\hat{g}(B[M_{qp}])$. Otherwise, $\Delta\hat{g}(B[M_{pq}]) = -\Delta\hat{g}(B[M_{qp}])$, implying that pairings with even values of $p = q$ produce zero shear bias. As described above, these symmetry patterns are displayed in Fig. 3.4.3. While not shown in the plot, we have explicitly confirmed that the above conclusions apply to the 5^{th} and 6^{th} moments as well, and they should hold beyond that as well.

3.D Generating the Gaussian Random Fields

In Fig. 3.D.1, we show the correlation functions of the PSF higher moment residual maps, described in Eq. (3.15), of the two groups of moments that determine the additive shear biases, defined in Section 3.5.2. These two groups of PSF higher moments are later used to propagate PSF higher moment error to the cosmoDC2 galaxies in Section 3.5.3. The blue dots are the measurements based on the HSC bright stars and PSFEx in Section 3.3.3.

We have devised empirical fitting formulae to describe the measurements of the correlation functions shown as blue dots. We fit the 'g_1 group' correlation functions with a power-arctan function,

$$\xi_{\rm fit}(\theta) = a\theta^{-b}\left[\frac{1}{2} - \frac{\tan^{-1}(\theta - \theta_{\rm cutoff})}{\pi}\right]. \tag{3.43}$$

This model is chosen because the correlation function takes the form of a power law on small scales (or a linear function when plotted on a log-log plot), and then rapidly drops to zero. The part in the parenthesis is designed to produce the rapid drop to zero on scales beyond $\theta_{\rm cutoff} = 1.7$ deg, a scale that is comparable to the size of the Subaru FOV. For the 'g_2 group' correlation functions, we use a power law,

$$\xi_{\rm fit}(\theta) = a\theta^{-b}, \tag{3.44}$$

as correlation functions in the 'g_2 group' moments are visually consistent with a power law.

Since the cosmoDC2 catalog has an area larger than any field in the HSC data we measure, we need to generate artificial PSF moment residual maps to cover the cosmoDC2 area. We convert the above fitting functions to angular power spectra by carrying out a Hankel transform, using SkyLens[13] (145), and use the power spectra to generate artificial Gaussian Random Fields (GRF) using Healpy (146; 147). To ensure the integration is stable and bug-free, we do a round-trip transformation test, where we transform the power spectrum back to real space, shown in the orange curves in Fig. 3.D.1. The round-trip transformations match the original data well in all cases, as a validation of the fitting function and the numerical accuracy of these transformations. The GRF is generated on the HEALPix sphere with $N_{\rm side} = 2048$, with a pixel size ~ 1.7 arcmin. We measure the correlation function of the GRF, shown as the green curves in Fig. 3.D.1. Except for the angular bins that are below the resolution of the HEALPix grid, the GRF is shown to match the original field well in terms of the two-point statistics.

[13] https://github.com/sukhdeep2/Skylens_public/tree/imaster_paper/

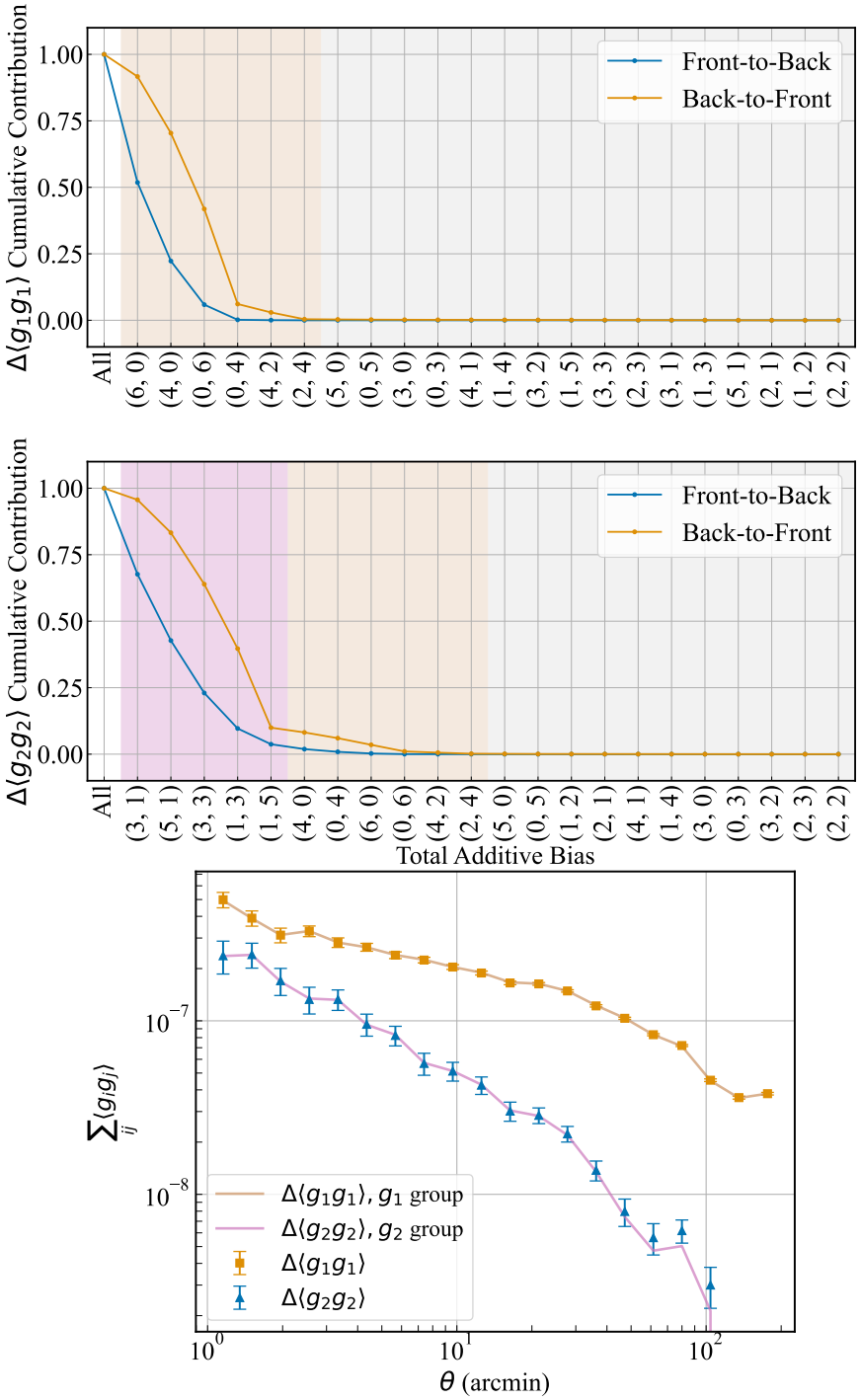

Figure 3.5.3: The estimate of the additive shear biases given the PSFEx modeling quality in the HSC PDR1. The upper and middle panels show the rankings of the cumulative contribution to the $\Delta\langle g_1 g_1\rangle$ and $\Delta\langle g_2 g_2\rangle$ (respectively) from 2 to 200 arcmin, from both the front-to-back and back-to-front methods described in Section 3.5.2. The light yellow region indicates the 'g_1 group' moments that are most relevant to the $\Delta\langle g_1 g_1\rangle$ term, and the pink region indicates the 'g_2 group' moments that are most relevant to the $\Delta\langle g_2 g_2\rangle$ term. The bottom panel shows the additive biases on $\langle g_1 g_1\rangle$ and $\langle g_2 g_2\rangle$ from all PSF higher moments, compared to just the 'g_1 group' and the 'g_2 group' – confirming that these two groups dominate the additive shear biases.

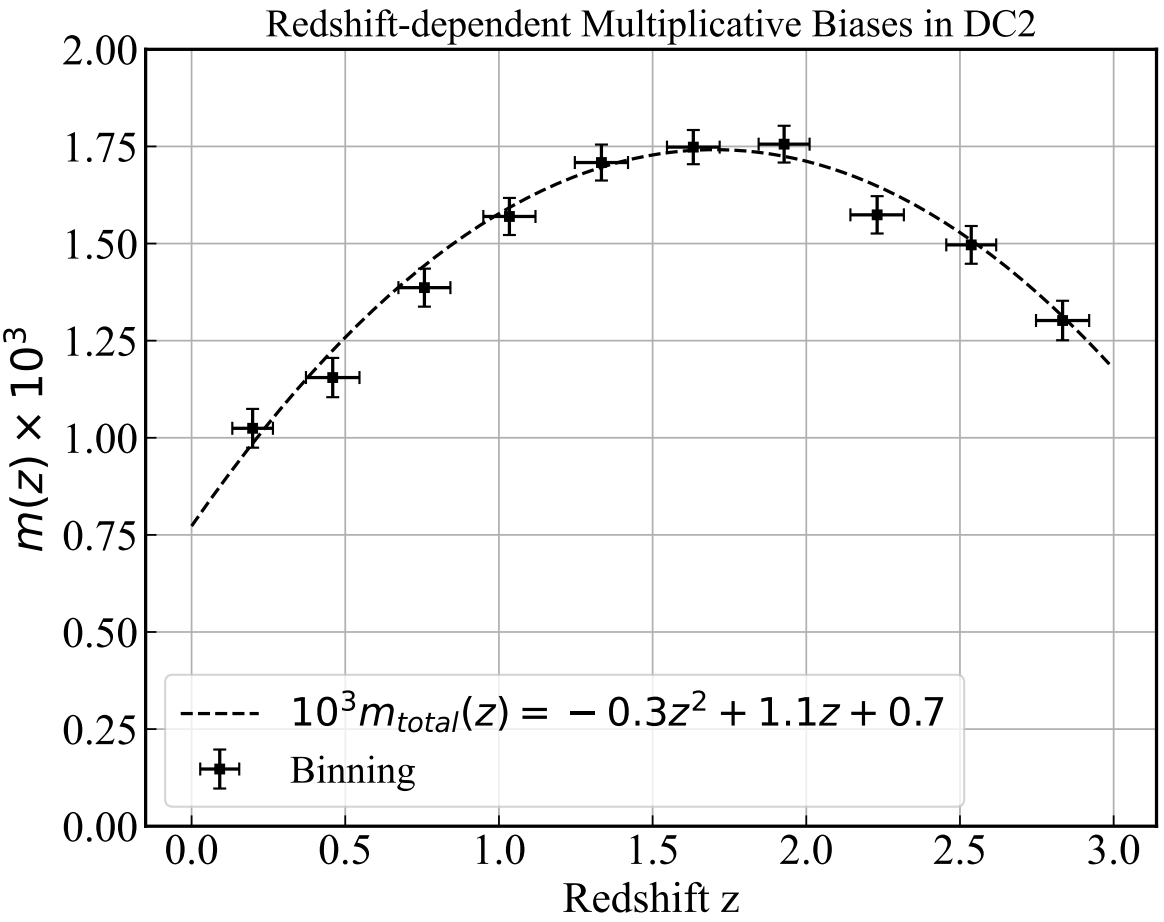

Figure 3.5.4: The redshift-dependent multiplicative shear biases for cosmoDC2 galaxies, due to PSF higher moment residuals comparable to those in HSC PDR1, in 10 redshift bins. We fit the data points to a quadratic function, shown as the dashed line.

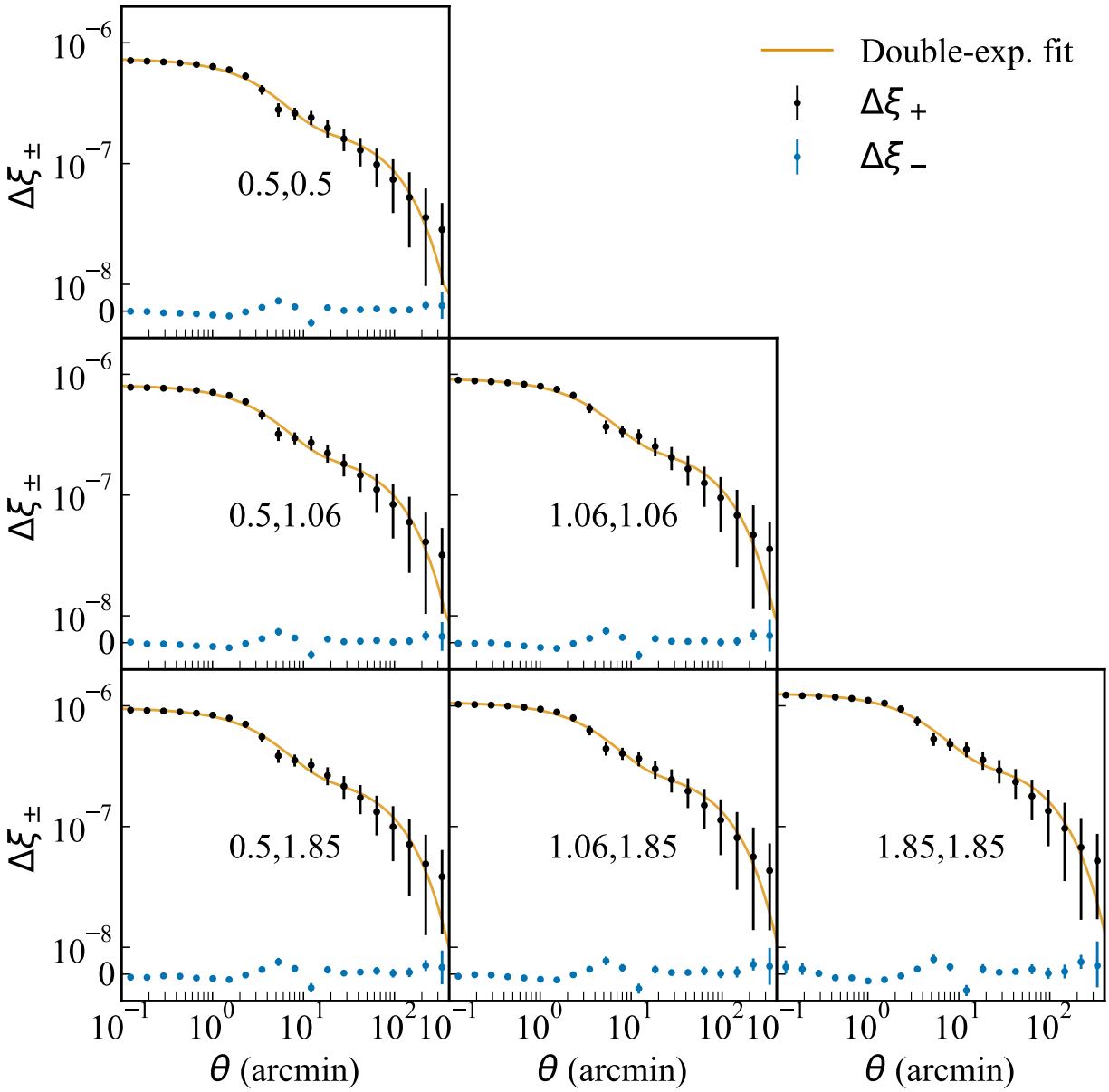

Figure 3.5.5: The additive biases on the weak lensing 2PCF $\xi_\pm$ for the cosmoDC2 galaxies when subjected to PSF higher moment residuals comparable to those in HSC PDR1. The galaxies are split into three tomographic bins based on their true redshifts, centred at $z = 0.5$, 1.06, and 1.85. The tomographic bin combination is labeled by the central redshifts of the corresponding pair of bins at the center of each panel. The y-axis uses a symmetric-log scale, with linear scale $= 3.0 \times 10^{-7}$; the linear region is shaded grey. $\Delta\xi_-$ is still consistent with zero, as for the preliminary results. We fit $\Delta\xi_+$ with a double-exponential function, shown as orange lines.

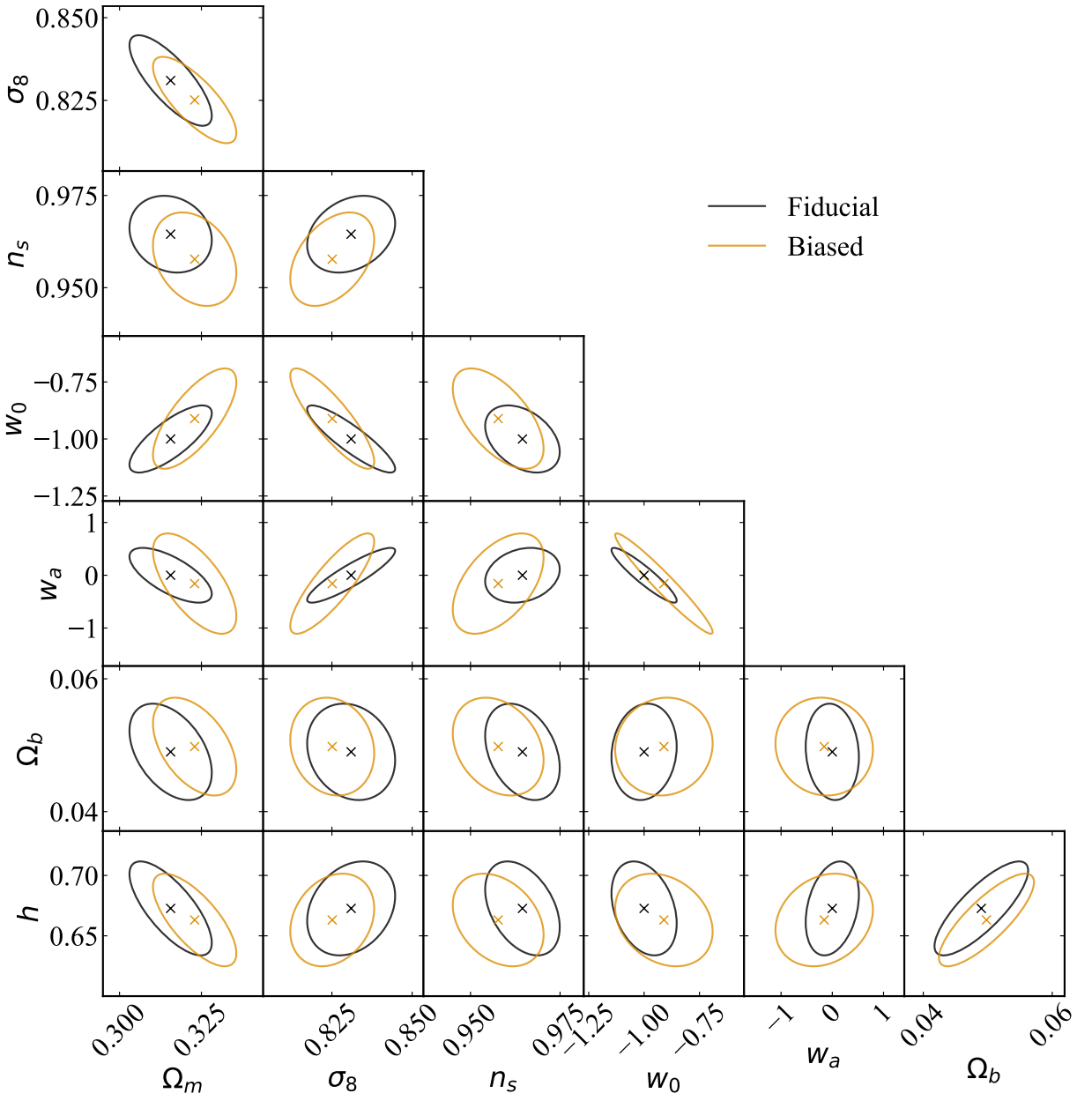

Figure 3.5.6: The 1σ constraint contours from the Fisher forecast for the fiducial (black) and shifted by additive shear biases (orange) cosmological parameters for LSST Y10. The centroids of the forecasts are shown by the "x". If not accounted for in the analysis, the additive shear biases caused by errors in the PSF higher moments at the level produced by PSFEx for HSC PDR1 are predicted to shift the inferred cosmological parameters by $\sim 1\sigma$, at the LSST Y10 level.

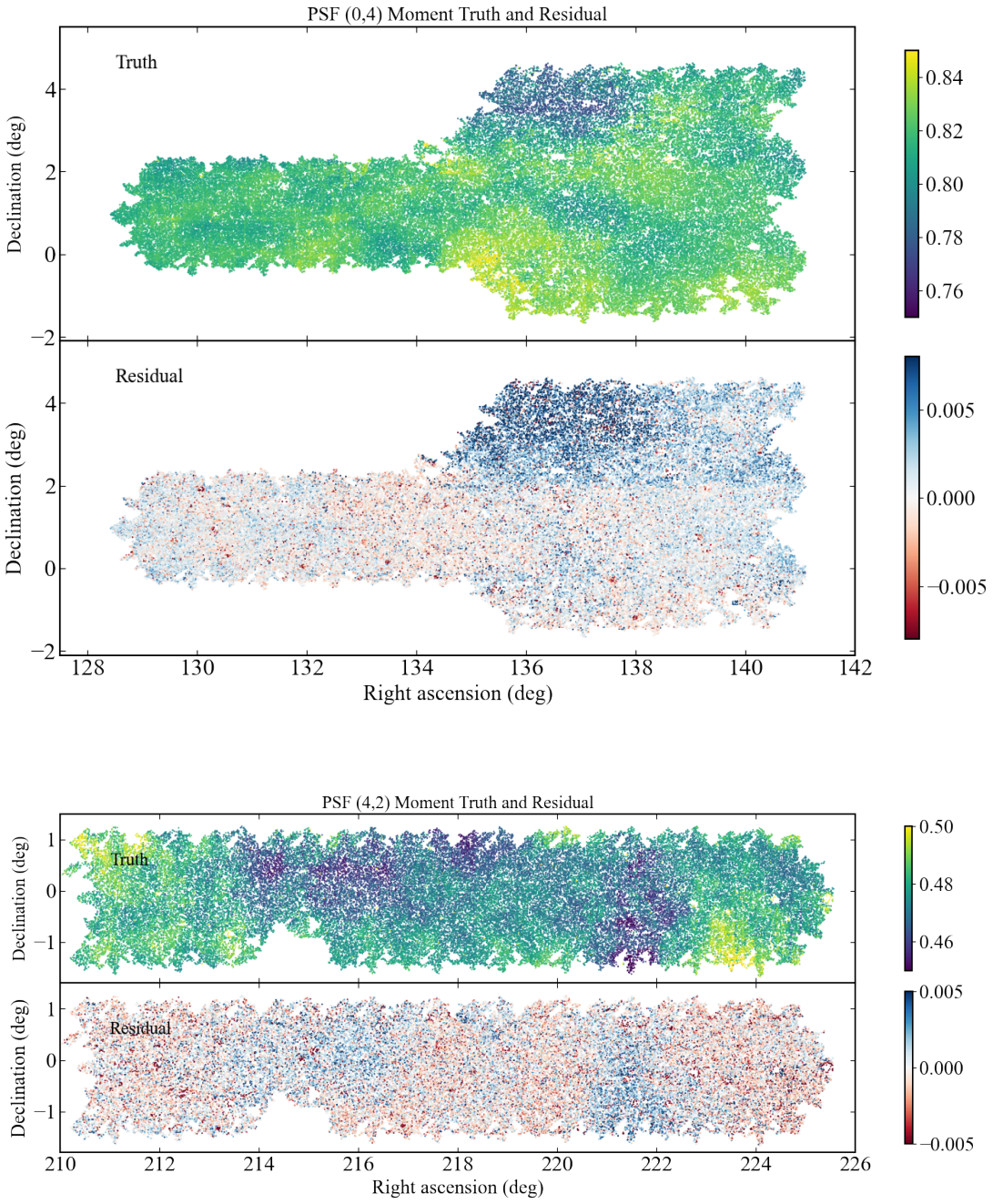

Figure 3.A.1: Two examples of the maps of PSF higher moments for the HSC PDR1 data, as modeled by PSFEx. For both examples, we show the true value and the moment residual $B[M_{pq}]$. The top panel shows a map of the (0,4) moment measured in the GAMA09H field, and the bottom panel shows the (4,2) moment measured in the GAMA15H field. There is coherent structure in both the true moments and their residuals, suggesting that the measurement is not noise dominated.

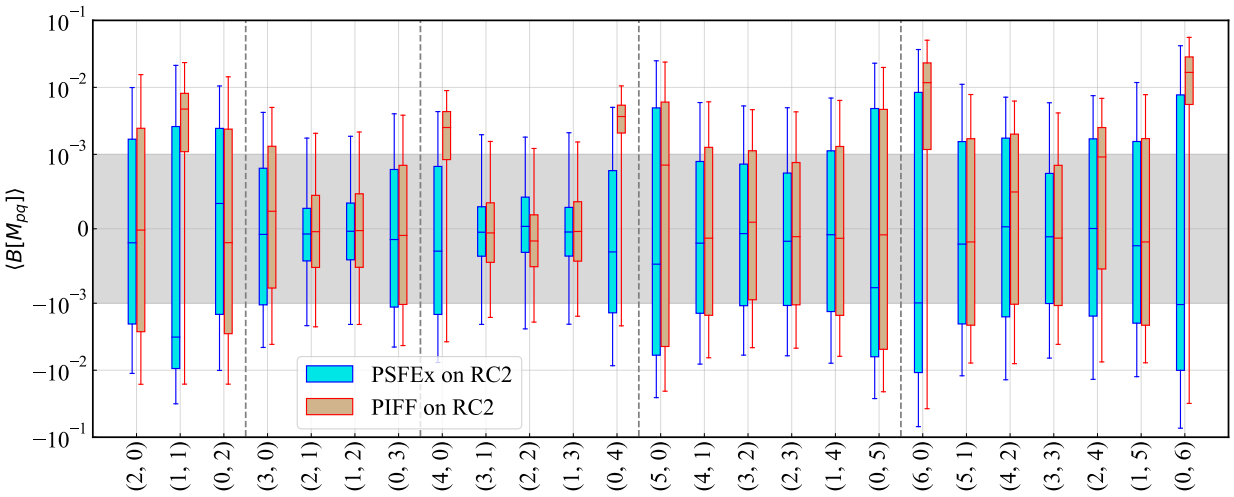

Figure 3.A.2: Box plot showing the PSF moment biases from the 2^{nd} to the 6^{th} moments, with the whiskers showing the 2σ range (from 3rd to 97th percentile), the boxes showing the interquartile range, and the bars showing the median. The PSFEx and Piff results, both runned on the RC2 dataset described in Section 3.3.2, are shown side-by-side. The y-axis is symmetrical log-scaled, with the linear region shown in grey.

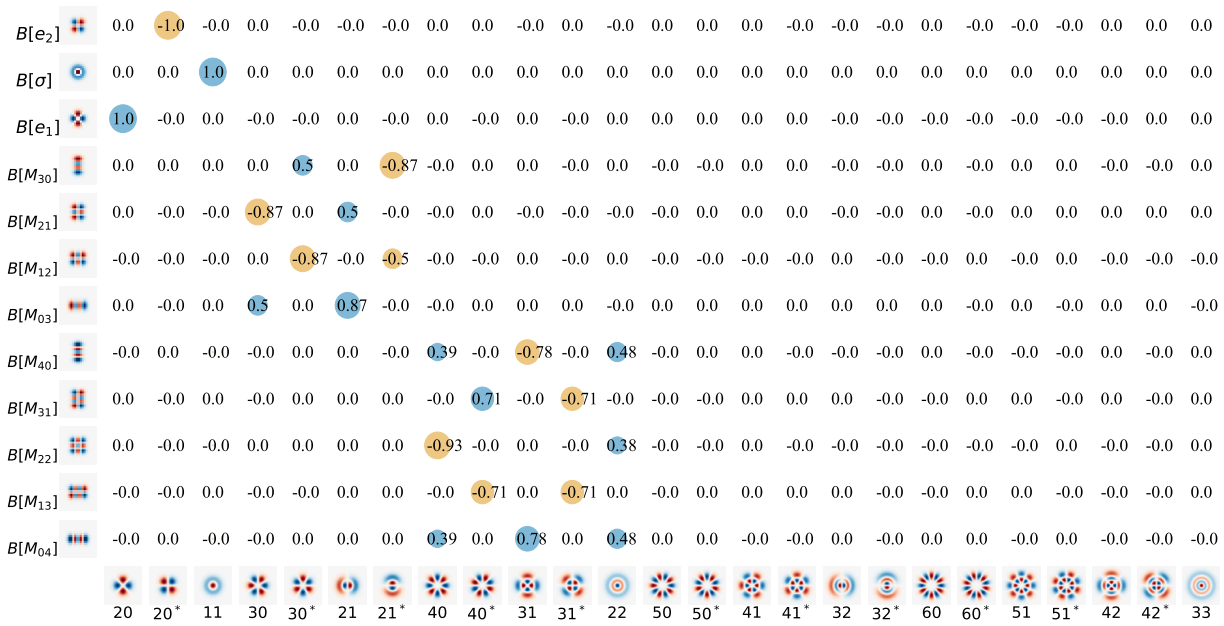

Figure 3.B.1: The Jacobian of PSF moments with respect to the shapelet coefficients, $T_{pq,jk} = \frac{\partial M_{pq}}{\partial b_{jk}}$ for a Kolmogorov PSF. We show the first 12 PSF moments starting from the second moments (i.e., 3 second moments, 4 third moments, and 5 fourth moments) and the first 25 shapelet components starting from $n = 2$ for the shapelets decomposition. The numbers that overlap the circle are the values of $T_{pq,jk}$, with each row normalized by the L^2-norm $\sqrt{\sum_{jk} T^2_{pq,jk}} = 1$. The sizes of the circles reflect the magnitude of the entry, and colors reflect the sign (blue for positive and yellow for negative). The column on the left shows the postage stamp images of the difference in PSF with only one moment being changed. The bottom row shows the first 25 shapelet bases, as the bases for the moment modification. We rank the shapelet coefficients by increasing the order n. For each n, we start with the real part of $j = n$, then its imaginary part, and decrease j until $j = k$ or $j = k + 1$. The labels on the shapelet basis functions should be interpreted as follows: jk is equivalent to $\mathrm{Re}[\psi_{jk}]$, jk^* is equivalent to $\mathrm{Im}[\psi_{jk}]$. We can see that the Jacobian matrix is very close to being a block-diagonal matrix, which means that the PSF higher moments are linear combinations of the shapelet components with the same order n.

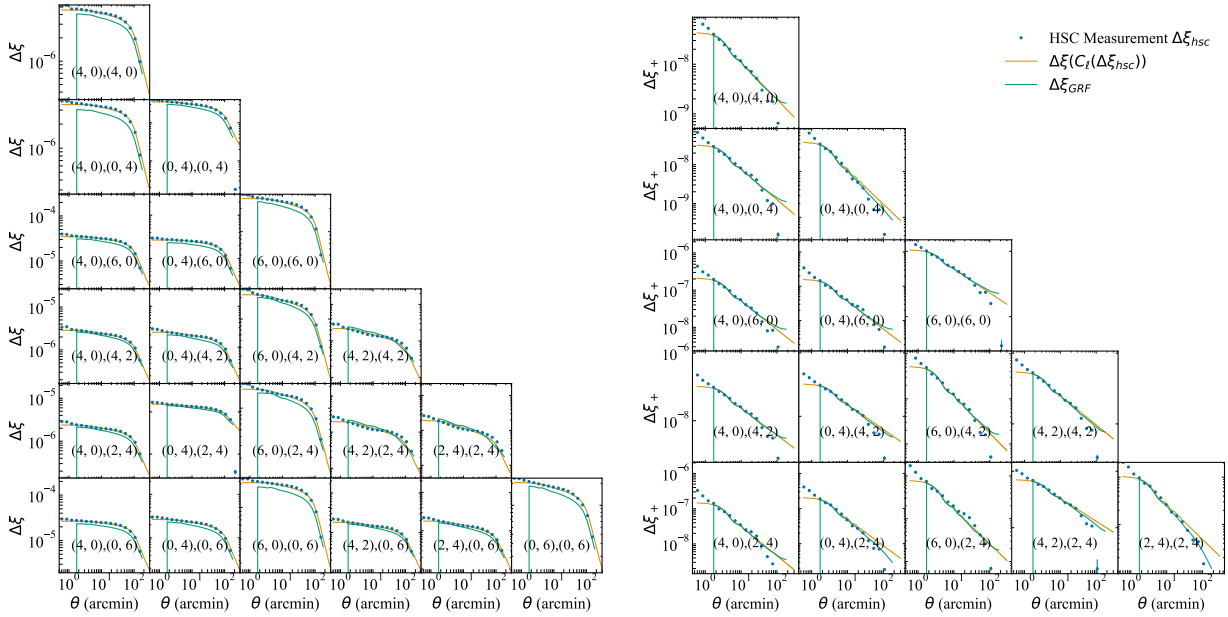

Figure 3.D.1: The original correlation function of the PSF higher moment residual fields measured from all six HSC PDR1 fields combined (blue dots), the "round-trip transformation" of the original correlation functions (orange curve), and the PSF moments residual correlation functions of the generated GRF. The upper panel shows the 'g_1 group' moments, and the lower panel shows the 'g_2 group' moments that we defined in Section 3.5.2. The 2PCFs of the GRFs generally match those in the HSC data, except at angular scales ≤ 1.7 arcmin, corresponding to the scale of the HEALPix grid.

Chapter 4

A General Framework for Removing Point Spread Function Additive Systematics in Cosmological Weak Lensing Analysis

Tianqing Zhang[1], Xiangchong Li[1], Roohi Dalal[2], Rachel Mandelbaum[1], Michael A. Strauss[2], Arun Kannawadi[2], Hironao Miyatake[3,4,5], Andrina Nicola[2,6], Andrés A. Plazas Malagón[7,8], Masato Shirasaki[9,10], Sunao Sugiyama[3], Masahiro Takada[3]

[1]McWilliams Center for Cosmology, Department of Physics, Carnegie Mellon University, 5000 Forbes Ave, Pittsburgh, PA 15213, USA.
[2]Department of Astrophysical Sciences, Princeton University, Peyton Hall, Princeton, NJ 08544, USA.
[3]Kavli Institute for the Physics and Mathematics of the Universe (WPI), The University of Tokyo Institutes for Advanced Study (UTIAS),
The University of Tokyo, Chiba 277-8583, Japan
[4]Kobayashi-Maskawa Institute for the Origin of Particles and the Universe (KMI), Nagoya University, Nagoya, 464-8602, Japan
[5]Institute for Advanced Research, Nagoya University, Nagoya 464-8601, Japan
[6]Argelander Institut für Astronomie, Universität Bonn, Auf dem Hügel 71, 53121 Bonn, Germany
[7]Kavli Institute for Particle Astrophysics and Cosmology, P.O. Box 20450, MS29, Stanford, CA 94309, USA
[8]SLAC National Accelerator Laboratory, 2575 Sand Hill Road, MS29, Menlo Park, CA 94025, USA
[9]National Astronomical Observatory of Japan (NAOJ), National Institutes of Natural Sciences, Osawa, Mitaka, Tokyo 181-8588, Japan
[10]The Institute of Statistical Mathematics, Tachikawa, Tokyo 190-8562, Japan

Abstract

Cosmological weak lensing measurements rely on a precise measurement of the shear two-point correlation function (2PCF) along with a deep understanding of systematics that affect it. In this work, we demonstrate a general framework for detecting and modeling the impact of PSF systematics on the cosmic shear 2PCF, and mitigating its impact on cosmological analysis. Our framework can detect PSF leakage and modeling error from all spin-2 quantities contributed by the PSF second and higher moments, rather than just the second moments, using the cross-correlations between galaxy shapes and PSF moments. We interpret null tests using the HSC Year 3 (Y3) catalogs with this formalism, and find that leakage from the spin-2 combination of PSF fourth moments is the leading contributor to additive shear systematics, with total contamination that is an order of magnitude higher than that contributed by PSF second moments alone. We conducted a mock cosmic shear analysis for HSC Y3, and find that, if uncorrected, PSF systematics can bias the cosmological parameters Ω_m and S_8 by $\sim 0.3\sigma$. The traditional second moment-based model can only correct for a 0.1σ bias, leaving the contamination largely uncorrected. We conclude it is necessary to model both PSF second and fourth moment contamination for HSC Y3 cosmic shear analysis. We also reanalyze the HSC Y1 cosmic shear analysis with our updated systematics model, and identify a 0.07σ bias on Ω_m when using the more restricted second moment model from the original analysis. We demonstrate how to self-consistently use the method in both real space and Fourier space, assess shear systematics in tomographic bins, and test for PSF model overfitting.

4.1 Introduction

In the past two decades, weak gravitational lensing, the slight distortions of the shape and size of the background (source) galaxies due to deflection of light rays by the foreground matter distribution, has become one of the most powerful probes to study the distribution of dark matter in the Universe due to its sensitivity to the matter density field along the line of sight (75; 76; 77). Measurements of cosmic shear, the coherent shape distortions of the source galaxies quantified via two-point correlation functions of galaxy shear estimates, are one of the most effective ways to measure the Large Scale Structure (LSS) and constrain the cosmological model. Stage-III imaging surveys (128) such as the Hyper Suprime-Cam survey (HSC; 81), the Dark Energy Survey (DES; 79), and the Kilo-Degree Survey (KiDS; 80) all conduct cosmic shear analysis (e.g., 1; 96; 153; 154; 155). Future galaxy surveys such as the *Vera C. Rubin* Observatory Legacy Survey of Space and Time (LSST) (LSST; 48; 82), the *Nancy Grace Roman* Space Telescope High Latitude Imaging Survey (49; 83) and *Euclid* (50) will measure cosmic shear with smaller statistical uncertainties by increasing the survey area, and in some cases by increasing the depth, and thus the number of galaxies, therefore putting more stringent requirements on controlling and modeling the systematic biases and uncertainties that affect cosmic shear measurements (33). Another major motivating factor

for improving our ability to control systematic uncertainties in weak lensing is the potential tension in the lensing amplitude, S_8 (156), an important parameter of the Λ-CDM cosmological model, between the weak lensing cosmology and the Cosmic Microwave Background (CMB) cosmology (20).

The Point Spread Function (PSF) describes the image response to the light of a point source, after passing through atmospheric turbulence and the telescope optics (129; 130). The PSF effectively acts as a convolution on the images of all observed objects, including galaxies. Therefore, the PSF is a major source of systematic biases and uncertainties in the measured galaxy shape, from which the weak lensing shear information is extracted. Biases in the estimated PSF size can give rise to multiplicative biases in the weak lensing shear signal as well, because the biases in PSF size result in an incorrect estimate of how much the PSF has rounded the observed galaxy shape (an effect for which we implicitly or explicitly correct). The PSF shape (ellipticity) can contaminate cosmic shear in two different ways: First, "PSF leakage" arises when the shape of the PSF coherently contaminates the inferred shear even when the PSF model is perfect. This effect originates from an imperfect shear estimation method. Second, when the PSF model inaccurately describes the actual PSF shape ("PSF modeling error"), the inferred shear can get an additive systematics term (e.g., 157). This second effect arises even for principled shear inference methods that should be unbiased with a perfect PSF model (e.g., 103; 158; 159). In many previous cosmic shear analyses, coherent biases in the PSF second moments (i.e., the shape and size) were monitored through the ρ statistics (88; 89). Null tests designed to identify potential additive shear systematics are typically conducted by cross-correlating the galaxy shapes, the PSF shape, and its modeling error (e.g., 85; 160), so that corresponding corrections can be made to the cosmic shear two-point correlation function (2PCF) through forward modeling. However, these PSF systematics formalisms have been limited to PSF second moments only.

(70; 71) showed that modeling error in PSF higher moments causes additive and multiplicative shear bias. (70) found sub-percent level multiplicative shear bias due to biases in a single PSF higher moment (radial kurtosis), while (71) provided a formalism for measuring PSF higher moments more generally, and studied the shear additive bias and its impact on cosmology analysis based on the HSC Public Data Release 1 (69). (71) suggested that the higher moments of the PSF can cause additive shear biases on a comparable level to the second moments, thereby motivating null tests involving PSF higher moments, and the development of a PSF systematics forward modeling formalism that considers PSF higher moments for current Stage-III surveys.

In this study, we develop a more rigorous and self-consistent framework for testing and modeling PSF systematics in the cosmic shear analysis. We generalize how PSF moments contaminate weak lensing shears by introducing the concept of a "spin-2 PSF quantity". Specifically, we derive the spin-2 quantities associated with PSF higher moments, which affect the inferred galaxy shears. We make a star catalog including PSF higher moment measurement, and inspect the overfitting issue of the PSF model. We articulate and carry out a more comprehensive set of null tests by correlating galaxy shapes in the HSC three-year (later referred to as HSC Y3, or Y3) shape catalog (160) with the PSF second and higher

moment spin-2 quantities that impact the galaxy shapes. We compare different models for modeling the additive shear biases associated with the PSF second and higher moments, provide a method to select models based on its complexity and level of impact on the cosmological probe, and propose the best-suited model for the HSC Y3 cosmic shear analysis. More importantly, we provide general guidelines for inspecting and modeling PSF systematics in future cosmic shear analyses. We demonstrate the impact of the new PSF systematics model on cosmological weak lensing analysis by re-analysing the HSC first-year (later referred to as HSC Y1) cosmic shear data and conducting a mock analysis of Y3, comparing models with or without the inclusion of the PSF higher moments. Finally, we investigate several aspects that complicate the PSF systematics model, including the redshift dependency of how PSF systematics affect galaxy shape measurements, a constant systematic shape, impact on ξ_-, and second order spin-2 terms. While this paper focuses on the real space analysis of weak lensing, we also provide a PSF formalism for the Fourier space analysis using cosmic shear power spectra, and study the internal consistency between the real and Fourier space formalisms.

The layout of this paper is as follows: we review the background of shear estimation and the associated PSF systematics in Section 4.2. We describe the HSC Y3 galaxy shape and mock galaxy catalogs, which we use to demonstrate the methods introduced in this work, in Section 4.3. We describe the HSC Y3 star catalog, the moment measurements we conducted, and the spin-2 quantities associated with the PSF, an important concept throughout the paper, in Section 4.4. We describe the methodology and results of modeling the PSF higher moments in shear, conducting cross-correlation null tests, and tests for potential redshift dependency of the model in Section 4.5. We demonstrate the impact on cosmological parameter analysis due to these PSF systematics by conducting a reanalysis of the HSC Y1 cosmic shear data vectors and an HSC Y3 mock analysis in Section 4.6. Our method is summarized with a concise list of steps in Section 4.7. In Section 4.8, we draw conclusions from the results of this paper and discuss its future implications and applicability to other weak lensing shear surveys.

4.2 Background

In this section, we briefly review the background to this study. In Section 4.2.1, we introduce cosmic shear: how it is estimated from the galaxy shapes, and how the likelihood analysis is carried out to extract cosmological information from the data. In Section 4.2.2, we introduce PSF-related systematic effects on weak lensing shear estimation.

4.2.1 Cosmic Shear

Cosmic shear is a way of measuring cosmological weak lensing, the coherent distortions of large ensembles of background galaxies by the foreground Large Scale Structure (LSS) of the Universe (For a review, see 34). Since these distortions are induced by all matter along the line of sight, cosmic shear is a powerful probe of the dark matter distribution,

which is otherwise challenging to observe. Cosmic shear was first measured in the early 2000s (e.g. 41; 42; 161; 162; 163) and consolidated in the late 2000s to early 2010s (e.g. 46; 104; 164) with larger volumes of survey data, improved redshift estimation (e.g., 104; 165) and statistical analysis (e.g. 166). Multiple ongoing and recently completed surveys have conducted successful cosmic shear analyses (e.g., 1; 96; 153; 154; 155). Future imaging surveys such as LSST (48), *Euclid* (50), and *Nancy Grace Roman* Space Telescope (49) will provide unprecedented statistical constraining power for cosmic shear observation, making requirements for controlling systematic biases and uncertainties more stringent. The decrease in statistical uncertainties and improvement in control of systematics may provide insights into the apparent S_8 tension between the cosmic microwave background and weak lensing (156).

In this section, we briefly describe how weak lensing shear is measured in imaging surveys (Section 4.2.1) and is used to constrain cosmological parameters (Section 4.2.1).

Shear Estimation

Galaxy ellipticity is widely used to quantify the spin-2 aspect of galaxy shape and infer the weak lensing shear distortion. We adopt the 'distortion' definition of ellipticity,

$$(e_1, e_2) = \frac{1-(b/a)^2}{1+(b/a)^2}(\cos 2\phi, \sin 2\phi), \tag{4.1}$$

where a and b are the major and minor axes and ϕ is the position angle of the galaxy major axis with respect to the x-axis of the sky coordinates taking the flat-sky approximation (with North being $+y$ and East being $+x$). Here we use this ellipticity definition as an example, but we note that other spin-2 observables (with two components) can also be used for shear inference, e.g., moments or derivatives of a galaxy's light profile (167; 168), projections of a galaxy's light profile onto basis functions (59; 169) or parameters used to fit a galaxy's light profile (170; 171).

For an isotropically-oriented galaxy ensemble distorted by a constant shear, the shear can be estimated as a weighted average of the distortion of all galaxies:

$$\hat{g}_\alpha = \frac{1}{2}\left\langle e_\alpha \right\rangle, \tag{4.2}$$

where the shear responsivity ($\mathcal{R}$) is the linear response of the average galaxy ellipticity to a small shear distortion (172; 173), and $\alpha = 1, 2$ are the indices for the two components of the ellipticity. Note that shear $\hat{g}_\alpha$ in this work is sometimes referred to as the "reduced shear", corresponding to the part of the shear that only changes the galaxy shape rather than the size. Since the galaxy detection and selection are dependent on the underlying shear distortion, an accurate shear responsivity should include the shear response of galaxy detection (158) and galaxy sample selection (174). In addition, since galaxy images are noisy, noise bias from the nonlinearity in the ellipticity and responsivity should be estimated and corrected for an accurate shear estimation (175). These biases can be corrected empirically

by shearing each observed galaxy and adding artificially sheared noise to galaxy images (158; 176; 177); analytically by correcting for the perturbations from shear and noise on the galaxy number distribution in the space of galaxy properties (59; 60; 159); or by calibrating the shear estimates with artificially sheared galaxy image simulations that are representative of the observed galaxy sample (55; 160; 178).

Moreover, in order to eliminate shear estimation bias due to PSF smearing, one can deconvolve the PSF from the galaxy image in Fourier space (59; 168; 176; 179); construct the PSF correction term based on analytic formalisms that connect this term to second moments of the galaxy and PSF (169; 172; 180); or convolve models fitted to each galaxy with the PSF (170; 171; 181). This paper focuses on the PSF-related systematics (including PSF leakage and PSF modelling error, see Section 4.2.2 for more detail) after the PSF correction step in the shear estimation and the shear calibration with image simulations.

Throughout this work, we will use the terms "additive bias" and "multiplicative bias" to quantify shear systematics. The observed shear $\hat{g}$ can be generally expressed by

$$\hat{g} = (1 + m)g + c. \tag{4.3}$$

Here g represents the true shear, m is called the multiplicative bias, and c is called the additive bias. Generally, any source of systematics that correlates with the shear or the galaxy shapes would contribute to the multiplicative bias, and systematics that are independent of the galaxy shape would enter as an additive bias.

Cosmic Shear Analysis

In this section, we describe how cosmic shear analyses allow one to constrain cosmological parameters starting from a galaxy catalog. The steps include measuring summary statistics of the shear catalog, forward modeling the summary statistics based on cosmology and systematics, and conducting likelihood analysis. The PSF systematics model described in this work is an integrated part of the forward model in the likelihood analysis, therefore impacting the overall results of the cosmological analysis.

A common method to extract summary statistics from a galaxy catalog is to measure the shear-shear two-point correlation function (2PCF) ξ_+^{ij} and ξ_-^{ij} of the galaxy shape (for reference, see 34), where i and j are the indices of the tomographic redshift bins used for the analysis (36). The shear-shear 2PCF is used in real-space cosmic shear analyses (e.g., 1; 154; 182). Other works use Fourier space and measure angular power spectra C_ℓ^{ij} as the summary statistics (153; 183; 184); we discuss the formalism relevant to power spectra in Appendix 4.G.1. To increase statistical constraining power, the $\xi_\pm^{ij}(\theta)$ measurements are averaged within angular bins with a range of separations θ for the galaxy pairs. The angular bins and tomographic bin-pairs form a cosmic shear data vector, which we denote $\boldsymbol{D}_{gg}$.

The next stage of the cosmic shear analysis is the likelihood analysis (see, e.g., 185), where the cosmic shear data vector $\boldsymbol{D}_{gg}$ is compared with a theoretical data vector $\boldsymbol{T}_{gg}$. $\boldsymbol{T}_{gg}$ is computed using a forward model that predicts the data vector based on cosmological parameters and any needed nuisance parameters, including PSF parameters, which will be

discussed in Section 4.5.1. The log-likelihood is defined as

$$\log(\mathcal{L}(\boldsymbol{\Omega}|\boldsymbol{D}_{gg})) = -\frac{1}{2}(\boldsymbol{D}_{gg} - \boldsymbol{T}_{gg}(\boldsymbol{\Omega}))^T \boldsymbol{\Sigma}_{gg}^{-1}(\boldsymbol{D}_{gg} - \boldsymbol{T}_{gg}(\boldsymbol{\Omega})), \tag{4.4}$$

where $\boldsymbol{\Omega}$ is a set of parameters, and $\boldsymbol{\Sigma}_{gg}^{-1}$ is the inverse of the covariance matrix of $\boldsymbol{D}_{gg}$. A sampling algorithm, e.g., EMCEE (186) or MULTINEST (187; 188; 189), traverses the parameter space to approximate the likelihood function across the parameter space, and eventually provides parameter constraints from the data vector. Models for additive shear systematics induced due to the PSF enter in the likelihood analysis; typically these are informed by null tests that reveal what types of systematics may be present, with priors on model parameters determined using those tests.

In Section 4.6, we describe the forward cosmological model we used to reanalyze the HSC Y1 cosmic shear data vector and to conduct a HSC Y3 mock analysis. Our new model for additive PSF systematics and their impact on weak lensing shear, which is part of the forward model, is described in Section 4.5.1.

4.2.2 PSF-related systematics

For a ground-based imaging survey telescope, e.g., the HSC and LSST, the PSF describes the smearing of the image by the turbulent atmosphere and the telescope optics. In this paper, the PSF also involves the pixelization effect in the CCD, described as a convolution by a unit-square function; the PSF including this effect is referred to as the "effective" PSF. The single exposures within the survey footprint are combined to produce a "coadded" image, as are the PSF models (110). For the HSC survey, shear estimation is carried out on the coadded image, making the coaddition procedure and production of the coadded PSF a crucial step that can affect shear estimation (53).

After convolution with the PSF, the observed size and shape of the galaxy differ from the true values, in a way that depends on the galaxy and PSF properties (157). Since almost all weak lensing science heavily relies on the precise measurement of the galaxy shape or some other spin-2 quantity based on galaxy second moments (33), it is crucial to precisely model the PSF and correct for its impacts on the galaxy shear estimate during the shape measurement phase of the image processing. Imperfections in PSF modeling cause a PSF modeling bias in shear (see Appendix A in 157), even for principled shear estimation methods that should be unbiased. If the shear estimation method is imperfect, it causes PSF leakage bias in shear (54). Typically, it is prudent to test for both leakage and modeling error, even when using a shear estimation method that should not have any leakage.

Weak lensing shear systematics related to the PSF second moments are well-studied in previous work. The PSF leakage of the second moment-based `reGauss` method is characterized in (180; 190). In (157), expressions for the additive shear systematics due to PSF modeling errors are derived under the assumption that both the galaxy and PSF profiles are Gaussian. In (88; 89), the propagation of the previously mentioned leakage and modeling error to the cosmic shear 2PCF is quantified using the "ρ statistics ".

Recent cosmic shear analyses made different choices for how to model these additive shear systematics due to the PSF. In (1), the additive bias on ξ_+ in HSC Y1 due to PSF second moment leakage and modeling error were modeled and marginalized with two parameters $\alpha_{\rm PSF}$ and $\beta_{\rm PSF}$ (see Eq. 4.22), which are taken to be the same across all tomographic bins. The additive bias on ξ_-, and any mean shear, are neglected after confirming that the mean shear in each survey region was consistent with zero within the uncertainty due to cosmic variance. In (154), the PSF second moment leakage, shape modeling error, and size modeling error were investigated. However, the additive bias on shear was not included in the fiducial analysis because the ρ statistics were within the survey requirement (191). In Section 3 of (192), the PSF contamination on ξ_+ was modeled by a leakage term, a modeling error term, and a constant term.

In (70), multiplicative bias induced by the modeling error of the PSF fourth radial moments, or kurtosis, were found using image simulations and the HSC Y1 dataset. The multiplicative bias predicted for the cosmic shear due to this effect is on the order of 10^{-3}, which is sub-dominant to other sources of multiplicative bias (e.g., the PSF size modeling error). For this reason, directly modeling it in the HSC Y3 analysis is not urgent. In (71), additive biases from the PSF higher moments modeling error were found to be of a similar magnitude to the second moment additive biases in the HSC Y1 data. Therefore, testing for and modeling additive biases due to PSF higher moment modeling errors in cosmic shear analyses is necessary. These two previous works are the main motivation for developing a framework to self-consistently identify and model PSF additive systematics to higher order than those caused by second moments. Crucially, our method includes a step to limit the model to only those terms that turn out to be present at a significant level in a given dataset, enabling different data-motivated choices of what terms to model in different datasets.

4.3 HSC Shape Catalog

In this section, we describe the galaxy catalog we used to explore PSF systematics modeling in HSC Y3 cosmic shear analysis. In Section 4.3.1, we describe the HSC Y3 shape catalog (160). In Section 4.3.2, we describe the mock catalogs we used for uncertainty estimation.

4.3.1 HSC Y3 Shape Catalog

In this section, we summarize the HSC three-year (Y3) (160) shear catalog for weak lensing science. In the HSC shear catalog, galaxy ellipticities are estimated from i-band coadded images with the re-Gaussianization (`reGauss`) shear estimator and PSF correction method (180), which is implemented in `GalSim` (193), an open-source package for image simulation and image processing. `reGauss` has been developed and used extensively on data from the Sloan Digital Sky Survey (SDSS; 31; 190) and the first HSC shape catalog (54). The `reGauss` estimator measures the two ellipticity components for each galaxy using its spin-2 elements in the second-order moment matrix.

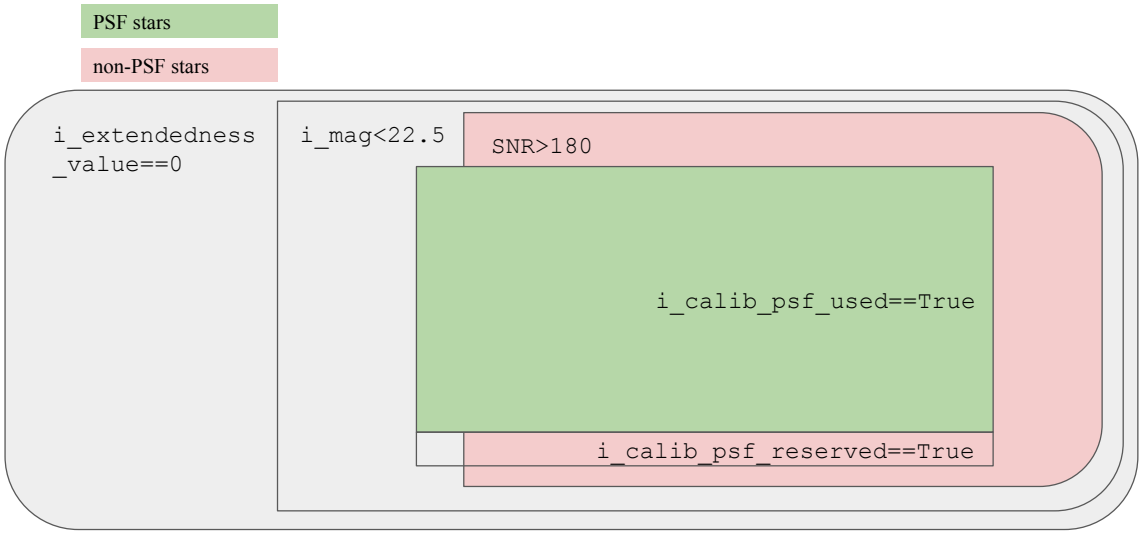

Figure 4.2.1: Schematic diagram describing the selection of the PSF and non-PSF star catalogs in this work. The selection on the i-band extendedness, magnitude and signal-to-noise ratio are done at the coadd level, while the selections of PSF used stars and reserved stars are done on the single visit level. The green region is the PSF star catalog, while the pink region is the non-PSF star catalog. We can see that the PSF and non-PSF stars are selected using different criteria, resulting in different results for the PSF systematics parameters (see Section 4.5.2). However, the impacts on cosmology are similar, as shown in Section 4.5.2. Note that a box within another box does not imply that one is a subset of the other; instead, it indicates a sequence of selections we imposed on our samples.

`reGauss` also computes the resolution factor, R_2 which is used to quantify the extent to which the galaxy is resolved compared to the PSF. The resolution factor is defined for each galaxy using the trace of the second moments of the PSF ($T_{\rm PSF}$) and those of the observed galaxy image ($T_{\rm gal}$):

$$R_2 = 1 - \frac{T_{\rm PSF}}{T_{\rm gal}}\,. \tag{4.5}$$

The inverse variance weights to be used while performing the ensemble average are the galaxy shape weights (w_i) defined as

$$w_i = \frac{1}{\sigma^2_{e;i} + e^2_{{\rm RMS};i}}, \tag{4.6}$$

where i is an index over galaxies, σ_e is the per-component 1σ uncertainty of the shape estimation error due to image noise, and $e_{\rm RMS}$ denotes the per-component root-mean-square (`RMS`) of the galaxy intrinsic ellipticity[1] (often referred to as 'shape noise'). The parameters

[1]While the RMS ellipticity is ostensibly associated with the entire sample, it does depend on the particular

$e_{\rm RMS}$ and σ_e are modeled and estimated for each galaxy using image simulations (160; 178). The shear responsivity for the source galaxy population is estimated as

$$\mathcal{R} = 1 - \frac{\sum_i w_i e^2_{{\rm RMS};i}}{\sum_i w_i} \,. \tag{4.7}$$

The measured shears are calibrated with realistic image simulations downgrading the galaxy images from COSMOS Hubble Space Telescope (104) to the HSC observing conditions (178). The calibration removes the galaxy property-dependent (galaxy resolution, galaxy SNR, and galaxy redshift) estimation bias and the detection and selection bias due to the correlation between detection/selection and the underlying shear distortion. The image simulation used for calibration includes the blending of light from neighboring galaxies; therefore, the calibration removes biases related to blending. The resulting systematic uncertainties in the shear estimation are below 1% after the calibration (160).

With conservative selection cuts on each galaxy's i-band magnitude (brighter than 24.5) and resolution (greater than 0.3), the full galaxy shear catalog has a raw (effective[2]) number density of 23 arcmin^{-2} (20 arcmin^{-2}) covering 417 deg^2, after removing a 20 deg^2 region that failed the cosmic shear B-mode test (more information found in Appendix 4.B). The full galaxy catalog is divided into 4 tomographic bins by selecting galaxies within redshift intervals of $(0.3, 0.6]$, $(0.6, 0.9]$, $(0.9, 1.2]$ and $(1.2, 1.5]$ using the best point estimate (195) of the Deep Neural Net Photometric Redshift (`dNNz`; Nishizawa et. al *in prep.*) conditional density estimates of individual galaxy redshift posteriors, where `dNNz` is a template based inference method. We found that some `mizuki` (195) and `dNNz` photometric redshift posteriors have a secondary peak at $z \gtrsim 3.0$. These photometric redshift posteriors are difficult to calibrate using spatial cross-correlations, since the secondary peak lies outside the redshift coverage of the CAMIRA sample (Cluster finding algorithm based on Multi-band Identification of Red-sequence gAlaxies; (196)), which we use as a reference sample and which is limited to $z < 1.2$. In order to prevent the secondary solution from biasing the sample redshift distribution inference, we remove galaxies with double solutions in the estimated photo-z posteriors (see Rau et. al *in prep.* for details). The cuts that are used to remove the galaxies with secondary peaks reduce the number of galaxies in the first (second) bin by 30% (8%). After the region cut and double solution cut, we have 5,889,826, 8,445,233, 7,023,314, and 3,902,504 galaxies in the corresponding four redshift bins, respectively. The corresponding raw (effective) galaxy number densities are 3.92 (3.77), 5.63 (5.07), 4.68 (4.00) and 2.60 (2.12) arcmin^{-2}, respectively.

4.3.2 HSC Mock Catalogs

We use the HSC three-year mock shear catalog to accurately quantify the uncertainties of our measured 2PCFs due to cosmic variance, galaxy shape noise, measurement errors due

subpopulation within the catalog. To enable division of the catalog into subsamples (e.g., for tomographic analysis), information is provided on this variation to enable a correct estimate of the RMS ellipticity for the selected subsample.

[2]See (194) for the definition of effective number density.

to photon noise, and photometric redshift uncertainties. The mock catalogs are created following (197), but with updates to incorporate the survey footprint, galaxy shape noise and shape measurement error of the three-year HSC shear catalog.

The mock shear catalog uses full-sky lensing simulations generated by (198) with 108 full-sky simulations. To increase the number of total realizations of the mock catalogs, we extract 13 separate regions from each full-sky simulation, obtaining $108 \times 13 = 1404$ mock catalogs in total.

These realizations of the lensing simulations are combined with the observed photometric redshifts, angular positions, and shapes of real galaxies (160) to generate mock shear catalogs. To be more specific, source galaxies are populated on the light-cone of the lensing simulations using the original angular positions and "best-fit" redshifts of the galaxies (estimated with `dNNz`) in the HSC three-year shear catalog. Each galaxy is assigned a source redshift estimate in the mock following the posterior distribution of photometric redshift estimated by the `dNNz` algorithm. The shape noise on each galaxy is generated with a random rotation of the galaxy's intrinsic shape according to the intrinsic shape dispersion estimated in the HSC shear catalog, and the measurement error is generated as a zero-mean Gaussian random number with the standard deviation measured in the HSC shear catalog (see Section 4.2 in 197).

4.4 Star Catalogs and Moments Measurements

In this section, we introduce the HSC Y3 star catalogs with the measurements of higher moments. In Section 4.4.1, we describe how the star sample is selected. In Section 4.4.2, we summarize the measurement of the PSF second and higher moments. In Section 4.4.3, we introduce a key concept in the paper: how to identify the PSF higher moments that form "spin-2" quantities, which will be included in the PSF systematics formalism in Section 4.5.1.

4.4.1 Sample Selections

In this section, we describe the star catalogs used in this work. The overall selection processes are shown in Figure 4.2.1, in which the PSF and non-PSF star catalogs are marked in green and pink, respectively. We describe each of these selections in this subsection.

The HSC Y3 star catalog used in this work is selected from the sample of point sources based on the star samples in Section 5.1 of (160) covering the same footprint as the galaxy shape catalog described in Section 4.3.1. Unlike (71), we measure the star moments on postage stamp images after deblending, as described in (110). Therefore, we did not apply any selection criteria to omit stars based on their blendedness.

The HSC data processing and PSF modeling is carried out independently in multiple exposures. Each exposure has a different random subset of the stars used for PSF model estimation. The exposures are then stacked to make the coadded image (see 110). In each exposure, a set of candidate PSF stars is selected using the k-means clustering algorithm in the magnitude-size plane. A randomly-selected 80% of the candidate stars is used

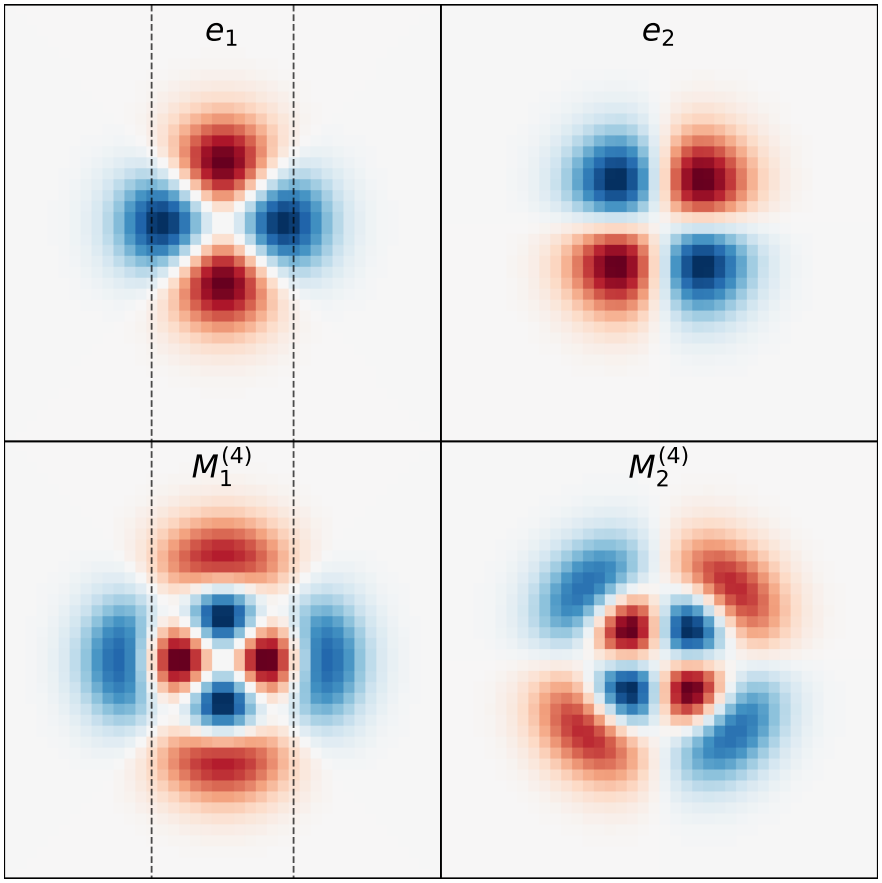

Figure 4.3.1: The image response to the spin-2 quantities of the second moments e_1 and e_2, and fourth moments $M_1^{(4)}$ and $M_2^{(4)}$. The fourth moment spin-2 quantities are sensitive to scales larger and smaller than those to which the second moment spin-2 quantities are sensitive, as the dashed reference lines show. The color scale for each base covers $[-A, A]$, where A is the maximum of the absolute value of the basis function.

for PSF modeling, with the random selection carried out independently for each exposure. On the coadd level, the stars with `i_calib_psf_used==True` are those that were used as PSF stars in more than 20% of the contributing i-band exposures, while those labelled as `i_calib_psf_reserved==True` were used as PSF stars in fewer than 20% of the contributing exposures. Because the random selection of stars for PSF modeling in single exposures is carried out independently, the `i_calib_psf_reserved==True` stars in the coadded image are very rare.

To mitigate the scarcity of the PSF reserved stars, we use a more lenient `i_extendedness==False` & `i_mag<22.5` cut on the coadd catalog to pre-select a star catalog. Within that catalog, those with `i_calib_psf_used=True` are defined to be the "PSF star" catalog. Stars with `i_calib_psf_used=False` are candidates for the "non-PSF stars". In addition, we find that the low SNR non-PSF stars have larger sizes and lower ellipticities to a statistically signifi-

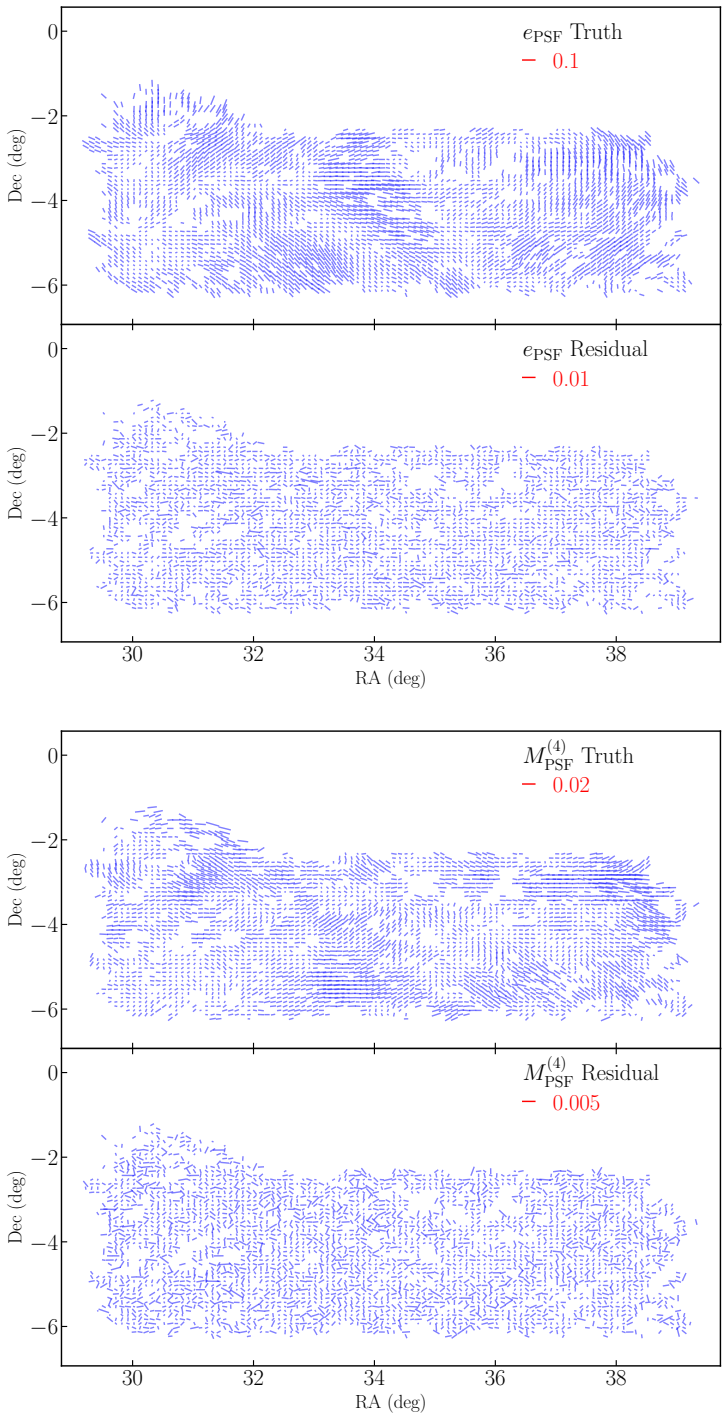

Figure 4.3.2: The whisker plots of the true and residual spin-2 components of the PSF second (top) and fourth moments (bottom) in the `XMM` field. There is an obviously coherent pattern in the whisker plots for the true moments, while the pattern is less visible in the moment residuals (later, we will see that the correlation length of the residual field is smaller, which makes the coherence less visible in the whisker plots). The spin-2 pattern of the true fourth moments is clearly different from that of the second moments, which indicates that contamination in the PSF higher moments must be separately modeled in cosmic shear, as we explore in Section 4.5.

cant degree, making them unrepresentative samples of the true PSF. This could potentially be caused by the increasing fraction of galaxy contamination at low SNR, which only affects non-PSF stars because the PSF stars have a preliminary SNR cut in the image processing pipeline. Therefore, we applied an empirical SNR cut to the non-PSF sample, requiring flux SNR$>$ 180, so that the non-PSF star sample has a nearly identical size distribution as the PSF star sample. Although the PSF star catalog also has low SNR samples, those samples have a similar size and ellipticity distribution to the rest, due to the strict star-galaxy separation done on the single visits for the PSF stars. This eliminated 23% of the potential non-PSF star sample. After these selections, of the coadd star samples, about 6% of the stars are "non-PSF" stars.

We also removed an area of 20 deg^2 (at RA $\in [132.5, 140]$, Dec $\in [1.6, 5]$) in the `GAMA09H` field that generated a strong B-mode shear signal, as will be described in Li et al. *in prep.* We explored this region of the sky and found a significant PSF fourth moment modeling error, described in Appendix 4.B.

After the previously mentioned cuts, there are 2,118,183 PSF stars and 132,687 non-PSF stars in our sample, where the former has an average density of 1.42 arcmin^{-2} and the latter, 0.09 arcmin^{-2}.

4.4.2 Second and Higher Moments

In this section, we briefly review the measurement of the PSF second and higher moments from a pixelized i-band postage-stamp image. This formalism follows the one in (71). We define the adaptive second moment matrix $\mathbf{M}$ of a light profile $I(x, y)$ in the image coordinate system with origin at the centroid of $I(x, y)$ as

$$M_{pq} = \frac{\int \mathrm{d}x\mathrm{d}y\, x^p y^q\, \omega(x, y) I(x, y)}{\int \mathrm{d}x\mathrm{d}y\, \omega(x, y) I(x, y)}. \tag{4.8}$$

Here (p, q) take the values of $(2, 0), (1, 1), \mathrm{and}(0, 2)$, and $\omega(x, y)$ is the adaptive Gaussian weight (180), defined as

$$\omega(x, y) = \exp\left(-\frac{1}{2}\begin{bmatrix} x & y \end{bmatrix}\begin{bmatrix} M_{20} & M_{11} \\ M_{11} & M_{02} \end{bmatrix}^{-1}\begin{bmatrix} x \\ y \end{bmatrix}\right). \tag{4.9}$$

The second moment trace T_{PSF} and shape $e_{\mathrm{PSF}} = e_{\mathrm{PSF},1} + ie_{\mathrm{PSF},2}$ are defined based on $\mathbf{M}$

$$T_{\mathrm{PSF}} = M_{20} + M_{02} \tag{4.10}$$

$$e_{\mathrm{PSF},1} = \frac{M_{20} - M_{02}}{M_{20} + M_{02}} \tag{4.11}$$

$$e_{\mathrm{PSF},2} = \frac{2M_{11}}{M_{20} + M_{02}}. \tag{4.12}$$

Notice that there is a different definition for the PSF second moment size σ_{PSF}, which approximates the standard deviation of the Gaussian that best fits the PSF profile. It is

defined by

$$\sigma_{\rm PSF} = [\det(\mathbf{M})]^{\frac{1}{4}} \,. \tag{4.13}$$

A natural way to define the higher moments is to integrate over $x^p y^q$, as in Eq. (4.8). However, the resulting higher moments will depend on the size and shape of the PSF. There are two approaches to disentangling the higher moments from the second moments: one is through a combination of the higher and second raw moments as defined above; the other is to define the higher moments in a transformed coordinate that normalizes second moments. In this work, we discuss both approaches, although the second approach is used in most parts of this work. To connect the two approaches, we describe the formalism of raw and standardized higher moments in Appendix 4.C, including the Gaussian and non-Gaussian parts of the raw moments. We also demonstrate empirically for the HSC survey data that you can use the raw moments to track PSF additive bias in shear-shear 2PCF, and get consistent results from the results using standardized moments, in Section 4.C.3.

In the "normalizing approach", the higher moments are defined by integrating over the image using $u^p\, v^q$, where (u, v) is a standardized coordinate defined by

$$\begin{bmatrix} u \\ v \end{bmatrix} = \mathbf{M}^{-\frac{1}{2}} \begin{bmatrix} x \\ y \end{bmatrix} . \tag{4.14}$$

In the (u, v) coordinate system, the second moment shapes of $I(x, y)$ are $e'_1 = e'_2 = 0$, and the second moment size $\sigma' = 1$. The higher moments, defined using the standardized coordinates, are

$$M_{pq} = \frac{\int \mathrm{d}x\, \mathrm{d}y\, u^p\, v^q\, \omega(x, y)\, I(x, y)}{\int \mathrm{d}x\, \mathrm{d}y\, \omega(x, y)\, I(x, y)}. \tag{4.15}$$

Note that here integrating in $\mathrm{d}x\, \mathrm{d}y$ is the same as in $\mathrm{d}u\, \mathrm{d}v$ since the $\mathbf{M}^{-1}$ factor cancels out between the denominator and the numerator. The connection between the standardized and raw higher moments is described in Appendix 4.C.2.

For the nth moments, p takes integer values from 0 to n, while $q = n - p$. Therefore, there are $n + 1$ nth moments. The standardized higher moments are not sensitive to any of the lower moments from $n = 0$ to 2 (the flux, centroid, size, or shape). They describe the non-Gaussian morphology of the PSF profile.

The HSC Y3 star catalog in this work contains second to sixth moments, 25 in total, measured using the i-band deblended coadded images of the stars and PSF model. The PSF model is a modified version of PSFEx (84), initially described in (110) and later updated in (135). We measure the moments of the PSF model images evaluated at the star positions as the model moments.

The residual for the moment M_{pq} is defined as

$$\Delta M_{pq} = M_{pq,\rm model} - M_{pq,*}, \tag{4.16}$$

where $M_{pq,\rm model}$ is the moment of the PSF model, and $M_{pq,*}$ is the true moment measured on the star image.

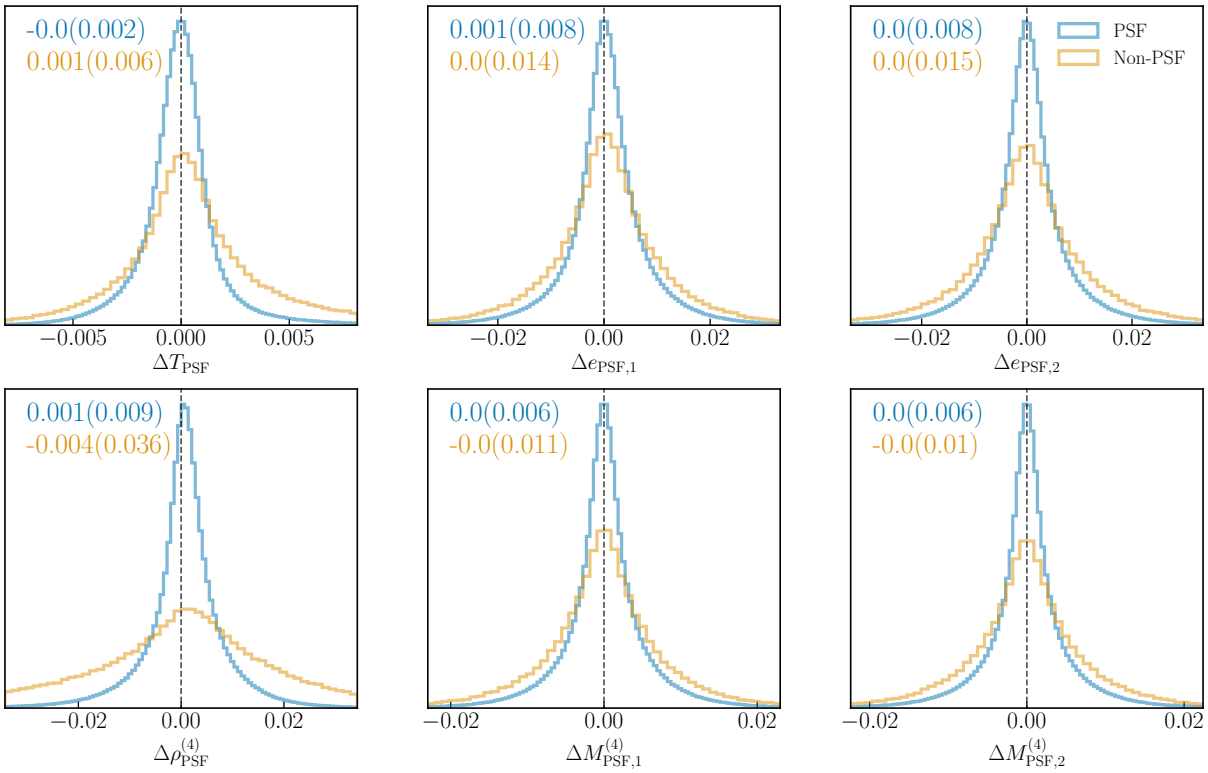

Figure 4.4.1: The modeling errors, defined in Eq. (4.16), in the spin-2 and spin-0 components of the PSF second and fourth moments, as defined in Section 4.4.3, are shown in the top and bottom rows, respectively. The results using the PSF (non-PSF) stars are in blue (orange). Text labels on each panel show the mean and standard deviation of the distributions with matching color. The PSF stars have a narrower residual distribution than the non-PSF stars, especially in the spin-0 components. We concluded that this is caused by PSF model overfitting, as described in Section 4.4.3.

4.4.3 Spin-2 and Spin-0 PSF Moment Combinations

The image simulations in (71) provide early evidence that (a) PSF even moments are far more important for weak lensing shear than PSF odd moments, and (b) the shear response to PSF higher moments exhibits symmetries in moment indices. In this section, we show that one linear combination of all higher moments at a given even order represents the "spin-2" contribution of those moments to the first order; and we prove that only the even moments can combine to form spin-2 moments in Appendix 4.A. This demonstration is important, because spin-2 PSF quantities are assumed to be the main contributor to the additive shear systematics (given that shear is spin-2). Additionally, the product of a spin-0 and spin-2 quantity is also a spin-2 property (89). Therefore, it is also relevant for us to define the spin-0 combinations of the second and higher moments of the PSF.

A spin-2 complex quantity, e.g., weak lensing shear, negates when coordinates are rotated by $\pi/2$ (see, e.g., Appendix A of (159)). We are interested in the spin-2 components of the PSF's fourth moments. Therefore, we find the spin-2 component of the 4th order complex polynomials in polar coordinates (r, ϕ):

$$\begin{aligned} r^4 e^{2i\phi} &= r^4 \left[\cos(2\phi) + i\sin(2\phi)\right] \\ &= r^4 \left[\cos^4(\phi) - \sin^4(\phi)\right] \\ &\quad + ir^4 \left[2\sin(\phi)\cos^3(\phi) + 2\sin^2(\phi)\cos(\phi)\right] \\ &= (x^4 - y^4) + i(2x^3y + 2xy^3). \end{aligned} \tag{4.17}$$

The first parenthetical polynomial leads to the combination of two moments, $M_{40} - M_{04}$, while the second parenthetical polynomial leads to an imaginary combination of two moments, $2M_{13} + 2M_{31}$. We therefore define the spin-2 combination of the PSF 4th moments as

$$M^{(4)}_{\rm PSF} = (M_{40} - M_{04}) + i(2M_{13} + 2M_{31}). \tag{4.18}$$

In support of this definition, Figure 6 of (71) provides numerical evidence that M_{40} and M_{04} are the only fourth moments that impact g_1, and M_{31} and M_{13} are the only ones that impact g_2 . In Fig. 4.3.1, we show the image responses to the spin-2 quantities of second and fourth moments. The image responses show the variation of a Gaussian PSF when only a specific spin-2 quantity is changed, while other moments remain constant. It is computed by PSFHOME[3] (71). Fig. 4.3.1 shows that the $M^{(4)}_{\rm PSF}$ values are sensitive to pixels with radius both larger and smaller than the pixels to which the $e_{\rm PSF}$ values are sensitive. The sensitivities of $M^{(4)}_{\rm PSF}$ to smaller and larger radii with the same polar angle have opposite signs, which means $M^{(4)}_{\rm PSF}$ is sensitive to the difference in spin-2 between pixels with small and large radii.

As shown in Appendix 4.A, there will in general be a spin-2 combination of even moments at any order. For example, for the 6th moments, we can expand $r^6 e^{2i\phi}$ as in Eq. (4.17) to define the spin-2 combination of the PSF 6th moments as $M^{(6)} = (M_{60} + M_{42} - M_{24} - M_{06}) +$

[3] `https://github.com/LSSTDESC/PSFHOME`

$i(2M_{51} + 4M_{33} + 2M_{15})$. In Appendix 4.E.3, we demonstrate that sixth moments do not need to be modeled in the PSF systematics for the HSC analysis in practice, since they are noise dominated and highly correlated with fourth moments.

In Fig. 4.3.2, we visualize the spin-2 combination of PSF second moments, i.e., the shape (upper panel), and of the PSF fourth moments, i.e., $M^{(4)}$ (lower panel), in one of the six HSC fields. In both cases, we show the true moments measured using star images and their residuals defined in Eq. (4.16). We can see distinctive patterns in the true second and fourth moment distributions, which suggest that they must both be modeled in the weak lensing shear analysis. The pattern in the residuals is less visible, mainly because they are coherent on a smaller angular scale than the resolution of these whisker plots, as we will see later in Section 4.5.2 through the two-point correlation functions.

As stated previously, the product of a spin-0 and spin-2 quantity is also spin-2. Therefore, it is relevant for us to define the spin-0 quantities of the PSF moments. We can find the spin-0 components of the second and fourth moments by doing a similar exercise for r^2 and r^4 instead of $r^4 e^{2i\phi}$ as in Eq. (4.17). For the second moments, that process yields the trace of the second moment matrix $\mathbf{M}$,

$$T_{\rm PSF} = M_{20} + M_{02}. \tag{4.19}$$

For the fourth moments, it yields the radial kurtosis,

$$\rho^{(4)}_{\rm PSF} = M_{40} + 2M_{22} + M_{04}. \tag{4.20}$$

In Fig. 4.4.1, we show the residual distributions of the spin-2 and spin-0 moment combinations (for the second and fourth moments) for the PSF and non-PSF stars in the Y3 star catalog. We see that the non-PSF stars have a wider spread in all moments, which can be caused by either overfitting of the PSF model, or different SNR distributions of the PSF and non-PSF stars. To rule out the SNR explanation, we inspected the moment residuals for SNR in the range $[300, 500]$, where the PSF and non-PSF stars have very similar SNR distributions, and also found a similarly wider spread for the non-PSF stars compared to the results shown in Fig. 4.4.1. Therefore, we conclude that the PSF model is overfitting the PSF, which means that the PSF stars have underestimated PSF model residuals compared to other locations (such as those where we expect to find galaxies).

The noise in the image can cause noise bias in the PSF higher moments for low signal-to-noise samples. We conducted a simple numerical test with an HSC-like PSF profile to ensure that the multiplicative noise bias to our higher moments measurement is on or below the order of 10^{-3} within the SNR range of the star samples used here. Due to this finding, we do not expect noise to cause significant bias in the higher moments measurement.

The identification of spin-2 combinations of PSF higher moments is a powerful tool to reduce the dimensionality of the data vector of PSF higher moments that must be considered as potential contaminants to weak lensing shear, which can greatly simplify the cosmic shear analysis while still allowing for effective mitigation of all relevant PSF systematics. In Section 4.5.1, we will build the PSF systematics model including spin-2 higher moment combinations.

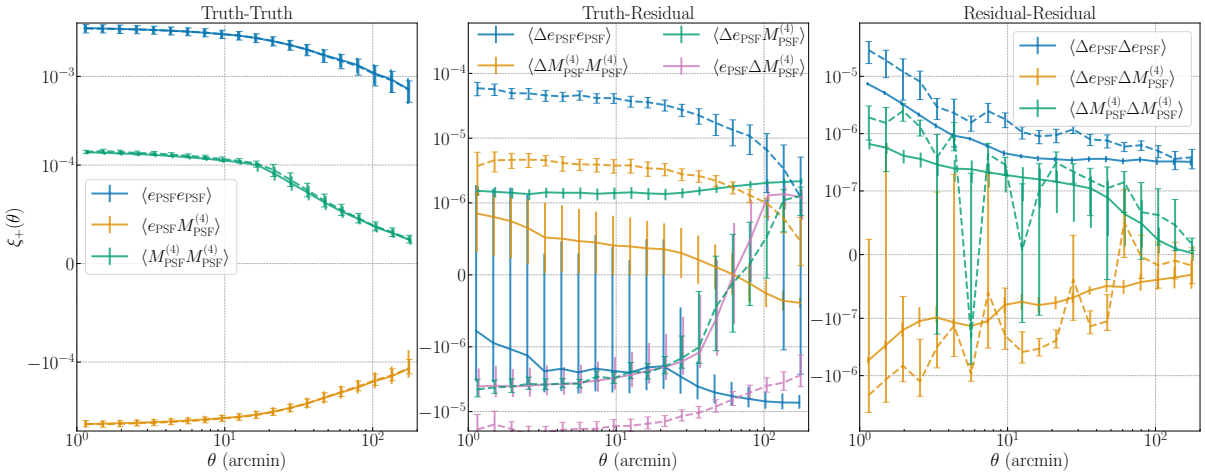

Figure 4.4.2: The PSF-PSF correlation functions between $[e_{\rm PSF}, \Delta e_{\rm PSF}, M^{(4)}_{\rm PSF}, \Delta M^{(4)}_{\rm PSF}]$ of the PSF stars (solid lines) and the non-PSF stars (dashed lines) in all six HSC Y3 fields. The 10 correlation functions are divided into truth-truth (left panel), truth-residual (middle panel), and residual-residual (right panel). The PSF and non-PSF stars have identical truth-truth correlations, as expected since they trace the same survey area in consistent ways. The truth-residual and residual-residual correlations of the non-PSF stars are all larger than those for PSF stars. This result is consistent with the evidence for PSF model overfitting that was identified in Figure 4.4.1. We use the symmetrical-logarithmic scale on the y-axes, with the linear region shaded in grey. All errorbars are obtained by the jackknife in TreeCorr (8) after dividing the entire HSC Y3 fields into 20 patches using k-means. Note that the truth are orders of magnitude larger than the residual, therefore the three panels have very different scale in y-axis. The errorbars on the correlation functions for PSF (non-PSF) stars have (do not have) caps.

4.5 PSF Systematics in Cosmic Shear

In Section 4.5.1, we present our formalism for describing PSF systematics in cosmic shear. In Section 4.5.2, we describe the process for model selection (demonstrating it by determining our fiducial model for HSC) and for determining the priors on the corresponding parameters. In Section 4.5.3, we describe the process for accounting for how PSF systematics may affect tomographic bins in different ways due to evolution in galaxy properties and shear with redshift.

We have also confirmed that a number of factors are subdominant and need not be included in our model. These aspects include the PSF systematics impact on ξ_-, PSF sixth order spin-2 quantity, and impact of second-order systematics terms. These are discussed in Appendix 4.E. These outcomes are specific to the HSC Y3 dataset, and we recommend that other surveys carry out these tests when determining their PSF systematics model as well. This section derives the PSF systematics models in the real space cosmic shear analysis. We provide the equivalent formalism in Fourier space and discuss the consistency between the real and Fourier space analyses in Appendix 4.G.

4.5.1 Formalism

The observed galaxy ellipticity can be expressed as

$$\hat{g}_{\rm gal} = g_{\rm gal} + g + g_{\rm sys}. \tag{4.21}$$

Here $g_{\rm gal} = e_{\rm gal}/(2\mathcal{R})$ is the shear of the intrinsic shape of the galaxy, g is the cosmic shear, introduced in Section 4.2.1, $\mathcal{R}$ is the responsivity of the shape to shear, and $g_{\rm sys}$ is the additive systematic shear due to the PSF. In this formalism, the multiplicative bias, which normally is a pre-factor of the shear, is absorbed in the responsivity matrix. The spin-2 quantities related to the PSF, described in Section 4.4.3, contribute to the additive bias $g_{\rm sys}$. Note that in some literature, the additive shear bias $g_{\rm sys}$ is referred to as $e_{\rm sys}$ (47; 153).

The past treatment of PSF systematics due to second moments in $g_{\rm sys}$ has included two terms: PSF leakage and PSF shape modeling error. The PSF leakage refers to the imperfect correction for the shear estimation method, which correlates the galaxy shape $\hat{g}_{\rm gal}$ with the PSF shape $e_{\rm PSF}$. For example, it is found in previous studies that `reGauss` is susceptible to PSF leakage (1; 54). The PSF modeling error term originates from the residual in PSF shape modeling and therefore the unavoidable bias in the galaxy shape estimation (157), which correlates the galaxy shape $\hat{g}_{\rm gal}$ with the PSF shape residual $\Delta e_{\rm PSF} = e_{\rm PSF,model} - e_{\rm PSF,*}$. Previous work often used α and β as prefactors for the leakage and modeling error terms (1; 154; 192). When only considering the PSF second moments,

$$g_{\rm sys} = \alpha e_{\rm PSF} + \beta \Delta e_{\rm PSF}. \tag{4.22}$$

Note that in (1), instead of $(\Delta)e_{\rm PSF}$, $(\Delta)g_{\rm PSF} = (\Delta)e_{\rm PSF}/2$ is used. We decided to use the distortion ($e_{\rm PSF}$) directly throughout the paper so that second and higher moments would be

treated consistently. This choice only results in a factor of 2 difference in the second moment PSF parameters, and do not impact the cosmological prediction.

We found a spin-2 quantity consisting of PSF fourth moments in Section 4.4.3. Therefore, a logical generalization of the PSF systematics formalism is to add and test for fourth moment leakage and modeling error terms as part of $g_{\rm sys}$. We also want to check the necessity of including a constant ellipticity parameter $e_c = e_{c,1} + ie_{c,2}$ in the formalism, to model the systematics from other sources that generate a non-zero mean shape in the catalog, other than that from the cosmic variance. Therefore, the full model for $g_{\rm sys}$ is

$$g_{\rm sys} = \alpha^{(2)} e_{\rm PSF} + \beta^{(2)} \Delta e_{\rm PSF} + \alpha^{(4)} M^{(4)}_{\rm PSF} + \beta^{(4)} \Delta M^{(4)}_{\rm PSF} + e_c. \tag{4.23}$$

Here $\alpha^{(2)}$ and $\beta^{(2)}$ are leakage and modeling error coefficients for second moments, and $\alpha^{(4)}$ and $\beta^{(4)}$ are comparable quantities for fourth moments. This formalism could in principle extend to all spin-2 quantities, including PSF sixth moments, and product of spin-0 and spin-2 quantities, etc. However, higher moments and higher order terms are increasingly noise dominated. In Appendix 4.E.2, we show that extending to sixth moments does not increase the overall estimated additive bias significantly, and therefore is not needed for HSC Y3. Similarly, we show in Appendix 4.E.3 that second order terms do not significantly contribute to additive shear biases for HSC Y3. However, we recommend that other surveys with more stringent requirement on systematics also test for the impact of these quantities when defining their PSF systematics model.

Since $g_{\rm sys}$ and $g_{\rm gal} + g$ are uncorrelated, the 2PCF of the observed galaxy shape is

$$\langle \hat{g}_{\rm gal} \hat{g}_{\rm gal} \rangle = \langle (g_{\rm gal} + g)(g_{\rm gal} + g) \rangle + \langle g_{\rm sys} g_{\rm sys} \rangle \,. \tag{4.24}$$

We focus on the last term, which is the additive shear contamination due to the PSF in the shear-shear 2PCF. To efficiently express $\langle g_{\rm sys} g_{\rm sys} \rangle$, we define the parameter vector $\boldsymbol{p} = [\alpha^{(2)}, \beta^{(2)}, \alpha^{(4)}, \beta^{(4)}, e_c]$, and define the PSF moments vectors $\boldsymbol{S} = [e_{\rm PSF}, \Delta e_{\rm PSF}, M^{(4)}_{\rm PSF}, \Delta M^{(4)}_{\rm PSF}, \mathbf{1}]$. Here $\boldsymbol{p}$ is a parameter set defined for the galaxy ensemble, while $\boldsymbol{S}$ is a set of PSF quantities that varies across the position on the sky. We include e_c in the PSF parameter vector to simplify the formalism for likelihood analysis. The expansion of $\langle g_{\rm sys} g_{\rm sys} \rangle$ from Eq. (4.23) becomes

$$\langle g_{\rm sys} g_{\rm sys} \rangle = \sum_{k=1}^{5} \sum_{q=1}^{5} \boldsymbol{p}_k \boldsymbol{p}_q \langle \boldsymbol{S}_k \boldsymbol{S}_q \rangle \tag{4.25}$$

Here the double summation includes the impact of (a) the 10 unique PSF-PSF correlation functions (p-p correlations), (b) the product of the mean shape systematic term e_c and mean PSF moments, and (c) the mean shape systematic term e_c itself. When two complex numbers are multiplied together, the complex conjugate must be used for one of them.

In Fig. 4.4.2, we show the p-p correlation functions between all PSF moment pairs in $\boldsymbol{S}$, for the PSF stars (solid lines) and non-PSF stars (dashed lines). We denote the moments of the PSF as "truth", and the difference expressed in Eq. (4.16) as "residual". The PSF and non-PSF samples are similar in truth-truth correlations. However, because the moment residuals are much larger for the non-PSF samples, all of the truth-residual and residual-residual correlations are significantly larger for the non-PSF stars.

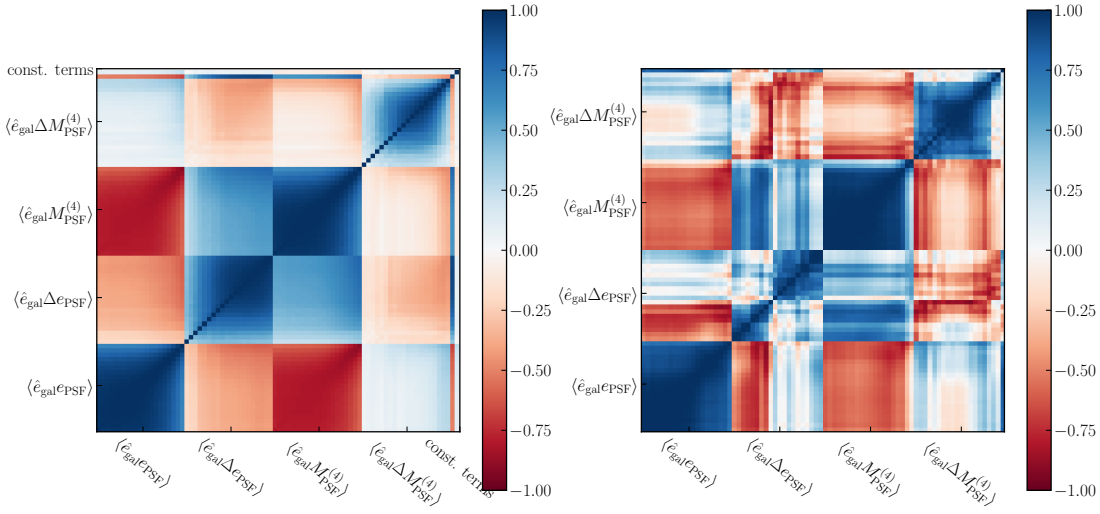

Figure 4.5.1: We show the correlation matrix of $\boldsymbol{D}_{gp}$ as defined in Eq. (4.34) in the left panel, and the correlation matrix of $\mathbf{K}(\boldsymbol{p})\boldsymbol{D}_{pp}$ in the right panel. We see that $\boldsymbol{D}_{gp}$ values at different angular scales are highly correlated, and there are significant anti-correlations between $\langle\hat{g}_{\rm gal}e_{\rm PSF}\rangle$ and $\langle\hat{g}_{\rm gal}M^{(4)}_{\rm PSF}\rangle$. $\mathbf{K}\boldsymbol{D}_{pp}$ across angular bins are also highly correlated for the correlation with the PSF truth. These significantly affect the outcome of the maximum-likelihood fitting process by penalizing cases where the theory data vector is such that the sign of $\boldsymbol{D}_{gp}-\boldsymbol{T}_{gp}$ differs across angular bins, or where the sign of $\boldsymbol{D}_{gp}-\boldsymbol{T}_{gp}$ is the same for $\langle\hat{g}_{\rm gal}e_{\rm PSF}\rangle$ and $\langle\hat{g}_{\rm gal}M^{(4)}_{\rm PSF}\rangle$. Notice that the correlation matrix of the p-p correlation is more noisy than that of the g-p data vector, because the former is calculated using the jackknife method, while the latter is calculated using a large number of the mock catalogs. We use the best-fitting parameters of the "4+c" model (listed in Table 4.5.1) to construct the correlation matrix of $\mathbf{K}(\boldsymbol{p})\boldsymbol{D}_{pp}$. On average, the covariance matrix from the p-p correlation contributes about 20% of $\boldsymbol{\Sigma}_{gp}$ to the total covariance matrix $\tilde{\boldsymbol{\Sigma}}_{gp}(\boldsymbol{p})$ at the best-fitting parameters of the fiducial model, introduced in Section 4.5.2.

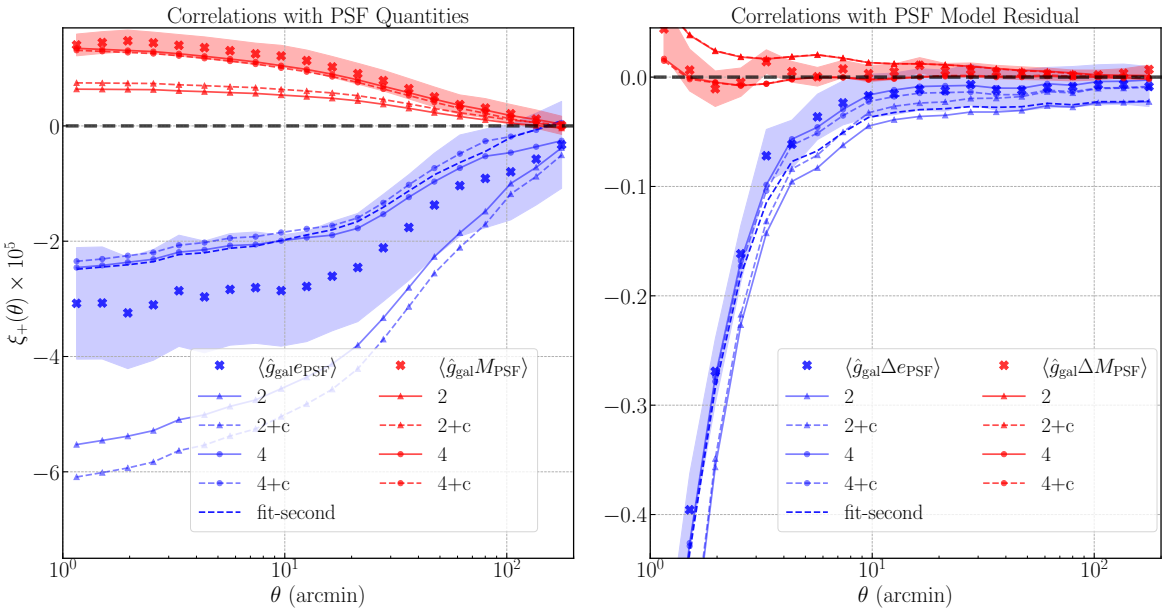

Figure 4.5.2: The correlations functions of galaxy shapes with PSF quantities (left panel, Eqs. 4.26 and 4.28) and with PSF modeling residuals (right panel, Eqs. 4.27 and 4.29) and the best-fitting PSF systematics models for the PSF stars. The correlations between the Y3 star catalog and shape catalog are shown as "x", with the shaded region representing the 1σ uncertainty. The best-fitting correlations from the models are shown in the solid and dashed lines, where the quantity being modelled is reflected by the color. "2" means that the model only includes second moments leakage and modeling error terms, "+c" means that the model includes the constant galaxy shape term, and "4" stands for the fiducial model, which includes both the PSF second and fourth moments. All models are fitted to all four galaxy-PSF correlation functions and to the average galaxy shape, except for "fit-second", which only fits to $\langle \hat{g}_{\rm gal} e_{\rm PSF} \rangle$ and $\langle \hat{g}_{\rm gal} \Delta e_{\rm PSF} \rangle$.

4.5.2 Building a Data-Driven PSF Systematics Model

In this section, we use data-driven approaches to define the PSF systematics model. In Section 4.5.2, we use the galaxy-PSF correlation as an observable to infer the posterior of the PSF parameter, by building models to predict galaxy-PSF correlations with the formalism in Section 4.5.1. In Section 4.5.2, we define the full models and their submodels, as well as the traditional second-moment-only model for comparison. In Section 4.5.2, we discuss the difference between PSF and non-PSF results. In Section 4.5.2, we show the impact on cosmological observable by the PSF systematics.In Section 4.5.2, we describe our model selection criteria.

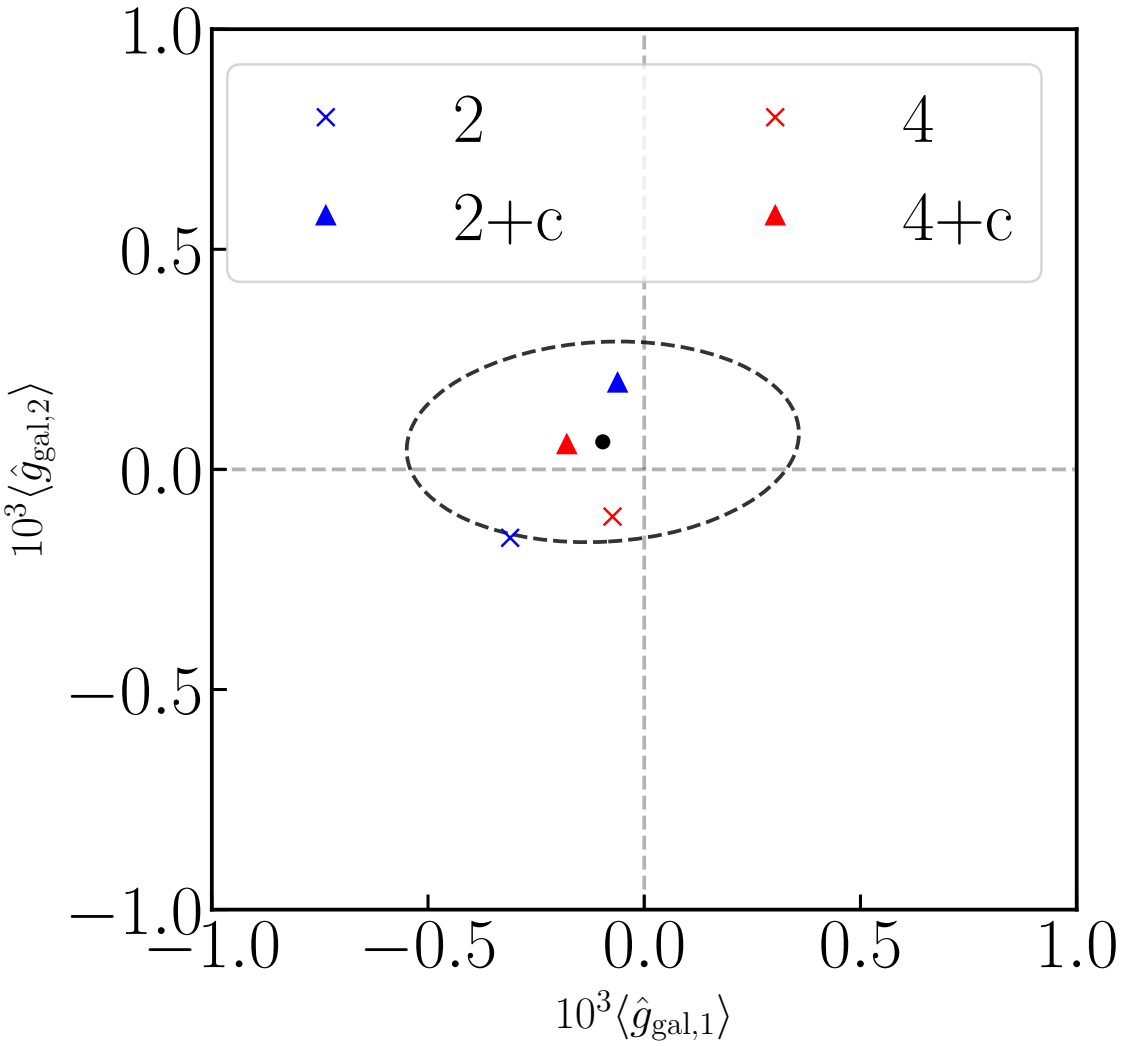

Figure 4.5.3: The dot shows the average galaxy shape $\langle\hat{g}_{\rm gal,1}\rangle$ and $\langle\hat{g}_{\rm gal,2}\rangle$, and its 1σ contour estimated using the Y3 mock catalog. The crosses and triangles show the best-fitting $\langle\hat{g}_{\rm gal,1}\rangle$ and $\langle\hat{g}_{\rm gal,2}\rangle$ predicted by Eq. (4.30), for the models labeled using the same notation as in Fig. 4.5.2.

Galaxy-PSF Cross Correlation and Model Fitting

Cross correlating galaxy and PSF spin-2 components is a common approach to identifying and quantify additive PSF systematics. When used for identifying systematics, these calculations are referred to as "null tests" (e.g., 54; 89). The PSF-PSF correlations are referred to as the ρ statistics. Here we employ galaxy-PSF correlation (g-p correlation) for two purposes: (a) identifying the contamination from PSF leakage and modeling error on weak lensing shears, and (b) quantifying the prior on any PSF systematics parameters that need

to be included in the cosmological likelihood analysis.

We cross-correlate galaxy shapes with the PSF spin-2 quantities and their residuals, both from second and fourth moments, and the constant systematics term. Since the true correlation between the galaxy's intrinsic shape and shear with any PSF moment $M_{\rm PSF}$ should be zero, we can assume that $\langle \hat{g}_{\rm gal} M_{\rm PSF}\rangle = \langle g_{\rm sys} M_{\rm PSF}\rangle$. Therefore, the cross-correlation between $\hat{g}_{\rm gal}$ in Eq. (4.21) and PSF moments in Eq. (4.23) becomes

$$\begin{aligned}
\langle \hat{g}_{\rm gal} e_{\rm PSF}\rangle &= \alpha^{(2)}\langle e_{\rm PSF} e_{\rm PSF}\rangle + \beta^{(2)}\langle \Delta e_{\rm PSF} e_{\rm PSF}\rangle + \alpha^{(4)}\langle M^{(4)}_{\rm PSF} e_{\rm PSF}\rangle \\
&\quad + \beta^{(4)}\langle \Delta M^{(4)}_{\rm PSF} e_{\rm PSF}\rangle + e_c\langle e_{\rm PSF}\rangle \qquad (4.26)\\
\langle \hat{g}_{\rm gal} \Delta e_{\rm PSF}\rangle &= \alpha^{(2)}\langle e_{\rm PSF} \Delta e_{\rm PSF}\rangle + \beta^{(2)}\langle \Delta e_{\rm PSF} \Delta e_{\rm PSF}\rangle + \alpha^{(4)}\langle M^{(4)}_{\rm PSF} \Delta e_{\rm PSF}\rangle \\
&\quad + \beta^{(4)}\langle \Delta M^{(4)}_{\rm PSF} \Delta e_{\rm PSF}\rangle + e_c\langle \Delta e_{\rm PSF}\rangle \qquad (4.27)\\
\langle \hat{g}_{\rm gal} M^{(4)}_{\rm PSF}\rangle &= \alpha^{(2)}\langle e_{\rm PSF} M^{(4)}_{\rm PSF}\rangle + \beta^{(2)}\langle \Delta e_{\rm PSF} M^{(4)}_{\rm PSF}\rangle + \alpha^{(4)}\langle M^{(4)}_{\rm PSF} M^{(4)}_{\rm PSF}\rangle \\
&\quad + \beta^{(4)}\langle \Delta M^{(4)}_{\rm PSF} M^{(4)}_{\rm PSF}\rangle + e_c\langle M^{(4)}_{\rm PSF}\rangle \qquad (4.28)\\
\langle \hat{g}_{\rm gal} \Delta M^{(4)}_{\rm PSF}\rangle &= \alpha^{(2)}\langle e_{\rm PSF} \Delta M^{(4)}_{\rm PSF}\rangle + \beta^{(2)}\langle \Delta e_{\rm PSF} \Delta M^{(4)}_{\rm PSF}\rangle + \alpha^{(4)}\langle M^{(4)}_{\rm PSF} \Delta M^{(4)}_{\rm PSF}\rangle \\
&\quad + \beta^{(4)}\langle \Delta M^{(4)}_{\rm PSF} \Delta M^{(4)}_{\rm PSF}\rangle + e_c\langle \Delta M^{(4)}_{\rm PSF}\rangle. \qquad (4.29)
\end{aligned}$$

Here the correlation functions on the left-hand-side (LHS) of the equations are what we call "galaxy-PSF correlations" (g-p correlations), and the correlation functions on the right are "PSF-PSF correlations" (p-p correlations). Additionally, we check if the average galaxy shape in the catalog follows the model

$$\begin{aligned}
\langle \hat{g}_{\rm gal}\rangle &= \alpha^{(2)}\langle e_{\rm PSF}\rangle + \beta^{(2)}\langle \Delta e_{\rm PSF}\rangle + \alpha^{(4)}\langle M^{(4)}_{\rm PSF}\rangle \\
&\quad + \beta^{(4)}\langle \Delta M^{(4)}_{\rm PSF}\rangle + e_c. \qquad (4.30)
\end{aligned}$$

In this work, we measure the p-p and g-p correlations in 20 angular bins from 1-200 arcmin. The range of angular bins was defined so that it covers the scales used from the HSC Y1 cosmic shear analyses, while also ensuring the small scales are not affected by blending. The upper scale cuts are extended to 200 arcmin to provide more constraining power on the PSF parameters. The data vector $\boldsymbol{D}_{gp} = [\langle \hat{g}_{\rm gal} e_{\rm PSF}\rangle, \langle \hat{g}_{\rm gal}\Delta e_{\rm PSF}\rangle, \langle \hat{g}_{\rm gal} M^{(4)}_{\rm PSF}\rangle, \langle \hat{g}_{\rm gal}\Delta M^{(4)}_{\rm PSF}\rangle, \langle \hat{g}_{\rm gal}\rangle]$, with 82 data points in total, is fitted by the theory data vector $\boldsymbol{T}_{gp}(\boldsymbol{p})$ predicted from Eqs. (4.26)–(4.30), by maximizing the log-likelihood function

$$\log(\mathcal{L}(\boldsymbol{p}|\boldsymbol{D}_{gp})) \propto -\frac{1}{2}\chi^2 - \frac{1}{2}\log(\det(\tilde{\boldsymbol{\Sigma}}_{gp})), \qquad (4.31)$$

where

$$\chi^2 = (\boldsymbol{D}_{gp} - \boldsymbol{T}_{gp}(\boldsymbol{p}))^T \tilde{\boldsymbol{\Sigma}}^{-1}_{gp}(\boldsymbol{p})(\boldsymbol{D}_{gp} - \boldsymbol{T}_{gp}(\boldsymbol{p})). \qquad (4.32)$$

Here $\tilde{\boldsymbol{\Sigma}}^{-1}_{gp}(\boldsymbol{p})$ is the parameterized inverse covariance matrix that includes the Gaussian covariance matrix of the p-p correlation functions

$$\tilde{\boldsymbol{\Sigma}}_{gp}(\boldsymbol{p}) = \boldsymbol{\Sigma}_{gp} + \mathbf{K}(\boldsymbol{p})\boldsymbol{\Sigma}_{pp}\mathbf{K}(\boldsymbol{p})^T. \qquad (4.33)$$

$\boldsymbol{\Sigma}_{gp}$ is the covariance matrix of $\boldsymbol{D}_{gp}$ computed using the HSC Y3 mock catalog described in Section 4.3.2, $\boldsymbol{\Sigma}_{pp}^{-1}$ is the covariance matrix of the p-p correlation vector $\boldsymbol{D}_{pp}$, which consists the p-p correlation functions ordered in the reading order of the RHS of Eq. (4.26)–(4.29). $\mathbf{K}(\boldsymbol{p})$ is the linearized transformation matrix of the RHS of Eq. (4.26)–(4.29). By having a parameterized covariance matrix in the likelihood, we effectively marginalize over the uncertainty of the p-p correlation function (199). In Eq. (4.31), the second term comes from the normalizing factor in the Gaussian likelihood, which changes during the fitting because of the parameterized covariance matrix.

In Fig. 4.5.1, we show the correlation matrix $\mathrm{Cor}(\boldsymbol{D}_{gp})$ of $\boldsymbol{D}_{gp}$, where

$$\mathrm{Cor}(\boldsymbol{D}_{gp})[i][j] = \frac{\boldsymbol{\Sigma}_{gp}[i][j]}{\sqrt{\boldsymbol{\Sigma}_{gp}[i][i]\boldsymbol{\Sigma}_{gp}[j][j]}} \tag{4.34}$$

in the left panel, and the correlation matrix of $\mathbf{K}(\boldsymbol{p})\boldsymbol{D}_{pp}$ at the right panel. The elements in the covariance matrix contributed by the p-p correlation $\mathbf{K}(\boldsymbol{p})\boldsymbol{\Sigma}_{pp}\mathbf{K}(\boldsymbol{p})^T$ are typically 20% of $\boldsymbol{\Sigma}_{gp}$ at the best-fitting parameters of fiducial model, introduced in Section 4.5.2. Therefore these are not negligible in the model fitting.

By maximizing Eq. (4.31), we get the best-fitting value of the parameters $\boldsymbol{p}$. We also used Markov Chain Monte Carlo (MCMC), implemented in EMCEE (186), to measure the posterior of the PSF parameters $P(\boldsymbol{p}|\boldsymbol{D}_{gp})$. The priors on all PSF systematics parameters are flat from $-\infty$ to $+\infty$.

Model Definition

Now we define the models we included in the model fitting and selection, assuming the PSF parameters are independent of the tomographic bins. The full model ("4+c") includes all 6 parameters in $\boldsymbol{p}$. We define sub-models by setting some parameters in $\boldsymbol{p}$ to zero while still fitting the entire data vector $\boldsymbol{D}_{gp}$. The fiducial model ("4") is a sub-model that only includes the first four parameters in $\boldsymbol{p}$; later in this section, we explain the statistical criteria used to identify this model as the fiducial one. The second-moments-only model, denoted as "2", only has the first two parameters in $\boldsymbol{p}$. The "2+c" model adds the e_c parameters to the second-moments-only model. The "4", "2" and "2+c" are all sub-models of the full model "4+c", defined in Eq. (4.26)–(4.30).

The "fit-second" model is not a sub-model of the full model: in particular, this corresponds to taking the "2" model and only fitting it to the second moment g-p correlations. The "fit-second" model is a logical choice if the fourth moment g-p correlation is ignored in the null testing. We introduced "fit-second" because it mirrors what was done in past shear analyses that did not consider fourth moments.

We validated our statistical inference on the PSF parameters by adding PSF shear bias to the mock catalog with known PSF parameters, and attempted to recover the PSF parameters through our inference. This process is described in Appendix 4.D.

PSF and non-PSF stars

We carried out the same analysis, now using the non-PSF stars. Since the PSF star sample shows that the models with only second moment leakage and modeling error cannot predict the galaxy shape correlations with PSF fourth moments, and the constant terms are later deemed unnecessary, we only used the fiducial model and the fit-second model. The p-values of these models as applied to the non-PSF star correlation functions are also included in Table 4.5.1. The fiducial model still performs well for the non-PSF star sample, as well as the fit-second model fitted to the g-p correlations with the second moments of the non-PSF stars.

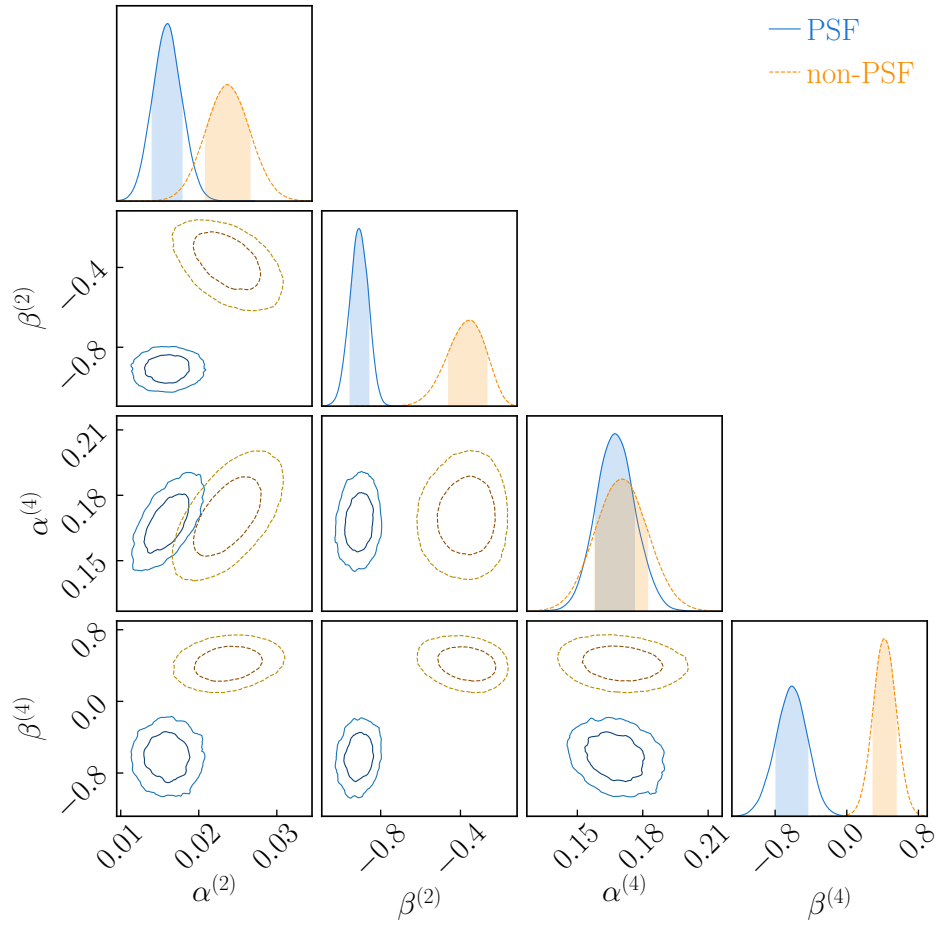

Figure 4.5.4: The posterior of the PSF systematics model parameters for the fiducial model, using the PSF and non-PSF stars as indicated in the legend. The PSF stars provide significantly larger estimates for both $\beta^{(2)}$ and $\beta^{(4)}$, which could be explained by the overfitting of the PSF model.

In Fig. 4.5.4, we show the PSF parameter posteriors for our fiducial model, for the PSF and non-PSF stars. The best-fitting parameters and their errorbars are shown in Table 4.5.1.

We see that the results from the two datasets provide statistically consistent values for $\alpha^{(4)}$, but inconsistent ones for $\alpha^{(2)}$, $\beta^{(2)}$ and $\beta^{(4)}$. Overall, the inconsistency between the PSF and non-PSF results is 8.2σ, ignoring the correlation between the two results. The mismatch of the β values can be explained by the overfitting of the PSF model: Fig. 4.4.1 shows that the second moment residual is overfitted by a factor of ~ 2, which means the $\Delta e_{\rm PSF}$ of the PSF stars are underestimated by a factor of 2. To compensate for this in the model fitting, the underestimation of $\Delta e_{\rm PSF}$ gives rise to a $\beta^{(2)}$ for PSF stars ~ 2 times larger than the one for non-PSF stars, as $g_{\rm sys}$ is ultimately the source of the inferred β values. In other words, we are fitting to correlation functions that carry information about the true systematic uncertainties in the galaxy shears, and hence using a star sample that underestimates the magnitude of $\Delta e_{\rm PSF}$ leads to a correspondingly higher value for β but effectively the same actual $\Delta\xi_+$ (which is the product of the two factors). The inconsistency in the $\alpha^{(2)}$ values is roughly 1.7σ, without considering the potential correlation between the two results. Next we will directly demonstrate that the two samples nonetheless predict a consistent impact on cosmic shear.

Impact on Cosmic Shear

With the best-fitting value and uncertainty contour for $\boldsymbol{p}$ for each model, we can also predict the impact on cosmic shear by the PSF systematics as a whole, expressed in Eq. (4.25). In Fig. 4.5.5, we show the additive bias on cosmic shear $\Delta\xi_+$, defined in Eq. (4.25), predicted by these models. In the upper panel, we compare the $\Delta\xi_+$ predicted by different models fitted to the galaxy shape correlations with PSF star moments. The traditional "fit-second" model omits the g-p correlation functions with PSF fourth moments and residuals, and its $\Delta\xi_+$ is therefore underestimated by up to an order of magnitude, which is significant. Although "2" and "2+c" predict a similar magnitude for $\Delta\xi_+$ as "4" and "4+c", they fail to fit the g-p correlations, according to Fig. 4.5.2 and Table 4.5.1, and thereby are suboptimal. The difference between the full model and the fiducial model is insignificant in terms of $\Delta\xi_+$, compared to the statistical uncertainty of the shear-shear 2PCF. Therefore, we can drop the e_c parameters in the HSC Y3 cosmic shear analysis. In the lower panel, we compare the $\Delta\xi_+$ predicted using PSF versus non-PSF stars, for the fiducial and fit-second model. We notice that the $\Delta\xi_+$ predicted by the fiducial model is very similar for both star samples, while there is a larger discrepancy between $\Delta\xi_+$ predicted using the fit-second model fits to the PSF and non-PSF stars. This is because, when including fourth moments, the PSF and non-PSF stars' predicted $\Delta\xi_+$ is dominated by the fourth moment leakage, which (unlike second order modeling error terms) is less affected by the difference between PSF and non-PSF stars.

For reference, we also plotted the statistical uncertainty of the shear-shear auto-correlation function predicted for the HSC Y3 cosmic shear analysis, and computed the statistical significance of the PSF systematics bias by

$$b^i = \sqrt{\Delta\xi_+^T \Sigma_{ii}^{-1} \Delta\xi_+}. \tag{4.35}$$

Here Σ_{ii}^{-1} is the estimated covariance matrix of the shear-shear auto correlation function of

bin i. We find the statistical significance of the additive shear systematics for our fiducial model from bins $1-4$ to be $1.74, 1.10, 0.66, 0.42$ for the PSF stars, and $2.03, 1.27, 0.75, 0.49$ for the non-PSF stars. Overall, the statistical significance for all 10 xi_+^{ij} is 2.0σ for the PSF stars, and 2.3σ for the non-PSF stars. Note that the statistical significance here might not directly correspond to the bias on the cosmological parameters. Rather, serves as an approximate indicator for the significance of the PSF systematics.

Model Comparison

Here we show the model fitting results and describe the methodology to select among the models.

In Fig. 4.5.2, we show the galaxy-PSF correlation functions (LHS of Eq. (4.26)–(4.29)) with their 1-σ uncertainties. The correlations with PSF quantities are shown in the left panel (second and fourth moments in blue and red, respectively), and the correlations with PSF model residuals are shown. Fig. 4.5.3 shows the average galaxy shape in the right panel. The 1-σ uncertainty of $\boldsymbol{D}_{gp}$ as assessed using mock catalogs (including cosmic variance) is shown with shaded regions for the correlation functions and an ellipse for $\langle\hat{g}_{\rm gal}\rangle$.

The best-fitting theory vectors $\hat{\boldsymbol{T}}_{gp}$ in Fig. 4.5.2 show that both the full model ("4+c") and the fiducial model ("4") can fit the data vectors within 1-σ in the full angular range from 1-200 arcmin. The models involving only second moments ("2" and "2+c") cannot fit the g-p correlations with PSF second moments and residuals nearly as well. The "fit-second" model also fits the second moment correlations well. All the models fit the average shape $\langle\hat{g}_{\rm gal}\rangle$ within 1-σ, as shown in Fig. 4.5.3.

We measure the goodness of fit using p-values, assuming the number of degrees of freedom is $82-k$, where k is the number of model parameters, and 82 is the length of $\boldsymbol{D}_{\rm gp}$. The p-values are shown in Table 4.5.1. A p-value over 0.05 is considered a good fit to the data, and our results show that we need to include the fourth moments explicitly ("4" or "4+c") to fit all g-p correlations.

Ultimately, we use the impact on the cosmic shear data vector to select which model we should use. The most efficient model should include the minimum number of parameters needed to capture most of the contamination to ξ_+. In our case, the statistical significance of the estimated contamination changed from 0.7σ for the second-moment model to 2.0σ for the fiducial model, with only two additional parameters. Therefore, the fiducial model is our preferred choice, so as to avoid underestimating the additive systematics by more than a factor of two. In Appendix 4.E.2 and Appendix 4.E.3, we will see that none of the sixth-order moments or second-order terms can contribute enough additive bias to be worth using.

4.5.3 Redshift Dependency

In this section, we discuss the necessity of including redshift dependence in our PSF systematics model. In principle, a dependence on redshift could arise because the PSF leakage and modeling error parameters $[\alpha^{(2)}, \beta^{(2)}, \alpha^{(4)}, \beta^{(4)}]$ may depend on the ensemble galaxy proper-

Sample	Model	$\alpha^{(2)}$	$\beta^{(2)}$	$\alpha^{(4)}$	$\beta^{(4)}$	$e_{\rm c,1} \times 10^4$	$e_{\rm c,2} \times 10^4$	p-value
PSF	"2'	-0.022 ± 0.002	-1.08 ± 0.06	0	0	0	0	0.0
	"2+c"	-0.023 ± 0.002	-1.09 ± 0.06	0	0	2 ± 2	3 ± 1	0.0
	"4"	0.016 ± 0.002	-0.88 ± 0.05	0.17 ± 0.01	-0.6 ± 0.2	0	0	0.92
	"4+c"	0.016 ± 0.002	-0.88 ± 0.05	0.17 ± 0.01	-0.6 ± 0.2	-1 ± 2	2 ± 1	0.54
	"fit-second"	-0.007 ± 0.002	-0.83 ± 0.05'	0	0	0	0	0.72
non-PSF	"4"	0.024 ± 0.003	-0.4 ± 0.1	0.17 ± 0.01	0.4 ± 0.1	0	0	0.84
	"fit-second"	-0.004 ± 0.002	-0.4 ± 0.1	0	0	0	0	0.78

Table 4.5.1: The best-fitting parameters, p-value of the models fitted to galaxy-PSF correlation functions in a single redshift bin (no tomography). A p-value indicates the probability that the data may be a random realization of the model given the uncertainties, and a threshold of 0.05 is commonly adopted. The models are defined in Section 4.5.2. The "4+c" model is the parent model among the first four models. The second-moment models ("2" and "2+c") failed when fitted to all g-p correlations, but provide an acceptable fit to the second moments' g-p correlation functions on their own ("fit-second").

Sample	Bin	$\alpha^{(2),\mathrm{i}}$	$\beta^{(2),\mathrm{i}}$	$\alpha^{(4),\mathrm{i}}$	$\beta^{(4),\mathrm{i}}$	p-value
PSF stars	1	0.014 ± 0.002	-0.5 ± 0.1	0.16 ± 0.01	0.1 ± 0.7	
	2	0.023 ± 0.002	-0.8 ± 0.2	0.18 ± 0.01	-0.7 ± 0.6	0.91
	3	0.014 ± 0.003	-1.0 ± 0.2	0.17 ± 0.02	-0.9 ± 0.5	
	4	0.014 ± 0.004	-1.3 ± 0.3	0.20 ± 0.02	-0.3 ± 0.75	
	all	0.018 ± 0.002	-0.86 ± 0.06	0.176 ± 0.007	-0.2 ± 0.1	0.28
non-PSF stars	1	0.023 ± 0.004	-0.4 ± 0.1	0.16 ± 0.013	0.2 ± 0.3	
	2	0.028 ± 0.004	-0.3 ± 0.1	0.16 ± 0.013	0.5 ± 0.2	0.63
	3	0.018 ± 0.005	-0.0 ± 0.1	0.14 ± 0.016	0.9 ± 0.3	
	4	0.020 ± 0.007	-0.1 ± 0.2	0.17 ± 0.021	1.4 ± 0.3	
	all	0.022 ± 0.002	-0.17 ± 0.06	0.156 ± 0.008	0.57 ± 0.1	0.12

Table 4.5.2: The best-fitting parameters, p-values of the models fitted to the set of g-p correlation function across all tomographic bins. The first section shows the best-fitting parameters and the p-values using the PSF stars, while the second section shows the results for the non-PSF stars. The last line of each section shows the results for a redshift-independent model that was fitted to the tomographic data vector. The results show a mild preference for the redshift-dependent model, but the redshift-independent model cannot be ruled out.

ties, e.g., galaxy size, Sérsic index distribution (70), which vary across tomographic bins. In past work in DES (154), the redshift dependence of the PSF systematics model parameters was investigated for the second moments model. Although the overall level of PSF systematics in that work is small, the redshift dependence of the parameters was found to be statistically significant.

We investigated the redshift dependency of our model by joint fitting all the g-p correlations and average galaxy shape per bin by defining one set of parameters $\boldsymbol{p}^i = [\alpha^{(2),\mathrm{i}}, \beta^{(2),\mathrm{i}}, \alpha^{(4),\mathrm{i}}, \beta^{(4),\mathrm{i}}]$ for each tomographic bins, where i stands for the tomographic bin index from 1-4. The redshift-dependent data vector $\boldsymbol{D}^z_{gp} = [\langle \hat{g}^1_{\mathrm{gal}} e_{\mathrm{PSF}} \rangle, \ldots, \langle \hat{g}^1_{\mathrm{gal}} \Delta M^{(4)}_{\mathrm{PSF}} \rangle, \langle \hat{g}^2_{\mathrm{gal}} e_{\mathrm{PSF}} \rangle, \ldots,$ $\langle \hat{g}^2_{\mathrm{gal}} \Delta M^{(4)}_{\mathrm{PSF}} \rangle, \ldots, \langle \hat{g}^4_{\mathrm{gal}} \Delta M^{(4)}_{\mathrm{PSF}} \rangle, \langle \hat{g}^1_{\mathrm{gal}} \rangle, \ldots, \langle \hat{g}^4_{\mathrm{gal}} \rangle]$, which has a total length of $4{\times}4{\times}20{+}4{\times}2 = 328$. The parameter set $\boldsymbol{p}^z = [\alpha^{(2),1}, \ldots, \beta^{(4),1}, \alpha^{(2),2}, \ldots, \beta^{(4),2}, \ldots, \beta^{(4),4}]$, which has a total length of 16. We call this the "redshift-dependent fiducial model". We conducted the joint fitting rather than fitting the data separately in each tomographic bin to account for the covariance between the tomographic bins. In Fig. 4.5.6, we showed the correlation matrix of $\boldsymbol{D}^z_{gp}$ and found the correlation between the tomographic bins are significant. For the redshift-dependent model, we use angular scales from 2-200 arcmin, because including the smaller angular scales will result in the model fits to non-PSF stars failing the p-value test. In comparison, we also fit a "redshift-independent" model to the same data vector $\boldsymbol{D}^z_{gp}$, by enforcing the PSF parameters to be the same across the 4 tomographic bins.

In Fig. 4.5.7, we show the g-p correlations of the four tomographic bins of the HSC Y3 shape catalog (160), and their best-fitting values according to the redshift-dependent fiducial model, using the PSF stars. The 1d marginal posteriors for the PSF parameters are shown in Fig. 4.5.8. The best-fitting parameters, p-values fitted using both PSF and non-PSF stars

are listed in Table 4.5.2. We see a slight statistical significance in the redshift-dependency in the PSF parameters, especially with the decreasing trend of $\beta^{(4)}$ with redshift. However, the redshift-independent model also has an acceptable p-value, while significantly decreasing the number of parameters needed to model PSF systematics, which is a practical issue of some importance. For this reason, we will want to use mock cosmic shear analyses to quantitatively assess the model performance for the simpler model and determine whether it is acceptable, even if not statistically preferred.

The impact on the cosmic shear 2PCF in bin-i and bin-j predicted by the redshift-dependent model is

$$\Delta\xi_+^{ij} = \sum_{k=1}^{4}\sum_{q=1}^{4} \boldsymbol{p}_k^i \boldsymbol{p}_q^j \langle \boldsymbol{S}_k \boldsymbol{S}_q \rangle \tag{4.36}$$

In Fig. 4.5.9, we show the impact on the cosmic shear auto-correlation functions in tomographic bins due to the PSF systematics, fitted by PSF stars, comparing the redshift-dependent model (colored lines) versus the redshift-independent model (black points). We also show the statistical uncertainty of the HSC Y3 cosmic shear ξ_+, which is predicted by the covariance matrix used in Section 4.6.2. We also show the redshift-independent model fitted to the tomographic g-p correlations in black circles for PSF stars and black triangles for the non-PSF stars. The $\Delta\xi_+^{ii}$ from bin 1 to 3 are statistically consistent with each other, but the bin 4 correlation is significantly higher than the others (in absolute value, not in its ratio to the cosmic shear signal). For the non-PSF stars, the predictions for $\Delta\xi_+^{ii}$ increase gradually with redshift from bin 1 to 3, and likewise increase quite sharply for bin 4, probably due to the fact that bin 4 has the largest $\alpha^{(4)}$ and $\beta^{(2)}$. To avoid overcrowding the plot, we do not show the lines for non-PSF stars. The redshift-independent models predict equal $\Delta\xi_+$ for all tomographic bin-pairs. Evaluating the model at its best-fitting parameters yields to a prediction for $\Delta\xi_+$ comparable to the amplitude of the redshift-dependent prediction from bin 1 to bin 3, while underestimating the $\Delta\xi_+$ for bin 4 by a factor of ~ 2.

Overall, the prediction of $\Delta\xi_+^{ii}$s by the redshift-dependent model are not statistically consistent with each other across tomographic bins. However, modeling the redshift dependence by assigning a separate set of parameters to each tomographic bin will significantly increase the number of PSF parameters from 4 to 16. While the redshift-independent model remains competitive in terms of p-value (see Table 4.5.2), we think the redshift-independent is still a potentially acceptable model of choice for the HSC Y3 analysis. Whether modeling the redshift dependency is worth increasing the number of nuisance parameters by 12 should be determined based on the impact on the cosmological results, which is inferred in Section 4.6.2.

An option to model the redshift dependence of the PSF systematics in shear without a drastic increase in the number of model parameters is to introduce parametrized models for the redshift dependence of selected PSF parameters. For example, based on our results for HSC Y3 analysis, a reasonable choice might be to model $\beta^{(2)}(z^i)$ as $\beta_0^{(2)} f_1(z)$, where $f_1(z)$ is a simple single-parameter function of redshift. Another option is to subtract the mean redshift-dependent $\Delta\xi_+^{ij}$ the cosmic shear data vector, and model a few principal components

of the uncertainty of the parameters. However, this approach relies on the assumption that the uncertainties of the PSF parameters are highly correlated with each other, so that a principal component analysis can be effective.

4.6 Cosmological Impact

In this section, we test the impact of the new PSF systematics model described in Section 4.5 in cosmological analyses. In Section 4.6.1, we present a re-analysis of HSC Y1 cosmic shear, using the Y1 cosmic shear data vector, covariance matrix, and redshift distribution from (1). In Section 4.6.2, we present a mock cosmological analysis for HSC Y3 cosmic shear using a noiseless mock data vector and covariance, and the galaxy-PSF correlations from the real HSC Y3 star and shape catalogs described in Section 4.4.1 and Section 4.3.

4.6.1 HSC Y1 Re-analysis

For the re-analysis of HSC Y1 cosmic shear, we adopted the cosmic shear 2PCF $\boldsymbol{\xi}_{\pm}$, its covariance matrix $\mathbf{\Sigma_{Y1}}$, and the redshift distribution of the four tomographic bins from (1)[4]. We built the forward model for the data vectors, including cosmological and astrophysical modeling choices, in CosmoSIS (200).

The choices of the cosmological model and the priors on the parameters are made to be as close as possible to those of (1). The only difference is that we marginalize over the multiplicative bias for each tomographic bin, instead of using one nuisance parameter for m. Here we briefly review the settings. We used CAMB (201; 202; 203) to compute the linear matter power spectrum, and HALOFIT (204) to compute the non-linear matter power spectrum. The optical depth τ was set to 0.0561, and neutrino mass was set to 0.06eV. The priors on the cosmological parameters are listed in the first section of Table 4.6.1.

Regarding the astrophysical and nuisance parameters of the re-analysis, we use the non-linear alignment model (NLA 205; 206) to model the intrinsic alignments (see 148, for the specification of the model). The prior on the NLA parameters $A_{\rm IA}$, η and z_0 are listed in the second section of Table 4.6.1. The priors on the multiplicative biases m^1–m^4 and the redshift uncertainty parameters Δz^1–Δz^4 are listed in the third section of Table 4.6.1. We use the same redshift distribution, astrophysical and systematics models and priors as (1).

We validate our forward modeling inference and model choices by comparing the cosmological parameter results when applying the same PSF systematics model as in (1). In (1), the fiducial model, which used the second-moment-only PSF systematics, results in the 68% confidence intervals[5] of $0.237 < \Omega_m < 0.383$ and $0.795 < S_8 < 0.855$. Our second moment model reports the 68% confidence interval of $0.253 < \Omega_m < 0.394$ and $0.795 < S_8 < 0.855$. There is a very small offset ($\sim 0.1\sigma$) on our Ω_m confidence interval, and the S_8 interval

[4] `http://th.nao.ac.jp/MEMBER/hamanatk/HSC16aCSTPCFbugfix/index.html`

[5] Slightly updated from the original version in an erratum, (207).

Parameter	Fiducial	Prior (Y1)	Prior (Y3)
$\log(A_s \times 10^9)$	0.322	$U[-1.5, 2.0]$	$U[-1.5, 2.0]$
Ω_b	0.0489	$U[0.038, 0.053]$	$U[0.038, 0.053]$
n_s	0.967	$U[0.87, 1.07]$	$U[0.87, 1.07]$
h_0	0.677	$U[0.64, 0.82]$	$U[0.64, 0.82]$
Ω_m	0.311	$U[0.039, 0.953]$	$U[0.039, 0.953]$
τ	0.0561	const.	const.
Ω_ν	0.06	const.	const.
w	-1.0	const.	const.
w_a	0.0	const.	const.
$A_{\rm IA}$	1.0	$U[-5, 5]$	$U[-5, 5]$
η	0.0	$U[-5, 5]$	$U[-5, 5]$
z_0	0.62	const.	const.
m^1	0.0	$\mathcal{N}(0.0086, 0.01)$	const.
m^2	0.0	$\mathcal{N}(0.0099, 0.01)$	const.
m^3	0.0	$\mathcal{N}(0.0241, 0.01)$	const.
m^4	0.0	$\mathcal{N}(0.0391, 0.01)$	const.
Δz^1	0.0	$\mathcal{N}(0, 0.0374)$	$\mathcal{N}(0, 0.012)$
Δz^2	0.0	$\mathcal{N}(0, 0.0124)$	$\mathcal{N}(0, 0.01)$
Δz^3	0.0	$\mathcal{N}(0, 0.0326)$	$\mathcal{N}(0, 0.018)$
Δz^4	0.0	$\mathcal{N}(0, 0.0343)$	$\mathcal{N}(0, 0.021)$

Table 4.6.1: The fiducial parameter values used to generate the mock data vector for the HSC Y3 cosmic shear mock analysis (described in Section 4.6.2), and priors for both the HSC Y1 re-analysis (described in Section 4.6.1) and Y3 mock analysis. $U[a, b]$ indicates a uniform distribution from a to b, while $\mathcal{N}(\mu, \sigma)$ indicates a Gaussian distribution with mean μ and standard deviation σ.

matches perfectly. We therefore conclude that our forward model is validated for the purpose of comparing the PSF systematics model.

In the re-analysis, we compared the original and our fiducial model PSF models for marginalizing the PSF systematics. We tested the model in (1) by adopting its prior and p-p correlations (ξ^{pp}, ξ^{pq}, and ξ^{qq}). We use our fiducial model to determine another set of priors for $\alpha^{(2)}$, $\beta^{(2)}$, $\alpha^{(4)}$, and $\beta^{(4)}$, using the HSC Y1 high-SNR star catalog described in (71). Both models lack a constant term. The priors used for both models are listed in Table 4.6.2. In addition, for the sake of comparison, we run another analysis with no correction for PSF systematics in shear.

In Fig. 4.6.1, we show the 2d contour and 1d errorbars in the Ω_m-S_8 plane for the HSC Y1 cosmic shear re-analysis. Our fiducial model reports $\Omega_m = 0.319^{+0.072}_{-0.071}$ and $S_8 = 0.824^{+0.030}_{-0.029}$. The analysis without any correction for PSF systematics shows that Ω_m would have been biased by 0.2σ if the PSF systematics is not modelled at all. The analysis using the PSF second moment-based model was able to remove 0.13σ from the bias, leaving 0.07σ

Param.	Original	Fiducial
$\alpha^{(2)}$	$\mathcal{N}(0.015, 0.05)$	$\mathcal{N}(0.035, 0.05)$
$\beta^{(2)}$	$\mathcal{N}(-0.7, 0.6)$	$\mathcal{N}(-0.67, 0.05)$
$\alpha^{(4)}$	$\mathcal{N}(0, 0)$	$\mathcal{N}(0.17, 0.02)$
$\beta^{(4)}$	$\mathcal{N}(0, 0)$	$\mathcal{N}(-0.32, 0.10)$

Table 4.6.2: The prior on the PSF parameters for the HSC Y1 re-analysis. The "Original" column presents the priors adopted in the original HSC Y1 cosmic shear analysis (1); when fitting with these priors, we also used the p-p correlations from that work. The 'Fiducial' column presents the priors on our extended PSF systematics model, which was applied to the p-p and p-q correlations for the HSC Y1 high-SNR star sample.

uncorrected. We use the effective number of parameters defined in (208)

$$n_{\rm eff} = 2\ln\mathcal{L}(\theta_p) - 2\langle\ln\mathcal{L}\rangle_\theta, \tag{4.37}$$

where $\mathcal{L}(\theta_p)$ is the posterior of the mean parameter θ_p, and $\langle\ln\mathcal{L}\rangle_\theta$ is the average posterior over the parameter space θ. The χ^2 values of the "no correction", second moment correction, and fiducial model correction are $160.3, 156.9, 143.7$, respectively. The effective degrees of freedom, $170 - n_{\rm eff}$, are $159.5, 159.4, 156.3$, respectively. The p-values are $0.47, 0.54, 0.76$, respectively – meaning that all models are nominally acceptable, presumably because the PSF systematics in shear are only a small contributor to the data vector that is being fit. Still, fiducial model obtains a substantially better fit while only increasing the number of parameters by ~ 2.

4.6.2 HSC Y3 mock analysis

Param.	Second moment	Fiducial
$\alpha^{(2)}$	$\mathcal{N}(-0.007, 0.002)$	$\mathcal{N}(0.016, 0.002)$
$\beta^{(2)}$	$\mathcal{N}(-0.85, 0.05)$	$\mathcal{N}(-0.91, 0.05)$
$\alpha^{(4)}$	$\mathcal{N}(0, 0)$	$\mathcal{N}(0.17, 0.01)$
$\beta^{(4)}$	$\mathcal{N}(0, 0)$	$\mathcal{N}(-0.6, 0.2)$

Table 4.6.3: The priors on the PSF systematics model parameters for the HSC Y3 mock analysis. "Second moment" model only fits the second moments galaxy-PSF correlations, setting the fourth moment parameters to zero. The fiducial model fits all the galaxy-PSF correlations with both second and fourth moments leakage and modeling error.

To study the impact of the PSF systematics modeling on the HSC Y3 cosmic shear analysis, we conducted a mock analysis that mimics the analysis scenario. The noise-free cosmic shear data vector is generated using the Planck cosmological parameters from (20) and astrophysical values listed in Table 4.6.1, without PSF contamination. We refer to this

parameter set the "fiducial cosmology". Then, mock PSF systematics are generated using the best-fitting parameters of the redshift-dependent fiducial model, described in Section 4.5.3,

$$\Delta\xi_+^{uv} = \sum_{i=1}^{4}\sum_{j=1}^{4} \boldsymbol{p}_i^u \boldsymbol{p}_j^v \langle S_i S_j \rangle, \tag{4.38}$$

where $\boldsymbol{p}_i^u$ takes the best-fitting values in Table 4.5.2. This PSF contamination term is added to the original noise-free data vector to generate a Y3 mock data vector. The priors on the cosmological, astrophysical, and nuisance parameters are listed in Table 4.6.1. The priors on the Y3 cosmological and astrophysical parameters are set to the same ranges as for Y1. The multiplicative biases are set to 0, while the photometric redshift uncertainty parameters take the Gaussian priors given in (209). We use the same scale cuts as the Y1 analysis, i.e., 7–56 arcmin for ξ_+ and 28–178 arcmin for ξ_-. The covariance matrix is estimated using $\boldsymbol{\Sigma}_{\rm Y3} = \boldsymbol{\Sigma}_{\rm Y1}/3$ to approximately account for the increase in survey area, while neglecting changes due to differences in survey edge effects. We use the redshift distributions and their priors estimated in (210), for which the marginalization method was validated in (209). Although the redshift distributions and their uncertainties are estimated in an earlier version of (210), and are likely to be slightly different in the actual Y3 analysis, they do not significantly impact our conclusion here. In the HSC Y3 cosmic shear analyses (5; 72), the scale cuts, covariance and some modeling choices are slightly different from the choice used for this test. However, they carried out the same mock analysis as was done here and found the same conclusion regarding the choice of the PSF systematics model.

In Fig. 4.6.2, we compare the results of using two different PSF systematics models in the Y3 mock analysis. The second moment correction model (in blue) only fits the Eqs. (4.26) and (4.27) using two free PSF parameters ($\alpha^{(2)}$ and $\beta^{(2)}$), setting the other parameters in those equations to 0. The fiducial model (in orange) uses the first four PSF parameters in $\boldsymbol{p}$, setting e_c to zero, and fits all of Eqs. (4.26)–(4.29). The priors on the PSF parameters, which are determined by carrying out our fitting process on the HSC Y3 shear and star catalogs, are listed in Table 4.6.3. Both models use the PSF stars for determining the prior and p-p correlations, as it is the better-understood sample of this work, with a larger sample size. In addition, we include the following two analyses: one with no PSF systematics added to the cosmic shear data vector and no attempt at PSF systematics correction, as a baseline; and one with PSF systematics added to the cosmic shear data vector, but with no attempt at correction, as the worst-case scenario. The input values of Ω_m and S_8 are shown as the dashed lines. The mean parameters of the analysis with no PSF systematics added to the data vector are shown in the solid vertical lines. The mean value of Ω_m in the "No Systematics" case is biased low compared to the true input value, even though this constraint is meant to be bias-free. We attribute this difference to the "projection effect" of the non-Gaussian posterior (e.g., see Section IV of 211).

To fully account for the uncertainty in the PSF systematics parameters, the fiducial model in this test accounts for the correlation between those parameters, by assuming the prior to be a 4D multivariate Gaussian. The details of modeling the correlated prior on PSF parameters are described in Appendix 4.F. We find no significant difference between

using an uncorrelated versus correlated prior. But for the sake of fully propagating the PSF systematic uncertainties, we recommend that the HSC Y3 analysis should use the correlated prior for the PSF parameters.

We can see that the second moments-only model barely corrected for the PSF systematics in shear, because it missed the leakage from the PSF fourth moments. The fiducial model comes closer to the baseline ("No Systematics"), although the correction overshoots the truth for Ω_m. This imperfect correction is likely because the fiducial model does not consider the redshift dependency in the real contamination. Compared to the "No Systematics" run, the PSF contamination causes a $+0.36\sigma$ bias on Ω_m, which the second moments correction does not remove; and the fiducial model over-corrects, resulting in a -0.06σ bias. For S_8, these effects are smaller: PSF systematics cause a bias of $+0.06\sigma$, while the second moment model overcorrects, resulting in a bias of -0.03σ, and the fiducial almost perfectly corrects the bias on S_8.

Regarding the errorbar size, the choice between the models shown here only affects the errorbars at the few-percent level, so this is not a significant factor in model selection.

We did not use the non-PSF stars to determine the contamination in this mock analysis, since the PSF stars provide better statistics for the p-p correlation functions. In a real analysis, if one uses the non-PSF stars to determine the prior and p-p correlation, the correction made by the second moment-only model will be even smaller than it was here, since $\Delta\xi_+$ is smaller for the non-PSF stars with the second moments model. For the fiducial model, we do not expect the cosmological results to change by much because the predicted $\Delta\xi_+$ for the PSF vs. non-PSF stars are similar for the fiducial model, shown in Fig. 4.5.2, due at least in part to the dominance of leakage rather than PSF modeling error.

4.7 Summary of Methodology

In this section, we summarize the process of building and selecting a PSF systematics model for a given cosmic shear survey, while we developed and tested this model with HSC Y3 data. This is a general approach that we recommend for any weak lensing survey, rather than being HSC-specific.

1. Build a star catalog with measured and residual moment measurements from second to higher moments, as described in Section 4.4.2. Care should be taken to ensure the purity of this sample, along with adoption of flag cuts and measures to avoid moment contamination due to blending in the images.

2. Derive the true and residual spin-2 combinations of those moments, as described in Section 4.4.3. (These can either be first order spin-2 quantities, or second order spin-2 quantities such as spin-0× spin-2, described in Section 4.E.3.)

3. Cross-correlate the spin-2 quantities in the star catalogs with the shear catalog, and conduct a likelihood analysis, including the following steps:

   (a) Estimate covariances through some method that includes relevant sources of uncertainty, including cosmic variance in the shears, and systematic variations in PSF properties across the sky.

   (b) Build the systematics model by assigning a parameter to each PSF spin-2 quantity, as explained in Section 4.5.1.

   (c) Define sub-models can be defined by putting very constraining priors on the parent model (Section 4.5.2).

   All models should be applied to the same set of galaxy-PSF cross correlations, as described in Section 4.5.2.

4. Define statistical criteria to distinguish the models. The preferred model should capture all of the additive systematic contamination to $\Delta\xi_+$ that is significant compared to their statistical uncertainty. This implies that, if a more complex model only changes the inferred $\Delta\xi_+$ insignificantly compared to the error budget, the simpler model should be selected. This is described in Section 4.5.2.

5. Test the robustness of the fiducial model by complicating it. These tests include:

   (a) testing and understanding the consistency between PSF and non-PSF stars (Section 4.5.2)

   (b) the redshift dependency of the model (Section 4.5.3)

   (c) other spin-2 quantities (Section 4.E.2 and Section 4.E.3)

   (d) impact on ξ_- (Section 4.E.1).

6. Conduct a mock cosmological analysis and confirm that the fiducial PSF systematics model can correct the bias to a level that satisfies the requirement of the given survey (Section 4.6.2).

4.8 Conclusions

The overall goal of this paper was to provide a general framework for describing additive weak lensing shear systematics due to the impact of PSF leakage and modeling error on inferred weak lensing shears. To do so, we defined a key concept underlying the PSF contamination in cosmic shear: this contamination is driven by spin-2 combinations of PSF moments (Section 4.4.3). In addition to PSF second moments, all even moments, e.g., fourth moments, contribute to PSF spin-2 quantities. The overall outline of our method is summarized in Section 4.7. To apply our method in a real-world scenario, we generated an HSC Y3 star catalog with higher moment measurement of the PSF and its modeling residuals, applying cuts to avoid contamination by galaxies and provide valid PSF and non-PSF star samples. We compared the moment residuals of the PSF and non-PSF stars, and concluded that the PSF model is overfitted for the HSC Y3 catalog.

Next, we defined a full PSF systematics model that considers PSF spin-2 quantity leakage from second and fourth moments, along with a constant shear systematics term (Section 4.5.2). Using the HSC Y3 galaxy and mock catalogs (Section 4.3) and the HSC Y3 star catalog with measurements of higher moments measurement (Section 4.4), we quantified the level of PSF contamination in cosmic shear data vector in Section 4.5.2 using that model. The full model can be considered to have nested models, each of which has a subset of the full model parameters set to zero. Our statistical metrics showed that a constant is not necessary in our particular case, but the second and fourth moments leakage and modeling errors are all impactful for cosmic shear. Therefore, our recommended fiducial model for the PSF systematics for HSC Y3 cosmic shear is a four parameters formula (Eq. (4.23) with $e_c = 0$).

In addition to the direct leakage and modeling error of the PSF fourth moments, we also investigated other possible contamination terms to $\xi_\pm$ from the PSF. These additional tests include the redshift dependency of the PSF contamination (Section 4.5.3), contamination to ξ_- (Appendix 4.E.1), contamination caused by moments higher than the fourth order (Appendix 4.E.2), and contamination caused by the second-order systematics (Appendix 4.E.3). These effects and additional contamination from the PSF are demonstrated to be subdominant in HSC Y3. Therefore, we do not recommend directly modeling them in the HSC Y3 cosmic shear analyses. However, we suggest that future surveys with different shear estimation methods and PSF modeling algorithms check for the importance of these effects, in case they become a significant contribution in a different setting.

Last but not least, we conducted a cosmological analysis to assess the impact of PSF systematics model selection on the cosmological results. We conducted a re-analysis on the HSC Y1 cosmic shear using our fiducial PSF systematics model, and obtain an cosmological results of $\Omega_m = 0.319^{+0.072}_{-0.071}$ and $S_8 = 0.824^{+0.030}_{-0.029}$. Both parameter are shifted from the original mean posterior by $< 0.1\sigma$. We produced a Y3-like mock data vector with redshift-dependent PSF systematics. This introduce a $+0.36\sigma$ bias on Ω_m, and $+0.06\sigma$ bias on S_8. After the correction by the fiducial PSF model, the bias is -0.06σ bias on Ω_m, and no bias on S_8, which means fiducial model is sufficient for HSC Y3. The second moment model is insufficient because the bias on Ω_m is $+0.36\sigma$ after correction.

There are several caveats in this work that are worth mentioning: (a) The cosmological mock analysis of the HSC Y3, which drives some of our conclusions, includes simple assumptions about the model for cosmological parameters and astrophysical systematics, redshift distributions, covariance, and scale cuts in relation to those from HSC Y1. These assumptions may not hold in the real Y3 analysis, though we do not think it will impact the overall conclusion. (b) In our prior for PSF systematics parameters for the mock and re-analysis, we do not consider correlations between the parameters. We leave such development to future work. (c) We do not consider a redshift-dependent PSF systematics model in the cosmological analysis, which might explain the imperfect correction made by the fiducial model in the mock analysis. We leave this implementation and its testing to future work. Note that these features do not affect the framework for modeling additive shear systematics that we have developed, and are simply limitations of how we applied it to HSC Y3.

This work motivates a few future studies: (a) This motivates other ongoing (DES, KiDS) and future (LSST, Roman, Euclid) weak lensing surveys to investigate the potential contamination by the PSF higher moments. As the survey area grows larger with the next generation of photometric surveys, the statistical uncertainties of both the shear-shear 2PCF (the error budget for the cosmological measurement) and the PSF-PSF/galaxy-PSF 2PCF (the detectability of systematics) will go down with the area, so the method will remain powerful for detecting the spin-2 leakage in shear signal. The depth increase of the Stage-IV surveys over the current surveys will increase the galaxy number density faster than the star number density, which can benefit this framework, as the uncertainty in the galaxy-PSF correlation functions for HSC Y3 is limited by the shape noise and cosmic variance. (b) Although we found that the PSF model of HSC Y3 is overfitting the PSF, we did not account for it by using non-PSF stars only, because there were too few of them to enable a study with reasonable uncertainties. A self-consistent selection of PSF stars in all exposures in the future data release will slightly increase the fraction of non-PSF stars in the catalog. (c) An extensive study of the PSF leakage from different shear estimation methods will be of interest for future weak lensing surveys, e.g., LSST and Euclid. Furthermore, a list of typical values of $\alpha^{(2)}$, $\beta^{(2)}$, $\alpha^{(4)}$, and $\beta^{(4)}$ will help translating the requirements on additive shear biases to the requirement on the image processing pipeline and PSF models, which is normally developed at an earlier stage of the survey, to increase the chances of meeting the ever more stringent requirement on shear systematics.

A final lesson learned from this work is that a systematic approach to null testing, including reliable uncertainty estimates, is a really important part of the validation for weak lensing analysis. The leading contributor to the PSF systematics in our case – the fourth moment leakage – was not previously considered as a potentially significant factor until the results of this work. With that said, any factor characterized as "minor" in this study, whether it is $\Delta\xi_-$, sixth moments, redshift dependency of the PSF contamination, or second-order spin-2 terms, could become a leading factor in a specific setting and silently bias the cosmological results. Therefore, the main future work that this work motivates is a comprehensive set of null testings that is used to make principled decisions about the model for PSF systematics in cosmological weak lensing analyses in any surveys.

Acknowledgments

We thank the referee for their helpful feedback on this paper. We thank Mike Jarvis for the helpful comments and discussion.

TZ, XL and RM are supported in part by the Department of Energy grant DE-SC0010118 and in part by a grant from the Simons Foundation (Simons Investigator in Astrophysics, Award ID 620789). RD acknowledges support from the NSF Graduate Research Fellowship Program under Grant No. DGE-2039656. Any opinions, findings, and conclusions or recommendations expressed in this material are those of the authors and do not necessarily reflect the views of the National Science Foundation. This work was supported in part by JSPS KAKENHI Grant Numbers 21J10314. SS is supported by International Graduate Program

for Excellence in Earth-Space Science (IGPEES), World-leading Innovative Graduate Study (WINGS) Program, the University of Tokyo. HM is supported by JSPS KAKENHI Grant Number JP20H01932.

The Hyper Suprime-Cam (HSC) collaboration includes the astronomical communities of Japan and Taiwan, and Princeton University. The HSC instrumentation and software were developed by the National Astronomical Observatory of Japan (NAOJ), the Kavli Institute for the Physics and Mathematics of the Universe (Kavli IPMU), the University of Tokyo, the High Energy Accelerator Research Organization (KEK), the Academia Sinica Institute for Astronomy and Astrophysics in Taiwan (ASIAA), and Princeton University. Funding was contributed by the FIRST program from the Japanese Cabinet Office, the Ministry of Education, Culture, Sports, Science and Technology (MEXT), the Japan Society for the Promotion of Science (JSPS), Japan Science and Technology Agency (JST), the Toray Science Foundation, NAOJ, Kavli IPMU, KEK, ASIAA, and Princeton University.

This paper makes use of software developed for Vera C. Rubin Observatory. We thank the Rubin Observatory for making their code available as free software at http://pipelines.lsst.io/.

This paper is based on data collected at the Subaru Telescope and retrieved from the HSC data archive system, which is operated by the Subaru Telescope and Astronomy Data Center (ADC) at NAOJ. Data analysis was in part carried out with the cooperation of Center for Computational Astrophysics (CfCA), NAOJ. We are honored and grateful for the opportunity of observing the Universe from Maunakea, which has the cultural, historical and natural significance in Hawaii.

The Pan-STARRS1 Surveys (PS1) and the PS1 public science archive have been made possible through contributions by the Institute for Astronomy, the University of Hawaii, the Pan-STARRS Project Office, the Max Planck Society and its participating institutes, the Max Planck Institute for Astronomy, Heidelberg, and the Max Planck Institute for Extraterrestrial Physics, Garching, The Johns Hopkins University, Durham University, the University of Edinburgh, the Queen's University Belfast, the Harvard-Smithsonian Center for Astrophysics, the Las Cumbres Observatory Global Telescope Network Incorporated, the National Central University of Taiwan, the Space Telescope Science Institute, the National Aeronautics and Space Administration under grant No. NNX08AR22G issued through the Planetary Science Division of the NASA Science Mission Directorate, the National Science Foundation grant No. AST-1238877, the University of Maryland, Eotvos Lorand University (ELTE), the Los Alamos National Laboratory, and the Gordon and Betty Moore Foundation.

Data Availability

This work is part of the HSC Year 3 cosmological analysis. The data and analysis products, as well as the software, will be made publicly available via the HSC-SSP website `https://hsc.mtk.nao.ac.jp/ssp/data-release/` upon journal acceptance. The correlation function data vectors, model fitting software, and cosmological analysis software will be shared upon reasonable request to the authors.

4.A Moments that contribute to spin-2 quantities

In this section, we prove that only the even moments with $n = p + q \geq 2$ has the spin-2 property, which supports our choice to only consider those moments in Section 4.4.3. A spin-2 moment negates under image rotation by $\pi/2$. As a result, it is invariant under rotation of $n\pi$ (for integer values of n) and negates under the rotation of $(2n+1)\pi/2$. The moments M_{pq} defined in Eq. (4.41) is the projection of the image onto the basis polynomial function of $x^p y^q$ (or $u^p v^q$ depending on whether it is defined in standardized coordinate). Note that the moment has the same spin property as the basis polynomial function $x^p y^q$. To be more specific, if the basis polynomial function negates under $\pi/2$ image rotation[6], the corresponding moment negates under $\pi/2$ rotation (159). Therefore, we focus on the spin-2 component of basis function $x^p y^q$ by projecting it onto the $m = 2$ spinor — $e^{2i\phi}$:

$$
\begin{aligned}
&\int_{-\infty}^{\infty}\int_{-\infty}^{\infty} \mathrm{d}x\,\mathrm{d}y\, x^p y^q e^{i2\phi} \\
=&\int_0^{\infty} r^{p+q+1}\mathrm{d}r \int_0^{2\pi} \mathrm{d}\phi \cos^p(\phi)\sin^q(\phi) e^{2i\phi} \\
=&\int_0^{\infty} r^{p+q+1}\mathrm{d}r \int_0^{2\pi} \mathrm{d}\phi\, [2^{-p}(e^{i\phi}+e^{-i\phi})^p][(2i)^{-q}(e^{i\phi}-e^{-i\phi})^q] e^{2i\phi} \\
=&2^{-p-q} i^{-q} \sum_{k=0}^{p}\sum_{j=0}^{q} \int_0^{\infty} r^{p+q+1}\mathrm{d}r \\
&\int_0^{2\pi} \mathrm{d}\phi (-1)^{q-j} \binom{p}{k}\binom{q}{j} e^{i(2k+2j-p-q+2)\phi}\,.
\end{aligned}
\tag{4.39}
$$

The last step uses the binomial theorem, and p, k, q, and j are all integers. Since $\int_0^{2\pi} \mathrm{d}\phi\, e^{im\phi} = 0$ if the integer $m \neq 0$. Therefore, Eq. (4.39) can only be nonzero if $2k + 2j - p - q + 2 = 0$. This means the order $n = p + q$ must obey

$$
n = 2k + 2j + 2. \tag{4.40}
$$

Since k (j) takes any natural number between 0 to p (q), n must be an even number that is greater than or equal to 2.

We further notice that M_{pq} contributes to the real part of the spin-2 quantity if q is even, and contributes to the imaginary part if q is odd, due to the i^{-q} factor in Eq. (4.39) (and that the rest of the integral is real).

Alternatively, one could derive the moment combinations with a specific spin number by expanding $(x + iy)^k(x - iy)^l$. Under this definition, the order $N = k + l$, and spin number $s = k - l$. For the fourth moment spin-2 combination, one can derive Eq. (4.17) with $k = 3$ and $l = 1$. One can also derive the sixth moment spin-2 with $k = 4$ and $l = 2$, and show that there is no spin-2 combination for odd number moments.

[6]Note, we rotate the image but do not rotate the basis polynomial function (see Appendix A of (159)). This is consistent with real observations, where we fix the basis polynomial function in the moment measurement and galaxy images are randomly orientated.

4.B Problematic Region in GAMA09H

In Fig. 4.B.1, we show a region within the GAMA09H field that has a particularly large PSF fourth moment residual. This region is also found to be responsible for a strong B-mode cosmic shear signal in Li et al. *in prep.* The region has a good seeing, and significant proportion of visits are lost due to the overflowing the warning flag `maxScaledSizeScatter`, which sets a maximum scatter in the PSF size residual allowed for a visit. As a results, this region has an lower visits, higher galaxy number density (due to good seeing, thus better resolution), and a significant B-mode signal on cosmic shear. In the HSC Y3 cosmic shear analysis and this work, we remove this region from the star and shear catalog.

It is worth noticing that the PSF modeling residual in this region only manifested itself in the fourth moment, rather than the second moment residual. We search through all six fields in the HSC Y3 star catalogs, and found a few other spots with a similar pattern, but the condition in Fig. 4.B.1 is the most severe. Understanding any potential causal connection between these fourth moment residual hot-spots and the B-mode in the cosmic shear signal is left for future work.

4.C Alternative Definition for Higher Moments

In this work, the higher moments are defined in a transformed coordinate system where the second moments are standardized, hereafter referred to as the standardized moments. There is an alternative way to define the higher moments, i.e., measuring the higher moments in the image coordinate, hereafter referred to as the raw moments. The raw moments are what functionally affect the raw second moments used for shear inference, but in practice we find it useful to measure standardized moments to separate out the contributions of moments at different orders. In Section 4.C.1, we define the raw higher moments, and discuss how to separate their Gaussian and non-Gaussian parts. In Section 4.C.2, we establish the analytical connection between the raw higher moments and standardized higher moments, which are used in the main text of this work. In Section 4.C.3, we use the raw higher moments to capture the PSF systematics using the same framework introduced in Section 4.5, and compare the impact on the cosmological probes between the two definitions of higher moments.

4.C.1 Raw Moments

The raw moments are measured in the image coordinates. In our case, we use coadded images, which are aligned with the equatorial coordinate system. In this work, we define the raw moments to be

$$\mathcal{M}_{pq} = \frac{\int \mathrm{d}x\,\mathrm{d}y\, x^p\, y^q\, \omega(x,y)\, I(x,y)}{\int \mathrm{d}x\,\mathrm{d}y\, \omega(x,y)\, I(x,y)}. \tag{4.41}$$

Again, $I(x,y)$ is the image profile, and $\omega(x,y)$ is the adaptive Gaussian weight defined in Eq. (4.9). The raw higher moments defined here are measured by PSFHOME. We cross-

checked our code with the functionality that measures raw higher moments in PIFF[7], and find consistent results.

Similar to the standardized moments, there is a combination of the raw moments that forms a spin-2 quantity. We call that $\mathcal{M}^{(4)}$.

$$\mathcal{M}^{(4)} = \mathcal{M}_{40} - \mathcal{M}_{04} + 2i(\mathcal{M}_{13} + \mathcal{M}_{31}) \tag{4.42}$$

Because of how raw moments are defined, $\mathcal{M}^{(4)}$ not only carries non-Gaussian information but also Gaussian information. In order to use the raw moments for capturing the spin-2 components of the PSF systematics, we need to find the Gaussian part of the $\mathcal{M}^{(4)}$. It turns out that $\mathcal{M}^{(4)}$ of an elliptical Gaussian PSF profile is just $3e_{\rm PSF}T^2_{\rm PSF}$, where $e_{\rm PSF}$ is the ellipticity of the PSF, and $T_{\rm PSF}$ is the trace.

This relationship can be proved by analytically finding the fourth moments of the Gaussian distribution. We start by defining the Moment Generating Function (MGF) of a two-dimensional Gaussian distribution

$$M_X(\boldsymbol{t}) = D^2 e^{\frac{1}{2}\boldsymbol{t}^T \mathbf{M}^{-1} \boldsymbol{t}}. \tag{4.43}$$

Here, $\boldsymbol{t}^T = \begin{bmatrix} t_1, t_2 \end{bmatrix}$ is the two-dimensional dummy variable of the MGF. $\mathbf{M}^{-1}$ is the inverse of second moment matrix

$$\mathbf{M}^{-1} = \begin{bmatrix} M_{20} & M_{11} \\ M_{11} & M_{02} \end{bmatrix}^{-1} = \frac{1}{D} \begin{bmatrix} M_{02} & -M_{11} \\ -M_{11} & M_{02}. \end{bmatrix} \tag{4.44}$$

And D is the determinant of $\mathbf{M}$.

The fourth moments are the fourth derivative of the MGT evaluated at $\boldsymbol{t} = \mathbf{0}$. One can show that

$$\mathcal{M}_{40} - \mathcal{M}_{04} = \frac{\mathrm{d}^4 M_X(t)}{\mathrm{d}t_1^4}\bigg|_{t_1=t_2=0} - \frac{\mathrm{d}^4 M_X(t)}{\mathrm{d}t_2^4}\bigg|_{t_1=t_2=0} \tag{4.45}$$

$$= 3(M_{20}^2 - M_{02}^2) = 3e_1 T^2 \tag{4.46}$$

Similarly, for the imaginary part,

$$2\left(\mathcal{M}_{13} + \mathcal{M}_{31}\right) = \frac{\mathrm{d}^4 M_X(t)}{\mathrm{d}t_1 \mathrm{d}t_2^3}\bigg|_{t_1=t_2=0} - \frac{\mathrm{d}^4 M_X(t)}{\mathrm{d}t_1^3 \mathrm{d}t_2}\bigg|_{t_1=t_2=0} \tag{4.47}$$

$$= 6M_{11}(M_{20} + M_{02}) = 3e_2 T^2. \tag{4.48}$$

We confirmed using our PSF star catalog that the raw fourth moments mostly consist of the Gaussian part. In Fig. 4.C.1, we show the 2-d histogram of the real and imaginary parts of $\mathcal{M}^{(4)}$ and $3eT^2$. The two quantities match closely, which justifies our choice to use standardized fourth moments for our analysis, as the raw fourth moments are so highly

[7] `https://github.com/rmjarvis/Piff`

correlated with the second moments. However, an alternative approach using raw moments is to construct a dimensionless quantity that only carries non-Gaussian spin-2 information

$$m^{(4)} = \frac{\mathcal{M}^{(4)}}{T^2} - 3e. \tag{4.49}$$

We will call $m^{(4)}$ the reduced raw fourth moment spin-2 quantity. In Section 4.C.3, we demonstrate that $m^{(4)}$ can be effectively used to track down PSF systematics in cosmic shear.

4.C.2 Connection between the Raw and Standardized Moments

In this section, we analytically derive the connection between the raw and standardized moments. This is a useful formalism in the circumstance that one wants to calculate one definition from the other.

We start by deriving the standardized moments from the raw moments. The standardized coordinates (u, v) in Eq. (4.41) can be expressed in terms of (x, y) using the second moments of the image,

$$\begin{bmatrix} u \\ v \end{bmatrix} = \mathbf{M}^{-\frac{1}{2}} \begin{bmatrix} x \\ y \end{bmatrix}. \tag{4.50}$$

where

$$\mathbf{M}^{-\frac{1}{2}} = \frac{1}{\sqrt{\zeta}} \begin{bmatrix} M_{02} + \sqrt{D} & -M_{11} \\ -M_{11} & M_{20} + \sqrt{D} \end{bmatrix}. \tag{4.51}$$

Here D is the determinant of $\mathbf{M}$ and $\zeta = D(M_{20} + M_{02} + 2\sqrt{D})$.

We can express u and v as linear functions of x and y,

$$u = \frac{M_{02} + \sqrt{D}}{\sqrt{\zeta}} x - \frac{M_{11}}{\sqrt{\zeta}} y \tag{4.52}$$

$$v = -\frac{M_{11}}{\sqrt{\zeta}} x + \frac{M_{20} + \sqrt{D}}{\sqrt{\zeta}} y. \tag{4.53}$$

Let's denote

$$A \equiv \frac{M_{02} + \sqrt{D}}{\sqrt{\zeta}} \tag{4.54}$$

$$B \equiv -\frac{M_{11}}{\sqrt{\zeta}} \tag{4.55}$$

$$C \equiv \frac{M_{20} + \sqrt{D}}{\sqrt{\zeta}} \tag{4.56}$$

The standardized fourth moments are then

$$\begin{aligned}
M_{40} =& A^4\mathcal{M}_{40} + 4A^3B\mathcal{M}_{31} + 6A^2B^2\mathcal{M}_{22} \\
&+ 4AB^3\mathcal{M}_{13} + B^4\mathcal{M}_{04} && (4.57)\\
M_{31} =& A^3B\mathcal{M}_{40} + (A^3C + 3A^2B^2)\mathcal{M}_{31} + (3A^2BC + 3AB^3)\mathcal{M}_{22} \\
&+ (3AB^2C + B^4)\mathcal{M}_{13} + B^3C\mathcal{M}_{04}. && (4.58)\\
M_{22} =& A^2B^2\mathcal{M}_{40} + (2A^2BC + 2AB^3)\mathcal{M}_{31} \\
&+ (A^2C^2 + 4AB^2C + B^4)\mathcal{M}_{22} \\
&+ (3AB^2C + B^4)\mathcal{M}_{13} + B^3C\mathcal{M}_{04}. && (4.59)\\
M_{13} =& AB^3\mathcal{M}_{40} + (3AB^2C + B^4)\mathcal{M}_{31} \\
&+ (3ABC^2 + 3B^3C)\mathcal{M}_{22} \\
&+ (AC^3 + 3B^2C^2)\mathcal{M}_{13} + BC^3\mathcal{M}_{04} && (4.60)\\
M_{04} =& B^4\mathcal{M}_{40} + 4B^3C\mathcal{M}_{31} + \\
&6B^2C^2\mathcal{M}_{22} + 4BC^3\mathcal{M}_{13} + C^4\mathcal{M}_{04}. && (4.61)
\end{aligned}$$

Here $\mathcal{M}_{pq}$ are the raw higher moments. PSFHOME has the functionality to carry out this transformation. We compared the standardized higher moments measured on the image and predicted by this formalism, and found the fractional difference to be on the order of 10^{-10}, which is an exquisite consistency. This formalism shows that given the second moments, the 5 raw fourth moments can be remapped to standardized fourth moments. Using a similar formalism, one can remap in the other direction, but we will not derive those equations.

We confirmed that changing the higher order spin-2 quantity in the raw moments will not only change the standardized spin-2 quantity, but also the standardized spin-0 quantity, and vice versa. This was implied by the above equations and can be demonstrated easily with image simulations as well.

4.C.3 Raw Moments for Capturing PSF Systematics

In this section, we demonstrate that one can use raw moments to measure the PSF systematics contamination in the cosmic shear 2PCF using our HSC catalog. Further, we empirically show that despite the complex mapping between the standardized and raw moments shown in Section 4.C.2, using raw moments to trace PSF systematics gives results for the cosmological contamination that are no different from using the standardized moments.

To remove the contribution from the second moments, we use the reduced raw higher moments spin-2 $m^{(4)}_{\rm PSF}$ defined in Eq. (4.49) to model the higher moments leakage and modeling error. Namely, Eq. (4.23) is modified to be

$$g_{\rm sys} = \alpha^{(2)}e_{\rm PSF} + \beta^{(2)}\Delta e_{\rm PSF} + \alpha^{(4)}m^{(4)}_{\rm PSF} + \beta^{(4)}\Delta m^{(4)}_{\rm PSF}. \quad (4.62)$$

With the raw moments, we only conducted cross-correlations using the PSF star catalog, and implemented the 4-parameter fiducial model. By cross-correlating with galaxy shapes

(described in Section 4.5.2) and maximizing the likelihood function defined in Eq. (4.4), we get $\alpha^{(2)} = -0.024 \pm 0.003$, $\beta^{(2)} = -0.72 \pm 0.06$, $\alpha^{(4)} = -0.15 \pm 0.01$, and $\beta^{(4)} = -0.6 \pm 0.2$. The reduced higher moments are still correlated with the second-moment shape. As a result, the correlation coefficient between α^2 and α^4 is 0.85, higher than the value of 0.62 found with standardized moments.

The most important quantity that we want to compare between standardized moments and raw moments is the impact on the shear-shear 2PCF. In Fig. 4.C.2, we show that the $\Delta\xi_+$ calculated using the reduced raw moments is highly consistent with the one calculated using the standardized moments. This means that both choices can effectively capture the additive bias due to second and higher PSF moments, as long as the data-driven procedure is followed.

Although we successfully demonstrated that the two approaches toward defining the PSF higher moments yield the same cosmological impact for HSC Y3, this is still an empirical demonstration that may be contingent on the moment distribution of the PSF in HSC Y3. We leave the study of the potential mathematical origin of this equivalence to future work. Before that, we suggest that future surveys conduct higher moments null tests using both definitions.

4.D Mock Catalog Test

We conducted a mock catalog test to validate the inference of the PSF systematics model parameters (as defined in Section 4.5.1). The crucial element of this test is to generate mock star and galaxy catalogs with systematics that we know follow our model on all scales. The steps for generating the mock star and galaxy catalogs are as follows:

1. Populate a healpix map (147) with `nside=512` with stars from the HSC Y3 star catalog (Section 4.4). Compute the average values of $e_{\rm PSF}$, $\Delta e_{\rm PSF}$, $M^{(4)}_{\rm PSF}$ and $\Delta M^{(4)}_{\rm PSF}$ using all stars within each pixel. Assign the average PSF moments in a pixel to the stars in that pixel to produce the mock star catalog.

2. Compute shear bias from Eq. (4.23) using the average PSF moments in the healpix pixel, and a set of input PSF parameters $\alpha^{(4)} = 0.04$, $\beta^{(2)} = -1$, $\alpha^{(4)} = 0.19$, and $\beta^{(4)} = -0.5$. Assign the shear bias to the mock galaxy catalogs (see Section 4.3.2) based on their corresponding pixels in the map to produce the mock shear catalog.

We use these mock star and shear catalogs to infer the PSF parameters using the pipeline developed for inference from the real data, to ensure that the pipeline is able to recover the input parameters. In doing so, we use the covariance matrix measured using the real data (as described in Section 4.5.2). We produced 10 mock catalogs with shear biases, and individually inferred their PSF systematics model parameters. Over the 10 mocks, we retrieve the averaged PSF parameters $\alpha^{(2)} = 0.040 \pm 0.001$, $\beta^{(2)} = -1.10 \pm 0.02$, $\alpha^{(4)} = 0.185 \pm 0.01$, and $\beta^{(4)} = -0.53 \pm 0.01$. Although there appears to be a statistically significant bias on the $\beta^{(2)}$ and $\beta^{(4)}$ parameter, the differences are within $\pm 10\%$ of the true PSF parameters.

Further investigation is needed for understanding the discrepancy between the inferred and true modeling error parameters in the mock catalog tests. We inspected the $\Delta\xi_+$s predicted by the true PSF parameters and by the inferred PSF parameters, and seeing no significant difference between the two.

4.E Subdominant effects

In this section, we discuss different aspects of the PSF systematics that could complicate the model. We implemented these extra terms on top of the fiducial model from Section 4.5.2, which describes the PSF systematics as an additive bias on ξ_+, including the leakage and modeling error caused separately by the PSF second moments and fourth moments. Most of these complications to the model do not significantly contribute to the HSC Y3 PSF systematics. However, they might be significant in other cosmic shear surveys with different shear estimation methods and PSF modeling algorithms. Therefore, we elaborate on these phenomena below.

In Appendix 4.E.1, we generalize the formalism in Section 4.5.1 and 4.5.2 from ξ_+ alone to include ξ_- as well. In Appendix 4.E.2 and 4.E.3, we considered other spin-2 quantities–the PSF sixth moments and second order spin-2 quantities (product of spin-2 and spin-0, etc.), and proved it is unnecessary to model these quantities for HSC Y3.

4.E.1 $\Delta\xi_-$

In this section, we discuss the additive PSF systematics in ξ_-. Previous studies have shown that the impact on ξ_- from PSF second moment contamination is sufficiently small that it can be ignored in the cosmic shear analysis (e.g., 1; 85). (71) also found the additive bias on ξ_- due to PSF fourth moment contamination to be consistent with zero. Here, we simply repeat the formalism in Section 4.5.1 and 4.5.2, and take ξ_- for all the correlation functions. In Fig. 4.E.1, we present the $\Delta\xi_-$ in comparison to the cosmic shear signal predicted by the fiducial cosmology. We found the $\Delta\xi_-$ to be below 1 per cent of the predicted shear signal in all of the tomographic bins, with a total statistical significance equal to 0.22σ and it therefore can be safely ignored.

4.E.2 Sixth Moment Terms

In Section 4.4.3, we pointed out that not just the second and fourth moments can combine to form a spin-2 quantity, but rather all even moments can do so (proof in Appendix 4.A). So a natural question is whether even higher order PSF moments need to be considered. In this section, we expand our model to accommodate the spin-2 combination of PSF sixth moments, which can be expressed as

$$M_{\rm PSF}^{(6)} = (M_{60} + M_{42} - M_{24} - M_{06}) + i(2M_{51} + 4M_{33} + 2M_{15}). \tag{4.63}$$

Similarly, we included $\langle \hat{g}_{\rm gal} M^{(6)}_{\rm PSF} \rangle$ and $\langle \hat{g}_{\rm gal} \Delta M^{(6)}_{\rm PSF} \rangle$ in the data vector and added sixth moments leakage and modeling error terms to the model ($\alpha^{(6)}$ and $\beta^{(6)}$, respectively). In this expanded framework, the data vector has a length of 122 and the parameter space grows to 6 from the fiducial model's 4.

In Fig. 4.E.2, we show the additive bias $\Delta\xi_+$ with and without the sixth moment leakage and modeling error, and the difference, which is the contribution of $M^{(6)}$. We see that the additional additive bias induced by the PSF sixth moments is $\lesssim 10\%$ of that from the fiducial model. The increase in statistical significance is only 0.1σ. We therefore neglect the spin-2 combination of PSF sixth moments, $M^{(6)}$, due to its subdominant impact.

We speculate that the reason that PSF sixth moments do not add much more additive bias to the overall $\Delta\xi_+$ is that (a) they are more susceptible to noise, which increases their statistical error; (b) they are shown to be highly correlated with the fourth moments (71). Most likely this correlation would be reduced if the sixth moments are measured on images with standardized second and fourth moments, instead of only standardized second moments.

4.E.3 Second Order Terms

So far, we limited our discussion to the first order terms of the PSF moments, which means they are either a single moment like $e_{\rm PSF}$, or a moment residual like $\Delta e_{\rm PSF}$. In this section, we discuss the second-order spin-2 quantities, which can take the form of a spin-2 quantity multiplied by a spin-0 quantity, e.g., $e_{\rm PSF}\Delta T_{\rm PSF}/T_{\rm PSF}$, which gives rise to the higher-order ρ statistics (89). Another possibility is a spin-4 quantity multiplied by a spin-2 quantity, or a spin-1 multiplied by a spin-1 quantity, which could arise from the product of two $N = 3$ moments; we will leave that for future work.

Since the first order spin-2 quantities $e_{\rm PSF}$, $\Delta e_{\rm PSF}$, $M^{(4)}_{\rm PSF}$, ΔM, ΔT are defined such that they are $\ll 1$, their second-order terms should be negligible (given that their pre-factors are of order 1). Therefore, we focused on first-order terms in the model. In this section, we discuss the potential impact of the second-order terms in PSF systematics.

The spin-2 combination of PSF fourth moments that serves as a counterpart to $e_{\rm PSF}$ is $M^{(4)}_{\rm PSF}$, defined in Eq. (4.18). The spin-0 combination of PSF fourth moments that serves as a counterpart to $T_{\rm PSF}$ (trace, defined in Eq. 4.19) is called the radial kurtosis, defined in Eq. (4.20). Errors in modeling either of these spin-0 quantities in the PSF can be a source of multiplicative bias in shear. As a demonstration, we show the image response to one of the second-order terms, $e_{\rm PSF}\Delta T_{\rm PSF}/T_{\rm PSF}$, and compare that to the image response to $M^{(4)}_{PSF}$ in Fig. 4.E.4. Because of the multiplication by $T_{\rm PSF}$, $e_{\rm PSF}\Delta T_{\rm PSF}/T_{\rm PSF}$ now has a very similar pattern to $M^{(4)}_{PSF}$, but is sensitive to pixels with different radii compared to $M^{(4)}_{PSF}$.

If we were to include $M^{(4)}_{\rm PSF}$ and $\rho^{(4)}_{\rm PSF}$ to form second order spin-2 terms, this would give rise to 3 more terms beyond the second-order term that is already in the ρ statistics ($e_{\rm PSF}\Delta T_{\rm PSF}/T_{\rm PSF}$): $e_{\rm PSF}\Delta\rho^{(4)}_{\rm PSF}/\rho^{(4)}_{\rm PSF}$, $M^{(4)}_{\rm PSF}\Delta\rho^{(4)}_{\rm PSF}/\rho^{(4)}_{\rm PSF}$, and $M^{(4)}_{\rm PSF}\Delta T_{\rm PSF}/T_{\rm PSF}$. We define these four spin-2 quantities as Ψ_j for $j = 1 \ldots 4$, and define their corresponding pre-factors in $\gamma^{\rm sys}$ to be η_j.

Including all four of these expands the total number of PSF spin-2 quantities from 4 to

8, which in principle generates $8 \times 9/2 = 36$ ρ statistics for which we want to know their impact on the overall $\Delta\xi_+$. We quantify the impact of the second order terms by adding four $\langle \hat{g}_{\rm gal}\Psi_j \rangle$ to the g-p correlation data vector, and adding four $\eta_j\Psi_j$ terms, for $j = 1 \ldots 4$, to $g_{\rm sys}$ in addition to the fiducial model terms. The Ψ_j and η_j are defined in the previous paragraph. We conducted a joint fitting process that considers all the second-order terms, their g-p correlations, and their auto- and cross-correlation with other PSF first-order terms. The additional additive bias in ξ_+ is shown in Fig. 4.E.3. We observe that the impact of the second-order spin-2×spin-0 terms is subdominant, only increasing the statistical significance of $\Delta\xi_+$ by 0.02σ. We include them in this work for completeness, even though they do not need to be modelled in the HSC Y3 analysis, and we recommend future cosmic shear surveys consider these possible sources of contamination to the cosmic shear.

4.F Correlation in PSF parameters

It is visually evident from Figure 4.3.2 that the fourth moment spin-2 $M^{(4)}_{\rm PSF}$ and the second moments $e_{\rm PSF}$ are anti-correlated. This correlation is also manifested in the correlation matrix in Figure 4.5.6, and the posterior of the PSF parameters in Figure 4.5.4.

To account for the correlation in the PSF parameters $\boldsymbol{p}$, we sample a standard multivariate Gaussian distribution $\tilde{\boldsymbol{p}} = [\tilde{\alpha}^{(2)}, \tilde{\beta}^{(2)}, \tilde{\alpha}^{(4)}, \tilde{\beta}^{(4)}]$, drawn from $\mathcal{N}(\mathbf{0}, \mathbf{I})$, where the null vector $\mathbf{0} \in R^4$ and $\mathbf{I}$ is a 4×4 identity matrix. We then transform $\tilde{\boldsymbol{p}}$ to get $\boldsymbol{p}$ in the fiducial model, by

$$\boldsymbol{p} = \boldsymbol{\Lambda}\mathbf{U}^{1/2}\tilde{\boldsymbol{p}} + \bar{\boldsymbol{p}}. \tag{4.64}$$

Here $\boldsymbol{\Lambda}$ is the eigenvalue vector of $\boldsymbol{p} - \bar{\boldsymbol{p}}$, $\mathbf{U}^{1/2}$ is the eigenvector matrix of $\boldsymbol{p} - \bar{\boldsymbol{p}}$, both inferred from the prior distribution of PSF parameters.

In Figure 4.F.1, we show that including the correlation of the PSF parameters in the cosmological parameter analysis does not cause a significant difference to the HSC Y3 mock analysis. Nonetheless, we recommend including the correlation for the completeness of the error propagation.

4.G Fourier Space Cosmic Shear Analysis

Cosmic shear are probed and analyzed in the configuration space by two-point correlation function, and also probed and analyzed in Fourier space using pseudo-C_ℓ (e.g., 153; 212). In this section, we discuss the PSF systematics formalism in Fourier space (Section 4.G.1), and the real-Fourier space consistency for the PSF additive bias modeling (Section 4.G.2).

4.G.1 PSF systematics formalism in Fourier Space

We also investigated the impact of PSF systematics on cosmic shear power spectra, C_ℓs, in addition to the above analysis using two-point correlation functions. In doing so, we use the

model for $g_{\rm sys}$ given by Eq. (4.23), without the mean ellipticity parameter, e_c, as the analysis with 2PCFs has shown that this parameter has negligible impact for HSC Y3:

$$g_{\rm sys} = \alpha^{(2)} e_{\rm PSF} + \beta^{(2)} \Delta e_{\rm PSF} + \alpha^{(4)} M^{(4)}_{\rm PSF} + \beta^{(4)} \Delta M^{(4)}_{\rm PSF}. \tag{4.65}$$

Upon adding $g_{\rm sys}$ to the observed galaxy ellipticity, the measured cosmic shear power spectrum becomes:

$$C_\ell \to C_\ell + \sum_{i=1}^{4} \sum_{j=1}^{4} \boldsymbol{p}_i \boldsymbol{p}_j C_\ell^{\boldsymbol{S}_i \boldsymbol{S}_j}. \tag{4.66}$$

where, as before, we define the parameter vector $\boldsymbol{p} = [\alpha^{(2)}, \beta^{(2)}, \alpha^{(4)}, \beta^{(4)}]$, and the PSF moments vectors $\boldsymbol{S} = [e_{\rm PSF}, \Delta e_{\rm PSF}, M^{(4)}_{\rm PSF}, \Delta M^{(4)}_{\rm PSF}]$. We refer to the additive term in Eq. (4.66) as ΔC_ℓ.

To get the best-fitting values of the parameters $\boldsymbol{p}$, we repeat the process carried out with 2PCFs, measuring the p-p power spectra and the g-p power spectra ($\boldsymbol{D}_{gp}$), in 6 ℓ bins, from $300 \leq \ell \leq 1800$ (the provisional scale cuts for the Fourier space cosmology analysis). We use the pseudo-C_ℓ code `NaMaster` (213) to measure the power spectra. Although the pseudo-C_ℓ method requires subtracting a noise spectrum from auto-correlations (212), this term is negligible for the PSF moments (unlike the case of galaxy shape auto-correlations). We then predict the theory data vector ($\boldsymbol{T}_{gp}$) for the g-p power spectra, given the p-p power spectra, which is equivalent to the real space fiducial model in Eq. (4.26)–(4.29) with $e_c = 0 + 0j$:

$$C_\ell^{\hat{g}_{\rm gal} e_{\rm PSF}} = \alpha^{(2)} C_\ell^{e_{\rm PSF} e_{\rm PSF}} + \beta^{(2)} C_\ell^{\Delta e_{\rm PSF} e_{\rm PSF}} + \alpha^{(4)} C_\ell^{M^{(4)}_{\rm PSF} e_{\rm PSF}} + \beta^{(4)} C_\ell^{\Delta M^{(4)}_{\rm PSF} e_{\rm PSF}} \tag{4.67}$$

$$C_\ell^{\hat{g}_{\rm gal} \Delta e_{\rm PSF}} = \alpha^{(2)} C_\ell^{e_{\rm PSF} \Delta e_{\rm PSF}} + \beta^{(2)} C_\ell^{\Delta e_{\rm PSF} \Delta e_{\rm PSF}} + \alpha^{(4)} C_\ell^{M^{(4)}_{\rm PSF} \Delta e_{\rm PSF}} + \beta^{(4)} C_\ell^{\Delta M^{(4)}_{\rm PSF} \Delta e_{\rm PSF}} \tag{4.68}$$

$$C_\ell^{\hat{g}_{\rm gal} M^{(4)}_{\rm PSF}} = \alpha^{(2)} C_\ell^{e_{\rm PSF} M^{(4)}_{\rm PSF}} + \beta^{(2)} C_\ell^{\Delta e_{\rm PSF} M^{(4)}_{\rm PSF}} + \alpha^{(4)} C_\ell^{M^{(4)}_{\rm PSF} M^{(4)}_{\rm PSF}} + \beta^{(4)} C_\ell^{\Delta M^{(4)}_{\rm PSF} M^{(4)}_{\rm PSF}} \tag{4.69}$$

$$C_\ell^{\hat{g}_{\rm gal} \Delta M^{(4)}_{\rm PSF}} = \alpha^{(2)} C_\ell^{e_{\rm PSF} \Delta M^{(4)}_{\rm PSF}} + \beta^{(2)} C_\ell^{\Delta e_{\rm PSF} \Delta M^{(4)}_{\rm PSF}} + \alpha^{(4)} C_\ell^{M^{(4)}_{\rm PSF} \Delta M^{(4)}_{\rm PSF}} + \beta^{(4)} C_\ell^{\Delta M^{(4)}_{\rm PSF} \Delta M^{(4)}_{\rm PSF}}. \tag{4.70}$$

We find the values of the parameters $\alpha^{(2)}$, $\beta^{(2)}$, $\alpha^{(4)}$, and $\beta^{(4)}$ which maximize the log-likelihood function given by Eq. (4.31). The covariance matrix of $\boldsymbol{D}_{gp}$ for the Fourier space analysis is computed from the HSC Y3 mock catalog, described in Section 4.3.2. Note that the covariance for the Fourier space cross power spectra does not include the uncertainty of the p-p power spectra, which is different from the real space analysis. The best-fitting $\boldsymbol{T}_{gp}$, as well as the measured g-p correlations, $\boldsymbol{D}_{gp}$, are shown in Fig. 4.G.1. As in the case of the 2PCF analysis, we also ran a Markov Chain Monte Carlo (MCMC) to measure the posterior of the PSF parameters $P(\boldsymbol{p}|\boldsymbol{D}_{gp})$, using a flat prior for the PSF parameters from $-\infty$ to $+\infty$. These posteriors are shown in Figure 4.G.2. We validate the parameter inference using the mock catalog test, described in Appendix 4.D.

Finally, we use the best-fitting values of the PSF parameters to compute the bias in the cosmic shear power spectra, ΔC_ℓ, for the parameter values estimated from both PSF and

non-PSF stars. As shown in Figure 4.G.3, the additive biases inferred from the two star catalogs are consistent with one another.

4.G.2 Consistency between Real and Fourier Space

In this section, we discuss the internal consistency between the PSF systematics manifested in the real and Fourier space analyses. By checking that the real space and Fourier space analysis provide consistent results across different stages of the analysis, we further validate our PSF systematics treatment[8].

Sample	Parameter	Real Space	Fourier Space
PSF	$\alpha^{(2)}$	0.016 ± 0.002	0.032 ± 0.004
	$\beta^{(2)}$	-0.84 ± 0.03	-0.45 ± 0.04
	$\alpha^{(4)}$	0.17 ± 0.01	0.20 ± 0.02
	$\beta^{(4)}$	-0.6 ± 0.10	-0.21 ± 0.08
non-PSF	$\alpha^{(2)}$	0.020 ± 0.004	0.040 ± 0.005
	$\beta^{(2)}$	-0.57 ± 0.07	-0.26 ± 0.06
	$\alpha^{(4)}$	0.17 ± 0.01	0.20 ± 0.02
	$\beta^{(4)}$	0.11 ± 0.12	0.18 ± 0.12

Table 4.G.1: The best-fitting parameters of the fiducial model in real space and Fourier space analysis, for both PSF and non-PSF stars. The dominant contributor to the additive bias in the power spectra/2PCFs, the fourth moment leakage parameter $\alpha^{(4)}$ matches well between real space and Fourier space, while $\alpha^{(2)}$, $\beta^{(2)}$, and $\beta^{(4)}$ are inconsistent between the two analyses.

In Table 4.G.1, we compare the best-fitting parameters of the fiducial PSF systematics model in real space and Fourier space, for both PSF and non-PSF samples. $\alpha^{(2)}$, $\beta^{(2)}$, and $\beta^{(4)}$ appear to be inconsistent, although the dominant contributor to the additive bias, $\alpha^{(4)}$, is consistent between the two analyses, for both the PSF and non-PSF samples. As a result of the consistency in $\alpha^{(4)}$, we expect the additive bias on the data vectors inferred from both methods to be roughly consistent. We compute the predicted $\Delta\tilde{C}_\ell$ by inverse-Wigner transforming the shear-shear contamination $\Delta\xi_+(\theta)$ (145)

$$\Delta\tilde{C}_\ell = 2\pi \int_0^{2\pi} \mathrm{d}\theta \sin(\theta) d^\ell_{2,2}(\theta) \Delta\xi_+(\theta). \tag{4.71}$$

Here $d^\ell_{2,2}$ is the Wigner matrix for two spin-2 fields at the given ℓ (214). We fit the $\Delta\xi_+(\theta)$ predicted by the real space fiducial model in the range $[1, 200]$ arcmin using a double exponential model (determined empirically), while setting the value outside the angular range to

[8]If the model is not sufficient to describe the data, we expect results to differ in real space and Fourier space, because they implicitly weight scales differently, which can affect how the model mismatch manifests in the fits. If the model is sufficient, however, they should agree within the uncertainties.

zero:

$$\Delta\xi_+ = a_1 e^{-s_1\theta} + a_2 e^{-s_2\theta}. \tag{4.72}$$

The best-fitting parameters of the double exponential model are $a_1 = 1.33 \times 10^{-5}$, $a_2 = 2.19 \times 10^{-6}$, $s_1 = 54.3$ deg^{-1}, $s_2 = 1.38$ deg^{-1}. We show the predicted $\Delta\tilde{C}_\ell$ using the 1σ uncertainty on the PSF systematics model parameters with the blue region in Fig. 4.G.3. Despite having different $\alpha^{(2)}$, $\beta^{(2)}$ and $\beta^{(4)}$, the impact on the cosmological observable still marginally matches, due to the fact that the fourth moment leakage is the largest contributor to the additive bias. The $\Delta\tilde{C}_\ell$ predicted from the real space $\Delta\xi_+$ matches the ΔC_ℓs predicted by the PSF and non-PSF stars of the Fourier space fiducial model, expressed in Eq. (4.66), within 2σ.

To demonstrate that the difference in Fourier and real space for the PSF systematics parameters will not significantly impact the cosmological results, we run an additional mock cosmological analysis on the Y3-like data vector and covariance. In Fig. 4.G.4, we show the 1-d Ω_m-S_8 constraints of the Y3 mock cosmological analysis. In addition to the green, red and orange lines that were shown in Fig. 4.6.2, we include another fiducial correction with the PSF parameters obtained in the Fourier space analysis. The difference results in a bias on Ω_m of about 0.15σ, and a 0.01σ bias on S_8. We conclude that these remaining systematics are subdominant for the Y3 cosmological results.

These results suggest that our PSF systematics model may not be fully sufficient to describe the data, but the real versus Fourier space comparison suggests this is not a problem for an analysis at our current level of precision. We therefore leave this issue for future work; with a larger area catalog it will be more important to understand this issue, if it persists. Since most image systematics are tied to particular physical scales (such as the size of the image focal plane, the typical correlation length of the atmospheric PSF anisotropies, etc.) we suspect that the issue could arise because the adopted range of ℓ values include information from values of θ on which our model does not include all relevant physics.

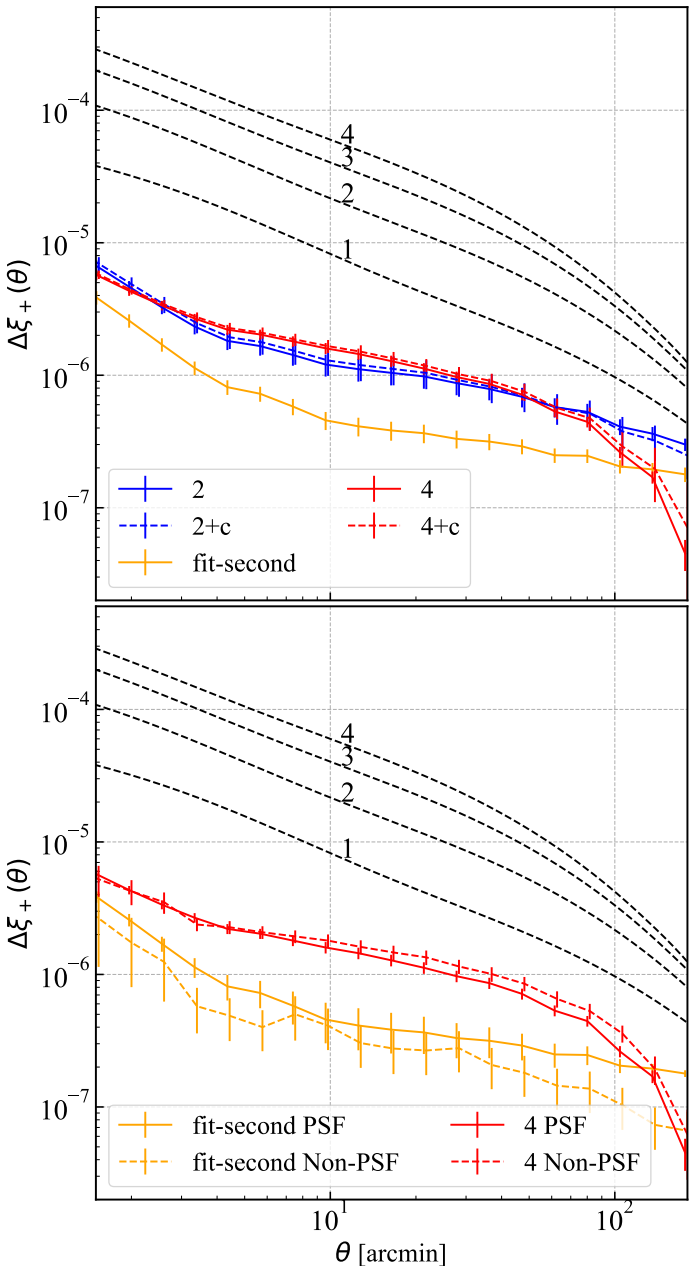

Figure 4.5.5: The additive bias on the cosmic shear 2PCF ξ_+ for the redshift-independent models. The statistical uncertainties on the shear-shear auto correlation are shown as the black dashed lines, with an index for the tomographic bin. The upper panel shows the $\Delta\xi_+$ of the different nested models of "4+c" using their best-fitting parameters. The model naming convention follows Fig. 4.5.2. We can see that including the galaxy shape correlations with the PSF fourth moments increases the estimated $\Delta\xi_+$ on some angular scales by almost an order of magnitude compared to when we fit to second moments only. And the $\Delta\xi_+$ predicted by the fiducial model on par with the statistical uncertainty of the first and second bin's auto correlation function, which is a significant contamination level. The bottom panel shows the comparison of the estimated $\Delta\xi_+$ for just two of the models using the PSF stars (solid lines) and non-PSF stars (dashed lines).

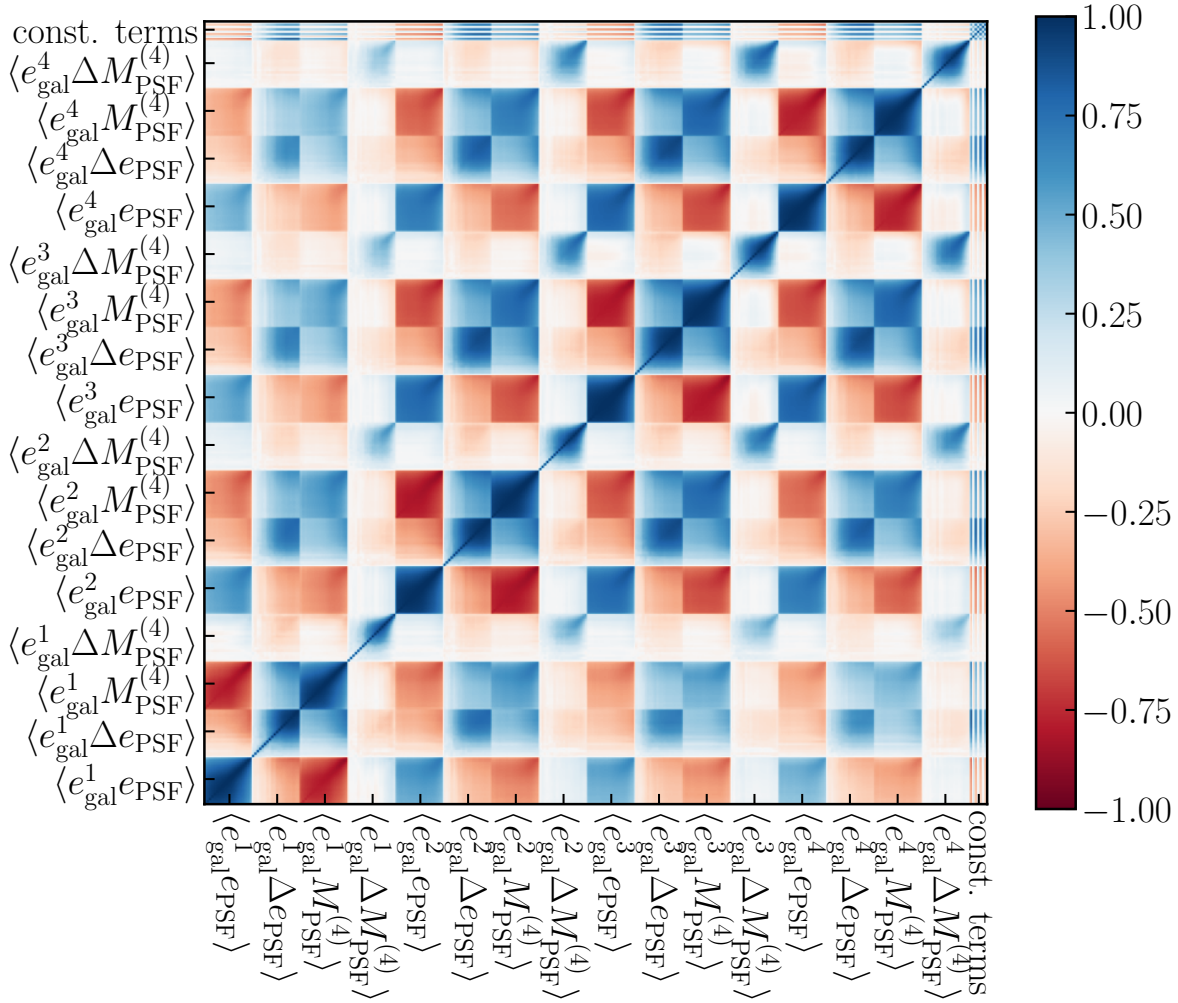

Figure 4.5.6: The correlation matrix of the data vector in the redshift-dependent model fitting. The quantity of the section in the data vector are shown in the x- and y-axis. Due to the correlation between the shear in different tomographic bins, g-p correlation functions across tomographic bins are also highly correlated. This is the primary reason that the PSF parameters for the 4 tomographic bins need to be jointly fitted, rather than individually fitted.

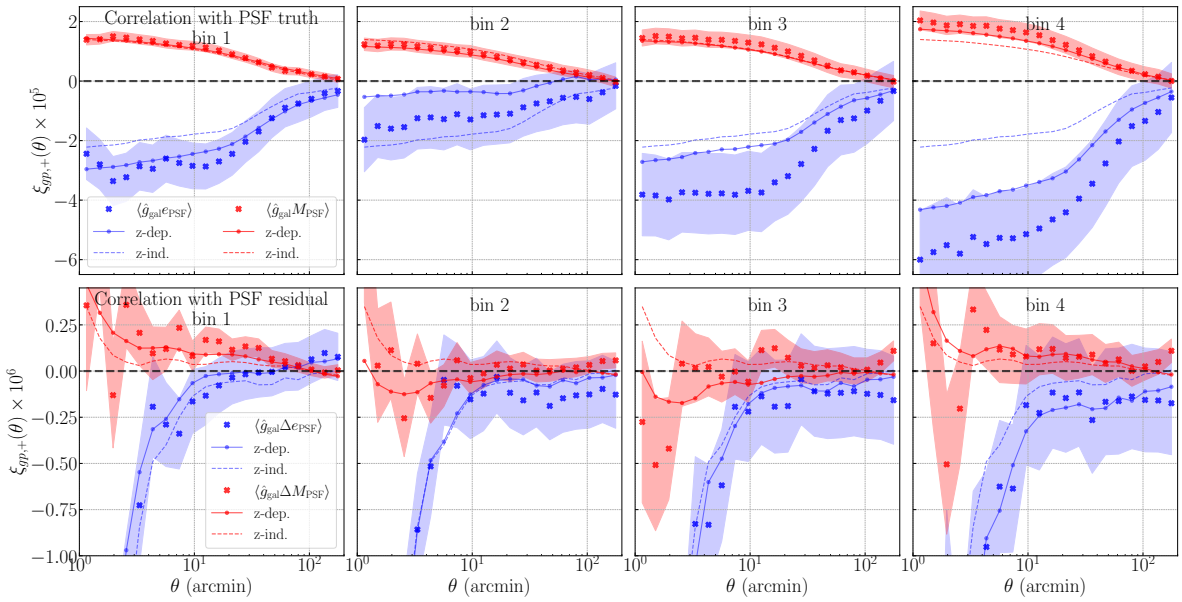

Figure 4.5.7: Galaxy-PSF correlation functions with galaxy samples subdivided into four tomographic bins as defined for the HSC Y3 cosmic shear analysis. The first row shows the correlations with the PSF truth terms, and second row with the PSF residual terms. The four columns correspond to the four tomographic bins. The stars are the best-fitting values for the redshift-dependent model, the dashed lines are the best-fitting values for the redshift-independent model. The shaded regions are excluded from the fits because the model is not able to fit the data there, as assessed using p-values.

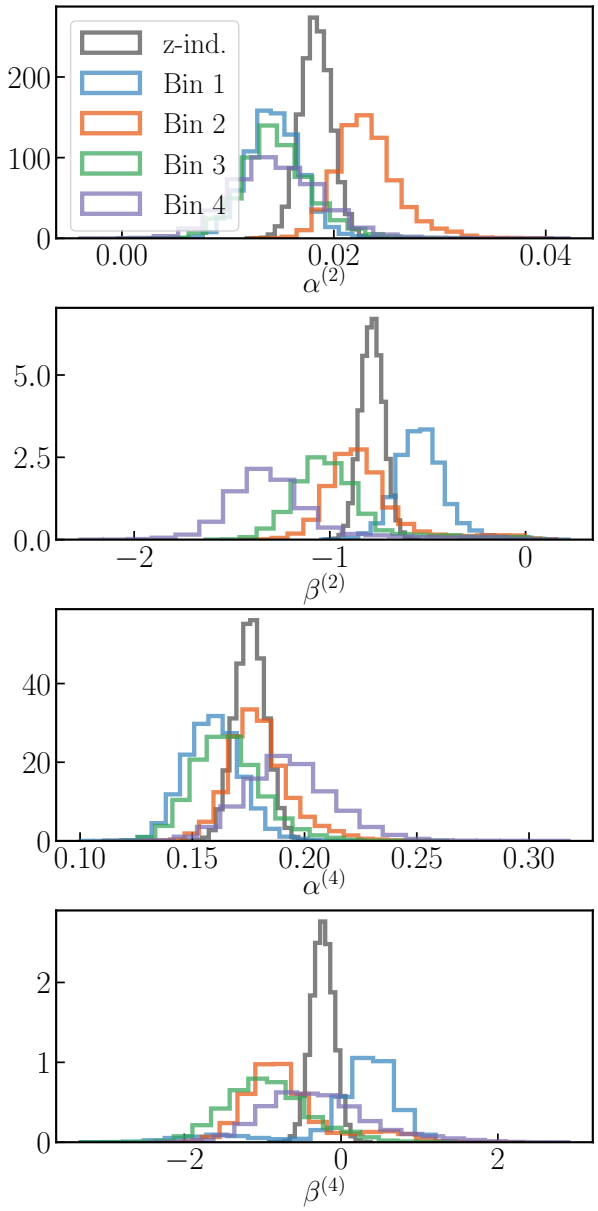

Figure 4.5.8: Marginalized 1D posterior distributions of the PSF systematics parameters for the redshift-dependent analysis. The parameters corresponding to different tomographic bins are color coded. The differences in the distributions for different tomographic bins may be caused by the differences in galaxy property distributions and the resulting difference in sensitivity to PSF systematics. The posterior of the redshift-independent model, shown in grey, corresponds roughly to the average of the distributions of the redshift-dependent model.

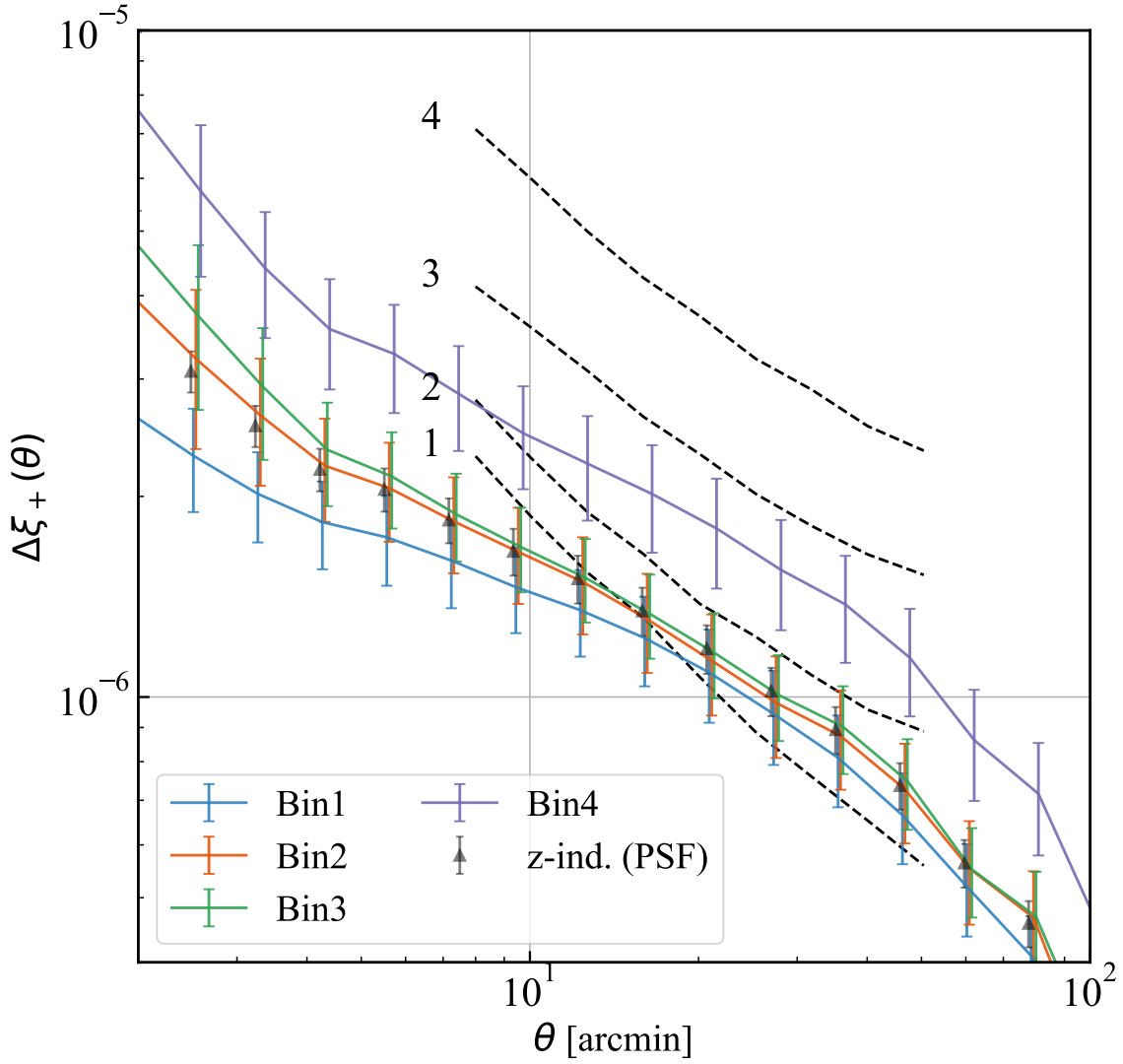

Figure 4.5.9: The additive bias on the auto-correlations of the cosmic shear 2PCF ξ_+ for the redshift-dependent models and redshift-independent model. We compare the $\Delta\xi_+(\theta)$ with the statistical uncertainty of $\xi_+(\theta)$. To avoid overcrowding, we only show the model fitted to the PSF stars. The black triangle line shows the $\Delta\xi_+(\theta)$ redshift-independent model fitted to PSF stars. We discuss the redshift dependency of the model in Section 4.5.3.

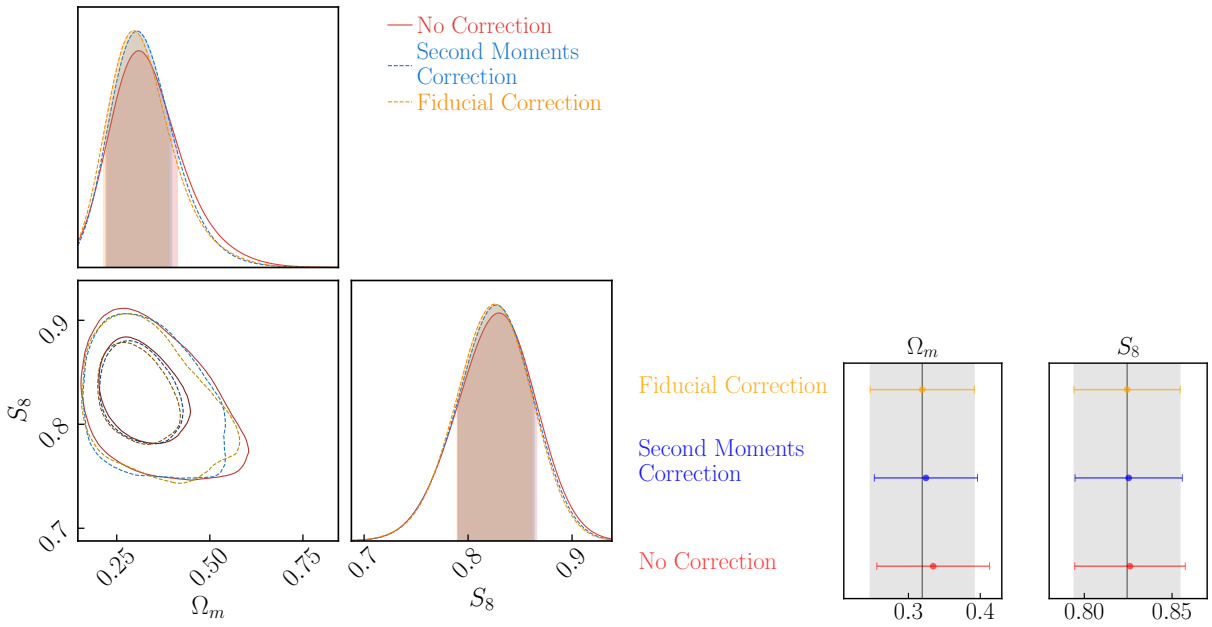

Figure 4.6.1: The Ω_m-S_8 constraints of the HSC Y1 cosmic shear re-analysis. The upper panel shows the 2d contours of the 68% and 95% confidence interval and the 1d marginal posterior distributions, while the lower panel shows the 1d marginalized 1σ errorbars. The vertical lines are the mean values of the posterior of the fiducial correction method, while, the shaded areas indicate the marginalized 1σ errorbars of the fiducial correction. Compared to the case of no correction for PSF systematics, the fiducial model correction shift the mean S_8 by 0.2σ. However, the correction based on only PSF second moments shifts Ω_m by 0.05σ, resulting a 0.15σ bias on Ω_m compared to our fiducial model. The impact on S_8 is more modest.

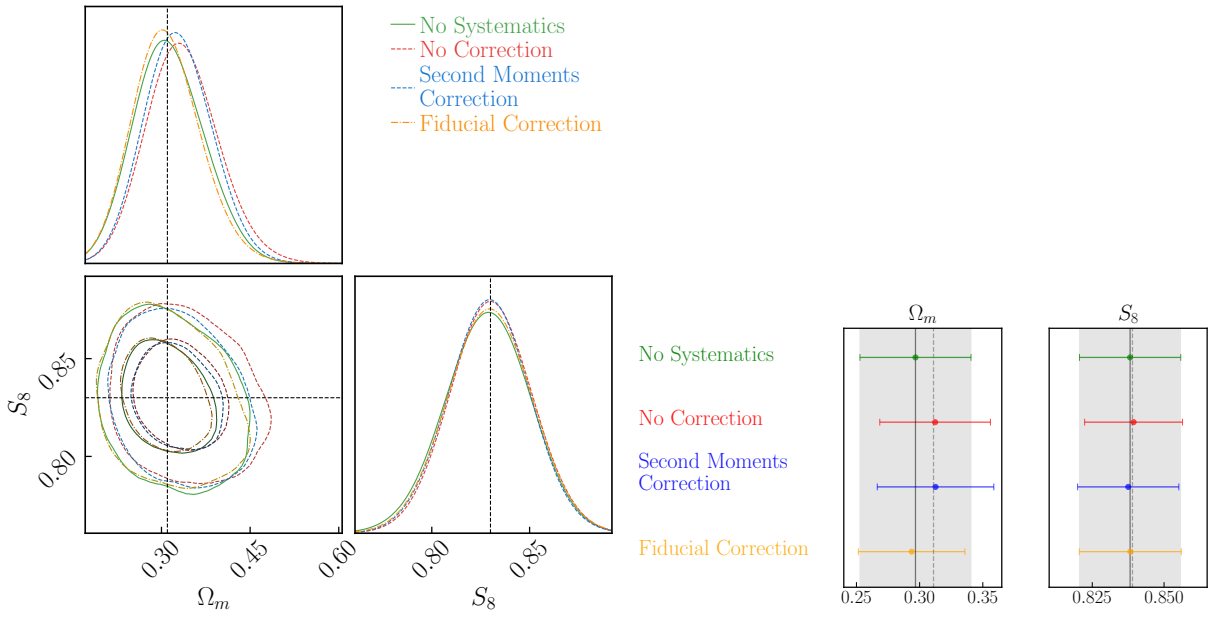

Figure 4.6.2: The Ω_m-S_8 constraints of the HSC Y3 mock cosmic shear analysis. The upper panel shows the 2d contours of the 68% and 95% confidence interval and the 1d marginal posterior distributions, while the lower panel shows the 1d marginalized 1σ errorbars. The dashed lines show the true input cosmological parameters. The green line shows the results of analyzing the data vector with no PSF systematics added, as a baseline. The vertical lines indicate the mean values of the posterior for the fiducial correction analysis, while the shaded areas indicate the 1σ errorbar when applying the fiducial correction. Due the skewness of the Ω_m posterior distribution, the mean Ω_m value in the "No Systematics" case is biased low. The red shows the worst-case scenario, where a realistic level of redshift-dependent PSF systematics are added but no attempt is made to correct for them. The blue shows the results of analysis using the redshift-independent second moments-only PSF systematics model, and the orange shows the results of analysis using the fiducial redshift-independent PSF systematics model. We see that the second moment-only model provides very similar results to applying no correction at all. The fiducial model is more successful at correcting the PSF systematics.

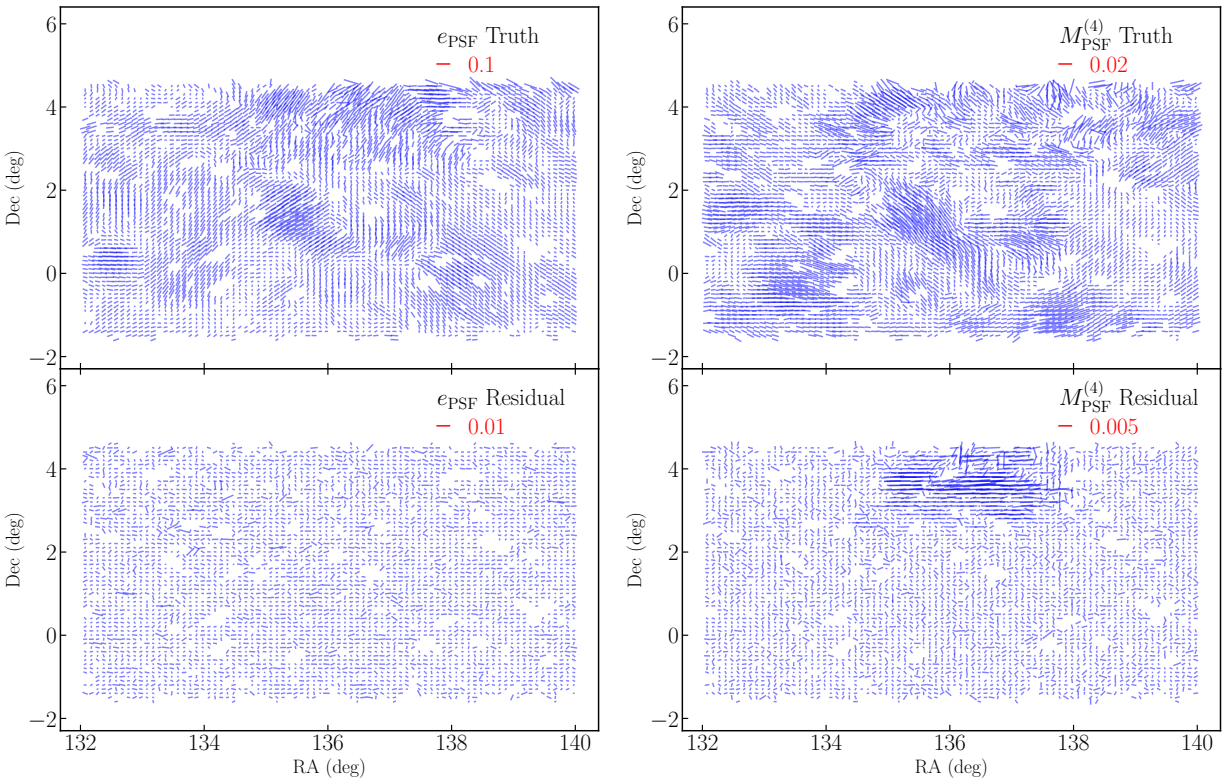

Figure 4.B.1: The truth and residual whisker plots of the spin-2 components of the PSF second (top) and fourth moments (bottom) in the field `GAMA09H` between RA $\in [132, 140]$ (deg). The region between RA $\in [135, 138]$ (deg) and Dec $\in [3, 5]$ (deg) has a particularly large fourth moment modeling error, which do not manifest in the second moment model residual. We have eliminated this problematic region in this work and the upcoming Y3 cosmic shear analysis.

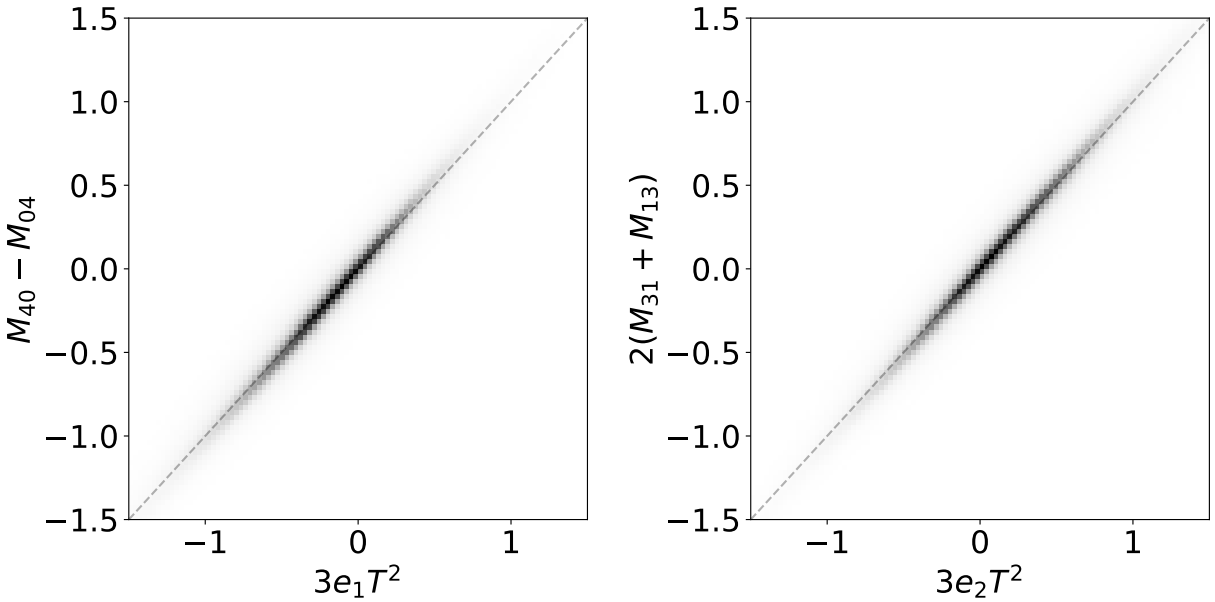

Figure 4.C.1: 2-d histograms of the raw higher moments $\mathcal{M}^{(4)}$ versus their Gaussian part – $3eT^2$. Since the Gaussian part dominates over the non-Gaussian part, the distribution is sharply peaked along the grey dashed $y = x$ lines.

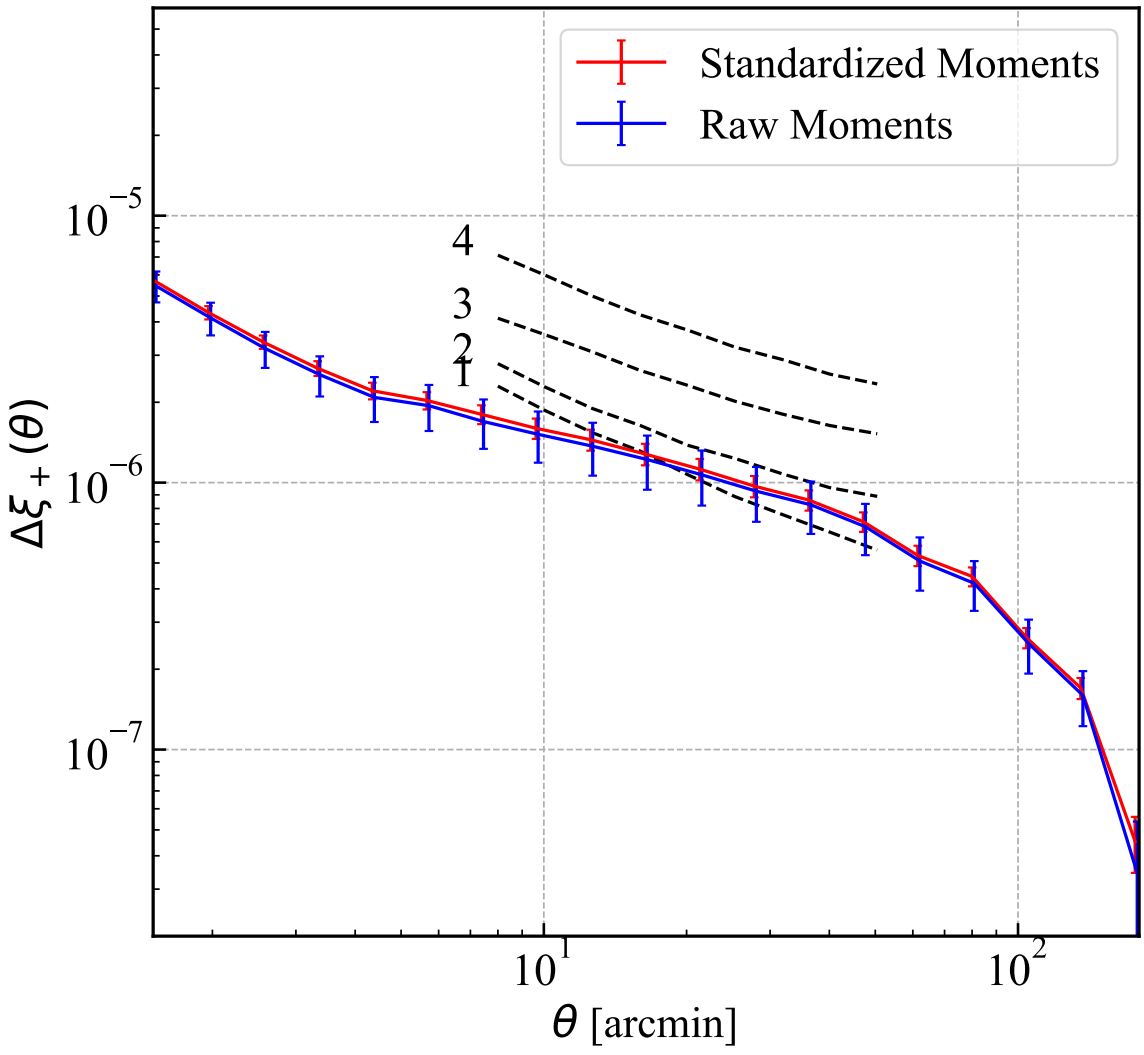

Figure 4.C.2: Total impact on shear-shear 2PCF caused by the PSF additive bias. The statistical uncertainty of the shear-shear auto correlations are plotted as dashed lines. We can see that the $\Delta\xi_+$ calculated using raw and standardized higher moments matches very well across all angular scales shown in this plot.

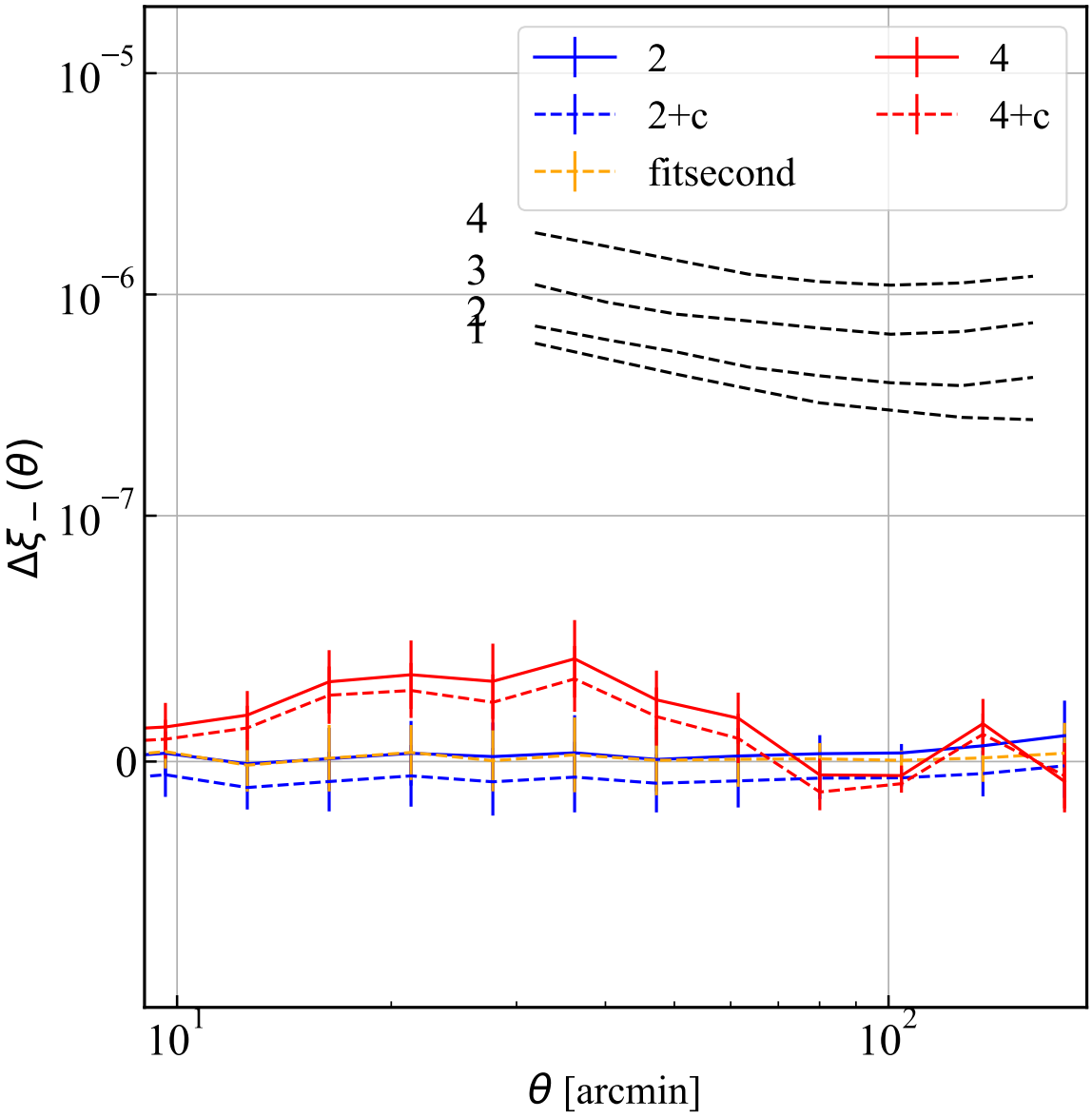

Figure 4.E.1: The additive bias on the cosmic shear 2PCF ξ_-. We find the $\Delta\xi_-$ to be below 10% of the predicted statistical uncertainty of ξ_- for all the tomographic bins, and therefore it can be ignored.

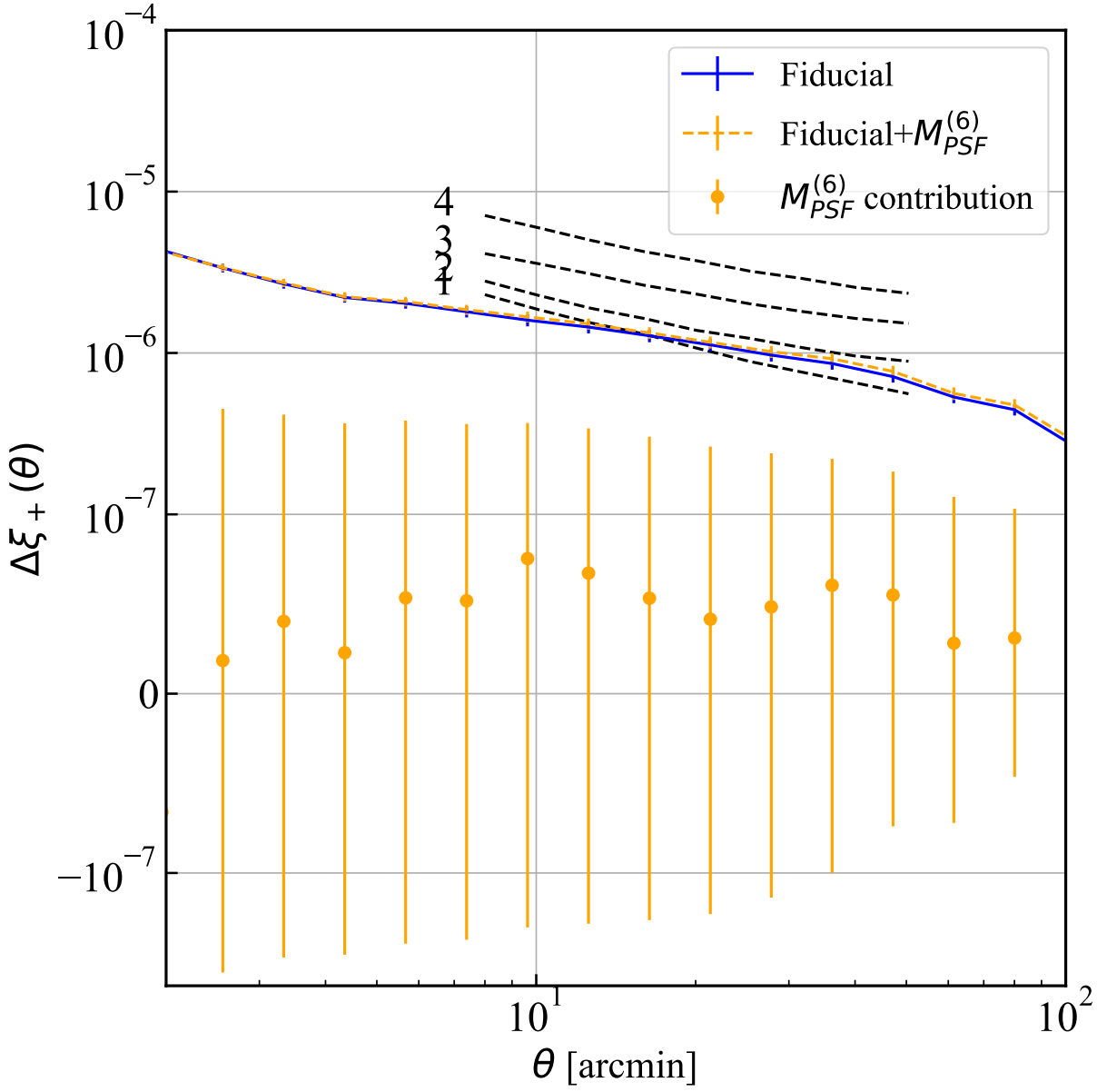

Figure 4.E.2: The additive bias on cosmic shear ξ_+ if the PSF sixth moments leakage and modeling error are considered. We include the PSF six moments as an extension to the fiducial model, which has the second and fourth moments. The PSF six moment contributes $< 10\%$ to the overall $\Delta\xi_+$, as well as to the statistical uncertainty, therefore is subdominant.

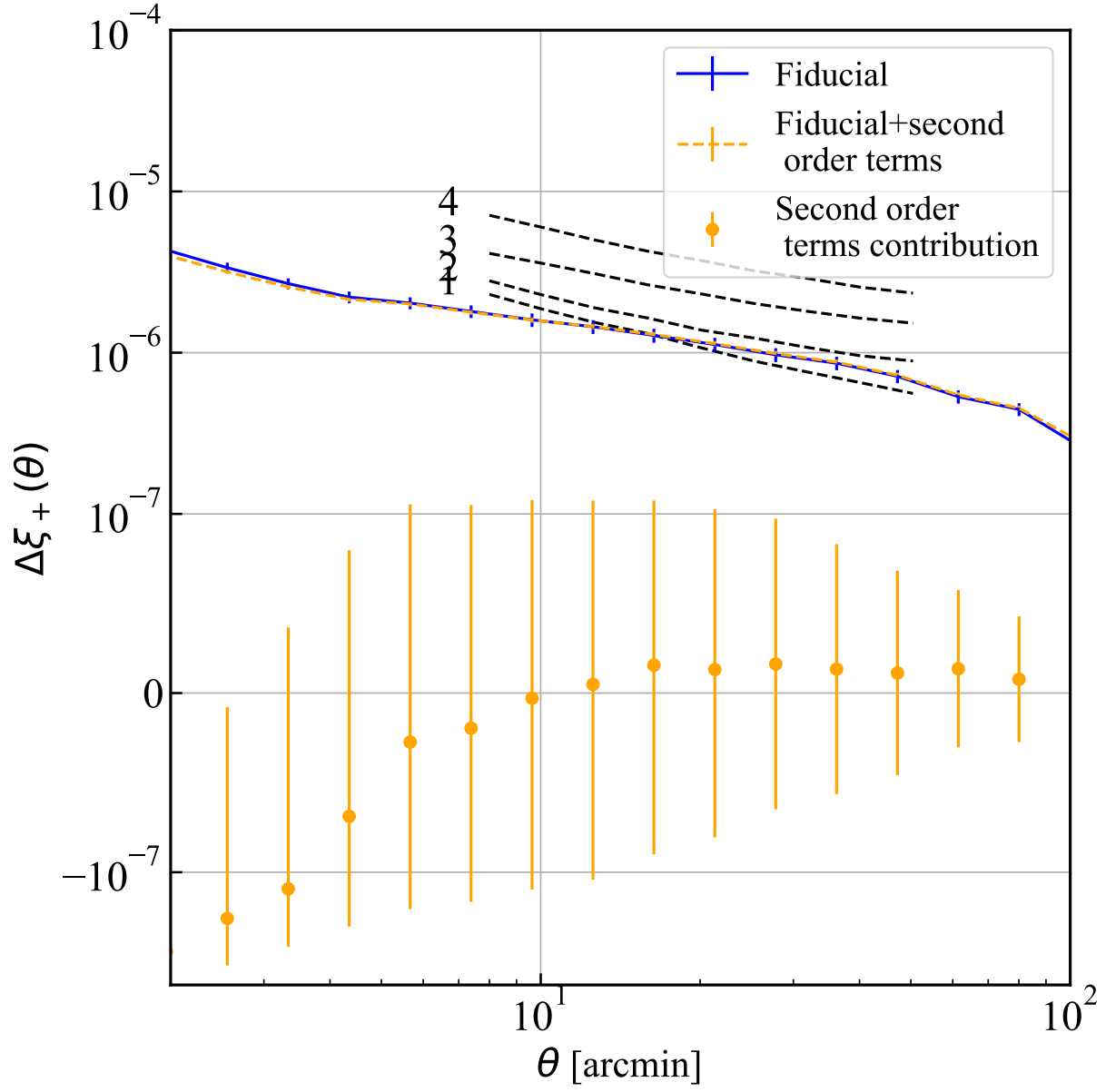

Figure 4.E.3: The additive bias on cosmic shear ξ_+ considering all second-order spin-2× spin-0 systematics. We included four spin-2 × spin-0 systematics described in Section 4.E.3 as an extension to the fiducial model, which has first-order contributions from the spin-2 combinations of PSF second and fourth moments. The second-order systematic biases induced by spin-2 × spin-0 terms are subdominant compared to those from the first order terms.

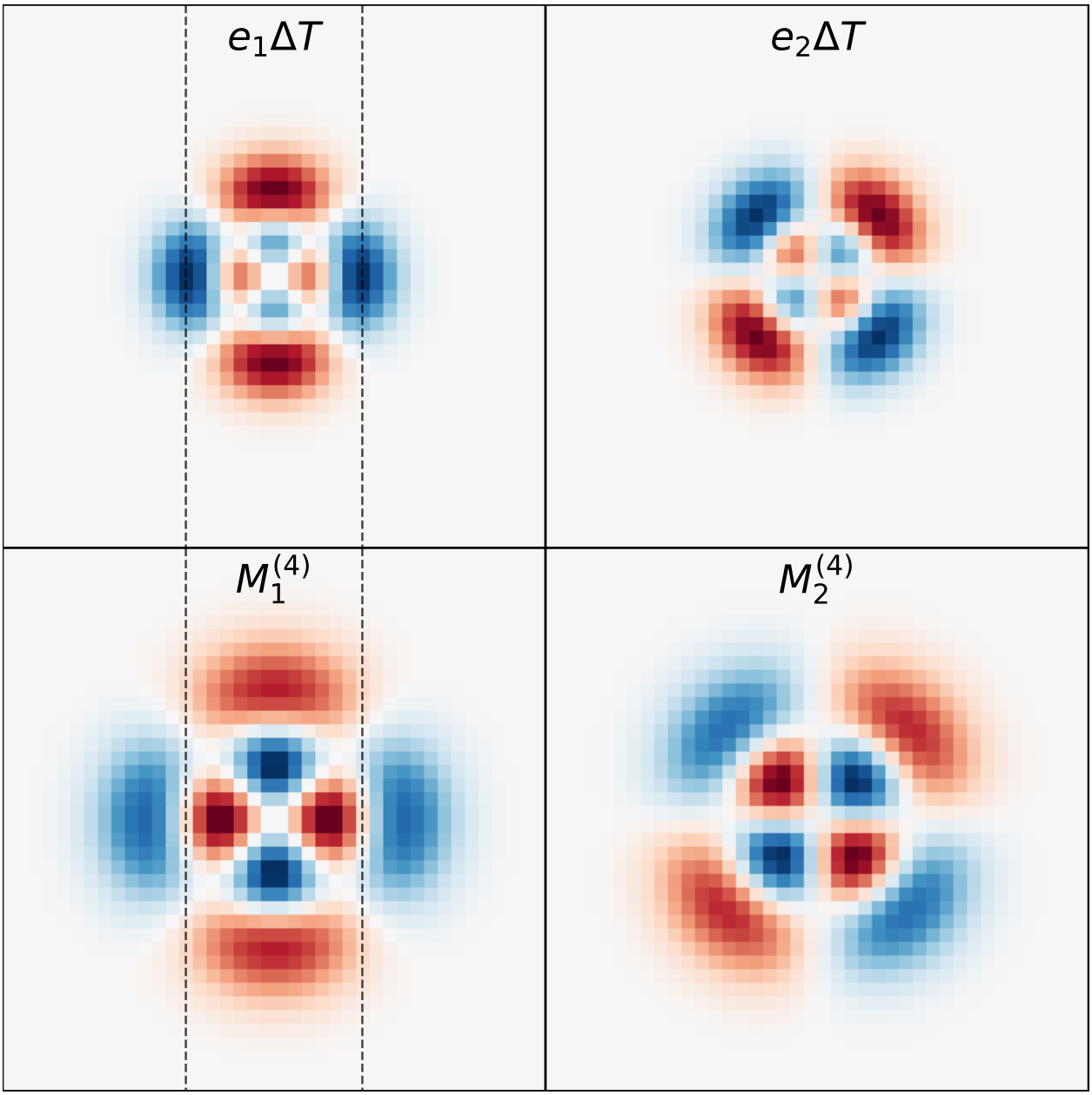

Figure 4.E.4: A comparison between the image response to $e_{\rm PSF}\Delta T_{\rm PSF}/T_{\rm PSF}$ and that to $M^{(4)}_{PSF}$. These two terms have very similar patterns, just with sensitivities to different scales, as the reference lines show.

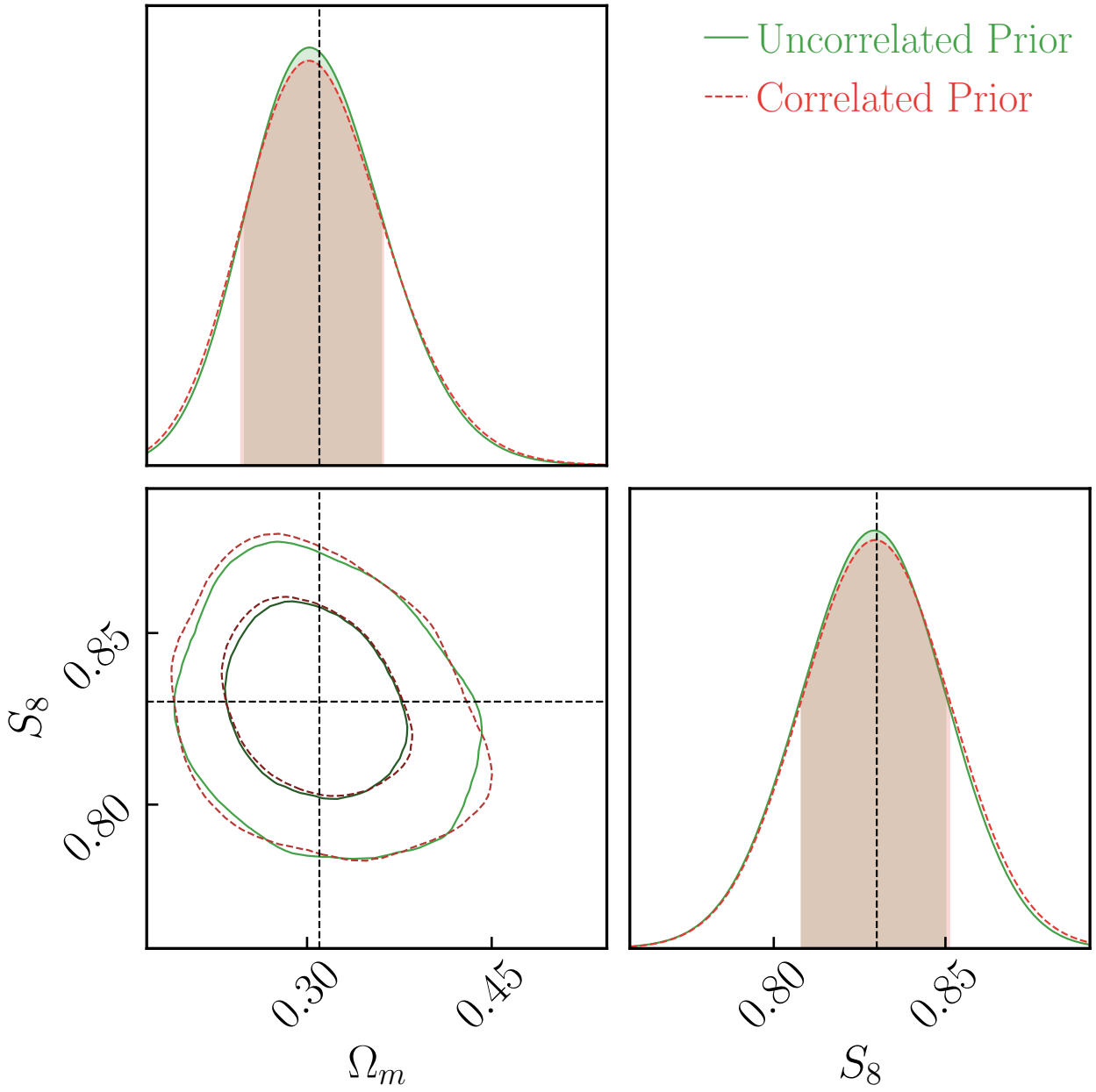

Figure 4.F.1: Comparison between the HSC Y3 mock cosmological analysis using an uncorrelated prior (green) versus correlated prior (red) for the two α parameters. We find no significant change in the cosmological constraints due to this difference in model choices.

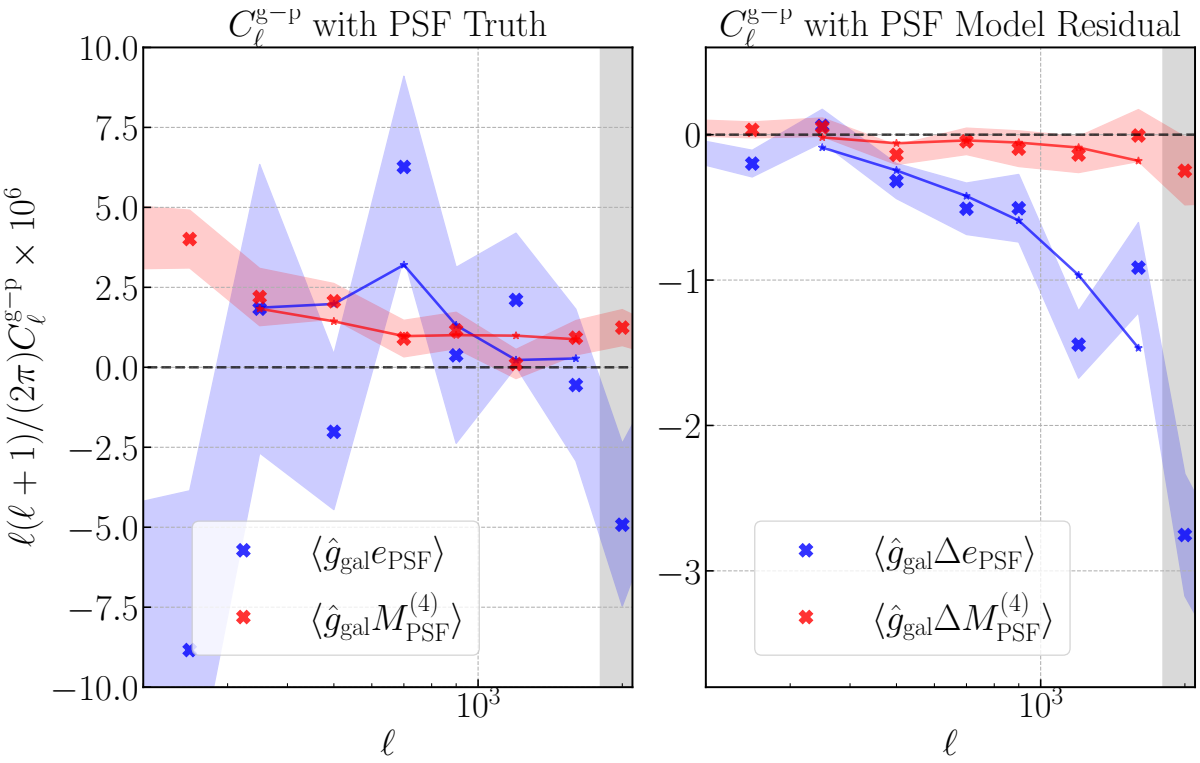

Figure 4.G.1: The measured Fourier space g-p angular power spectrum $\boldsymbol{D}_{gp}$ and the bestfit $\boldsymbol{T}_{gp}$ for the fiducial PSF systematics model. The left panel shows the g-p power spectra with the PSF truth terms expressed by Eqs. (4.67) and (4.69), and the right panel shows the power spectra with the PSF model residual expressed by Eqs. (4.68) and (4.70). We only use scales between $300 \leq \ell \leq 1800$ in our fit (unshaded region).

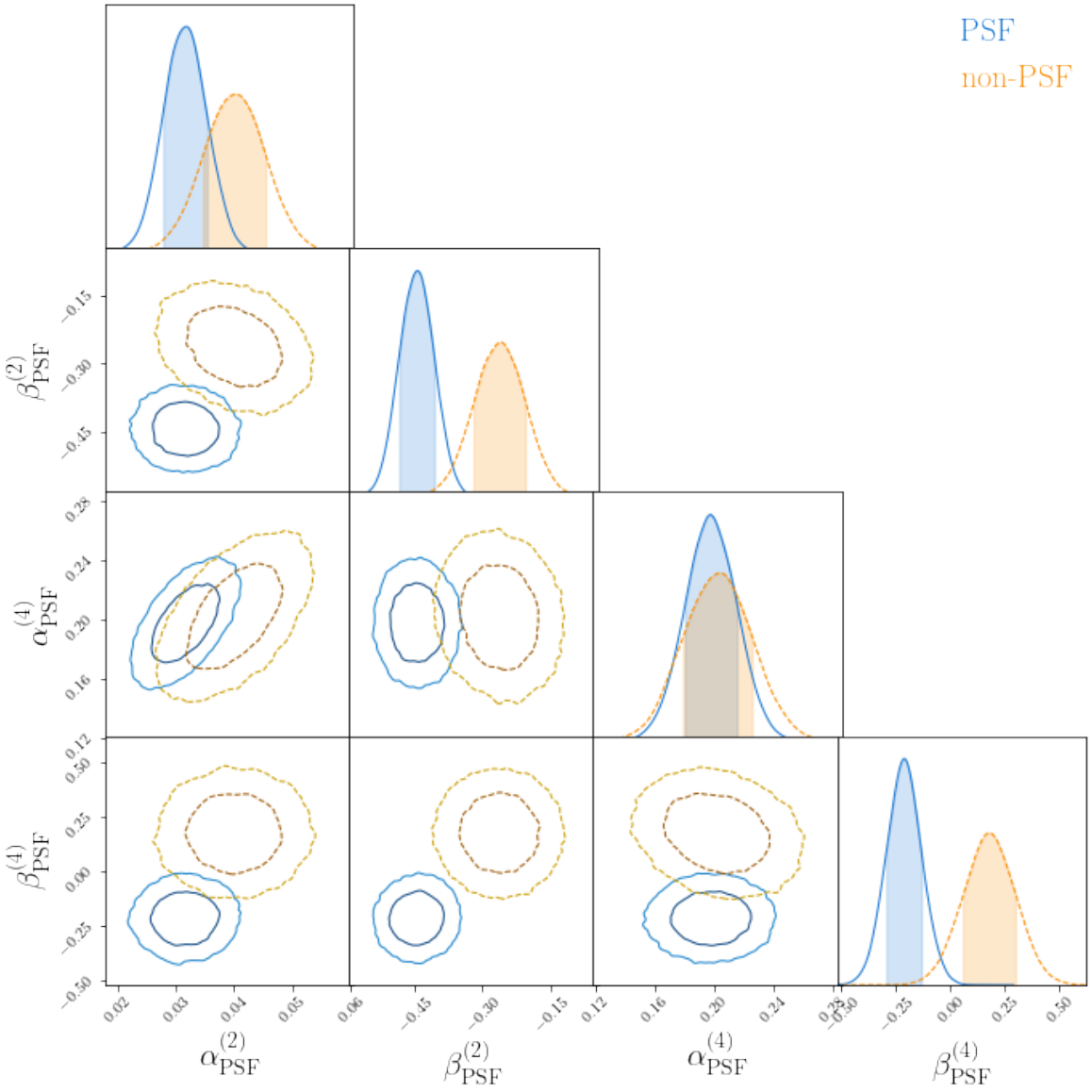

Figure 4.G.2: The posterior probability distribution of the fiducial PSF systematics model parameters applied to the angular power spectra, using the PSF and non-PSF stars.

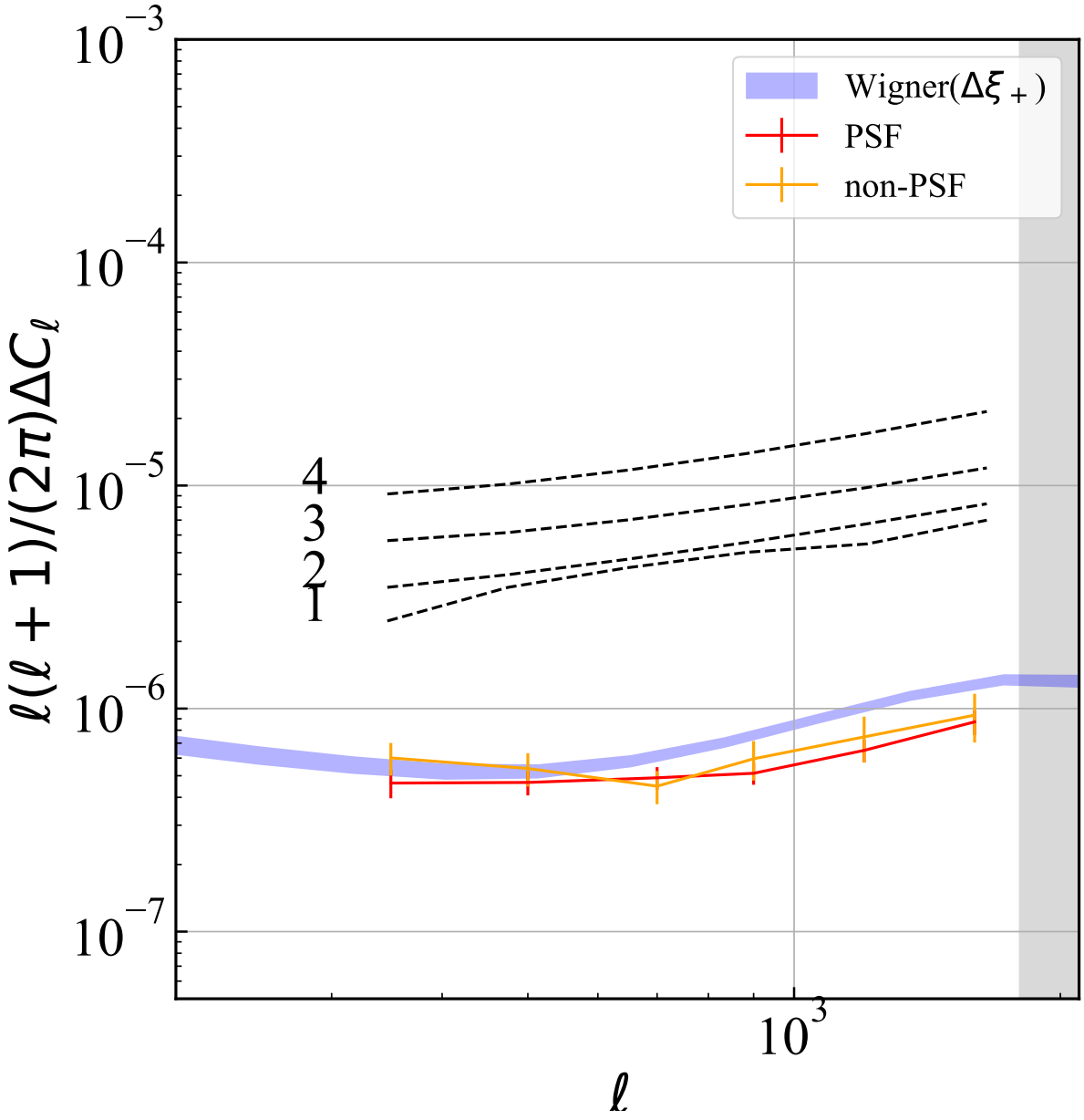

Figure 4.G.3: The additive bias in cosmic shear power spectra from PSF systematics (see Eq. (4.66)), based on the best-fitting values of $\boldsymbol{p}$ (red for PSF stars, yellow for non-PSF), compared to the expected bias based on an inverse-Wigner transform of the bias in the cosmic shear 2PCF predicted by the fiducial model in real space $\Delta\xi_+$ (blue). The theory cosmic shear power spectra in each tomographic bin, based on the fiducial cosmology (see Table 4.6.1), are shown in black. This figure is the Fourier space equivalence to Fig. 4.5.5.

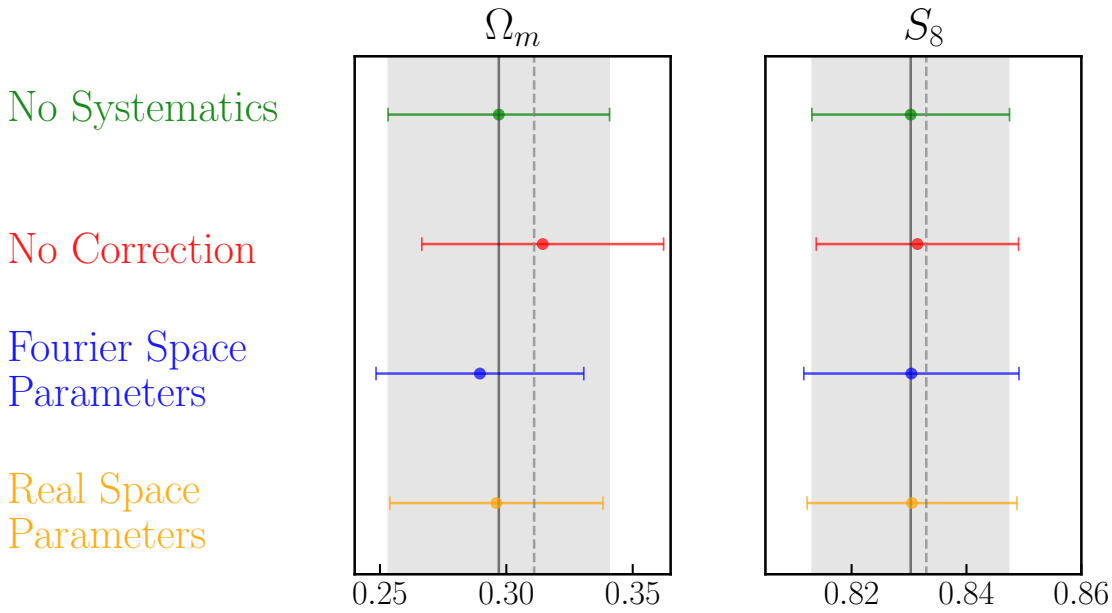

Figure 4.G.4: The 1d constraints on Ω_m and S_8 in the HSC Y3 mock cosmic shear analysis. The green and red lines are the same as in Fig. 4.6.2. The orange lines are the parameter constraints using the fiducial model with PSF parameters inferred in real space, while the blue lines are the parameter constraints using the PSF systematics parameters obtained in the Fourier space. The difference between the correction using real and Fourier space parameters with the fiducial model causes a Ω_m bias around 0.15σ, which is subdominant.

Chapter 5

Photometric Redshift Uncertainties in Weak Gravitational Lensing Shear Analysis: Models and Marginalization

Tianqing Zhang[1], Markus Michael Rau[1,2], Rachel Mandelbaum[1], Xiangchong Li[1], Ben Moews[1,3]

[1]McWilliams Center for Cosmology, Department of Physics, Carnegie Mellon University, 5000 Forbes Ave, Pittsburgh, PA 15213, USA.
[2]High Energy Physics Division, Argonne National Laboratory, Lemont, IL 60439, USA
[3]Pittsburgh Supercomputing Center, Carnegie Mellon University & University of Pittsburgh, 300 S Craig St, Pittsburgh, PA 15213, USA.

Abstract

Recovering credible cosmological parameter constraints in a weak lensing shear analysis requires an accurate model that can be used to marginalize over nuisance parameters describing potential sources of systematic uncertainty, such as the uncertainties on the sample redshift distribution $n(z)$. Due to the challenge of running Markov Chain Monte-Carlo (MCMC) in the high dimensional parameter spaces in which the $n(z)$ uncertainties may be parameterized, it is common practice to simplify the $n(z)$ parameterization or combine MCMC chains that each have a fixed $n(z)$ resampled from the $n(z)$ uncertainties. In this work, we propose a statistically-principled Bayesian resampling approach for marginalizing over the $n(z)$ uncertainty using multiple MCMC chains. We self-consistently compare the new method to existing ones from the literature in the context of a forecasted cosmic shear analysis for the HSC three-year shape catalog, and find that these methods recover statistically consistent errorbars for the cosmological parameter constraints for predicted HSC three-year analysis, implying that using the most computationally efficient of the approaches is appropriate. However, we find that for datasets with the constraining power of the full HSC survey dataset (and, by implication, those upcoming surveys with even tighter constraints), the choice of method for marginalizing over $n(z)$ uncertainty among the several

methods from the literature may modify the 1σ uncertainties on $\Omega_m - S_8$ constraints by $\sim$4%, and a careful model selection is needed to ensure credible parameter intervals.

5.1 Introduction

Over the past decade, wide-field imaging surveys, e.g., the Dark Energy Survey (DES; 79), the Kilo-Degree Survey (KiDS; 80), and the Hyper Suprime-Cam Subaru Strategic Program (HSC SSP; 81), became increasingly powerful, reaching fainter magnitudes and larger areas, and employing improved methods for controlling systematic biases and uncertainties (for a review, see 33). Future surveys such as the Vera C. Rubin Observatory Legacy Survey of Space and Time (LSST; 48; 82), the *Nancy Grace Roman* Space Telescope High Latitude Imaging Survey (49; 83) and *Euclid* (50) will provide even larger data volumes and require more stringent control of systematic errors. With these developments, cosmic shear, the coherent weak gravitational lensing effect on the light from the distant galaxies caused by the large scale structure, becomes one of the most powerful probes to test the standard model of cosmology (1; 75; 76; 126; 154; 155).

The prevalent method of cosmological parameter analysis based on cosmic shear currently relies on tomographic binning (36) and measuring the two-point correlation function (2PCF) of the source galaxy shapes (e.g., 1; 154; 155; 215). For this approach to cosmological analysis, the distribution of the source galaxy distances along the line-of-sight, commonly known as the sample redshift distribution $n(z)$, is an important quantity for forward modeling the auto- or cross-2PCF of cosmic shear within or between tomographic bins, respectively (e.g., 216).

Due to the expense of spectroscopic observations for galaxy samples at the depths of current imaging surveys, weak lensing measurements typically rely on multi-band photometric redshifts as their initial source of redshift information, having only limited and typically not representative training samples with spectroscopic redshifts. There two primary categories of photometric redshift estimation methods (for a review, see 217) are as follows: (a) template fitting, which is based on finding the best-fit spectral energy distributions (SED) template by fitting to the broad-band photometry; and (b) machine learning methods, which use the training sample to learn a relationship between redshift, photometry, and potentially other information, e.g., morphological parameters. The outputs of these photo-z methods are normally probability density functions for individual galaxies, which we will call $p(z)$.

Deriving the aforementioned sample redshift distributions $n(z)$ based on uncertain and potentially biased individual galaxy $p(z)$ is highly non-trivial (e.g., 218), as doing so properly requires deconvolution of the uncertainties and correction for any biases. Methods for reconstructing properly calibrated $n(z)$ include direct calibration based on magnitude re-weighting to match a reference sample with known redshifts (DIR; 219) and cross-correlating spectroscopic samples and photometric samples (CC; 220; 221; 222). Additionally, some methods aim to estimate $n(z)$ directly from photometric observables instead of using photometric redshifts (see, e.g., 223), with the latter branching into machine learning and related approaches in recent years (224; 225). More recent work permits the combination of the $p(z)$ with a

regularized deconvolution of their uncertainty, in combination with the CC method (226) – a method that is being applied in practice by Rau et al., *in prep.* to data from the HSC survey.

Since the cosmic shear signal is sensitive to the sample redshift distribution, it is necessary to carefully model the uncertainties on $n(z)$ and marginalize over them for the current and upcoming surveys (61). The marginalization is not a trivial task, since the uncertainties on $n(z)$ are often modeled in a high dimensional space, making attempts to run a full MCMC extremely computationally intensive. Therefore, several methods have been used to approximately marginalize over the redshift distribution uncertainties. This includes allowing just a shift in the mean redshift of the $n(z)$ for each tomographic bin, a method that has been adopted in many cosmology analyses (e.g., 1; 154; 155; 182). In other cases, methods have been developed to marginalize over realistic uncertainties on $n(z)$, for example by (a) combining 750 MCMC chains each run with a different random realization sampled from the prior for $n(z)$ (227), (b) analytically approximating the likelihood function on the redshift nuisance parameters (228; 229), and (c) ranking $n(z)$ realizations in a lower dimensionality latent space to reduce the number of nuisance parameters (230).

In this study, we develop and apply methodology to systematically compare the performance of methods of $n(z)$ uncertainty marginalization for cosmic shear. Our goal is to quantify tradeoffs such as systematic bias, credible uncertainty estimation, and computational costs. For this purpose, we start by presenting the new resampling approaches for marginalizing over uncertainties in the sample redshift distribution $n(z)$. We apply the new method and compare it with several existing approaches in the literature, in the context of cosmic shear with the three-year HSC shear catalog (HSC Y3; 231). We consider the above-mentioned tradeoffs and make a recommendation for methodology that would be appropriate for cosmology analysis of the HSC Y3 shear catalog.

The structure of this paper is as follows. In Section 5.2, we provide brief background on $n(z)$ uncertainty modeling and the tomographic 2PCF cosmological analysis of cosmic shear. In Section 5.3, we outline the approaches we will explore for marginalization over ensemble redshift uncertainties, including the new method and several pre-existing methods in the literature. We also explain the specific setup for the cosmological analysis we use for comparing these methods. In Section 5.4, we show the results for the cosmological parameter inference using multiple approaches for redshift uncertainty marginalization. In Section 5.5, we summarize our findings in this paper and discuss their practical implications.

5.2 Background

In this section, we provide the background that motivates this study. In Section 5.2.1, we introduce the weak lensing shear analysis paradigm of this paper, and describe the modeling and marginalization of redshift distribution uncertainties in previous shear analyses. Section 5.2.2 describes our flexible parametrization for the sample redshift distribution and discusses our choice of prior on the associated sample redshift distribution model parameters.

5.2.1 Weak Lensing Shear Analysis

In this work, we discuss marginalization over the $n(z)$ uncertainties in a tomographic weak lensing shear analysis (36) based on the two-point correlation function (2PCF;e.g., 46; 161; 232; 233). In this section, we provide a brief background of this analysis paradigm. We define terms, e.g., the data vector (observable) and its covariance matrix, and the forward model that predicts the theoretical value of the observable given cosmological and nuisance parameters. Among nuisance parameters, we emphasize the parameterization of the redshift distribution uncertainties, which is the focus of this paper.

The goal of the weak lensing shear analysis is to extract information about the cosmological model from the shear 2PCF. The cosmic shear observable that is commonly measured in real space analyses (e.g., 1; 154; 155; 182) is the correlation functions of the observed galaxy shears $\xi_{\pm}^{ij}(\theta)$, where θ is the angular separation of the galaxies, and i and j are the indices of the tomographic bin pair. The data vector is obtained by concatenating $\xi_{\pm}^{ij}(\theta)$ from different tomographic bin pairs across all angular bins used for the measurement.

The observed data vector $\boldsymbol{D}$ is compared to the theoretical data vector $\boldsymbol{T}$, which is predicted by a forward modeling pipeline that considers the cosmological parameters and systematic biases and uncertainties, e.g., the uncertainties on the redshift distribution, and the intrinsic alignment of galaxy shapes due to gravitational tidal effects (IA; 62; 63). The log-likelihood of a model parameter vector $\boldsymbol{\Omega}$ is computed by

$$\log(\mathcal{L}(\boldsymbol{\Omega}|\boldsymbol{D})) = (\boldsymbol{D} - \boldsymbol{T}(\boldsymbol{\Omega}))\boldsymbol{\Sigma}^{-1}(\boldsymbol{D} - \boldsymbol{T}(\boldsymbol{\Omega}))^T, \tag{5.1}$$

where $\boldsymbol{\Sigma}$ is the covariance matrix of $\boldsymbol{D}$. MCMC samplers such as MultiNest (187; 188; 189) are used to efficiently sample over the parameter space and provide parameter inferences based on the likelihood in Eq. (5.1) and the prior information on the parameters.

An important step to forward model the shear-shear 2PCF in tomographic bin pairs is to project the 3-D matter power spectrum $P(k, z)$ to the 2-D angular shear power spectrum C_ℓ^{ij}. Under the Limber approximation, the angular shear power spectrum (35; 36) between bins i and j is

$$C_\ell^{ij} = \int \frac{\mathrm{d}\chi}{\chi^2} P(\ell/\chi; z(\chi)) q^i(\chi) q^j(\chi), \tag{5.2}$$

where $P(\ell/\chi; z(\chi))$ is the matter power spectrum at z. $q^i(\chi)$ and $q^j(\chi)$ are the corresponding lensing efficiency function for tomographic bins i and j. $q^i(\chi)$ is directly determined by the underlying redshift distribution $n^i(z)$:

$$q^i(\chi) = \frac{3\Omega_m H_0^2}{2c^2} \frac{\chi}{a(\chi)} \int_\chi^{\chi_h} \mathrm{d}\chi' n^i(\chi'(z)) \frac{\chi' - \chi}{\chi'}, \tag{5.3}$$

where Ω_m is the matter density parameter, H_0 is the Hubble constant, χ is the comoving radial distance, a is the scale factor, and c is the speed of light (e.g., 148; 234). Here we have used the formalism for a flat geometry. We can see that $n^i(z)$ is a key factor determining the angular shear power spectrum, which itself directly determines the shear-shear 2PCF $\xi_{\pm}^{ij}$

(235; 236). Under the flat-sky approximation, $\xi_{\pm}^{ij}$ is expressed as

$$\xi_{\pm}^{ij}(\theta) = \frac{1}{2\pi} \int \mathrm{d}\ell \ell C_{\ell}^{ij} J_{2\mp2}(\ell\theta), \tag{5.4}$$

where J_n is the n-th order Bessel function of the first kind. This deep connection between the redshift distribution and the cosmic shear observables is the reason why it is important to marginalize over the uncertainties on $n(z)$ to recover credible cosmological parameter constraints.

The sample redshift distribution $n(z)$ is often modeled as arrays of histogram bin heights $\boldsymbol{\phi}_{\mathrm{nz}}$, as is further described in Sec. 5.2.2. Since sampling in high dimensional parameter spaces is very computationally expensive, it may not be possible to model the sample redshift distribution uncertainties in every redshift bin that $n(z)$ is estimated on. A majority of previous shear analysis (e.g., 1; 154; 155; 182) parameterized the redshift distribution of bin i by allowing its mean redshift to shift,

$$n^i(z) = n^i(z - \Delta z^i). \tag{5.5}$$

With the shift model, the number of free parameters is equal to the number of the tomographic bins. The priors on these parameters are determined by the prior distributions of the calibrated $n(z)$. The shift model tremendously reduces the number of parameters compared to use of all histogram bin heights $\boldsymbol{\phi}_{\mathrm{nz}}$, though it suffers from a limited number of degrees of freedom compared to the realistic $n(z)$ uncertainties. With cosmic shear analysis becoming increasingly systematics-dominated as the statistical uncertainties become smaller, various methods have been introduced to marginalize over a more realistic estimate of the $n(z)$ prior. In (215), 750 realizations were drawn from the $n(z)$ prior, after which cosmic shear analyses were run on each realization. The chains were then directly concatenated to derive constraints on the cosmological parameters, including their uncertainties. (229) applied the Laplace approximation to the prior of the redshift parameters and assumed the likelihood function is a multivariate Gaussian, thereby analytically marginalizing over the redshift parameter using the self-calibration algorithm. In (230), realizations of $n(z)$ were drawn from the prior distribution, then mapped into a lower-dimensional latent space, within which the likelihood function is smooth.

In this paper, we revisit some of the methods mentioned above to marginalize over the $n(z)$ uncertainties, carrying out tests on mock cosmic shear analyses. We propose a new method of marginalizing over the $n(z)$ uncertainties based on statistical principles. By comparing the new method to other options, we aim to provide the optimal approach for the HSC Y3 cosmic shear analysis.

5.2.2 Prior Specification on the Sample Redshift Distribution

In this section, we briefly summarize how a prior on the sample redshift distribution was specified. For a discussion on the $n(z)$ inference methodology we refer to Rau et al. (in prep.).

As shown in Eq. (5.2), the sample redshift distribution enters the modelling of two point functions via the transfer function in Eq. (5.3). The entire redshift range is subdivided into $N_{\rm bins}$ histogram bins, and the sample redshift distribution in the i-th tomographic bin is parametrized as

$$n^i(z;\boldsymbol{\phi}^i_{\rm nz}) = \sum_{k=1}^{N_{\rm bins}} \boldsymbol{\phi}^i_{\rm nz,k}\mathbf{1}(z\in[z^k_L,z^k_R])\,, \tag{5.6}$$

where $[z^k_L, z^k_R]$ denotes the left/right edges of histogram bin k. $\boldsymbol{\phi}^i_{\rm nz,k}$ is the k-th histogram bin height in the i-th tomographic bin. $\mathbf{1}$ is the indicator function. The distinction between 'histogram bin' and tomographic bin is as follows: the former denotes the bins of the histogram parametrization, the latter denotes the selection bins of the tomography. Eq. 5.6 defines the histogram heights vector $\boldsymbol{\phi}^i_{\rm nz}$ as the parameters of a linear basis function model for the sample redshift distribution with tophat basis functions.

The prior $p(\boldsymbol{\phi}^i_{\rm nz})$, i.e., uncertainties on the sample redshift distribution histogram bin heights in the i-th tomographic bin, is inferred using an extension of the methodology developed in (226). It combines information from both spatial cross-correlations of a reference sample with spectroscopic redshifts and a sample with photometric redshift information. We reiterate that a future publication will provide more details of the inference methodology (Rau, et al, *in prep.*). The method utilizes the 'S16A CAMIRA-LRG sample' (237), a sample of Luminous Red Galaxies selected using the CAMIRA algorithm (238) from the HSC data observed in the first observing season of 2016, as a reference sample. This choice can be motivated by the accurate photometric redshift estimates that are available for the LRGs (relative to the photometric redshift errors in the full HSC S16A sample), and a sufficiently high number density.

The spatial cross-correlation between the CAMIRA-LRG sample (c) and a photometric sample (p) can be predicted as

$$\boldsymbol{w_{\rm sc}} \propto \boldsymbol{\phi}_{\rm nz,p}\,\boldsymbol{b_p}\,\boldsymbol{b_c}\,\boldsymbol{w_{\rm DM}}\,, \tag{5.7}$$

where $\boldsymbol{\phi}_{\rm nz,p}$ denotes the parameters of the sample redshift distribution, ($\boldsymbol{b_p}$/$\boldsymbol{b_c}$) denote the galaxy-dark matter bias parameters of the (photometric/CAMIRA-LRG) samples in each redshift bin and $\boldsymbol{w_{\rm DM}}$ denotes the dark-matter contribution to the cross-correlation signal. We present a simplified vector notation, where the elements in Eq. 5.7 correspond to the cross-correlation measurements in each redshift bin, obtained by measuring the correlation amplitude within a spatial annulus of physical distance as described in (239). Using the auto-correlation of the CAMIRA-LRG galaxies the method fits the linear bias model $b_c(z) = b_0(1+z)$, where $b_0 = 1.06\pm0.03$, consistent with previous measurements from (240). The covariance of the cross-correlation likelihoods is estimated using bootstrap resampling and approximated to be diagonal. This is done for simplicity and can be an inaccurate approximation due to the high correlation of neighboring bins. The method uses THE-WIZZ[1] (239) for the cross-correlation measurements, and selects a scale annulus of $1.5 - 5.0\,$Mpc in analogy to (241).

[1] `https://github.com/morriscb/The-wiZZ/`

We include information from the photometry into the inference by combining the individual galaxy redshift uncertainties of a set of models. Our model set consists of a template fitting code MIZUKI (242) that defines a likelihood, empirical codes MLZ[2] (243) and EPHOR (195) that define a conditional probability density function obtained on a training set and FRANKEN-Z[3] (244) that uses a flux-error weighted score function to map training set objects to galaxies in the photometric dataset. We refer to (195) for a summary of the different methodologies that are available to us. We note that the machine learning-based algorithms do not produce likelihoods (unlike SED fitting techniques). However we will treat their estimates as likelihoods within this framework and refer to a future publication for a description of the technical details.

Following the methodology developed in (226), we infer posteriors of sample redshift distributions as shown in Fig. 5.3.1 using information from both the cross-correlation data vector and the photometry of galaxies. The horizontal axis shows the redshift, the vertical the normalized sample redshift distribution. The legend lists the redshift ranges selected on the best fitting redshift derived using the MIZUKI template fitting code that we use to define the tomographic bins. The error contours correspond to the 68% confidence intervals. The aforementioned posteriors of sample redshift distributions constructed using the joint likelihood of spatial cross-correlations and photometry is then used as the prior distribution on the sample redshift distribution in the following analysis. We neglect here the covariance between the spatial cross-correlations and the lensing observables.

In this work, we assume that the uncertainties in the ensemble redshift distribution for the HSC three-year and full analysis do not significantly decrease compared with those for the first-year HSC analysis. Constraints on the sample redshift distribution are limited by (a) practical issues such as the redshift range of the LRG sample and our knowledge of the galaxy-dark matter bias; (b) the model uncertainty between photometric redshift codes, estimated using the COSMOS2015 field (245). The modeling uncertainty is limited by the cosmic variance, and is independent of the survey area, therefore will not decrease for the HSC three-year analysis compared with the first-year analysis. As a result, the redshift uncertainties are expected to decrease much more slowly than the cosmic shear covariance matrix as the survey area grows.

5.3 Methods

In this section, we describe the methods used to carry out this work. In Section 5.3.1, we describe our parameter inference pipeline, implemented using CosmoSIS (200). In Section 5.3.2, we describe the methods to marginalize over the $n(z)$ uncertainties during the cosmological parameter inference. In addition to employing existing approaches from the literature, we also propose a new method for marginalizing $n(z)$ uncertainties for cosmic shear analysis: a statistically accurate formulation for sampling from the $n(z)$ covariance.

[2] `https://github.com/mgckind/MLZ`

[3] `https://github.com/joshspeagle/frankenz`

Terminology	Symbol	Description
$n^i(z)$ prior	$P(\boldsymbol{\phi}^i_{\rm nz}\|\boldsymbol{\alpha}^i)$	The prior on the $n^i(z)$ histogram bin heights in the i-th tomographic bin. Specifically, we adapt the posterior in Rau et al. (in prep.) $P(\boldsymbol{\phi}^i_{\rm nz}\|\boldsymbol{\alpha}^i)$ parameterized on the Dirichlet parameter $\boldsymbol{\alpha}^i$ for the i-th tomographic bin, as the prior, which is described in Section 5.2.2. We sometimes refer to this as $n(z)$ prior, when the tomographic bin is not specified.
Average $n^i(z)$	$\langle\boldsymbol{\phi}^i_{\rm nz}\rangle$	The average histogram bin heights for $n^i(z)$ in the i-th tomographic bin, averaged over 10000 realizations of $\boldsymbol{\phi}^i_{\rm nz}$ sampled from the $n(z)$ prior.
Mean redshift	$\langle z^i\rangle$	The mean redshift of the i-th tomographic bin, calculated by $\langle z^i\rangle = \int zP(\boldsymbol{\phi}^i_{\rm nz}\|\boldsymbol{\alpha}^i)\mathrm{d}z$, where $P(\boldsymbol{\phi}^i_{\rm nz}\|\boldsymbol{\alpha}^i)$ is the $n^i(z)$ prior of the samples in the i-th tomographic bin.
Data vector	$\boldsymbol{D}$	Shear data vector $\boldsymbol{D} = [\boldsymbol{\xi}^{ij}_+, \boldsymbol{\xi}^{ij}_-]$, where ij is ordered in $[11, 12, 13, 14, 22, 23, 24, 33, 34, 44]$. The generation of data vector is described in Section 5.3.1.
Covariance (matrix)	$\boldsymbol{\Sigma}$	Covariance matrix of the data vector $\boldsymbol{D}$, $\Sigma_{ij} = \langle D_i D_j\rangle$. The covariance matrix used in this work is described in Section 5.3.1.
Inference posterior	$P(\boldsymbol{\Omega}\|\boldsymbol{D})$	The posterior distribution on the cosmological and astrophysical parameters $\boldsymbol{\Omega}$ after marginalizing over the nuisance parameters. In this paper, we specifically consider the $n(z)$ parameters as the nuisance parameters.
Log evidence	$\log(P(\boldsymbol{D}\|\boldsymbol{\phi}_{\rm nz,s}))$	The log-evidence of a particular realization of the $\boldsymbol{\phi}_{\rm nz,s}$, expressed in Eq. (5.12).

Terminology	Symbol	Description
Number of tomographic bins	$N_{\rm tomo}$	The number of tomographic bins, which results in the number of nuisance parameters for the multiplicative bias and shift model. In this work, $N_{\rm tomo} = 4$
Number of resampling $\boldsymbol{\phi}_{\rm nz}$	$N_{\rm sample}$	The number of realizations sampled from the $n(z)$ prior for the direct and Bayesian resampling methods, described in Sec. 5.3.2. For the full analyses in this work, $N_{\rm sample} = 250$.
Number of histogram bins	$N^i_{\rm bins}$	Number of histogram bin heights in the i-th tomographic bins. This is the same as the length of $\boldsymbol{\phi}^i_{\rm nz}$. In this work, $N^i_{\rm bins} = 18(18, 25, 20)$ for tomographic bins 1(2,3,4), respectively.

Table 5.2.1: Table of the redshift distribution and statistics terminologies used for quantities throughout Section 5.3. We also provide a short description of each quantity and the specific values used in this work or a reference to the section where they are described.

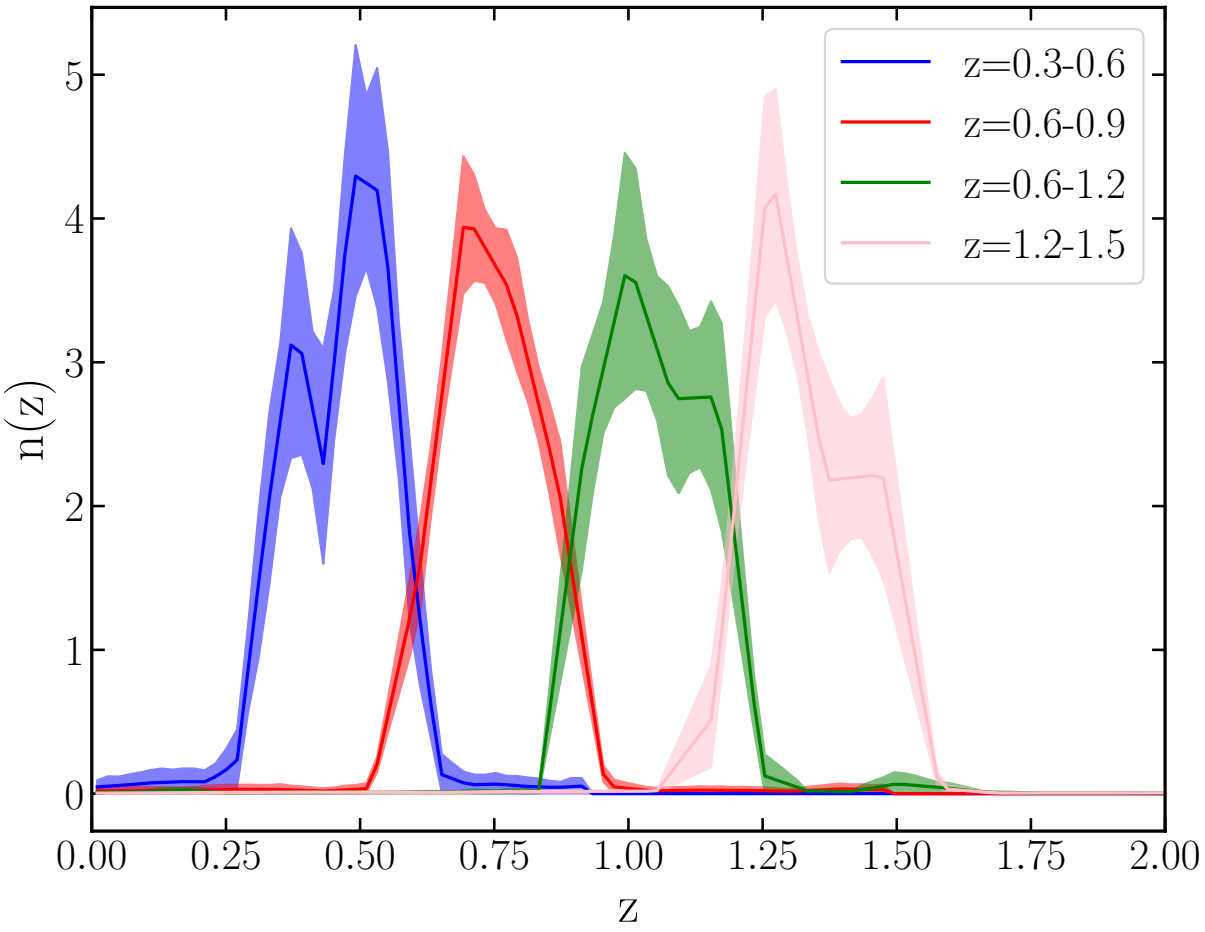

Figure 5.3.1: The sample redshift distribution estimated by cross correlation with 4 tomographic bins, for HSC S16A (Rau, et al., *in prep.*) The shaded regions represent the 68% confidence intervals of the distributions.

The key terminology used for redshift distribution and statistical inference throughout this section, their mathematical symbols, and description are listed in Table 5.2.1.

5.3.1 Cosmological forward modeling

In this section, we describe the cosmic shear forward modeling process, including the cosmological model, the astrophysical model, and other nuisance parameters, for computing the mock data vector and parameter inference. For an initial exploration, we considered a 2-parameter Λ-CDM model that only varies Ω_m and σ_8. We then considered a full analysis with 5 Λ-CDM parameters, 2 astrophysical nuisance parameters, $N_{\rm tomo} = 4$ multiplicative bias parameters and 2 PSF systematics parameters, for a total of 13 parameters. $N_{\rm tomo} = 4$ additional parameters were added for marginalizing over $n(z)$ uncertainties for the shift model. The modeling pipeline used CosmoSIS (200), which is a well-tested and validated

platform for cosmological inference (e.g., in 37).

The cosmological model is described in Section 5.3.1, while the astrophysical and other nuisance parameters are described in Section 5.3.1. The analysis setup (tomographic bins, angular scales, etc.) and mock data vector are described in Section 5.3.1. The sampler and covariance matrices are described in Section 5.3.1.

Cosmological Model

We adopted a Λ-CDM cosmological model throughout this work. We computed the linear matter power spectrum using CAMB (201; 202; 203), and the nonlinear matter power spectrum using the updated HALOFIT (204) from the original version (246). The neutrino mass Ω_ν was fixed to zero, since the weak lensing shear is relatively insensitive to it. The cosmological parameters in our model are provided in Table 5.3.1, including their fiducial values, priors, and whether they are varied or fixed in our analysis.

Astrophysical and Nuisance Parameters

Throughout the analysis, we used the nonlinear alignment model (NLA 148) to model the intrinsic alignment (IA) signal (see also 205; 206, for the development and further extension of the NLA model). In this paper, we adopted the NLA model with an additional term that includes redshift evolution of the alignment amplitude, namely,

$$A(z) = A_{\rm IA}\left[\frac{1+z}{1+z_0}\right]^{\eta}, \tag{5.8}$$

where the fiducial values and priors of the parameters $A_{\rm IA}$, η, and z_0 are shown in Table 5.3.2. In practice, the redshift evolution parameter may absorb some evolution of the source sample properties with redshift, since intrinsic alignments depend on galaxy properties.

Since the IA model in this work has redshift evolution, the intrinsic alignment model parameters may have some degeneracy with the redshift distribution $n(z)$, which motivates marginalizing over the $n(z)$ uncertainty in the analysis.

We computed the shear-shear angular power spectrum from the matter power spectrum and the input $n(z)$, using the formalism in Section 5.2.1. We then added the NLA model shear-IA and IA-IA angular power spectrum to the shear-shear angular power spectrum. Next, we included a per-bin multiplicative shear bias into the observed shear power spectrum using

$$\hat{C}_\ell^{ij} = (1 + m^i + m^j)C_\ell^{ij}, \tag{5.9}$$

where m^i and m^j are the multiplicative biases of bins i and j, respectively. We used Eq. (5.4) to compute the shear-shear correlation function $\xi_\pm^{ij}$.

Finally, we employed a simple model for the additive shear biases at the correlation function level. We included the PSF leakage term α and PSF shape error term β, using the same model as in (1). Our model of the shear-shear correlation function with PSF

systematics is

$$\xi_{\pm}^{ij,\mathrm{model}} = \xi_{\pm}^{ij} + \alpha^2\langle e_{\mathrm{PSF}} e_{\mathrm{PSF}}\rangle + \alpha\beta\langle e_{\mathrm{PSF}}\delta e_{\mathrm{PSF}}\rangle + \beta^2\langle \delta e_{\mathrm{PSF}}\delta e_{\mathrm{PSF}}\rangle, \tag{5.10}$$

where e_{PSF} and δe_{PSF} are the PSF shape and the modeling error of the PSF shape, respectively.

Table 5.3.2 lists the astrophysical and other nuisance parameters, with their fiducial values, priors, and whether they are varied or fixed in our analysis.

Analysis settings and mock data vector

In this work, we used 4 tomographic bins, resulting in 10 tomographic bin pairs. We adopted the angular binning used in the real-space cosmic shear analysis of the first-year HSC catalog (1), i.e., 9 angular bins between 8.06 arcmin and 50.89 arcmin for ξ_+, and 8 angular bins between 32.11 arcmin and 160.93 arcmin for ξ_-. Our data vector $\boldsymbol{D}$, which includes ξ_+ and ξ_-, has a length of 170.

We generated mock data vectors using the forward modeling pipeline described above. To be able to compare the recovered parameter values with their true values, we did not add noise to the data vectors.

We used the Planck results in (20) for the fiducial cosmological parameters in Table 5.3.1. For the IA parameters in Table 5.3.2, we adopted typical integer values for the amplitude A_{IA} and redshift power η, and $z_0 = 0.62$ for the pivot redshift[4] (1; 47). We adopted the prior on α and β from (1), and set the fiducial values to zero.

Our mock shear data vector was generated by averaging the $\xi_\pm$ over 1000 realizations of $n(z)$ sampled from its prior. Note that the auto-correlation $\xi_\pm^{ii}(\langle n(z)\rangle) \neq \langle \xi_\pm^{ii}(n(z))\rangle$, with up to 0.75% difference, as is demonstrated in Appendix **??**. Therefore, we cannot simply use the mean value of the $n(z)$ prior to generate the mock data vector.

Sampler and Covariance Matrices

We sampled the parameter space and estimate the Bayesian evidence using MultiNest (187; 188; 189), due to its rapid speed for relatively accurate evidence evaluation in constant efficiency mode[5]. We fixed the efficiency to 0.1, which is the default value for MultiNest, throughout this work. The log-likelihood of the model is computed by Eq (5.1), with the corresponding covariance matrices.

In this work, we carried out our analyses with two covariance matrices: (a) We estimated the covariance matrix for cosmic shear using the HSC three-year shear catalog. For this

[4]We have used $z_0 = 0.62$ for consistency with previous analysis. However, as described in (247), this choice does not affect the results much; choosing the mean redshift for the HSC survey gives consistent results.

[5]In (248), it is shown that varying the efficiency can bias the model evidence for MultiNest, therefore, we fixed the efficiency of MultiNest to eliminate this bias and for its speed over PolyChord (249; 250)

Parameter	Fiducial	Prior	2-p	full analysis
σ_8	0.824	$U[0.4, 1.2]$	✓	✓
Ω_b	0.0489	$U[0.03, 0.07]$		✓
n_s	0.967	$U[0.87, 1.07]$		✓
h_0	0.677	$U[0.55, 0.9]$		✓
Ω_m	0.311	$U[0.1, 0.8]$	✓	✓
τ	0.0561	const.		
Ω_ν	0.0	const.		
w	-1.0	const.		
w_a	0.0	const.		

Table 5.3.1: Fiducial values and priors of the cosmological parameters used in this paper, along with whether or not they are varied (✓) or not (blank) in the two-parameter (2-p) and full analysis. $U[a, b]$ represents a uniform distribution from a to b.

Parameter	Fiducial	Prior	2-p	full analysis
$A_{\rm IA}$	1.0	$U[-5, 5]$		✓
η	0.0	$U[-5, 5]$		✓
z_0	0.62	const.		
m_1	0.0	$\mathcal{N}(0, 0.01)$		✓
m_2	0.0	$\mathcal{N}(0, 0.01)$		✓
m_3	0.0	$\mathcal{N}(0, 0.01)$		✓
m_4	0.0	$\mathcal{N}(0, 0.01)$		✓
α	0.0	$\mathcal{N}(0, 0.01)$		✓
β	0.0	$\mathcal{N}(0, 1.11)$		✓

Table 5.3.2: Fiducial values and priors of the astrophysical and nuisance parameters used in this paper, along with whether or not they are varied (✓) or not (blank) in the two-parameter (2-p) and full analysis. $U[a, b]$ represents a uniform distribution from a to b, while $\mathcal{N}(\mu, \sigma)$ represents a Gaussian distribution with mean value μ and standard deviation σ.

purpose, we divided every element in the HSC first-year covariance $\mathbf{\Sigma}_{y1}$ (1) by 3, since the survey area is roughly 3 times larger. We denote this covariance matrix as $\mathbf{\Sigma}_{y3} = \mathbf{\Sigma}_{y1}/3$. (b) We estimated the covariance matrix for cosmic shear with the full HSC survey, which is roughly 10 times the area of the first-year catalog. We denote this covariance as $\mathbf{\Sigma}_{\rm full} = \mathbf{\Sigma}_{y1}/10$. There are several significant limitations of this approximation to the future HSC analyses: (a) We decreased the covariance by a factor of the increase in survey area, without considering that the survey footprint has become considerably more contiguous, so the survey edge effects become less important. (b) We adopted the same angular binning and scale cuts as for the HSC first-year analysis, while those cuts are likely to be different for the upcoming three-year analysis and future analyses.

However, we used the covariance matrix of the $n(z)$ prior from the first-year HSC shape catalog when analyzing the three-year and full data vector. In the real analyses, the covariance of the $n(z)$ for the three-year and full catalogs is likely to decrease. However, it is a systematics-dominated quantity, so its uncertainty will not decrease with area as rapidly as does the cosmic shear data vector. Our choice to keep it fixed represents a conservative assumption regarding our ability to understand and control systematic biases and uncertainties in the photometric redshift estimation and the cross-correlation calibration of $n(z)$. As a result of this choice, the impact of $n(z)$ uncertainty on the cosmological parameter constraints gets worse as the dataset grows.

5.3.2 Marginalizing over $n(z)$ uncertainty

In this section, we introduce the different approaches for marginalizing over uncertainty in the ensemble $n(z)$ that are implemented on the mock cosmic shear analysis described in Section 5.3.1. In Section 5.3.2, we introduce the shift model's parameterization. In Section 5.3.2, we introduce the resampling approach, i.e., marginalizing over the sample redshift distribution uncertainties by running many chains with different realizations drawn from the $n(z)$ prior. We propose a new technique for weighting the chains when combining them, based on model evidence, motivated by Bayes theorem.

The $n(z)$ prior that is marginalized over in this work is specified by the histogram bin heights $\boldsymbol{\phi}^i_{\rm nz,k}$ at the center redshift of the histogram z_k for tomographic bin i. respectively, modeled by 4 independent Dirichlet distributions. The Dirichlet distributions are parameterized by arrays $\boldsymbol{\alpha}^i$, with length equal to the number of histogram bins in the corresponding tomographic bin, specified in Section 5.2.2.

Shift Model

The shift model is a simple and approximate model for representing uncertainties in $n(z)$. It allows the sample redshift distribution to shift coherently in redshift space following Eq. (5.5). It is used to marginalize over $n(z)$ uncertainties in many cosmic shear analysis (e.g., 1; 154; 155; 215). For this model, we use the average histogram bin heights $\langle\boldsymbol{\phi}^i_{\rm nz}\rangle$ as the fiducial redshift distribution, specified in row 2 of Table 5.2.1. We let the $\langle\boldsymbol{\phi}^i_{\rm nz}\rangle$ of each tomographic bin shift individually. Therefore, using this model involves introducing $N_{\rm tomo} = 4$ nuisance parameters. We determined the prior on the Δz^i by computing the distribution of the mean redshift $\langle z^i\rangle$ of the tomographic bin i over 10000 realizations of histogram bin heights drawn from the $n^i(z)$ prior. We used a Gaussian distribution for the prior, with zero means and standard deviations determined by the distributions of $\langle z^i\rangle$. The priors on the shift parameters for the four tomographic bins are listed in Table 5.3.3.

In Fig. 5.3.2, we show a comparison of the $n(z)$ uncertainty included by the shift model (in dark shaded regions), versus the total uncertainty of the $n(z)$ prior (in light shaded regions). The uncertainty of the shift model is generated by shifting $\langle n^i(z)\rangle$ with Δz^i sampled from the prior listed in Table 5.3.3. Compared to the full $n(z)$ prior, the shift model underestimates the uncertainties at most redshifts, especially for redshifts where $\langle n^i(z)\rangle$ is relatively flat. The

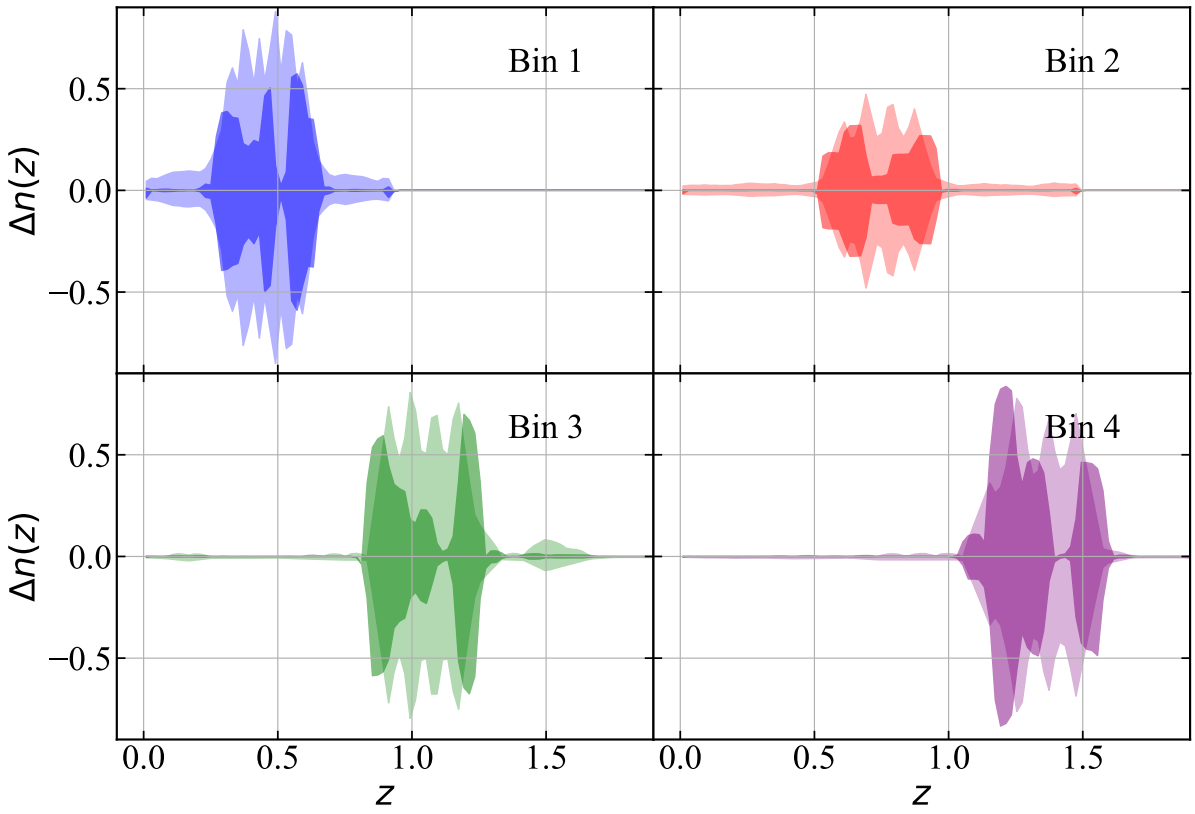

Figure 5.3.2: The 68% confidence intervals of the $n^i(z)$ uncertainties of the fiducial $n(z)$ prior (light shaded regions) and the shift model (dark shaded regions). The shift model generates an unrealistic distribution of $n(z)$ uncertainties, underestimating the uncertainty at most redshifts but overestimating it around the edges of bins 2, 3 and 4.

shift model also overestimates the uncertainties in the wings of the redshift distribution for some the tomographic bins. At the $n(z)$ level, the shift model is an inaccurate representation of the real uncertainty.

Parameter	Fiducial	Prior
Δz^1	0.0	$\mathcal{N}(0, 0.012)$
Δz^2	0.0	$\mathcal{N}(0, 0.01)$
Δz^3	0.0	$\mathcal{N}(0, 0.018)$
Δz^4	0.0	$\mathcal{N}(0, 0.021)$

Table 5.3.3: Fiducial values and priors used for the shift model parameterization of $n(z)$ uncertainties. The standard deviation of the Gaussian prior is calculated from the σ of $\langle z^i \rangle$ from 1000 draws from the $n(z)$ prior.

Resampling Approaches

A different approach for marginalizing over the $n(z)$ uncertainty, with fewer approximations, is to sample many realizations of histogram bin heights from the $n(z)$ prior, and run the cosmological parameter estimation process on each realization as if there are no $n(z)$ uncertainties. To incorporate the $n(z)$ uncertainties in the cosmological parameter estimates, the final step is to combine the results from the different MCMC chains. We refer to this approach as the "resampling approach".

In this work, we propose a resampling method that is based on Bayes' theorem to marginalize over the $n(z)$ uncertainty. We start by deriving the posterior on the cosmological and astrophysical parameters, $P(\boldsymbol{\Omega}|\boldsymbol{D})$, after marginalizing over the uncertainty in the $n(z)$ histogram bin heights, which we denoted $\boldsymbol{\phi}_{\rm nz}$. Here $\boldsymbol{D}$ is the observed cosmic shear data vector $\boldsymbol{D} = [\boldsymbol{\xi}_+, \boldsymbol{\xi}_-]$, see row 4 of Table. 5.2.1. This posterior is as follows:

$$\begin{aligned} P(\boldsymbol{\Omega}|\boldsymbol{D}) &= \int \mathrm{d}\boldsymbol{\phi}_{\rm nz} P(\boldsymbol{\Omega}, \boldsymbol{\phi}_{\rm nz}|\boldsymbol{D}) = \int \mathrm{d}\boldsymbol{\phi}_{\rm nz} P(\boldsymbol{\Omega}|\boldsymbol{D}, \boldsymbol{\phi}_{\rm nz}) P(\boldsymbol{\phi}_{\rm nz}|\boldsymbol{D}) \\ &= \frac{1}{P(\boldsymbol{D})} \int \mathrm{d}\boldsymbol{\phi}_{\rm nz} P(\boldsymbol{\Omega}|\boldsymbol{D}, \boldsymbol{\phi}_{\rm nz}) P(\boldsymbol{D}|\boldsymbol{\phi}_{\rm nz}) P(\boldsymbol{\phi}_{\rm nz}). \end{aligned} \tag{5.11}$$

The first line of the equation is based on conditional probability, and the second line is based on Bayes' theorem. Here $P(\boldsymbol{\Omega}|\boldsymbol{D}, \boldsymbol{\phi}_{\rm nz})$ is the posterior on $\boldsymbol{\Omega}$ with a specific realisation of the redshift distribution $\boldsymbol{\phi}_{\rm nz}$. $P(\boldsymbol{\phi}_{\rm nz})$ is the $n^i(z)$ prior, for which we chose to use $P(\boldsymbol{\phi}_{\rm nz}|\boldsymbol{\alpha})$, the posterior probability distribution for the redshift distribution derived using an extension of the methodology from (226). $P(\boldsymbol{D}|\boldsymbol{\phi}_{\rm nz})$ is the Bayesian evidence of the data given $\boldsymbol{\phi}_{\rm nz}$, evaluated by integrating the joint conditional probability over $\boldsymbol{\Omega}$,

$$P(\boldsymbol{D}|\boldsymbol{\phi}_{\rm nz}) = \int \mathrm{d}\boldsymbol{\Omega} P(\boldsymbol{D}|\boldsymbol{\Omega}, \boldsymbol{\phi}_{\rm nz}) P(\boldsymbol{\Omega}). \tag{5.12}$$

We rely on the MultiNest estimation to the log-evidence, which is shown to have a constant bias from the truth in (248), if the efficiency is kept fixed. This is fine for our purpose: the constant bias on the log-evidence results in a constant factor in the evidence, which is normalized out for the Bayesian weight ω_s.

We now describe how we utilize the resampling approach to estimate $P(\boldsymbol{\Omega}|\boldsymbol{D})$ in Eq. (5.11). We sampled $N_{\rm sample}$ realizations of the redshift distribution $\boldsymbol{\phi}_{\rm nz,s}$, where $s = 1 \ldots N_{\rm sample}$, is the index of a particular realization from the $n(z)$ prior, i.e., $P(\boldsymbol{\phi}_{\rm nz}|\boldsymbol{\alpha})$. We combined the inferred posterior distributions for each one (as represented by the MCMC chains), $P(\boldsymbol{\Omega}|\boldsymbol{D}, \boldsymbol{\phi}_{\rm nz,s})$. By doing so, we effectively evaluated the integral of Eq. (5.11), which can be written the form of a summation,

$$P(\boldsymbol{\Omega}|\boldsymbol{D}) = \frac{1}{N_{\rm sample} P(D)} \sum_{s=1}^{N} P(\boldsymbol{\Omega}|\boldsymbol{D}, \boldsymbol{\phi}_{\rm nz,s}) P(\boldsymbol{D}|\boldsymbol{\phi}_{\rm nz,s}), \tag{5.13}$$

where $\boldsymbol{\phi}_{\rm nz,s}$ is the sth sample of the redshift distribution. Based on Eq. (5.13), we designed a Bayesian weight ω_s for combining the posteriors $P(\boldsymbol{\Omega}|\boldsymbol{D}, \boldsymbol{\phi}_{\rm nz,s})$ that satisfies the following

two conditions:

$$\omega_s \propto P(\boldsymbol{D}|\boldsymbol{\phi}_{\rm nz,s}) \tag{5.14}$$

$$\sum_{s=1}^{N_{\rm sample}} \omega_s = 1. \tag{5.15}$$

Finally, the marginalized posterior of $\boldsymbol{\Omega}$ from the Bayesian resampling can be expressed as

$$P(\boldsymbol{\Omega}|\boldsymbol{D}) = \sum_{s=1}^{N} P(\boldsymbol{\Omega}|\boldsymbol{D}, \boldsymbol{\phi}_{\rm nz,s})\omega_s. \tag{5.16}$$

Note that the constant $1/(N_{\rm sample}P(\boldsymbol{D}))$ in Eq. (5.11) is absorbed in ω_s since summation of ω_s is normalized to 1. This weight ω_s, which is proportional to the Bayesian evidence shown in Eq (5.12), preserves Bayes' theorem, effectively downweighting the $n(z)$ realizations that are not likely to generate the cosmic shear data vector $\boldsymbol{D}$. A similar resampling approach was used in (215); however, the MCMC chains were concatenated with equal weights, which does not preserve Bayes' theorem. We therefore call our approach "Bayesian resampling", and call the method from (215) "direct resampling", throughout the paper.

In principle, with enough samples of the redshift distribution, the Bayesian resampling approach should accurately marginalize over the full prior on $n(z)$ in the cosmic shear analysis, giving more credible parameter constraints than simplified parameterizations, e.g., the shift model. However, it does have its drawbacks: (a) it is computationally intensive to run the full analysis for $N_{\rm sample}$ times, where $N_{\rm sample}$ is the number of redshift distribution samples, (b) it requires the sample redshift distribution $n(z)$ to have a well-defined probability distribution from which samples can be drawn, which might not be the case for some surveys depending on how they infer the ensemble $n(z)$.

Methods Summary

In this section, we briefly summarize the methods for marginalizing over $n(z)$ uncertainty in this work, including the notation and terminology of the marginalization methods.

- No $n(z)$ Uncertainty: We use the average histogram bin height of the $n(z)$ prior, $\langle\boldsymbol{\phi}^i_{\rm nz}\rangle$, as the sample redshift distribution, without marginalizing over any $n(z)$ uncertainties. This is the baseline that other methods are compared to.

- Direct Resampling: We sample $N_{\rm sample}$ realizations of $\boldsymbol{\phi}_{\rm nz,s}$ from the $n(z)$ prior and run cosmological parameter inference on each realization without explicitly accounting for the evidence of the $\boldsymbol{\phi}_{\rm nz,s}$. The chains for different $\boldsymbol{\phi}_{\rm nz,s}$ are then combined with equal weights, implicitly incorporating the $n(z)$ uncertainties into the resulting parameter constraints.

- Bayesian Resampling: This method begins as does direct resampling, but the chains for different $\boldsymbol{\phi}_{\rm nz,s}$ are weighted by their Bayesian evidence, as described in Section 5.3.2.

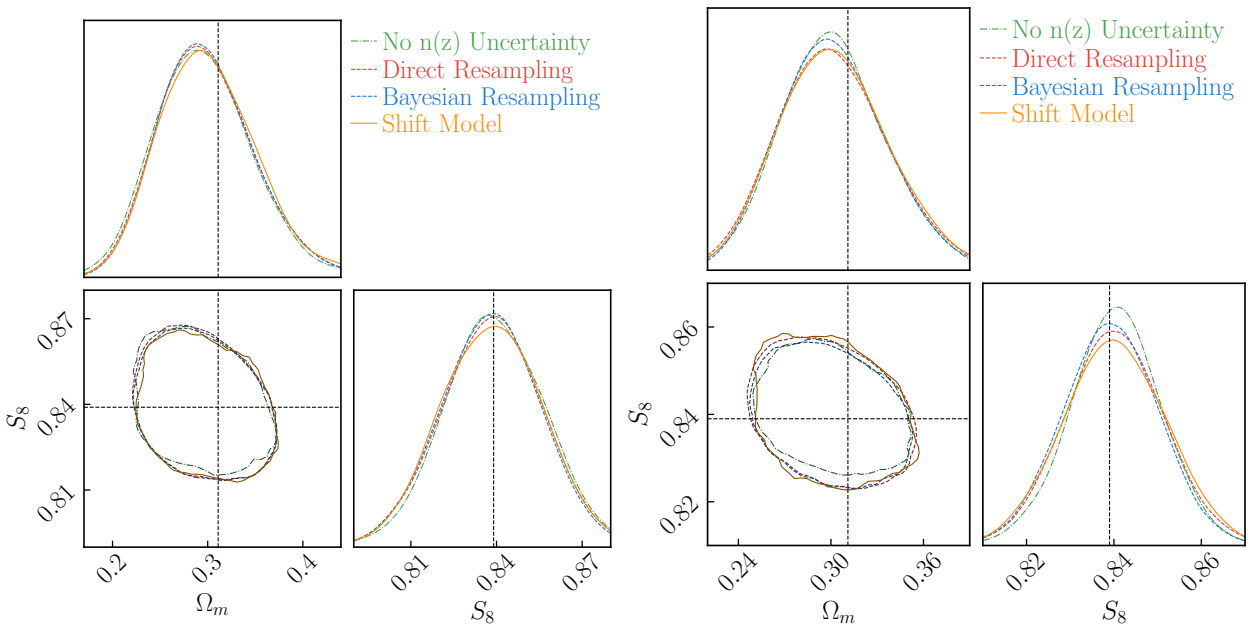

Figure 5.3.3: Parameter constraints for the full analyses, with the three-year covariance matrix Σ_{y3} (top), and the full-data covariance matrix Σ_{full} (bottom), with parameters listed in Table 5.3.1 and 5.3.2, and with $n(z)$ uncertainty marginalized using three different approaches. The green contour shows the results using the average $n(z)$ with no uncertainties, while the red and blue contours show the results using the direct and Bayesian resampling approaches described in Section 5.3.2. The orange contours use the shift model parameterization, with $N_{\text{tomo}} = 4$ nuisance shift model parameters, described in Section 5.3.2. The dashed lines are the true values used to generate data vector. This plot is made using CHAINCONSUMER (9)

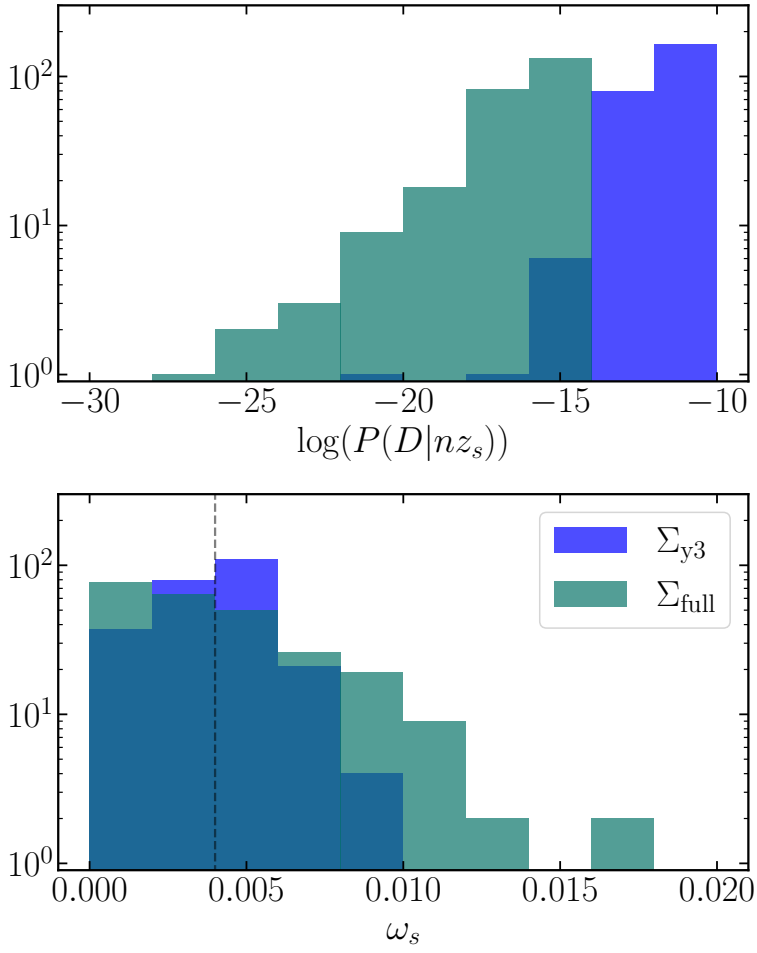

Figure 5.3.4: **Top row:** the distributions of the log-evidence $\log(P(\boldsymbol{D}|\boldsymbol{\phi}_{\rm nz,s}))$, defined in Eq. (5.12). **Bottom row:** the Bayesian weight, ω_s, defined in Eq. (5.16) and applied to the chains in the Bayesian resampling approach. The vertical dashed line in the bottom panel is the constant weight applied to each chain in the 'direct resampling' method, $\omega_c = 1/250$. The distributions of log-evidence and Bayesian weight are broader for $\boldsymbol{\Sigma}_{\rm full}$ than for $\boldsymbol{\Sigma}_{\rm y3}$, because the same amount of $n(z)$ uncertainty has a larger impact on the more statistically powerful dataset, i.e., the full HSC dataset.

- Shift Model: The average histogram bin heights $\langle \boldsymbol{\phi}^i_{\rm nz} \rangle$ is allowed to shift on redshift individually for each tomographic bins, resulting in $N_{\rm tomo} = 4$ nuisance parameters for marginalizing over redshift uncertainty, as described in Section 5.3.2.

5.3.3 Probability Integral Transformation

In this section, we introduce our validation method for the parameter inference results. We note that validating the probability calibration of inference results is an integral part of testing novel inference methodology. Since the 'true value' of a parameter of interest is viewed in the Bayesian picture as a random variable, the posteriors derived using an inference methodology have to present an accurate estimate of that unknown distribution.

A necessary requirement is that our inference adheres to Bayes theorem, which forms the basis of the statistical test presented in the following. To test this, we perform a statistical test based on the probability integral transformation (PIT; 251; 252) to test the validity of the inference statistics. We perform PIT on the cumulative density function (CDF) of S_8, as it is the parameter that the cosmic shear constrains most precisely. The true posterior of the inferred S_8 can be yielded by Bayes' theorem:

$$P(S_8|\boldsymbol{D}) = \frac{P(\boldsymbol{D}|S_8)P(S_8)}{P(D)}. \tag{5.17}$$

We define the CDF of S_8 to be

$$F_{S_8}(S_8) = \int_0^{S_8} \mathrm{d}S_8' P(S_8'|\boldsymbol{D}). \tag{5.18}$$

According to the PIT theorem, a random variable Y drawn from the distribution of $F_{S_8}(S_8)$ in Eq. (5.18), has a range of $[0, 1]$, and the CDF of Y follows

$$F_Y(y) = y, \tag{5.19}$$

where y is a specific value of Y between $[0, 1]$.

To test the credibility of our inference pipeline, we estimate the CDF of S_8, namely, $\hat{F}_{S_8}(y)$, by generating pairs of data vectors $\boldsymbol{D}^\mu$ and S_8^μ, where $\mu = 1, 2 \ldots N_{\rm PIT}$, and $N_{\rm PIT} = 50$. For each μ, we sample a pair of $(\Omega_m^\mu, \sigma_8^\mu)$ with the uniform prior $U_{\Omega_m}[0.2, 0.4]$ and $U_{\sigma_8}[0.7, 1.0]$, and compute the corresponding $S_8^\mu = \sigma_8^\mu \sqrt{\Omega_m^\mu / 0.3}$. We first produce a noiseless data vector using the average $n(z)$, and then add a random noise realization generated using $\boldsymbol{\Sigma}_{\rm y3}$. The noisy data vector is denoted $\boldsymbol{D}^\mu$.

We run the full inference pipeline on each pair of $\boldsymbol{D}^\mu$ and S_8^μ, which generates a posterior $P^\mu(S_8|\boldsymbol{D}^\mu)$. For each μ, we estimate

$$\hat{Y}^\mu = F_{S_8}^\mu(S_8^\mu), \tag{5.20}$$

where $F_{S_8}^\mu$ is the CDF of the S_8 posterior for the μ-th sample. We compare the CDF of $\hat{Y}$ with the expected uniform distribution in Sec. 5.4.2.

By conducting the PIT test, we are checking that the posterior distribution of the cosmological parameters inferred in the inference pipeline is statistically consistent with the true posterior given by Bayes' theorem. This is a crucial validation test for the results of this work, since our conclusion that compares marginalization methods relies on accurate posterior errorbars of the inferred parameters. Crucially, this test must be done using data vectors with noise added according to the covariance matrix, since that noise is what broadens the parameter distribution that we are trying to infer.

5.4 Results

In this section, we show the results of forecasting cosmic shear analyses with different marginalization approaches, following the methods outlined in Sec. 5.3. In Section 5.4.1, we show results of the full analyses, where 5 cosmological parameters, 2 IA parameters, 4 multiplicative biases, 2 PSF systematics parameters, and any parameters used to parametrize uncertainty in $n(z)$ are jointly fit. In Section 5.4.2, we show the PIT validation on noisy data vectors. In Section 5.4.3, we compare the results in this work to that of other work.

5.4.1 Full analysis

In this section, we show the results of the full cosmic shear analysis on the noiseless mock data vector using the redshift marginalization methods listed in Section 5.3.2. We consider 5 cosmological parameters, listed in Table 5.3.1 and explained in Section 5.3.1. Additionally, we consider 2 IA parameters, $N_{\rm tomo} = 4$ multiplicative biases, and 2 PSF systematics parameters, listed in Table 5.3.2 and explained in Section 5.3.1.

We ran a baseline analysis with the average $n(z)$ and no marginalization for comparison, and three marginalization approaches: the direct and Bayesian resampling, described in Section 5.3.2, and the shift model, described in Section 5.3.2. For the resampling approach, we ran $N_{\rm sample} = 250$ chains for both $\mathbf{\Sigma}_{y3}$ and $\mathbf{\Sigma}_{\rm full}$ covariance matrices. There are $N_{\rm tomo} = 4$ nuisance parameters for the shift model, for which the fiducial values and priors are listed in Table 5.3.3.

In the top row of Fig. 5.3.3, we show the 2-d posterior contours and their 1-d projections on the Ω_m-S_8 plane for all four analyses, for the $\mathbf{\Sigma}_{y3}$ covariance (left), and $\mathbf{\Sigma}_{\rm full}$ covariance (right). For the three-year HSC analyses, the different methods of redshift marginalization do not make a visible difference in the contour plot. However, the contours are visibly different for the future full data set of HSC. For $\mathbf{\Sigma}_{y3}$, the number of resampling for both covariances are $N_{\rm sample,y3} = N_{\rm sample,full} = 250$.

In Fig. 5.3.4, we show the distribution of log-evidence $\log(P(\boldsymbol{D}|\boldsymbol{\phi}_{\rm nz,s}))$ and the Bayesian weight ω_s, defined in Eq. (5.12) and Eq. (5.16), of the chains in the resampling approach. The direct resampling method applies uniform weights, while the Bayesian resampling method applies the Bayesian weights ω_s. Since the HSC full data-set has a three-times smaller covariance matrix than the three-year data-set, the same $n(z)$ uncertainty causes a more significant scatter in both the log-evidence and Bayesian weight. This means that Bayesian resampling will become increasingly favoured over direct resampling as the dataset becomes more statistically powerful. In practice, the Bayesian resampling approach is assigning more weight to realizations of the $n(z)$ that produce data vectors that are more consistent with the expected one, while down-weighting realizations with less evident $n(z)$.

In Fig. 5.4.1, we show the uncertainty for individual cosmological parameters from the full analysis chains in Fig. 5.3.3. We used the mean parameter value as the point estimation and the 68% confidence interval as the error bars of the “No $n(z)$ uncertainty" run for the reference. We also show the true value of the parameters in dashed line, as a comparison.

For the three-year analyses, shown on the left, marginalizing over the redshift distribution uncertainty does not noticably increase the error bars on either Ω_m and S_8, except when using the "Direct resampling" method. Since the Bayesian resampling method provides a principled approach to incorporation of redshift distribution uncertainties, we take the consistency between that method and the no marginalization method as a sign that the uncertainty in the cosmic shear data vector dominates the uncertainties on cosmological parameters. Therefore, the "Direct resampling" may be introducing spurious uncertainty by failing to down-weight $n(z)$ realizations that are inconsistent with the data vectors, and is not recommended. For the full HSC dataset analyses, shown on the right, we can see that the conclusion of the three-year analyses holds, though the differences between the methods are more visible. The mean posteriors of the Ω_m are systematically lower than the true input value across different methods. We suspect that the banana-shaped $\Omega_m - \sigma_8$ degeneracy that occurs in the full analysis skews the projected distribution of Ω_m to the lower end, which also causes the underestimation of Ω_m in Fig. 5.4.3.

We further computed the Figure of Merit (FoM) in the Ω_m-S_8 plane (or Ω_m-S_8-$A_{\rm IA}$ space) to compare the methods, defining the FoM as

$$\mathrm{FoM} = \frac{1}{\sqrt{|\mathbf{F}^{-1}|}}, \tag{5.21}$$

where $\mathbf{F}$ is the Fisher matrix of $[\Omega_m, S_8]$(or $[\Omega_m, S_8, A_{\rm IA}]$). $\mathbf{F}$ is calculated by taking the inverse of the covariance matrix of $[\Omega_m, S_8]$ (or $[\Omega_m, S_8, A_{\rm IA}]$), approximating the MultiNest posterior as a 2(3)-d Gaussian distribution. This approximation effectively marginalizes over the other parameters that are varied during the parameter inference. The FoM is proportional to the reciprocal of the contour area. In Fig. 5.4.2, we plot the FoM of all the marginalization methods, divided by the FoM value of the "No $n(z)$ Uncertainty". The two oranges lines correspond to the full analyses in this section. Unsurprisingly, the direct resampling method provides more conservative parameter constraints compared to the Bayesian resampling method, since it does not downweight the outlier $n(z)$ realizations even though they are unlikely to produce the observed shear data vector. The shift model is slightly conservative for $\mathbf{\Sigma}_{\rm full}$, and slightly optimistic for $\mathbf{\Sigma}_{y3}$, compared to the Bayesian resampling. The errorbars on the FoM values are obtained by bootstrapping the chains. As a cross-check on our errorbars, we also ran 10 chains using the shift model for the Y3 analysis, with different sampling seeds. The errorbars obtained using the standard deviations of the inferred cosmological parameters using these 10 chains is within 5% of those from bootstrapping, which suggests that seeding noise cannot explain the differences in FoM between the methods.

Additionally, we report the ratio of FoMs to the fiducial one in the 3D Ω_m-S_8-$A_{\rm IA}$ space using the full covariance matrix $\mathbf{\Sigma}_{\rm full}$. Since the amplitude of intrinsic alignment is also sensitive to the redshift distribution, different marginalization methods also impact its constraints. The FoM in the Ω_m-S_8-$A_{\rm IA}$ space (purple line) follows the same trend as the orange dashed lines in Figure 5.4.2, however, the difference between Bayesian resampling and shift model decreases from 3% to 1% of 1-σ, while the difference between the Bayesian resampling

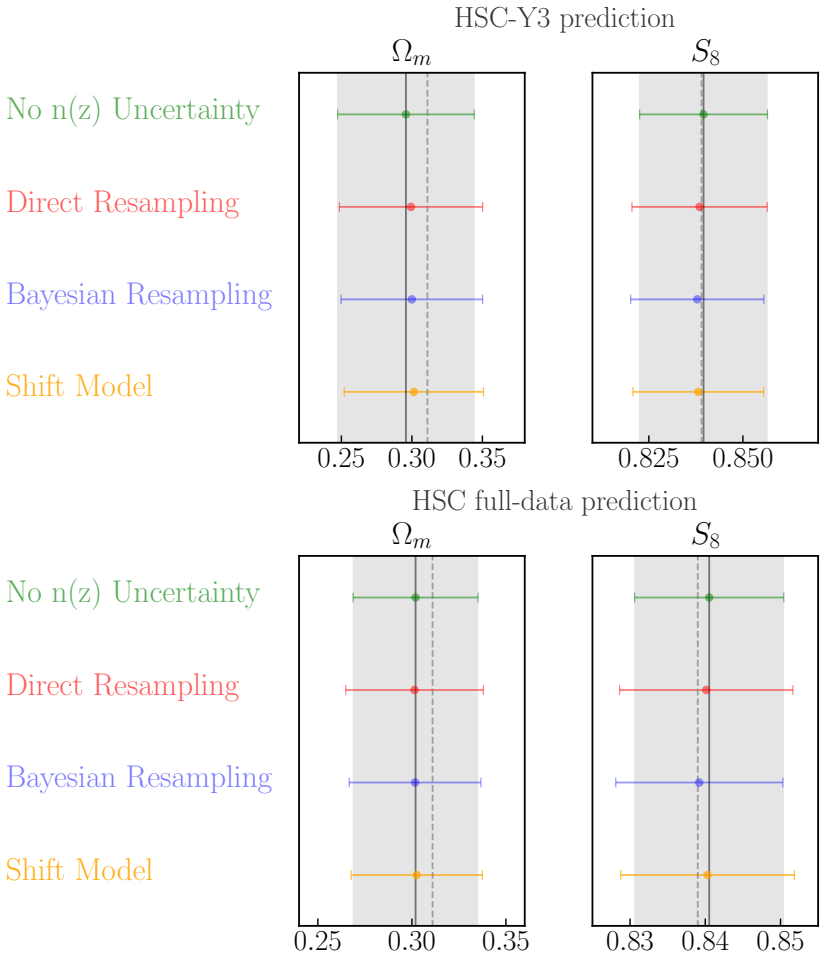

Figure 5.4.1: The 68% confidence intervals (bars) and mean values (dots) of the 1-d projection for the $n(z)$ marginalization approaches compared to the 'No $n(z)$ uncertainty' run, for the $\mathbf{\Sigma}_{y3}$ covariance matrix (top), and $\mathbf{\Sigma}_{\rm full}$ covariance matrix (bottom), for the full analysis. The solid reference lines and the shaded area are the mean values and the 68% confidence intervals of the "No $n(z)$ uncertainty" run. The dashed lines are the parameter truth in Table 5.3.1. We find that the mean values of Ω_m are systematically lower than the true input across different methods. The could be caused by the skewness of the posterior distribution.

and direct resampling decreases from 4% to 3.3% of 1-σ[6]. This further strengthens the conclusion that the Bayesian resampling method behaves comparably to the shift model in HSC Y3 cosmic shear analyses, while direct resampling tends to overestimate the uncertainty in the parameter constraints.

Finally, Fig. 5.4.2 also shows a FoM comparison for an analysis with only two free cosmological parameters, σ_8 and Ω_m, rather than with all cosmological parameters free. For

[6] ΔFoM/FoM0 is proportional to $-2\Delta\sigma/\sigma_0$ for two parameters, while ΔFoM/FoM0 is proportional to $-3\Delta\sigma/\sigma_0$ for three parameters, where σ_0 is the $< 68\%$ confidence range of 'no marginalization'

more details of this analysis, see Appendix 5.B. For this more limited analysis, the direct resampling method overestimates the uncertainties in the (Ω_m, S_8) plane compared to the Bayesian resampling, and therefore is not recommended. The shift model is slightly conservative in this more limited analysis for the full dataset, and slightly optimistic for the three year analysis.

In Fig. 5.4.3, we show the 1-d mean posterior points of 250 chains in the resampling approach, run with $\mathbf{\Sigma}_{\rm full}$. The color of the points are coded by the Bayesian weight ω_s of the chain, which is proportional to the model evidence $P(\boldsymbol{D}|\boldsymbol{\phi}_{\rm nz})$. We can see that drawing different samples from the $n(z)$ posterior introduces scatter in the mean values in the Ω_m-S_8 plane, but generally the samples with mean closer to the centre of the cluster receive a higher weight, while the $n(z)$ samples that generate outliers are down-weighted. This plot demonstrates the necessity of considering whether a given $n(z)$ sample is likely to have generated the data vector that we are observing during the resampling process – as is done in the Bayesian resampling approach, but not direct resampling. We notice that there are nz_s samples that generate mean posterior at the centre of the cluster, but receive a very low weight. There are two possible explanations: (a) the realization nz_s has a best-fit data vector that is on average unbiased compared to the mock data vector $\boldsymbol{D}$, but for certain redshifts or θ values there are significant deviations (with opposite signs, so they compensate on average); (b) the best-fit data vector deviated from that for the true cosmological parameters in a way that is compensated by biases in other cosmological parameters besides Ω_m and S_8. The mean values of the Ω_m are systematically lower than the true value of the input, as we explained earlier in this section.

Following the above presentation of the analysis results, we also compare the computational performance of each redshift distribution marginalization method. In Table 5.4.1, we show the MultiNest settings used for each method, and the computational expense of the full analysis in CPU-hours. The resampling approaches are two orders of magnitude slower than the shift model. While the Bayesian resampling and shift methods lead to comparable uncertainties, as is shown in Fig. 5.4.2, the tremendous computational efficiency of the shift model compared to the Bayesian resampling makes it the recommended choice for the HSC three-year analyses.

For the full HSC three-year cosmic shear analysis, our results suggest that the shift model will produce uncertainties on cosmological parameters that are consistent with the principled Bayesian resampling method to within 3% of 1-σ. Considering that the orders of magnitude difference in computational expense, we recommend the shift model as a well-understood and sufficiently accurate approach for the HSC three-year analysis.

5.4.2 Inference Validation

In this section, we present the inference validation by performing the probability integral transformation (PIT), as described in Sec. 5.3.3. We will focus our analysis on the shift model since it represents the simplest methodology that is appropriate for our data as described in the previous sections. While computationally more expensive, we could also

Method	Live Points	Efficiency	Tolerance	# of chains	CPU-hour/chain	total CPU-hour
No $n(z)$ uncertainty	500	0.1	0.2	1	1.76h*56	98.9h
Direct Resampling	200	0.1	0.2	250	1.05h*28	7350.0h
Bayesian Resampling	200	0.1	0.2	250	1.05h*28	7350.0h
Shift Model	500	0.1	0.2	1	1.77h*56	99.1h

Table 5.4.1: The MultiNest settings used in this work, and computational expense for different marginalization methods, for the full analysis using $\boldsymbol{\Sigma_{y3}}$. The chains are run on Vera, a dedicated server for the McWilliams Center for Cosmology. Each node is equipped with 2 Intel Haswell (E5-2695 v3) CPUs, which have 14 cores per CPU. The resampling approaches, due to the need to run hundreds of individual analyses, are two orders of magnitude slower than the shift model. All chains are ran in constant efficiency mode for more accurate evidence estimation.

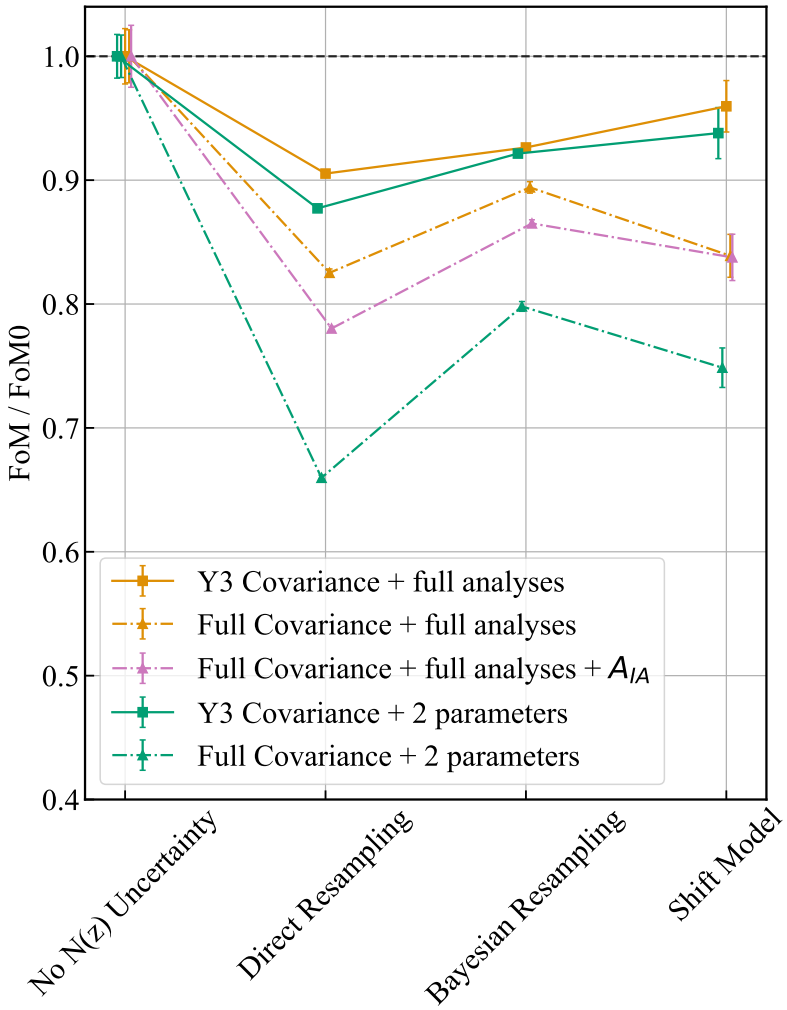

Figure 5.4.2: The Figure of Merit (FoM) comparison in the Ω_m-S_8 plane for each marginalization method. The uncertainties on the FoM are computed by bootstrapping the MCMC chains 100 times. All FoMs are divided by the FoM of the "No $n(z)$ uncertainty" run. The purple line shows FoM ratio for the 3D Ω_m-S_8-$A_{\rm IA}$ space, while other lines shows the FoM in the Ω_m-S_8 space. The direct resampling method is clearly the most conservative method of those tested in this work. The shift model shows similar performance to the Bayesian resampling method. The errorbars on the FoM are given by bootstrapping the chains, which matches the errorbars given by running the analysis with different sampling seeds.

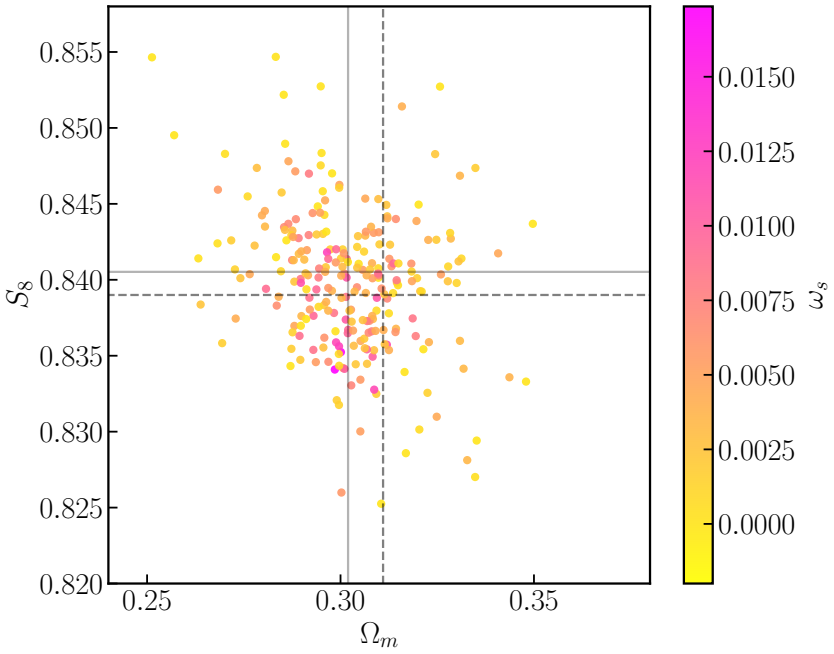

Figure 5.4.3: A scatter plot showing the mean posterior values for the $N_{\rm sample} = 250$ chains with different samples drawn from the $n(z)$ prior, analyzed with all 17 parameters (using the shift model) and with $\mathbf{\Sigma}_{\rm full}$. The colors indicate the Bayesian weight ω_s that the chain receives, determined by its evidence $P(\boldsymbol{D}|\boldsymbol{\phi}_{\rm nz})$, defined in Eq. (5.12). The solid line represents the mean statistics of the 'No $n(z)$ uncertainties' run, while the dashed line represents the true input parameters.

perform the same test for the Bayesian and direct Resampling methods. Given that the three aforementioned methods perform similarly in the context of HSC Y3 analysis, we defer a more detailed investigation to future work and concentrate here on the shift model case.

We sample $N_{\rm pit} = 50$ Ω_m-σ_8 pairs, generate a corresponding noisy data vector, obtain the marginalized S_8 posterior from the full inference with shift model, and compute the CDF of the corresponding true S_8 values.

In Fig. 5.4.4, we compare the CDF of $\hat{Y}$, the CDF of S_8 evaluated at the true S_8, with the CDF of an expected uniform distribution, shown in the black dashed line. On visual inspection, the estimated CDF follows the expected $y = x$ line nicely. We also conduct an Kolmogorov–Smirnov (K-S) test, which computes the maximum difference between the CDF and the expected CDF. The K-S results is $D = 0.094$, with a p-value of 0.737. This means that $\hat{Y}$ is highly consistent with the uniform distribution, which validates our inference pipeline.

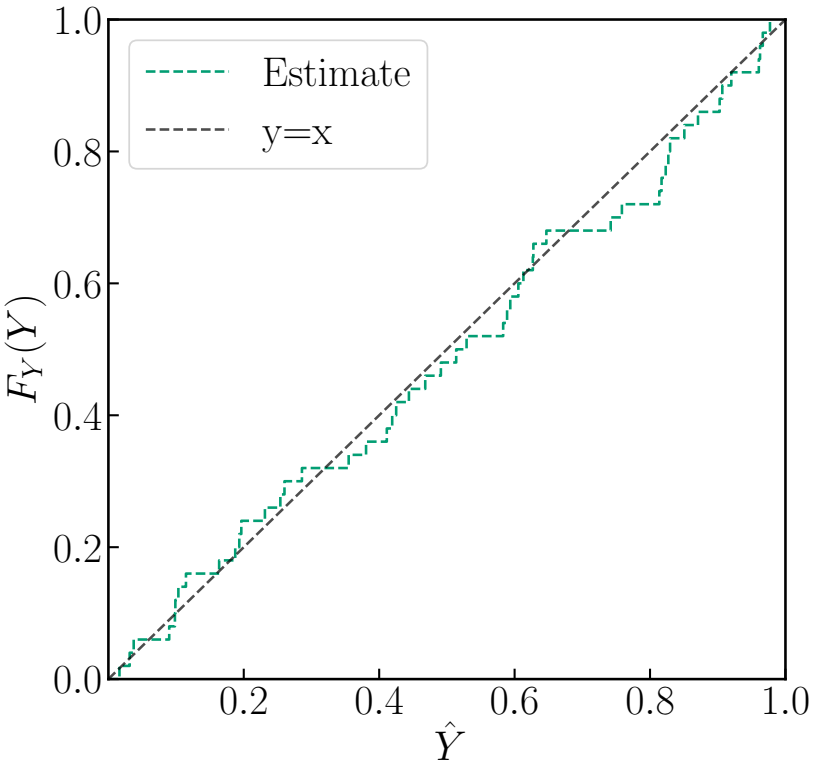

Figure 5.4.4: The CDF of $\hat{Y}$, defined in Sec. 5.3.3. If the statistical inference preserves Bayes' theorem, the CDF of $\hat{Y}$ should follow $y = x$, which is plotted as the black dashed line. This plot shows a high level of consistency between the estimated and expected distribution of $\hat{Y}$.

5.4.3 Literature Comparison

In this section, we compare our Y3 results with the results of marginalizing over $n(z)$ uncertainties in other cosmic shear analysis works. This comparison necessarily excludes the Bayesian resampling approach outlined in this paper, as to the authors' knowledge it has not previously been applied.

In (227), direct resampling marginalization is tested using 3 different $n(z)$ uncertainty distributions: weighted direct calibration (DIR; 223), angular cross-correlation calibration (CC; 220), and a recalibration of $p(z)$ estimated by BPZ (BOR; 253). Compared to 'no $n(z)$ marginalization', the DIR, CC, and BOR approaches increase the uncertainty on S_8 by $14\%, 90\%$, and 19% of 1-σ, respectively. In comparison, we find that direct resampling increases the S_8 errorbar by 5.8% of 1-σ for $\mathbf{\Sigma}_{\rm y3}$, and 15.3% of 1-σ for $\mathbf{\Sigma}_{\rm full}$. This smaller increase in uncertainty is likely due to the larger covariance matrix and a tighter $n(z)$ prior for the HSC Y3 analysis.

In (1), the shift model is adopted as the fiducial approach to marginalizing over $n(z)$

uncertainty, and is compared with 'no $n(z)$ marginalization'. The uncertainty on S_8 increased by 1.4% of 1-σ after marginalizing over the $n(z)$ uncertainties with the shift model, with a wider prior than the one in this work. In this work, the errorbar on S_8 increased by 2.0% of 1-σ after marginalizing using the shift model. Given that (1) has a larger covariance on the shear data vector, as well as a larger prior on the shift model parameters, the results should not agree exactly, and there is no reason to believe they are inconsistent.

In (47), the shift model is compared with 'no $n(z)$ marginalization'. The prior on the shift model parameters are comparable to this work, while the covariance matrix of (47) is smaller than this work. (47) found a 4.4% of 1-σ increase in the S_8 uncertainty, which slightly larger than this work. Given the differences in the data covariance for the analyses, the fact that marginalization had a greater impact in (47) is consistent with expectations.

In (154), the shift model is compared with a more sophisticated $n(z)$ marginalization method, called HYPERRANK (230). The shift model is found to be sufficient for cosmic shear analyses for DES Y3, as validated by HYPERRANK. The fact that a current survey found the shift model to be sufficient is consistent with our finding for HSC Y3.

In (229), a self-calibrated method that models the histogram bin heights $\boldsymbol{\phi}_{\rm nz}$ as a series of comb Gaussian functions is used to analytically marginalize over the $n(z)$ uncertainties. The results are compared to the analysis in (254), which uses a shift model. There are only 1% differences in χ^2 between the results from the self-calibration method and the shift model, though there is a 10% of 1-σ difference in the intrinsic alignment amplitude A_{IA}. This once again shows that the shift model is sufficient for the current generation of cosmic shear analysis for the purpose of cosmological parameter inference, which is consistent with our conclusion.

5.4.4 Summary of results

Overall, our results show that the shift model is a computationally efficient and credible marginalization method for the HSC three-year analysis. Therefore, we recommend that the HSC three-year analysis adopt the shift model for marginalizing $n(z)$ uncertainty.

For the resampling approaches, we find that using the direct resampling approach consistently results in larger contours compared to the Bayesian resampling, as expected. Therefore, we suggest future cosmological analysis adopt the Bayesian resampling method, if resampling is necessary.

For cosmic shear analyses with a substantial uncertainties on the sample redshift distribution, we recommend comparing any candidate marginalization methods for $n(z)$ with the results from the Bayesian resampling method, as the Bayesian resampling method provide a statistically-principled posterior on the marginalized parameters.

5.5 Conclusions

The goal of this work was to understand the performance of methods for incorporating uncertainty in the ensemble redshift distribution in cosmological weak lensing shear analyses,

including their impact on computational expense and on the estimated uncertainties on cosmological parameters.

We proposed a statistically-principled method, called Bayesian resampling, for marginalizing over the uncertainties of the sample redshift distribution $n(z)$ in the cosmic shear analysis. By adding a weight proportional to the model evidence of each $n(z)$ realization, Bayesian resampling effectively down-weights those realizations that are unlikely to generate the observed cosmic shear data vector. The Bayesian resampling method can be applied to any $n(z)$ uncertainties that can be modeled by a probability distribution, even if such parameterization is at a high dimensionality that makes it impossible to model in MCMC.

We ran mock analyses for the HSC three-year and full-data cosmic shear, with 3 $n(z)$ marginalization methods: (a) the newly developed Bayesian resampling method; (b) the direct resampling, for which the weights of all $n(z)$ realizations are the same; (c) the shift model, the most prevalent parameterization used in cosmic shear analyses. Additionally, we ran analyses without marginalizing over the $n(z)$ as a comparison. Our mock data vector is the average cosmic shear signal from the fiducial cosmology, and its covariance is estimated by reducing the covariance compared to that in (1) to account for survey area increases, for the three-year analysis and full analysis correspondingly. Our full theoretical model consists 5 Λ-CDM parameters, 2 intrinsic alignment parameters, 4 multiplicative biases and 2 PSF systematics parameters, plus the 4 redshift parameters when the shift model is adopted.

We compared the 3 marginalization methods and the analysis without marginalization in terms of their impact on the Ω_m-S_8 contours, their 1-d errorbars, the figure of merit (FoM), and computational cost. Here is a high-level summary of how the methods compared to each other.

- Marginalizing over $n(z)$ uncertainties yields larger errorbars on both Ω_m and S_8 for all methods.
- Bayesian resampling yields significant tighter errorbars than direct resampling, implying that the direct resampling is overly-conservative for marginalization.
- The shift model produces consistent errorbars to the Bayesian resampling for HSC Y3. Given that the computational cost for the shift model is $\sim$ 100 times less, it is the recommended method for the upcoming HSC Y3 cosmic shear analyses. For the HSC full analysis, the shift model can yield errorbars that differ by $\sim 3\%$ of 1-σ compared to Bayesian resampling, so it is unclear even in that case whether alternative methods are worthwhile.
- Although the differences between the marginalization methods are statistically evident, the visual differences in the parameter constraint contours are not particularly noticeable.

To test the credibility of our inferred posterior probability distributions of cosmological parameters, we conducted the probability interval transformation (PIT) test on noisy data vectors generated with a range of cosmological parameters, to ensure the applicability of our

results to real cosmic shear analyses. We sampled 50 pairs of Ω_m-σ_8-$\boldsymbol{D}$, and compare the CDF distribution of S_8 at the true S_8^μ values with a uniform distribution. Our estimated CDF distribution passes the K-S test, thus validating our inference pipeline using the shift model.

These results have a few implications for future cosmic shear analyses. First, our results suggest that the shift model should be compared with Bayesian resampling for specific survey scenarios (statistical constraining power, etc.) to assess whether the shift model performs sufficiently well to be usable, given its far lower computational expense. The shift model is fundamentally a different $n(z)$ uncertainty model from the original $n(z)$ distribution. Second, when using the resampling approach to marginalizing over $n(z)$ uncertainties is necessary for a weak lensing measurement, the Bayesian resampling approach is preferred over direct resampling, because of its consistency with Bayesian statistics. Moreover, Bayesian resampling does require an accurate estimate of the ratio of the Bayesian evidences between realizations of redshift distributions.

There are several caveats in this work. (a) We reach the conclusion that a sophisticated marginalization method is going to be increasingly preferred based on the assumption that lensing measurements become more powerful as survey area increases, but the uncertainty on $n(z)$ is presumed to be systematics dominated. The reason for this assumption is that the $n(z)$ uncertainties are limited by the cosmic variance of the COSMOS2015 field, which we used to assess the modeling uncertainties. If this assumption changes, then the comparison needs to be revisited. This assumption is discussed in detail in Section 5.2.2. (b) We use the same angular and tomographic binning for the mock analyses in this paper, though the actual analyses of HSC Y3 and full data are likely to have different binning strategies. We also make very simple estimates of the covariance matrices in the mock analyses, ignoring the evolving footprint shape of the HSC survey. (c) The assumption in this work is that we can place a prior on the source redshift distribution that is statistically independent of our data vector. That was a good approximation in this case, for $n(z)$ calibration based on photometry and cross-correlations, and for the data vector involving shear-shear only. However, future analyses with more complex data vectors (e.g., including large-scale structure clustering) and/or $n(z)$ posteriors may violate this assumption in our formalism, which would require additional efforts to take into account.

We conclude by mentioning some avenues for future investigations. First, the cosmic shear data vector is sensitive to the mean redshift of the tomographic bin, which is likely the reason why the shift model is sufficient for current surveys in practice. However, galaxy clustering is sensitive to other statistics of the ensemble redshift distribution, such as its width (e.g., 37). Therefore, the validity of the shift model in galaxy-galaxy lensing, clustering and 3x2pt analyses should be directly tested.

Finally, the resampling approach for the $n(z)$ marginalization requires thousands of CPU-hours. Importance sampling methods can be added to the method to reduce the number of realizations needed. However, importance sampling faces other challenges: since $n(z)$ distributions normally are parameterized with high dimensionality, the importance weights are easily dominated by a few samples. It might also be extremely challenging to perform

importance sampling on some $n(z)$ priors. It would be valuable to identify solutions to this problem and demonstrate how to effectively accelerate $n(z)$ resampling approaches using importance sampling.

5.A Impact of $\xi_{\pm}(\langle\phi_{\rm nz}\rangle)$

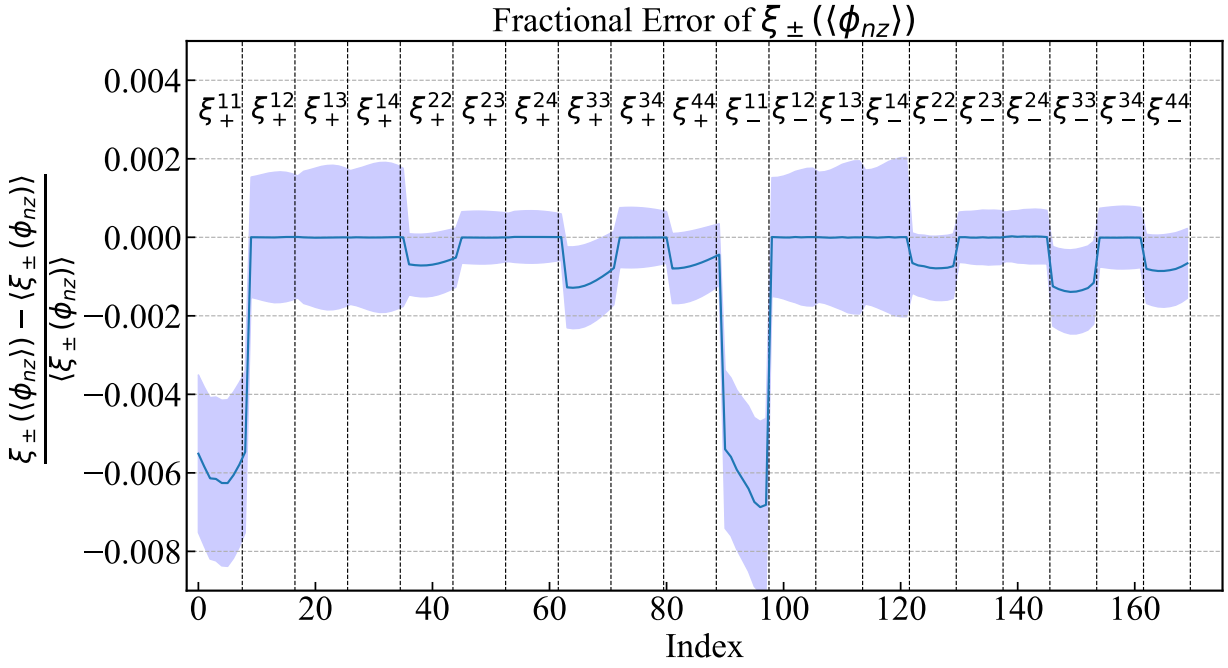

Figure 5.A.1: The fractional error of the $\xi_{\pm}^{ij}(\langle n(z)\rangle)$ compared to $\langle\xi_{\pm}^{ij}(n(z))\rangle$. The x-axis is the index of the value in the data vector, with 9 angular bins for each tomographic ξ_{+}^{ij} bin pair, and 8 angular bins for each ξ_{-}^{ij} bin pair. There is a statistically significant sub-percent difference between the auto-correlations, which shows that taking the average of $n(z)$ does not commute with computing the 2PCF. Therefore $\langle\xi_{\pm}^{ij}(n(z))\rangle$ should be used to avoid sub-percent bias when this level of precision matters. This fractional difference is largest at low redshift because the uncertainties in the mean redshifts are comparable in magnitude for all bins, but the 2PCF is lower at low redshift.

In Figure **??**, we demonstrate that generating the auto-correlation of the mock data vector using the average $n(z)$ is different from the taking the average of data vectors generated by random draws from the posterior for $n(z)$. Therefore, for this work, in which the conclusion is sensitive to bias at the sub-percentage level, we choose to use $\langle\xi_{\pm}^{ii}(n(z))\rangle$ from 1000 $n(z)$ samples to generate the mock data vector in Section 5.3.1.

The reason that only the auto-correlation is affected in Figure 5.A.1 can be explained by

Eqs. (5.2) and (5.3). Since $n^i(\chi(z))$ is independent of $n^j(\chi(z))$ if $i \neq j$, the transfer functions $q^i(\chi)$ and $q^j(\chi)$ are thus independent. As a result, when $i \neq j$,

$$\langle C_\ell^{ij} \rangle = \int \frac{\mathrm{d}\chi}{\chi^2} P(\ell/\chi; z(\chi)) \langle q^i(\chi) \rangle \langle q^j(\chi) \rangle. \tag{5.22}$$

Notice that Eq. (5.22) only holds when $n^i(\chi(z))$ is independent of $n^j(\chi(z))$. Otherwise, both auto- and cross-correlations in the mock data vector will be affected by using the average $n(z)$. Also note that in the case that some overall source of uncertainty was to lead to correlations between the uncertainties in the redshift distributions for different bins, both auto- and cross-correlations would be affected.

5.B Two-Parameter Analyses

In this work, we also carried out the cosmological parameter inference for a case where only Ω_m and σ_8, along with $n(z)$ marginalization nuisance parameters, are freed. This scaled-down test is initially designed for testing and sanity-checking our inference and analysis software. The constant values for other cosmological and nuisance parameters, and the priors for Ω_m and σ_8, are listed in Tables 5.3.1 and 5.3.2.

We carried out cosmological parameter estimation for the three marginalization methods in the 2-parameter cases, along with the "no $n(z)$ uncertainty" run for comparison. The contour plots in the Ω_m and S_8 plane are well-behaved, and the results lead to similar conclusions as for the full analyses, so we do not show them in the paper. The Figure-of-Merit ratio of the three marginalization methods to that of "no $n(z)$ uncertainty" is shown in green lines in Figure 5.4.2, and the conclusion based on the 2-parameter cases is similar to ones drawn from the full analyses.

Chapter 6

Conclusion and Discussion

In the past two decades, weak lensing has witnessed exponential growth in the available data volume. This trend is set to continue in the next two decades with deeper and wider extragalactic surveys, e.g., Vera C. Rubin Observatory LSST and the High-Latitude Survey on the Roman space telescope. The rapid increase in data volume will significantly increase the figure-of-merit that the weak lensing measurement has on constraining the dark energy. It also posts harder challenges in understanding its systematics in image processing, data analysis, and astrophysical modeling stages. This thesis improves the understanding of two sources of systematics in weak lensing, the Point Source Function (PSF) and redshift distribution uncertainty. The methods I developed guided corresponding model selection in the HSC Year-3 cosmological analysis, and are projected to provide valuable insights into the future cosmological analyses of HSC, DES, Rubin Observatory, and Roman HLS.

§ 2 to § 4 is a sequence of three projects that study the impact of the PSF higher moments on weak lensing. § 2 is a proof-of-concept demonstration that the PSF higher moments modeling residuals are coupled with shear bias. In particular, I demonstrated that the residual in modeling PSF radial fourth moments can cause multiplicative shear bias, and the level of the multiplicative bias is comparable that of the PSF second moments, revealing its underestimated significance.

§ 3 builds upon § 2, by extending the scope of interest to the modeling error of the entire PSF higher moments space. I developed a numerical method that is based on basis expansion and gradient descent for generating PSF images given input moments. This technique enables us to connect the PSF higher moments bias to the shear bias quantitatively. I utilize the Gaussian random map to generate HSC-like mocks for the higher moments residual and use Fisher forecasts to predict the level of multiplicative and additive bias for the LSST Y1 and Y10 analysis. Our results show that the PSF higher moments can cause significant systematics to the weak lensing observables if not actively monitored and modeled.

§ 4 takes the understanding of § 2 and § 3 to a real shear catalog and cosmic shear analysis. It demonstrates the benefit of active monitoring proposed in § 3 by conducting extensive null tests with the dataset. The null tests revealed an otherwise undetected leakage by the PSF fourth moments. I demonstrate that our new model can fully mitigate the additive

contamination that PSF cause on the shear-shear TPCF in mock tests. This work guided PSF systematics modeling choice in the HSC Year-3 cosmic shear analysis (5; 72).

With continuous effort in open software development, I expect the PSF higher moments effects in weak lensing will be closely monitored and modeled in the upcoming analysis and surveys. This can be achieved by improving multiple steps in the data analysis pipeline of weak lensing. Firstly, higher moments measurement of the star samples should be done in the measurement pipeline, at least for the moments that are deemed critical. Secondly, ρ-statistics for the higher moments should be calculated in the quality check software. Lastly, the higher moments null tests should be conducted after the shear catalog is produced for each analysis.

There are other aspects of the PSF systematics problem that we need to improve our understanding of. One example is how null tests are conducted given a chromatic PSF model since it breaks the assumption that the star catalog shares the same PSF field as the galaxy catalog. Another challenge is how to generate a more realistic and complex mock catalog for stress testing the mitigation model – as a simplified mock catalog might obscure the downside of the model. Such generation likely requires advanced statistical and machine learning techniques.

§ 5 shifts the focus to another very important source of systematic to weak lensing, the redshift distribution uncertainty. The redshift distribution $n(z)$ of the weak lensing source sample is an important part of the modeling of the weak lensing signal since it is directly coupled with the amplitude of the correlation function of a galaxy ensemble pair. However, the high dimensionality of the $n(z)$ uncertainty makes it computationally infeasible to marginalize in an MCMC inference. We proposed a statistically principled method for marginalizing the full uncertainty of the $n(z)$, by resampling the $n(z)$ distribution and recombining the posterior from each $n(z)$ realization weighted by their Bayesian evidence. We compare our methods to a traditional method and a slightly different resampling method, and show that while our method is computationally expensive, it provides a feasible way to marginalize over the full $n(z)$ uncertainty in a cosmic shear analysis. For the current surveys, the difference between our model and the traditional model is still negligible, but we show the gap will increase for future surveys.

There is much future work in the realm of redshift distribution treatment in weak lensing. For the Bayesian resampling method, an extension of the method to the joint analysis of clustering and weak lensing is valuable, since the joint analysis will be sensitive to more modes in the redshift distribution. Another important aspect is to speed up the algorithm. Currently, the resampling marginalization requires hundreds of independent MCMC runs to produce one posterior, which is very expensive. A resampling method that utilizes importance sampling is a promising pathway to achieve this goal. Further work is also required to study the impact of double counting in cases where the spectroscopic samples are used as both lens and redshift calibration samples.

Looking at a broader picture, photometric redshift uncertainty is likely one of the most complicated systematics in wide-field imaging surveys for the future decade. Extensive work is needed to understand and develop a pathway to compare and combine different methods

of the photometric redshift, along with incomplete spectroscopic redshift datasets at a scale of billions of galaxies. Wider and deeper spectroscopic datasets from instruments such as the Dark Energy Spectroscopic Instrument and the prism survey of Roman HLS bring exciting assets to improve the redshift calibration on the high redshift end and faint end.

The next decade will be an exciting era for weak lensing science amid various challenges of understanding the systematics error. However, the weak lensing community is not lacking in ideas to tackle these challenges or lacking in motivation. End-to-end validation for the science analysis pipeline can systemically catch modeling bias and bugs in software. Additionally, the call for open software makes the scientific results less prone to human error. Novel analysis methods such as higher-order statistics or machine learning-based inference aim at extracting more information from the datasets, but the systematics error specific to the new probes will need additional attention. With a collaborative international weak lensing community, weak lensing has a promising future in providing precise measurements on the large-scale structure and nature of dark energy, providing impetus for the advancement of modern physics and cosmology.

Bibliography

[1] T. Hamana, M. Shirasaki, S. Miyazaki, C. Hikage, M. Oguri, S. More, R. Armstrong, A. Leauthaud, R. Mandelbaum, H. Miyatake, A. J. Nishizawa, M. Simet, M. Takada, H. Aihara, J. Bosch, Y. Komiyama, R. Lupton, H. Murayama, M. A. Strauss, and M. Tanaka, "Cosmological constraints from cosmic shear two-point correlation functions with HSC survey first-year data," *PASJ*, vol. 72, p. 16, Feb. 2020.

[2] S. Dodelson and F. Schmidt, *Modern Cosmology*. 2020.

[3] F. van den Bosch, "Yale graduate course astro 610: Theory of galaxy formation."

[4] S. More, S. Sugiyama, H. Miyatake, M. M. Rau, M. Shirasaki, X. Li, A. J. Nishizawa, K. Osato, T. Zhang, M. Takada, T. Hamana, R. Takahashi, R. Dalal, R. Mandelbaum, M. A. Strauss, Y. Kobayashi, T. Nishimichi, M. Oguri, A. Kannawadi, R. Armstrong, Y. Komiyama, R. H. Lupton, N. B. Lust, S. Miyazaki, H. Murayama, Y. Okura, P. A. Price, P. J. Tait, M. Tanaka, and S.-Y. Wang, "Hyper Suprime-Cam Year 3 Results: Measurements of Clustering of SDSS-BOSS Galaxies, Galaxy-Galaxy Lensing and Cosmic Shear," *arXiv e-prints*, p. arXiv:2304.00703, Apr. 2023.

[5] X. Li, T. Zhang, S. Sugiyama, R. Dalal, M. M. Rau, R. Mandelbaum, M. Takada, S. More, M. A. Strauss, H. Miyatake, M. Shirasaki, T. Hamana, M. Oguri, W. Luo, A. J. Nishizawa, R. Takahashi, A. Nicola, K. Osato, A. Kannawadi, T. Sunayama, R. Armstrong, Y. Komiyama, R. H. Lupton, N. B. Lust, S. Miyazaki, H. Murayama, T. Nishimichi, Y. Okura, P. A. Price, P. J. Tait, M. Tanaka, and S.-Y. Wang, "Hyper Suprime-Cam Year 3 Results: Cosmology from Cosmic Shear Two-point Correlation Functions," *arXiv e-prints*, p. arXiv:2304.00702, Apr. 2023.

[6] H. Miyatake, S. Sugiyama, M. Takada, T. Nishimichi, X. Li, M. Shirasaki, S. More, Y. Kobayashi, A. J. Nishizawa, M. M. Rau, T. Zhang, R. Takahashi, R. Dalal, R. Mandelbaum, M. A. Strauss, T. Hamana, M. Oguri, K. Osato, W. Luo, A. Kannawadi, B.-C. Hsieh, R. Armstrong, Y. Komiyama, R. H. Lupton, N. B. Lust, L. A. MacArthur, S. Miyazaki, H. Murayama, Y. Okura, P. A. Price, T. Sunayama, P. J. Tait, M. Tanaka, and S.-Y. Wang, "Hyper Suprime-Cam Year 3 Results: Cosmology from Galaxy Clustering and Weak Lensing with HSC and SDSS using the Emulator Based Halo Model," *arXiv e-prints*, p. arXiv:2304.00704, Apr. 2023.

[7] S. Sugiyama, H. Miyatake, S. More, X. Li, M. Shirasaki, M. Takada, Y. Kobayashi, R. Takahashi, T. Nishimichi, A. J. Nishizawa, M. M. Rau, T. Zhang, R. Dalal, R. Mandelbaum, M. A. Strauss, T. Hamana, M. Oguri, K. Osato, A. Kannawadi, R. Armstrong, Y. Komiyama, R. H. Lupton, N. B. Lust, S. Miyazaki, H. Murayama, Y. Okura, P. A. Price, P. J. Tait, M. Tanaka, and S.-Y. Wang, "Hyper Suprime-Cam Year 3 Results: Cosmology from Galaxy Clustering and Weak Lensing with HSC and SDSS using the Minimal Bias Model," *arXiv e-prints*, p. arXiv:2304.00705, Apr. 2023.

[8] M. Jarvis, G. Bernstein, and B. Jain, "The skewness of the aperture mass statistic," *MNRAS*, vol. 352, pp. 338–352, July 2004.

[9] S. R. Hinton, "ChainConsumer," *The Journal of Open Source Software*, vol. 1, p. 00045, Aug. 2016.

[10] A. Rothman, *The Dawn of Modern Cosmology*. Penguin Books Ltd, 2023.

[11] V. M. Slipher, "Nebulae," *Proceedings of the American Philosophical Society*, vol. 56, pp. 403–409, Jan. 1917.

[12] E. Hubble, "A Relation between Distance and Radial Velocity among Extra-Galactic Nebulae," *Proceedings of the National Academy of Science*, vol. 15, pp. 168–173, Mar. 1929.

[13] A. Friedmann, "Über die Krümmung des Raumes," *Zeitschrift fur Physik*, vol. 10, pp. 377–386, Jan. 1922.

[14] A. Einstein, "Die Grundlage der allgemeinen Relativitätstheorie," *Annalen der Physik*, vol. 354, pp. 769–822, Jan. 1916.

[15] A. G. Riess, A. V. Filippenko, P. Challis, A. Clocchiatti, A. Diercks, P. M. Garnavich, R. L. Gilliland, C. J. Hogan, S. Jha, R. P. Kirshner, B. Leibundgut, M. M. Phillips, D. Reiss, B. P. Schmidt, R. A. Schommer, R. C. Smith, J. Spyromilio, C. Stubbs, N. B. Suntzeff, and J. Tonry, "Observational Evidence from Supernovae for an Accelerating Universe and a Cosmological Constant," *AJ*, vol. 116, pp. 1009–1038, Sept. 1998.

[16] S. Perlmutter, G. Aldering, G. Goldhaber, R. A. Knop, P. Nugent, P. G. Castro, S. Deustua, S. Fabbro, A. Goobar, D. E. Groom, I. M. Hook, A. G. Kim, M. Y. Kim, J. C. Lee, N. J. Nunes, R. Pain, C. R. Pennypacker, R. Quimby, C. Lidman, R. S. Ellis, M. Irwin, R. G. McMahon, P. Ruiz-Lapuente, N. Walton, B. Schaefer, B. J. Boyle, A. V. Filippenko, T. Matheson, A. S. Fruchter, N. Panagia, H. J. M. Newberg, W. J. Couch, and T. S. C. Project, "Measurements of Ω and Λ from 42 High-Redshift Supernovae," *ApJ*, vol. 517, pp. 565–586, June 1999.

[17] J. J. Condon, W. D. Cotton, E. W. Greisen, Q. F. Yin, R. A. Perley, G. B. Taylor, and J. J. Broderick, "The NRAO VLA Sky Survey," *AJ*, vol. 115, pp. 1693–1716, May 1998.

[18] J. A. Frieman, "The Sloan Digital Sky Survey and large-scale structure.," *Phys. Rep.*, vol. 307, pp. 61–66, Dec. 1998.

[19] G. F. Smoot, C. L. Bennett, A. Kogut, E. L. Wright, J. Aymon, N. W. Boggess, E. S. Cheng, G. de Amici, S. Gulkis, M. G. Hauser, G. Hinshaw, P. D. Jackson, M. Janssen, E. Kaita, T. Kelsall, P. Keegstra, C. Lineweaver, K. Loewenstein, P. Lubin, J. Mather, S. S. Meyer, S. H. Moseley, T. Murdock, L. Rokke, R. F. Silverberg, L. Tenorio, R. Weiss, and D. T. Wilkinson, "Structure in the COBE Differential Microwave Radiometer First-Year Maps," *ApJ*, vol. 396, p. L1, Sept. 1992.

[20] Planck Collaboration, N. Aghanim, Y. Akrami, M. Ashdown, J. Aumont, C. Baccigalupi, M. Ballardini, A. J. Banday, R. B. Barreiro, N. Bartolo, S. Basak, R. Battye, K. Benabed, J. P. Bernard, M. Bersanelli, P. Bielewicz, J. J. Bock, J. R. Bond, J. Borrill, F. R. Bouchet, F. Boulanger, M. Bucher, C. Burigana, R. C. Butler, E. Calabrese, J. F. Cardoso, J. Carron, A. Challinor, H. C. Chiang, J. Chluba, L. P. L. Colombo, C. Combet, D. Contreras, B. P. Crill, F. Cuttaia, P. de Bernardis, G. de Zotti, J. Delabrouille, J. M. Delouis, E. Di Valentino, J. M. Diego, O. Doré, M. Douspis, A. Ducout, X. Dupac, S. Dusini, G. Efstathiou, F. Elsner, T. A. Enßlin, H. K. Eriksen, Y. Fantaye, M. Farhang, J. Fergusson, R. Fernandez-Cobos, F. Finelli, F. Forastieri, M. Frailis, A. A. Fraisse, E. Franceschi, A. Frolov, S. Galeotta, S. Galli, K. Ganga, R. T. Génova-Santos, M. Gerbino, T. Ghosh, J. González-Nuevo, K. M. Górski, S. Gratton, A. Gruppuso, J. E. Gudmundsson, J. Hamann, W. Handley, F. K. Hansen, D. Herranz, S. R. Hildebrandt, E. Hivon, Z. Huang, A. H. Jaffe, W. C. Jones, A. Karakci, E. Keihänen, R. Keskitalo, K. Kiiveri, J. Kim, T. S. Kisner, L. Knox, N. Krachmalnicoff, M. Kunz, H. Kurki-Suonio,

G. Lagache, J. M. Lamarre, A. Lasenby, M. Lattanzi, C. R. Lawrence, M. Le Jeune, P. Lemos, J. Lesgourgues, F. Levrier, A. Lewis, M. Liguori, P. B. Lilje, M. Lilley, V. Lindholm, M. López-Caniego, P. M. Lubin, Y. Z. Ma, J. F. Macías-Pérez, G. Maggio, D. Maino, N. Mandolesi, A. Mangilli, A. Marcos-Caballero, M. Maris, P. G. Martin, M. Martinelli, E. Martínez-González, S. Matarrese, N. Mauri, J. D. McEwen, P. R. Meinhold, A. Melchiorri, A. Mennella, M. Migliaccio, M. Millea, S. Mitra, M. A. Miville-Deschênes, D. Molinari, L. Montier, G. Morgante, A. Moss, P. Natoli, H. U. Nørgaard-Nielsen, L. Pagano, D. Paoletti, B. Partridge, G. Patanchon, H. V. Peiris, F. Perrotta, V. Pettorino, F. Piacentini, L. Polastri, G. Polenta, J. L. Puget, J. P. Rachen, M. Reinecke, M. Remazeilles, A. Renzi, G. Rocha, C. Rosset, G. Roudier, J. A. Rubiño-Martín, B. Ruiz-Granados, L. Salvati, M. Sandri, M. Savelainen, D. Scott, E. P. S. Shellard, C. Sirignano, G. Sirri, L. D. Spencer, R. Sunyaev, A. S. Suur-Uski, J. A. Tauber, D. Tavagnacco, M. Tenti, L. Toffolatti, M. Tomasi, T. Trombetti, L. Valenziano, J. Valiviita, B. Van Tent, L. Vibert, P. Vielva, F. Villa, N. Vittorio, B. D. Wandelt, I. K. Wehus, M. White, S. D. M. White, A. Zacchei, and A. Zonca, "Planck 2018 results. VI. Cosmological parameters," *A&A*, vol. 641, p. A6, Sept. 2020.

[21] S. Aiola, E. Calabrese, L. Maurin, S. Naess, B. L. Schmitt, M. H. Abitbol, G. E. Addison, P. A. R. Ade, D. Alonso, M. Amiri, S. Amodeo, E. Angile, J. E. Austermann, T. Baildon, N. Battaglia, J. A. Beall, R. Bean, D. T. Becker, J. R. Bond, S. M. Bruno, V. Calafut, L. E. Campusano, F. Carrero, G. E. Chesmore, H.-m. Cho, S. K. Choi, S. E. Clark, N. F. Cothard, D. Crichton, K. T. Crowley, O. Darwish, R. Datta, E. V. Denison, M. J. Devlin, C. J. Duell, S. M. Duff, A. J. Duivenvoorden, J. Dunkley, R. Dünner, T. Essinger-Hileman, M. Fankhanel, S. Ferraro, A. E. Fox, B. Fuzia, P. A. Gallardo, V. Gluscevic, J. E. Golec, E. Grace, M. Gralla, Y. Guan, K. Hall, M. Halpern, D. Han, P. Hargrave, M. Hasselfield, J. M. Helton, S. Henderson, B. Hensley, J. C. Hill, G. C. Hilton, M. Hilton, A. D. Hincks, R. Hložek, S.-P. P. Ho, J. Hubmayr, K. M. Huffenberger, J. P. Hughes, L. Infante, K. Irwin, R. Jackson, J. Klein, K. Knowles, B. Koopman, A. Kosowsky, V. Lakey, D. Li, Y. Li, Z. Li, M. Lokken, T. Louis, M. Lungu, A. MacInnis, M. Madhavacheril, F. Maldonado, M. Mallaby-Kay, D. Marsden, J. McMahon, F. Menanteau, K. Moodley, T. Morton, T. Namikawa, F. Nati, L. Newburgh, J. P. Nibarger, A. Nicola, M. D. Niemack, M. R. Nolta, J. Orlowski-Sherer, L. A. Page, C. G. Pappas, B. Partridge, P. Phakathi, G. Pisano, H. Prince, R. Puddu, F. J. Qu, J. Rivera, N. Robertson, F. Rojas, M. Salatino, E. Schaan, A. Schillaci, N. Sehgal, B. D. Sherwin, C. Sierra, J. Sievers, C. Sifon, P. Sikhosana, S. Simon, D. N. Spergel, S. T. Staggs, J. Stevens, E. Storer, D. D. Sunder, E. R. Switzer, B. Thorne, R. Thornton, H. Trac, J. Treu, C. Tucker, L. R. Vale, A. Van Engelen, J. Van Lanen, E. M. Vavagiakis, K. Wagoner, Y. Wang, J. T. Ward, E. J. Wollack, Z. Xu, F. Zago, and N. Zhu, "The Atacama Cosmology Telescope: DR4 maps and cosmological parameters," *J. Cosmology Astropart. Phys.*, vol. 2020, p. 047, Dec. 2020.

[22] A. G. Riess, S. Casertano, W. Yuan, J. B. Bowers, L. Macri, J. C. Zinn, and D. Scolnic, "Cosmic Distances Calibrated to 1% Precision with Gaia EDR3 Parallaxes and Hubble Space Telescope Photometry of 75 Milky Way Cepheids Confirm Tension with ΛCDM," *ApJ*, vol. 908, p. L6, Feb. 2021.

[23] E. Di Valentino, O. Mena, S. Pan, L. Visinelli, W. Yang, A. Melchiorri, D. F. Mota, A. G. Riess, and J. Silk, "In the realm of the Hubble tension-a review of solutions," *Classical and Quantum Gravity*, vol. 38, p. 153001, July 2021.

[24] H. Mo, F. C. van den Bosch, and S. White, *Galaxy Formation and Evolution*. 2010.

[25] C. L. Bennett, D. Larson, J. L. Weiland, N. Jarosik, G. Hinshaw, N. Odegard, K. M. Smith, R. S. Hill, B. Gold, M. Halpern, E. Komatsu, M. R. Nolta, L. Page, D. N. Spergel, E. Wollack, J. Dunkley, A. Kogut, M. Limon, S. S. Meyer, G. S. Tucker, and E. L. Wright, "Nine-year Wilkinson Microwave Anisotropy Probe (WMAP) Observations: Final Maps and Results," *ApJS*, vol. 208, p. 20, Oct. 2013.

[26] D. J. Eisenstein, I. Zehavi, D. W. Hogg, R. Scoccimarro, M. R. Blanton, R. C. Nichol, R. Scranton, H.-J. Seo, M. Tegmark, Z. Zheng, S. F. Anderson, J. Annis, N. Bahcall, J. Brinkmann, S. Burles,

F. J. Castander, A. Connolly, I. Csabai, M. Doi, M. Fukugita, J. A. Frieman, K. Glazebrook, J. E. Gunn, J. S. Hendry, G. Hennessy, Z. Ivezić, S. Kent, G. R. Knapp, H. Lin, Y.-S. Loh, R. H. Lupton, B. Margon, T. A. McKay, A. Meiksin, J. A. Munn, A. Pope, M. W. Richmond, D. Schlegel, D. P. Schneider, K. Shimasaku, C. Stoughton, M. A. Strauss, M. SubbaRao, A. S. Szalay, I. Szapudi, D. L. Tucker, B. Yanny, and D. G. York, "Detection of the Baryon Acoustic Peak in the Large-Scale Correlation Function of SDSS Luminous Red Galaxies," *ApJ*, vol. 633, pp. 560–574, Nov. 2005.

[27] S. Dodelson, *Gravitational Lensing*. 2017.

[28] T. Treu, "Strong Lensing by Galaxies," , vol. 48, pp. 87–125, Sept. 2010.

[29] P. Schneider, "Weak Gravitational Lensing," *arXiv e-prints*, pp. astro–ph/0509252, Sept. 2005.

[30] A. Refregier, "Weak Gravitational Lensing by Large-Scale Structure," , vol. 41, pp. 645–668, Jan. 2003.

[31] R. Mandelbaum, A. Slosar, T. Baldauf, U. Seljak, C. M. Hirata, R. Nakajima, R. Reyes, and R. E. Smith, "Cosmological parameter constraints from galaxy-galaxy lensing and galaxy clustering with the SDSS DR7," *MNRAS*, vol. 432, pp. 1544–1575, June 2013.

[32] J. Prat, C. Sánchez, Y. Fang, D. Gruen, J. Elvin-Poole, N. Kokron, L. F. Secco, B. Jain, R. Miquel, N. MacCrann, M. A. Troxel, A. Alarcon, D. Bacon, G. M. Bernstein, J. Blazek, R. Cawthon, C. Chang, M. Crocce, C. Davis, J. De Vicente, J. P. Dietrich, A. Drlica-Wagner, O. Friedrich, M. Gatti, W. G. Hartley, B. Hoyle, E. M. Huff, M. Jarvis, M. M. Rau, R. P. Rollins, A. J. Ross, E. Rozo, E. S. Rykoff, S. Samuroff, E. Sheldon, T. N. Varga, P. Vielzeuf, J. Zuntz, T. M. C. Abbott, F. B. Abdalla, S. Allam, J. Annis, K. Bechtol, A. Benoit-Lévy, E. Bertin, D. Brooks, E. Buckley-Geer, D. L. Burke, A. Carnero Rosell, M. Carrasco Kind, J. Carretero, F. J. Castander, C. E. Cunha, C. B. D'Andrea, L. N. da Costa, S. Desai, H. T. Diehl, S. Dodelson, T. F. Eifler, E. Fernandez, B. Flaugher, P. Fosalba, J. Frieman, J. García-Bellido, E. Gaztanaga, D. W. Gerdes, T. Giannantonio, D. A. Goldstein, R. A. Gruendl, J. Gschwend, G. Gutierrez, K. Honscheid, D. J. James, T. Jeltema, M. W. G. Johnson, M. D. Johnson, D. Kirk, E. Krause, K. Kuehn, S. Kuhlmann, O. Lahav, T. S. Li, M. Lima, M. A. G. Maia, M. March, J. L. Marshall, P. Martini, P. Melchior, F. Menanteau, J. J. Mohr, R. C. Nichol, B. Nord, A. A. Plazas, A. K. Romer, A. Roodman, M. Sako, E. Sanchez, V. Scarpine, R. Schindler, M. Schubnell, I. Sevilla-Noarbe, M. Smith, R. C. Smith, M. Soares-Santos, F. Sobreira, E. Suchyta, M. E. C. Swanson, G. Tarle, D. Thomas, D. L. Tucker, V. Vikram, A. R. Walker, R. H. Wechsler, B. Yanny, Y. Zhang, and DES Collaboration, "Dark Energy Survey year 1 results: Galaxy-galaxy lensing," *Phys. Rev. E*, vol. 98, p. 042005, Aug. 2018.

[33] R. Mandelbaum, "Weak lensing for precision cosmology," *Ann. Rev. Astron. Astrophys.*, vol. 56, pp. 393–433, 2018.

[34] M. Kilbinger, "Cosmology with cosmic shear observations: a review," *Rept. Prog. Phys.*, vol. 78, p. 086901, 2015.

[35] U. Seljak, "Weak Lensing Reconstruction and Power Spectrum Estimation: Minimum Variance Methods," *ApJ*, vol. 506, pp. 64–79, Oct. 1998.

[36] W. Hu, "Power Spectrum Tomography with Weak Lensing," *ApJ*, vol. 522, pp. L21–L24, Sept. 1999.

[37] T. M. C. Abbott, M. Aguena, A. Alarcon, S. Allam, O. Alves, A. Amon, F. Andrade-Oliveira, J. Annis, S. Avila, D. Bacon, E. Baxter, K. Bechtol, M. R. Becker, G. M. Bernstein, S. Bhargava, S. Birrer, J. Blazek, A. Brandao-Souza, S. L. Bridle, D. Brooks, E. Buckley-Geer, D. L. Burke, H. Camacho, A. Campos, A. Carnero Rosell, M. Carrasco Kind, J. Carretero, F. J. Castander, R. Cawthon, C. Chang, A. Chen, R. Chen, A. Choi, C. Conselice, J. Cordero, M. Costanzi, M. Crocce, L. N. da

Costa, M. E. da Silva Pereira, C. Davis, T. M. Davis, J. De Vicente, J. DeRose, S. Desai, E. Di Valentino, H. T. Diehl, J. P. Dietrich, S. Dodelson, P. Doel, C. Doux, A. Drlica-Wagner, K. Eckert, T. F. Eifler, F. Elsner, J. Elvin-Poole, S. Everett, A. E. Evrard, X. Fang, A. Farahi, E. Fernandez, I. Ferrero, A. Ferté, P. Fosalba, O. Friedrich, J. Frieman, J. García-Bellido, M. Gatti, E. Gaztanaga, D. W. Gerdes, T. Giannantonio, G. Giannini, D. Gruen, R. A. Gruendl, J. Gschwend, G. Gutierrez, I. Harrison, W. G. Hartley, K. Herner, S. R. Hinton, D. L. Hollowood, K. Honscheid, B. Hoyle, E. M. Huff, D. Huterer, B. Jain, D. J. James, M. Jarvis, N. Jeffrey, T. Jeltema, A. Kovacs, E. Krause, R. Kron, K. Kuehn, N. Kuropatkin, O. Lahav, P. F. Leget, P. Lemos, A. R. Liddle, C. Lidman, M. Lima, H. Lin, N. MacCrann, M. A. G. Maia, J. L. Marshall, P. Martini, J. McCullough, P. Melchior, J. Mena-Fernández, F. Menanteau, R. Miquel, J. J. Mohr, R. Morgan, J. Muir, J. Myles, S. Nadathur, A. Navarro-Alsina, R. C. Nichol, R. L. C. Ogando, Y. Omori, A. Palmese, S. Pandey, Y. Park, F. Paz-Chinchón, D. Petravick, A. Pieres, A. A. Plazas Malagón, A. Porredon, J. Prat, M. Raveri, M. Rodriguez-Monroy, R. P. Rollins, A. K. Romer, A. Roodman, R. Rosenfeld, A. J. Ross, E. S. Rykoff, S. Samuroff, C. Sánchez, E. Sanchez, J. Sanchez, D. Sanchez Cid, V. Scarpine, M. Schubnell, D. Scolnic, L. F. Secco, S. Serrano, I. Sevilla-Noarbe, E. Sheldon, T. Shin, M. Smith, M. Soares-Santos, E. Suchyta, M. E. C. Swanson, M. Tabbutt, G. Tarle, D. Thomas, C. To, A. Troja, M. A. Troxel, D. L. Tucker, I. Tutusaus, T. N. Varga, A. R. Walker, N. Weaverdyck, R. Wechsler, J. Weller, B. Yanny, B. Yin, Y. Zhang, J. Zuntz, and DES Collaboration, "Dark Energy Survey Year 3 results: Cosmological constraints from galaxy clustering and weak lensing," *Phys. Rev. E*, vol. 105, p. 023520, Jan. 2022.

[38] C. Heymans, T. Tröster, M. Asgari, C. Blake, H. Hildebrandt, B. Joachimi, K. Kuijken, C.-A. Lin, A. G. Sánchez, J. L. van den Busch, A. H. Wright, A. Amon, M. Bilicki, J. de Jong, M. Crocce, A. Dvornik, T. Erben, M. C. Fortuna, F. Getman, B. Giblin, K. Glazebrook, H. Hoekstra, S. Joudaki, A. Kannawadi, F. Köhlinger, C. Lidman, L. Miller, N. R. Napolitano, D. Parkinson, P. Schneider, H. Shan, E. A. Valentijn, G. Verdoes Kleijn, and C. Wolf, "KiDS-1000 Cosmology: Multi-probe weak gravitational lensing and spectroscopic galaxy clustering constraints," *A&A*, vol. 646, p. A140, Feb. 2021.

[39] M. Lochner, D. M. Scolnic, H. Awan, N. Regnault, P. Gris, R. Mandelbaum, E. Gawiser, H. Almoubayyed, C. N. Setzer, S. Huber, M. L. Graham, R. Hložek, R. Biswas, T. Eifler, D. Rothchild, J. Allam, Tarek, J. Blazek, C. Chang, T. Collett, A. Goobar, I. M. Hook, M. Jarvis, S. W. Jha, A. G. Kim, P. Marshall, J. D. McEwen, M. Moniez, J. A. Newman, H. V. Peiris, T. Petrushevska, J. Rhodes, I. Sevilla-Noarbe, A. Slosar, S. H. Suyu, J. A. Tyson, and P. Yoachim, "Optimizing the LSST Observing Strategy for Dark Energy Science: DESC Recommendations for the Wide-Fast-Deep Survey," *arXiv e-prints*, p. arXiv:1812.00515, Nov. 2018.

[40] J. Kruk *Roman Space Telescope Science Requirements Document*, Jun 2021.

[41] D. J. Bacon, A. R. Refregier, and R. S. Ellis, "Detection of weak gravitational lensing by large-scale structure," *MNRAS*, vol. 318, pp. 625–640, Oct. 2000.

[42] D. M. Wittman, J. A. Tyson, D. Kirkman, I. Dell'Antonio, and G. Bernstein, "Detection of weak gravitational lensing distortions of distant galaxies by cosmic dark matter at large scales," *Nature*, vol. 405, pp. 143–148, May 2000.

[43] L. van Waerbeke, "Cosmic Shear with the CFHT," in *Cosmological Physics with Gravitational Lensing* (J. Tran Thanh Van, Y. Mellier, and M. Moniez, eds.), p. 165, Jan. 2001.

[44] M. Jarvis, G. M. Bernstein, P. Fischer, D. Smith, B. Jain, J. A. Tyson, and D. Wittman, "Weak-Lensing Results from the 75 Square Degree Cerro Tololo Inter-American Observatory Survey," *AJ*, vol. 125, pp. 1014–1032, Mar. 2003.

[45] M. Velander, E. van Uitert, H. Hoekstra, J. Coupon, T. Erben, C. Heymans, H. Hildebrandt, T. D. Kitching, Y. Mellier, L. Miller, L. Van Waerbeke, C. Bonnett, L. Fu, S. Giodini, M. J. Hudson, K. Kuijken, B. Rowe, T. Schrabback, and E. Semboloni, "CFHTLenS: the relation between galaxy dark matter haloes and baryons from weak gravitational lensing," *MNRAS*, vol. 437, pp. 2111–2136, Jan. 2014.

[46] E. M. Huff, T. Eifler, C. M. Hirata, R. Mandelbaum, D. Schlegel, and U. Seljak, "Seeing in the dark - II. Cosmic shear in the Sloan Digital Sky Survey," *MNRAS*, vol. 440, pp. 1322–1344, May 2014.

[47] M. A. Troxel, N. MacCrann, J. Zuntz, T. F. Eifler, E. Krause, S. Dodelson, D. Gruen, J. Blazek, O. Friedrich, S. Samuroff, J. Prat, L. F. Secco, C. Davis, A. Ferté, J. DeRose, A. Alarcon, A. Amara, E. Baxter, M. R. Becker, G. M. Bernstein, S. L. Bridle, R. Cawthon, C. Chang, A. Choi, J. De Vicente, A. Drlica-Wagner, J. Elvin-Poole, J. Frieman, M. Gatti, W. G. Hartley, K. Honscheid, B. Hoyle, E. M. Huff, D. Huterer, B. Jain, M. Jarvis, T. Kacprzak, D. Kirk, N. Kokron, C. Krawiec, O. Lahav, A. R. Liddle, J. Peacock, M. M. Rau, A. Refregier, R. P. Rollins, E. Rozo, E. S. Rykoff, C. Sánchez, I. Sevilla-Noarbe, E. Sheldon, A. Stebbins, T. N. Varga, P. Vielzeuf, M. Wang, R. H. Wechsler, B. Yanny, T. M. C. Abbott, F. B. Abdalla, S. Allam, J. Annis, K. Bechtol, A. Benoit-Lévy, E. Bertin, D. Brooks, E. Buckley-Geer, D. L. Burke, A. Carnero Rosell, M. Carrasco Kind, J. Carretero, F. J. Castander, M. Crocce, C. E. Cunha, C. B. D'Andrea, L. N. da Costa, D. L. DePoy, S. Desai, H. T. Diehl, J. P. Dietrich, P. Doel, E. Fernandez, B. Flaugher, P. Fosalba, J. García-Bellido, E. Gaztanaga, D. W. Gerdes, T. Giannantonio, D. A. Goldstein, R. A. Gruendl, J. Gschwend, G. Gutierrez, D. J. James, T. Jeltema, M. W. G. Johnson, M. D. Johnson, S. Kent, K. Kuehn, S. Kuhlmann, N. Kuropatkin, T. S. Li, M. Lima, H. Lin, M. A. G. Maia, M. March, J. L. Marshall, P. Martini, P. Melchior, F. Menanteau, R. Miquel, J. J. Mohr, E. Neilsen, R. C. Nichol, B. Nord, D. Petravick, A. A. Plazas, A. K. Romer, A. Roodman, M. Sako, E. Sanchez, V. Scarpine, R. Schindler, M. Schubnell, M. Smith, R. C. Smith, M. Soares-Santos, F. Sobreira, E. Suchyta, M. E. C. Swanson, G. Tarle, D. Thomas, D. L. Tucker, V. Vikram, A. R. Walker, J. Weller, Y. Zhang, and DES Collaboration, "Dark Energy Survey Year 1 results: Cosmological constraints from cosmic shear," *Phys. Rev. E*, vol. 98, p. 043528, Aug. 2018.

[48] v. Z. Ivezić *et al.*, "LSST: from Science Drivers to Reference Design and Anticipated Data Products," *Astrophys. J.*, vol. 873, no. 2, p. 111, 2019.

[49] R. Akeson, L. Armus, E. Bachelet, V. Bailey, L. Bartusek, A. Bellini, D. Benford, D. Bennett, A. Bhattacharya, R. Bohlin, M. Boyer, V. Bozza, G. Bryden, S. Calchi Novati, K. Carpenter, S. Casertano, A. Choi, D. Content, P. Dayal, A. Dressler, O. Doré, S. M. Fall, X. Fan, X. Fang, A. Filippenko, S. Finkelstein, R. Foley, S. Furlanetto, J. Kalirai, B. S. Gaudi, K. Gilbert, J. Girard, K. Grady, J. Greene, P. Guhathakurta, C. Heinrich, S. Hemmati, D. Hendel, C. Henderson, T. Henning, C. Hirata, S. Ho, E. Huff, A. Hutter, R. Jansen, S. Jha, S. Johnson, D. Jones, J. Kasdin, P. Kelly, R. Kirshner, A. Koekemoer, J. Kruk, N. Lewis, B. Macintosh, P. Madau, S. Malhotra, K. Mandel, E. Massara, D. Masters, J. McEnery, K. McQuinn, P. Melchior, M. Melton, B. Mennesson, M. Peeples, M. Penny, S. Perlmutter, A. Pisani, A. Plazas, R. Poleski, M. Postman, C. Ranc, B. Rauscher, A. Rest, A. Roberge, B. Robertson, S. Rodney, J. Rhoads, J. Rhodes, J. Ryan, Russell, K. Sahu, D. Sand, D. Scolnic, A. Seth, Y. Shvartzvald, K. Siellez, A. Smith, D. Spergel, K. Stassun, R. Street, L.-G. Strolger, A. Szalay, J. Trauger, M. A. Troxel, M. Turnbull, R. van der Marel, A. von der Linden, Y. Wang, D. Weinberg, B. Williams, R. Windhorst, E. Wollack, H.-Y. Wu, J. Yee, and N. Zimmerman, "The Wide Field Infrared Survey Telescope: 100 Hubbles for the 2020s," *arXiv e-prints*, p. arXiv:1902.05569, Feb. 2019.

[50] R. Laureijs, J. Amiaux, S. Arduini, J. L. Augueres, J. Brinchmann, R. Cole, M. Cropper, C. Dabin, L. Duvet, A. Ealet, B. Garilli, P. Gondoin, L. Guzzo, J. Hoar, H. Hoekstra, R. Holmes, T. Kitching, T. Maciaszek, Y. Mellier, F. Pasian, W. Percival, J. Rhodes, G. Saavedra Criado, M. Sauvage,

R. Scaramella, L. Valenziano, S. Warren, R. Bender, F. Castander, A. Cimatti, O. Le Fèvre, H. Kurki-Suonio, M. Levi, P. Lilje, G. Meylan, R. Nichol, K. Pedersen, V. Popa, R. Rebolo Lopez, H. W. Rix, H. Rottgering, W. Zeilinger, F. Grupp, P. Hudelot, R. Massey, M. Meneghetti, L. Miller, S. Paltani, S. Paulin-Henriksson, S. Pires, C. Saxton, T. Schrabback, G. Seidel, J. Walsh, N. Aghanim, L. Amendola, J. Bartlett, C. Baccigalupi, J. P. Beaulieu, K. Benabed, J. G. Cuby, D. Elbaz, P. Fosalba, G. Gavazzi, A. Helmi, I. Hook, M. Irwin, J. P. Kneib, M. Kunz, F. Mannucci, L. Moscardini, C. Tao, R. Teyssier, J. Weller, G. Zamorani, M. R. Zapatero Osorio, O. Boulade, J. J. Foumond, A. Di Giorgio, P. Guttridge, A. James, M. Kemp, J. Martignac, A. Spencer, D. Walton, T. Blümchen, C. Bonoli, F. Bortoletto, C. Cerna, L. Corcione, C. Fabron, K. Jahnke, S. Ligori, F. Madrid, L. Martin, G. Morgante, T. Pamplona, E. Prieto, M. Riva, R. Toledo, M. Trifoglio, F. Zerbi, F. Abdalla, M. Douspis, C. Grenet, S. Borgani, R. Bouwens, F. Courbin, J. M. Delouis, P. Dubath, A. Fontana, M. Frailis, A. Grazian, J. Koppenhöfer, O. Mansutti, M. Melchior, M. Mignoli, J. Mohr, C. Neissner, K. Noddle, M. Poncet, M. Scodeggio, S. Serrano, N. Shane, J. L. Starck, C. Surace, A. Taylor, G. Verdoes-Kleijn, C. Vuerli, O. R. Williams, A. Zacchei, B. Altieri, I. Escudero Sanz, R. Kohley, T. Oosterbroek, P. Astier, D. Bacon, S. Bardelli, C. Baugh, F. Bellagamba, C. Benoist, D. Bianchi, A. Biviano, E. Branchini, C. Carbone, V. Cardone, D. Clements, S. Colombi, C. Conselice, G. Cresci, N. Deacon, J. Dunlop, C. Fedeli, F. Fontanot, P. Franzetti, C. Giocoli, J. Garcia-Bellido, J. Gow, A. Heavens, P. Hewett, C. Heymans, A. Holland, Z. Huang, O. Ilbert, B. Joachimi, E. Jennins, E. Kerins, A. Kiessling, D. Kirk, R. Kotak, O. Krause, O. Lahav, F. van Leeuwen, J. Lesgourgues, M. Lombardi, M. Magliocchetti, K. Maguire, E. Majerotto, R. Maoli, F. Marulli, S. Maurogordato, H. McCracken, R. McLure, A. Melchiorri, A. Merson, M. Moresco, M. Nonino, P. Norberg, J. Peacock, R. Pello, M. Penny, V. Pettorino, C. Di Porto, L. Pozzetti, C. Quercellini, M. Radovich, A. Rassat, N. Roche, S. Ronayette, E. Rossetti, B. Sartoris, P. Schneider, E. Semboloni, S. Serjeant, F. Simpson, C. Skordis, G. Smadja, S. Smartt, P. Spano, S. Spiro, M. Sullivan, A. Tilquin, R. Trotta, L. Verde, Y. Wang, G. Williger, G. Zhao, J. Zoubian, and E. Zucca, "Euclid Definition Study Report," *arXiv e-prints*, p. arXiv:1110.3193, Oct. 2011.

[51] P. Antilogus, P. Astier, P. Doherty, A. Guyonnet, and N. Regnault, "The brighter-fatter effect and pixel correlations in CCD sensors," *Journal of Instrumentation*, vol. 9, p. C03048, Mar. 2014.

[52] A. Guyonnet, P. Astier, P. Antilogus, N. Regnault, and P. Doherty, "Evidence for self-interaction of charge distribution in charge-coupled devices," *A&A*, vol. 575, p. A41, Mar. 2015.

[53] R. Mandelbaum, M. Jarvis, R. H. Lupton, J. Bosch, A. Kannawadi, M. D. Murphy, T. Zhang, and the LSST Dark Energy Science Collaboration, "PSFs of coadded images," *arXiv e-prints*, p. arXiv:2209.09253, Sept. 2022.

[54] R. Mandelbaum, H. Miyatake, T. Hamana, M. Oguri, M. Simet, R. Armstrong, J. Bosch, R. Murata, F. Lanusse, A. Leauthaud, J. Coupon, S. More, M. Takada, S. Miyazaki, J. S. Speagle, M. Shirasaki, C. Sifón, S. Huang, A. J. Nishizawa, E. Medezinski, Y. Okura, N. Okabe, N. Czakon, R. Takahashi, W. R. Coulton, C. Hikage, Y. Komiyama, R. H. Lupton, M. A. Strauss, M. Tanaka, and Y. Utsumi, "The first-year shear catalog of the Subaru Hyper Suprime-Cam Subaru Strategic Program Survey," *PASJ*, vol. 70, p. S25, Jan. 2018.

[55] N. MacCrann, M. R. Becker, J. McCullough, A. Amon, D. Gruen, M. Jarvis, A. Choi, M. A. Troxel, E. Sheldon, B. Yanny, K. Herner, S. Dodelson, J. Zuntz, K. Eckert, R. P. Rollins, T. N. Varga, G. M. Bernstein, R. A. Gruendl, I. Harrison, W. G. Hartley, I. Sevilla-Noarbe, A. Pieres, S. L. Bridle, J. Myles, A. Alarcon, S. Everett, C. Sánchez, E. M. Huff, F. Tarsitano, M. Gatti, L. F. Secco, T. M. C. Abbott, M. Aguena, S. Allam, J. Annis, D. Bacon, E. Bertin, D. Brooks, D. L. Burke, A. Carnero Rosell, M. Carrasco Kind, J. Carretero, M. Costanzi, M. Crocce, M. E. S. Pereira, J. De Vicente, S. Desai, H. T. Diehl, J. P. Dietrich, P. Doel, T. F. Eifler, I. Ferrero, A. Ferté, B. Flaugher, P. Fosalba, J. Frieman, J. García-Bellido, E. Gaztanaga, D. W. Gerdes, T. Giannantonio, J. Gschwend,

G. Gutierrez, S. R. Hinton, D. L. Hollowood, K. Honscheid, D. J. James, O. Lahav, M. Lima, M. A. G. Maia, M. March, J. L. Marshall, P. Martini, P. Melchior, F. Menanteau, R. Miquel, J. J. Mohr, R. Morgan, J. Muir, R. L. C. Ogando, A. Palmese, F. Paz-Chinchón, A. A. Plazas, M. Rodriguez-Monroy, A. Roodman, S. Samuroff, E. Sanchez, V. Scarpine, S. Serrano, M. Smith, M. Soares-Santos, E. Suchyta, M. E. C. Swanson, G. Tarle, D. Thomas, C. To, R. D. Wilkinson, R. D. Wilkinson, and DES Collaboration, "Dark Energy Survey Y3 results: blending shear and redshift biases in image simulations," *MNRAS*, vol. 509, pp. 3371–3394, Jan. 2022.

[56] E. Huff and R. Mandelbaum, "Metacalibration: Direct Self-Calibration of Biases in Shear Measurement," *arXiv e-prints*, p. arXiv:1702.02600, Feb. 2017.

[57] E. S. Sheldon and E. M. Huff, "Practical Weak Lensing Shear Measurement with Metacalibration," *Astrophys. J.*, vol. 841, no. 1, p. 24, 2017.

[58] E. S. Sheldon, M. R. Becker, N. MacCrann, and M. Jarvis, "Mitigating Shear-dependent Object Detection Biases with Metacalibration," *ApJ*, vol. 902, p. 138, Oct. 2020.

[59] X. Li, N. Katayama, M. Oguri, and S. More, "Fourier Power Function Shapelets (FPFS) shear estimator: performance on image simulations," *MNRAS*, vol. 481, pp. 4445–4460, Dec. 2018.

[60] X. Li, Y. Li, and R. Massey, "Weak gravitational lensing shear measurement with FPFS: analytical mitigation of noise bias and selection bias," *MNRAS*, vol. 511, pp. 4850–4860, Apr. 2022.

[61] A. I. Malz and D. W. Hogg, "How to obtain the redshift distribution from probabilistic redshift estimates," *ApJ*, vol. 928, p. 127, mar 2022.

[62] R. A. C. Croft and C. A. Metzler, "Weak-Lensing Surveys and the Intrinsic Correlation of Galaxy Ellipticities," *ApJ*, vol. 545, pp. 561–571, Dec. 2000.

[63] A. Heavens, A. Refregier, and C. Heymans, "Intrinsic correlation of galaxy shapes: implications for weak lensing measurements," *MNRAS*, vol. 319, pp. 649–656, Dec. 2000.

[64] M. A. Troxel and M. Ishak, "The intrinsic alignment of galaxies and its impact on weak gravitational lensing in an era of precision cosmology," *Phys. Rep.*, vol. 558, pp. 1–59, Feb. 2015.

[65] B. Joachimi, M. Cacciato, T. D. Kitching, A. Leonard, R. Mandelbaum, B. M. Schäfer, C. Sifón, H. Hoekstra, A. Kiessling, D. Kirk, and A. Rassat, "Galaxy Alignments: An Overview," *Space Sci. Rev.*, vol. 193, pp. 1–65, Nov. 2015.

[66] D. Sivia and J. Skilling, *Data Analysis: A Bayesian Tutorial*. Oxford science publications, OUP Oxford, 2006.

[67] C. M. Bishop and N. M. Nasrabadi, "Pattern Recognition and Machine Learning," *Journal of Electronic Imaging*, vol. 16, p. 049901, Jan. 2007.

[68] T. Eifler, P. Schneider, and J. Hartlap, "Dependence of cosmic shear covariances on cosmology. Impact on parameter estimation," *A&A*, vol. 502, pp. 721–731, Aug. 2009.

[69] H. Aihara, R. Armstrong, S. Bickerton, J. Bosch, J. Coupon, H. Furusawa, Y. Hayashi, H. Ikeda, Y. Kamata, H. Karoji, S. Kawanomoto, M. Koike, Y. Komiyama, D. Lang, R. H. Lupton, S. Mineo, H. Miyatake, S. Miyazaki, T. Morokuma, Y. Obuchi, Y. Oishi, Y. Okura, P. A. Price, T. Takata, M. M. Tanaka, M. Tanaka, Y. Tanaka, T. Uchida, F. Uraguchi, Y. Utsumi, S.-Y. Wang, Y. Yamada, H. Yamanoi, N. Yasuda, N. Arimoto, M. Chiba, F. Finet, H. Fujimori, S. Fujimoto, J. Furusawa,

T. Goto, A. Goulding, J. E. Gunn, Y. Harikane, T. Hattori, M. Hayashi, K. G. Hełminiak, R. Higuchi, C. Hikage, P. T. P. Ho, B.-C. Hsieh, K. Huang, S. Huang, M. Imanishi, I. Iwata, A. T. Jaelani, H.-Y. Jian, N. Kashikawa, N. Katayama, T. Kojima, A. Konno, S. Koshida, H. Kusakabe, A. Leauthaud, C.-H. Lee, L. Lin, Y.-T. Lin, R. Mandelbaum, Y. Matsuoka, E. Medezinski, S. Miyama, R. Momose, A. More, S. More, S. Mukae, R. Murata, H. Murayama, T. Nagao, F. Nakata, M. Niida, H. Niikura, A. J. Nishizawa, M. Oguri, N. Okabe, Y. Ono, M. Onodera, M. Onoue, M. Ouchi, T.-S. Pyo, T. Shibuya, K. Shimasaku, M. Simet, J. Speagle, D. N. Spergel, M. A. Strauss, Y. Sugahara, N. Sugiyama, Y. Suto, N. Suzuki, P. J. Tait, M. Takada, T. Terai, Y. Toba, E. L. Turner, H. Uchiyama, K. Umetsu, Y. Urata, T. Usuda, S. Yeh, and S. Yuma, "First data release of the Hyper Suprime-Cam Subaru Strategic Program," *PASJ*, vol. 70, p. S8, Jan. 2018.

[70] T. Zhang, R. Mandelbaum, and LSST Dark Energy Science Collaboration, "Impact of point spread function higher moments error on weak gravitational lensing," *MNRAS*, vol. 510, pp. 1978–1993, Feb. 2022.

[71] T. Zhang, H. Almoubayyed, R. Mandelbaum, J. E. Meyers, M. Jarvis, A. Kannawadi, M. A. Schmitz, A. Guinot, and LSST Dark Energy Science Collaboration, "Impact of point spread function higher moments error on weak gravitational lensing - II. A comprehensive study," *MNRAS*, vol. 520, pp. 2328–2350, Apr. 2023.

[72] R. Dalal, X. Li, A. Nicola, J. Zuntz, M. A. Strauss, S. Sugiyama, T. Zhang, M. M. Rau, R. Mandelbaum, M. Takada, S. More, H. Miyatake, A. Kannawadi, M. Shirasaki, T. Taniguchi, R. Takahashi, K. Osato, T. Hamana, M. Oguri, A. J. Nishizawa, A. A. Plazas Malagón, T. Sunayama, D. Alonso, A. Slosar, R. Armstrong, J. Bosch, Y. Komiyama, R. H. Lupton, N. B. Lust, L. A. MacArthur, S. Miyazaki, H. Murayama, T. Nishimichi, Y. Okura, P. A. Price, P. J. Tait, M. Tanaka, and S.-Y. Wang, "Hyper Suprime-Cam Year 3 Results: Cosmology from Cosmic Shear Power Spectra," *arXiv e-prints*, p. arXiv:2304.00701, Apr. 2023.

[73] T. Zhang, X. Li, R. Dalal, R. Mandelbaum, M. A. Strauss, A. Kannawadi, H. Miyatake, A. Nicola, A. A. Plazas Malagón, M. Shirasaki, S. Sugiyama, and M. Takada, "A General Framework for Removing Point Spread Function Additive Systematics in Cosmological Weak Lensing Analysis," *arXiv e-prints*, p. arXiv:2212.03257, Dec. 2022.

[74] T. Zhang, M. M. Rau, R. Mandelbaum, X. Li, and B. Moews, "Photometric redshift uncertainties in weak gravitational lensing shear analysis: models and marginalization," *MNRAS*, vol. 518, pp. 709–723, Jan. 2023.

[75] W. Hu, "Dark synergy: Gravitational lensing and the CMB," *Phys. Rev. D*, vol. 65, p. 023003, 2002.

[76] D. Huterer, "Weak lensing, dark matter and dark energy," *General Relativity and Gravitation*, vol. 42, pp. 2177–2195, Sept. 2010.

[77] D. H. Weinberg, M. J. Mortonson, D. J. Eisenstein, C. Hirata, A. G. Riess, and E. Rozo, "Observational probes of cosmic acceleration," *Phys. Rep.*, vol. 530, pp. 87–255, Sept. 2013.

[78] A. Albrecht, G. Bernstein, R. Cahn, W. L. Freedman, J. Hewitt, W. Hu, J. Huth, M. Kamionkowski, E. W. Kolb, L. Knox, J. C. Mather, S. Staggs, and N. B. Suntzeff, "Report of the dark energy task force," 9 2006.

[79] Dark Energy Survey Collaboration, T. Abbott, F. B. Abdalla, J. Aleksić, S. Allam, A. Amara, D. Bacon, E. Balbinot, M. Banerji, K. Bechtol, A. Benoit-Lévy, G. M. Bernstein, E. Bertin, J. Blazek, C. Bonnett, S. Bridle, D. Brooks, R. J. Brunner, E. Buckley-Geer, D. L. Burke, G. B. Caminha,

D. Capozzi, J. Carlsen, A. Carnero-Rosell, M. Carollo, M. Carrasco-Kind, J. Carretero, F. J. Castander, L. Clerkin, T. Collett, C. Conselice, M. Crocce, C. E. Cunha, C. B. D'Andrea, L. N. da Costa, T. M. Davis, S. Desai, H. T. Diehl, J. P. Dietrich, S. Dodelson, P. Doel, A. Drlica-Wagner, J. Estrada, J. Etherington, A. E. Evrard, J. Fabbri, D. A. Finley, B. Flaugher, R. J. Foley, P. Fosalba, J. Frieman, J. García-Bellido, E. Gaztanaga, D. W. Gerdes, T. Giannantonio, D. A. Goldstein, D. Gruen, R. A. Gruendl, P. Guarnieri, G. Gutierrez, W. Hartley, K. Honscheid, B. Jain, D. J. James, T. Jeltema, S. Jouvel, R. Kessler, A. King, D. Kirk, R. Kron, K. Kuehn, N. Kuropatkin, O. Lahav, T. S. Li, M. Lima, H. Lin, M. A. G. Maia, M. Makler, M. Manera, C. Maraston, J. L. Marshall, P. Martini, R. G. McMahon, P. Melchior, A. Merson, C. J. Miller, R. Miquel, J. J. Mohr, X. Morice-Atkinson, K. Naidoo, E. Neilsen, R. C. Nichol, B. Nord, R. Ogando, F. Ostrovski, A. Palmese, A. Papadopoulos, H. V. Peiris, J. Peoples, W. J. Percival, A. A. Plazas, S. L. Reed, A. Refregier, A. K. Romer, A. Roodman, A. Ross, E. Rozo, E. S. Rykoff, I. Sadeh, M. Sako, C. Sánchez, E. Sanchez, B. Santiago, V. Scarpine, M. Schubnell, I. Sevilla-Noarbe, E. Sheldon, M. Smith, R. C. Smith, M. Soares-Santos, F. Sobreira, M. Soumagnac, E. Suchyta, M. Sullivan, M. Swanson, G. Tarle, J. Thaler, D. Thomas, R. C. Thomas, D. Tucker, J. D. Vieira, V. Vikram, A. R. Walker, R. H. Wechsler, J. Weller, W. Wester, L. Whiteway, H. Wilcox, B. Yanny, Y. Zhang, and J. Zuntz, "The Dark Energy Survey: more than dark energy - an overview," *MNRAS*, vol. 460, pp. 1270–1299, Aug. 2016.

[80] J. de Jong *et al.*, "The third data release of the Kilo-Degree Survey and associated data products," *Astron. Astrophys.*, vol. 604, p. A134, 2017.

[81] H. Aihara, N. Arimoto, R. Armstrong, S. Arnouts, N. A. Bahcall, S. Bickerton, J. Bosch, K. Bundy, P. L. Capak, J. H. H. Chan, M. Chiba, J. Coupon, E. Egami, M. Enoki, F. Finet, H. Fujimori, S. Fujimoto, H. Furusawa, J. Furusawa, T. Goto, A. Goulding, J. P. Greco, J. E. Greene, J. E. Gunn, T. Hamana, Y. Harikane, Y. Hashimoto, T. Hattori, M. Hayashi, Y. Hayashi, K. G. Hełminiak, R. Higuchi, C. Hikage, P. T. P. Ho, B.-C. Hsieh, K. Huang, S. Huang, H. Ikeda, M. Imanishi, A. K. Inoue, K. Iwasawa, I. Iwata, A. T. Jaelani, H.-Y. Jian, Y. Kamata, H. Karoji, N. Kashikawa, N. Katayama, S. Kawanomoto, I. Kayo, J. Koda, M. Koike, T. Kojima, Y. Komiyama, A. Konno, S. Koshida, Y. Koyama, H. Kusakabe, A. Leauthaud, C.-H. Lee, L. Lin, Y.-T. Lin, R. H. Lupton, R. Mand elbaum, Y. Matsuoka, E. Medezinski, S. Mineo, S. Miyama, H. Miyatake, S. Miyazaki, R. Momose, A. More, S. More, Y. Moritani, T. J. Moriya, T. Morokuma, S. Mukae, R. Murata, H. Murayama, T. Nagao, F. Nakata, M. Niida, H. Niikura, A. J. Nishizawa, Y. Obuchi, M. Oguri, Y. Oishi, N. Okabe, S. Okamoto, Y. Okura, Y. Ono, M. Onodera, M. Onoue, K. Osato, M. Ouchi, P. A. Price, T.-S. Pyo, M. Sako, M. Sawicki, T. Shibuya, K. Shimasaku, A. Shimono, M. Shirasaki, J. D. Silverman, M. Simet, J. Speagle, D. N. Spergel, M. A. Strauss, Y. Sugahara, N. Sugiyama, Y. Suto, S. H. Suyu, N. Suzuki, P. J. Tait, M. Takada, T. Takata, N. Tamura, M. M. Tanaka, M. Tanaka, M. Tanaka, Y. Tanaka, T. Terai, Y. Terashima, Y. Toba, N. Tominaga, J. Toshikawa, E. L. Turner, T. Uchida, H. Uchiyama, K. Umetsu, F. Uraguchi, Y. Urata, T. Usuda, Y. Utsumi, S.-Y. Wang, W.-H. Wang, K. C. Wong, K. Yabe, Y. Yamada, H. Yamanoi, N. Yasuda, S. Yeh, A. Yonehara, and S. Yuma, "The Hyper Suprime-Cam SSP Survey: Overview and survey design," *PASJ*, vol. 70, p. S4, Jan. 2018.

[82] LSST Science Collaboration, P. A. Abell, J. Allison, S. F. Anderson, J. R. Andrew, J. R. P. Angel, L. Armus, D. Arnett, S. J. Asztalos, T. S. Axelrod, S. Bailey, D. R. Ballantyne, J. R. Bankert, W. A. Barkhouse, J. D. Barr, L. F. Barrientos, A. J. Barth, J. G. Bartlett, A. C. Becker, J. Becla, T. C. Beers, J. P. Bernstein, R. Biswas, M. R. Blanton, J. S. Bloom, J. J. Bochanski, P. Boeshaar, K. D. Borne, M. Bradac, W. N. Brandt, C. R. Bridge, M. E. Brown, R. J. Brunner, J. S. Bullock, A. J. Burgasser, J. H. Burge, D. L. Burke, P. A. Cargile, S. Chand rasekharan, G. Chartas, S. R. Chesley, Y.-H. Chu, D. Cinabro, M. W. Claire, C. F. Claver, D. Clowe, A. J. Connolly, K. H. Cook, J. Cooke, A. Cooray, K. R. Covey, C. S. Culliton, R. de Jong, W. H. de Vries, V. P. Debattista, F. Delgado, I. P. Dell'Antonio, S. Dhital, R. Di Stefano, M. Dickinson, B. Dilday, S. G. Djorgovski, G. Dobler, C. Donalek, G. Dubois-Felsmann, J. Durech, A. Eliasdottir, M. Eracleous, L. Eyer, E. E.

Falco, X. Fan, C. D. Fassnacht, H. C. Ferguson, Y. R. Fernandez, B. D. Fields, D. Finkbeiner, E. E. Figueroa, D. B. Fox, H. Francke, J. S. Frank, J. Frieman, S. Fromenteau, M. Furqan, G. Galaz, A. Gal-Yam, P. Garnavich, E. Gawiser, J. Geary, P. Gee, R. R. Gibson, K. Gilmore, E. A. Grace, R. F. Green, W. J. Gressler, C. J. Grillmair, S. Habib, J. S. Haggerty, M. Hamuy, A. W. Harris, S. L. Hawley, A. F. Heavens, L. Hebb, T. J. Henry, E. Hileman, E. J. Hilton, K. Hoadley, J. B. Holberg, M. J. Holman, S. B. Howell, L. Infante, Z. Ivezic, S. H. Jacoby, B. Jain, R, Jedicke, M. J. Jee, J. Garrett Jernigan, S. W. Jha, K. V. Johnston, R. L. Jones, M. Juric, M. Kaasalainen, Styliani, Kafka, S. M. Kahn, N. A. Kaib, J. Kalirai, J. Kantor, M. M. Kasliwal, C. R. Keeton, R. Kessler, Z. Knezevic, A. Kowalski, V. L. Krabbendam, K. S. Krughoff, S. Kulkarni, S. Kuhlman, M. Lacy, S. Lepine, M. Liang, A. Lien, P. Lira, K. S. Long, S. Lorenz, J. M. Lotz, R. H. Lupton, J. Lutz, L. M. Macri, A. A. Mahabal, R. Mandelbaum, P. Marshall, M. May, P. M. McGehee, B. T. Meadows, A. Meert, A. Milani, C. J. Miller, M. Miller, D. Mills, D. Minniti, D. Monet, A. S. Mukadam, E. Nakar, D. R. Neill, J. A. Newman, S. Nikolaev, M. Nordby, P. O'Connor, M. Oguri, J. Oliver, S. S. Olivier, J. K. Olsen, K. Olsen, E. W. Olszewski, H. Oluseyi, N. D. Padilla, A. Parker, J. Pepper, J. R. Peterson, C. Petry, P. A. Pinto, J. L. Pizagno, B. Popescu, A. Prsa, V. Radcka, M. J. Raddick, A. Rasmussen, A. Rau, J. Rho, J. E. Rhoads, G. T. Richards, S. T. Ridgway, B. E. Robertson, R. Roskar, A. Saha, A. Sarajedini, E. Scannapieco, T. Schalk, R. Schindler, S. Schmidt, S. Schmidt, D. P. Schneider, G. Schumacher, R. Scranton, J. Sebag, L. G. Seppala, O. Shemmer, J. D. Simon, M. Sivertz, H. A. Smith, J. Allyn Smith, N. Smith, A. H. Spitz, A. Stanford, K. G. Stassun, J. Strader, M. A. Strauss, C. W. Stubbs, D. W. Sweeney, A. Szalay, P. Szkody, M. Takada, P. Thorman, D. E. Trilling, V. Trimble, A. Tyson, R. Van Berg, D. Vand en Berk, J. VanderPlas, L. Verde, B. Vrsnak, L. M. Walkowicz, B. D. Wand elt, S. Wang, Y. Wang, M. Warner, R. H. Wechsler, A. A. West, O. Wiecha, B. F. Williams, B. Willman, D. Wittman, S. C. Wolff, W. M. Wood-Vasey, P. Wozniak, P. Young, A. Zentner, and H. Zhan, "LSST Science Book, Version 2.0," *arXiv e-prints*, p. arXiv:0912.0201, Dec. 2009.

[83] D. Spergel, N. Gehrels, C. Baltay, D. Bennett, J. Breckinridge, M. Donahue, A. Dressler, B. S. Gaudi, T. Greene, O. Guyon, C. Hirata, J. Kalirai, N. J. Kasdin, B. Macintosh, W. Moos, S. Perlmutter, M. Postman, B. Rauscher, J. Rhodes, Y. Wang, D. Weinberg, D. Benford, M. Hudson, W. S. Jeong, Y. Mellier, W. Traub, T. Yamada, P. Capak, J. Colbert, D. Masters, M. Penny, D. Savransky, D. Stern, N. Zimmerman, R. Barry, L. Bartusek, K. Carpenter, E. Cheng, D. Content, F. Dekens, R. Demers, K. Grady, C. Jackson, G. Kuan, J. Kruk, M. Melton, B. Nemati, B. Parvin, I. Poberezhskiy, C. Peddie, J. Ruffa, J. K. Wallace, A. Whipple, E. Wollack, and F. Zhao, "Wide-Field InfrarRed Survey Telescope-Astrophysics Focused Telescope Assets WFIRST-AFTA 2015 Report," *arXiv e-prints*, p. arXiv:1503.03757, Mar. 2015.

[84] E. Bertin, "Automated Morphometry with SExtractor and PSFEx," in *Astronomical Data Analysis Software and Systems XX* (I. N. Evans, A. Accomazzi, D. J. Mink, and A. H. Rots, eds.), vol. 442 of *Astronomical Society of the Pacific Conference Series*, p. 435, July 2011.

[85] M. Jarvis, G. M. Bernstein, A. Amon, C. Davis, P. F. Léget, K. Bechtol, I. Harrison, M. Gatti, A. Roodman, C. Chang, R. Chen, A. Choi, S. Desai, A. Drlica-Wagner, D. Gruen, R. A. Gruendl, A. Hernandez, N. MacCrann, J. Meyers, A. Navarro-Alsina, S. Pandey, A. A. Plazas, L. F. Secco, E. Sheldon, M. A. Troxel, S. Vorperian, K. Wei, J. Zuntz, T. M. C. Abbott, M. Aguena, S. Allam, S. Avila, S. Bhargava, S. L. Bridle, D. Brooks, A. Carnero Rosell, M. Carrasco Kind, J. Carretero, M. Costanzi, L. N. da Costa, J. De Vicente, H. T. Diehl, P. Doel, S. Everett, B. Flaugher, P. Fosalba, J. Frieman, J. García-Bellido, E. Gaztanaga, D. W. Gerdes, G. Gutierrez, S. R. Hinton, D. L. Hollowood, K. Honscheid, D. J. James, S. Kent, K. Kuehn, N. Kuropatkin, O. Lahav, M. A. G. Maia, M. March, J. L. Marshall, P. Melchior, F. Menanteau, R. Miquel, R. L. C. Ogando, F. Paz-Chinchón, E. S. Rykoff, E. Sanchez, V. Scarpine, M. Schubnell, S. Serrano, I. Sevilla-Noarbe, M. Smith, E. Suchyta, M. E. C. Swanson, G. Tarle, T. N. Varga, A. R. Walker, W. Wester, R. D. Wilkinson, and DES Collaboration, "Dark Energy Survey year 3 results: point spread function modelling," *MNRAS*, vol. 501, pp. 1282–1299, Feb. 2021.

[86] C. M. Hirata and U. Seljak, "Shear calibration biases in weak lensing surveys," *Mon. Not. Roy. Astron. Soc.*, vol. 343, pp. 459–480, 2003.

[87] S. Paulin-Henriksson, A. Amara, L. Voigt, A. Refregier, and S. Bridle, "Requirements on PSF Calibration for Dark Energy from Cosmic Shear," *Astron. Astrophys.*, vol. 484, p. 67, 2008.

[88] B. Rowe, "Improving PSF modelling for weak gravitational lensing using new methods in model selection," *MNRAS*, vol. 404, pp. 350–366, May 2010.

[89] M. Jarvis, E. Sheldon, J. Zuntz, T. Kacprzak, S. L. Bridle, A. Amara, R. Armstrong, M. R. Becker, G. M. Bernstein, C. Bonnett, C. Chang, R. Das, J. P. Dietrich, A. Drlica-Wagner, T. F. Eifler, C. Gangkofner, D. Gruen, M. Hirsch, E. M. Huff, B. Jain, S. Kent, D. Kirk, N. MacCrann, P. Melchior, A. A. Plazas, A. Refregier, B. Rowe, E. S. Rykoff, S. Samuroff, C. Sánchez, E. Suchyta, M. A. Troxel, V. Vikram, T. Abbott, F. B. Abdalla, S. Allam, J. Annis, A. Benoit-Lévy, E. Bertin, D. Brooks, E. Buckley-Geer, D. L. Burke, D. Capozzi, A. Carnero Rosell, M. Carrasco Kind, J. Carretero, F. J. Castander, J. Clampitt, M. Crocce, C. E. Cunha, C. B. D'Andrea, L. N. da Costa, D. L. DePoy, S. Desai, H. T. Diehl, P. Doel, A. Fausti Neto, B. Flaugher, P. Fosalba, J. Frieman, E. Gaztanaga, D. W. Gerdes, R. A. Gruendl, G. Gutierrez, K. Honscheid, D. J. James, K. Kuehn, N. Kuropatkin, O. Lahav, T. S. Li, M. Lima, M. March, P. Martini, R. Miquel, J. J. Mohr, E. Neilsen, B. Nord, R. Ogando, K. Reil, A. K. Romer, A. Roodman, M. Sako, E. Sanchez, V. Scarpine, M. Schubnell, I. Sevilla-Noarbe, R. C. Smith, M. Soares-Santos, F. Sobreira, M. E. C. Swanson, G. Tarle, J. Thaler, D. Thomas, A. R. Walker, and R. H. Wechsler, "The DES Science Verification weak lensing shear catalogues," *MNRAS*, vol. 460, pp. 2245–2281, Aug. 2016.

[90] The LSST Dark Energy Science Collaboration, R. Mandelbaum, T. Eifler, R. Hložek, T. Collett, E. Gawiser, D. Scolnic, D. Alonso, H. Awan, R. Biswas, J. Blazek, P. Burchat, N. E. Chisari, I. Dell'Antonio, S. Digel, J. Frieman, D. A. Goldstein, I. Hook, Ž. Ivezić, S. M. Kahn, S. Kamath, D. Kirkby, T. Kitching, E. Krause, P.-F. Leget, P. J. Marshall, J. Meyers, H. Miyatake, J. A. Newman, R. Nichol, E. Rykoff, F. J. Sanchez, A. Slosar, M. Sullivan, and M. A. Troxel, "The LSST Dark Energy Science Collaboration (DESC) Science Requirements Document," *arXiv e-prints*, p. arXiv:1809.01669, Sept. 2018.

[91] P. Melchior, M. Viola, B. M. Schäfer, and M. Bartelmann, "Weak gravitational lensing with DEIMOS," *MNRAS*, vol. 412, pp. 1552–1558, Apr. 2011.

[92] M. A. Schmitz, J. L. Starck, F. Ngole Mboula, N. Auricchio, J. Brinchmann, R. I. Vito Capobianco, R. Clédassou, L. Conversi, L. Corcione, N. Fourmanoit, M. Frailis, B. Garilli, F. Hormuth, D. Hu, H. Israel, S. Kermiche, T. D. Kitching, B. Kubik, M. Kunz, S. Ligori, P. B. Lilje, I. Lloro, O. Mansutti, O. Marggraf, R. J. Massey, F. Pasian, V. Pettorino, F. Raison, J. D. Rhodes, M. Roncarelli, R. P. Saglia, P. Schneider, S. Serrano, A. N. Taylor, R. Toledo-Moreo, L. Valenziano, C. Vuerli, and J. Zoubian, "Euclid: Nonparametric point spread function field recovery through interpolation on a graph Laplacian," *A&A*, vol. 636, p. A78, Apr. 2020.

[93] B. T. P. Rowe, M. Jarvis, R. Mandelbaum, G. M. Bernstein, J. Bosch, M. Simet, J. E. Meyers, T. Kacprzak, R. Nakajima, J. Zuntz, H. Miyatake, J. P. Dietrich, R. Armstrong, P. Melchior, and M. S. S. Gill, "GALSIM: The modular galaxy image simulation toolkit," *Astronomy and Computing*, vol. 10, pp. 121–150, Apr. 2015.

[94] J. Zuntz, E. Sheldon, S. Samuroff, M. A. Troxel, M. Jarvis, N. MacCrann, D. Gruen, J. Prat, C. Sánchez, A. Choi, S. L. Bridle, G. M. Bernstein, S. Dodelson, A. Drlica-Wagner, Y. Fang, R. A. Gruendl, B. Hoyle, E. M. Huff, B. Jain, D. Kirk, T. Kacprzak, C. Krawiec, A. A. Plazas, R. P. Rollins, E. S. Rykoff, I. Sevilla-Noarbe, B. Soergel, T. N. Varga, T. M. C. Abbott, F. B. Abdalla, S. Allam, J. Annis, K. Bechtol, A. Benoit-Lévy, E. Bertin, E. Buckley-Geer, D. L. Burke, A. Carnero Rosell,

M. Carrasco Kind, J. Carretero, F. J. Castander, M. Crocce, C. E. Cunha, C. B. D'Andrea, L. N. da Costa, C. Davis, S. Desai, H. T. Diehl, J. P. Dietrich, P. Doel, T. F. Eifler, J. Estrada, A. E. Evrard, A. Fausti Neto, E. Fernandez, B. Flaugher, P. Fosalba, J. Frieman, J. García-Bellido, E. Gaztanaga, D. W. Gerdes, T. Giannantonio, J. Gschwend, G. Gutierrez, W. G. Hartley, K. Honscheid, D. J. James, T. Jeltema, M. W. G. Johnson, M. D. Johnson, K. Kuehn, S. Kuhlmann, N. Kuropatkin, O. Lahav, T. S. Li, M. Lima, M. A. G. Maia, M. March, P. Martini, P. Melchior, F. Menanteau, C. J. Miller, R. Miquel, J. J. Mohr, E. Neilsen, R. C. Nichol, R. L. C. Ogando, N. Roe, A. K. Romer, A. Roodman, E. Sanchez, V. Scarpine, R. Schindler, M. Schubnell, M. Smith, R. C. Smith, M. Soares-Santos, F. Sobreira, E. Suchyta, M. E. C. Swanson, G. Tarle, D. Thomas, D. L. Tucker, V. Vikram, A. R. Walker, R. H. Wechsler, Y. Zhang, and DES Collaboration, "Dark Energy Survey Year 1 results: weak lensing shape catalogues," *MNRAS*, vol. 481, pp. 1149–1182, Nov. 2018.

[95] B. Giblin, C. Heymans, M. Asgari, H. Hildebrandt, H. Hoekstra, B. Joachimi, A. Kannawadi, K. Kuijken, C.-A. Lin, L. Miller, T. Tröster, J. L. van den Busch, A. H. Wright, M. Bilicki, C. Blake, J. de Jong, A. Dvornik, T. Erben, F. Getman, N. R. Napolitano, P. Schneider, and H. Shan, "KiDS-1000 catalogue: weak gravitational lensing shear measurements," *arXiv e-prints*, p. arXiv:2007.01845, July 2020.

[96] M. Asgari, C.-A. Lin, B. Joachimi, B. Giblin, C. Heymans, H. Hildebrandt, A. Kannawadi, B. Stölzner, T. Tröster, J. L. van den Busch, A. H. Wright, M. Bilicki, C. Blake, J. de Jong, A. Dvornik, T. Erben, F. Getman, H. Hoekstra, F. Köhlinger, K. Kuijken, L. Miller, M. Radovich, P. Schneider, H. Shan, and E. Valentijn, "KiDS-1000 Cosmology: Cosmic shear constraints and comparison between two point statistics," *arXiv e-prints*, p. arXiv:2007.15633, July 2020.

[97] P. Schneider, L. van Waerbeke, M. Kilbinger, and Y. Mellier, "Analysis of two-point statistics of cosmic shear. I. Estimators and covariances," *A&A*, vol. 396, pp. 1–19, Dec. 2002.

[98] M. Kilbinger and P. Schneider, "Analysis of two-point statistics of cosmic shear. II. Optimizing the survey geometry," *A&A*, vol. 413, pp. 465–476, Jan. 2004.

[99] R. Mandelbaum, B. Rowe, R. Armstrong, D. Bard, E. Bertin, J. Bosch, D. Boutigny, F. Courbin, W. A. Dawson, A. Donnarumma, I. Fenech Conti, R. Gavazzi, M. Gentile, M. S. S. Gill, D. W. Hogg, E. M. Huff, M. J. Jee, T. Kacprzak, M. Kilbinger, T. Kuntzer, D. Lang, W. Luo, M. C. March, P. J. Marshall, J. E. Meyers, L. Miller, H. Miyatake, R. Nakajima, F. M. Ngolé Mboula, G. Nurbaeva, Y. Okura, S. Paulin-Henriksson, J. Rhodes, M. D. Schneider, H. Shan, E. S. Sheldon, M. Simet, J.-L. Starck, F. Sureau, M. Tewes, K. Zarb Adami, J. Zhang, and J. Zuntz, "GREAT3 results - I. Systematic errors in shear estimation and the impact of real galaxy morphology," *MNRAS*, vol. 450, pp. 2963–3007, July 2015.

[100] L. Miller, C. Heymans, T. D. Kitching, L. van Waerbeke, T. Erben, H. Hildebrandt, H. Hoekstra, Y. Mellier, B. T. P. Rowe, J. Coupon, J. P. Dietrich, L. Fu, J. Harnois-Déraps, M. J. Hudson, M. Kilbinger, K. Kuijken, T. Schrabback, E. Semboloni, S. Vafaei, and M. Velander, "Bayesian galaxy shape measurement for weak lensing surveys - III. Application to the Canada-France-Hawaii Telescope Lensing Survey," *MNRAS*, vol. 429, pp. 2858–2880, Mar. 2013.

[101] I. Fenech Conti, R. Herbonnet, H. Hoekstra, J. Merten, L. Miller, and M. Viola, "Calibration of weak-lensing shear in the Kilo-Degree Survey," *MNRAS*, vol. 467, pp. 1627–1651, May 2017.

[102] A. Kannawadi, H. Hoekstra, L. Miller, M. Viola, I. Fenech Conti, R. Herbonnet, T. Erben, C. Heymans, H. Hildebrandt, K. Kuijken, M. Vakili, and A. H. Wright, "Towards emulating cosmic shear data: revisiting the calibration of the shear measurements for the Kilo-Degree Survey," *A&A*, vol. 624, p. A92, Apr. 2019.

[103] G. M. Bernstein, R. Armstrong, C. Krawiec, and M. C. March, "An accurate and practical method for inference of weak gravitational lensing from galaxy images," *MNRAS*, vol. 459, pp. 4467–4484, July 2016.

[104] A. Leauthaud, R. Massey, J.-P. Kneib, J. Rhodes, D. E. Johnston, P. Capak, C. Heymans, R. S. Ellis, A. M. Koekemoer, O. Le Fèvre, Y. Mellier, A. Réfrégier, A. C. Robin, N. Scoville, L. Tasca, J. E. Taylor, and L. Van Waerbeke, "Weak Gravitational Lensing with COSMOS: Galaxy Selection and Shape Measurements," *ApJS*, vol. 172, pp. 219–238, Sept. 2007.

[105] B. R. Gillis, T. Schrabback, O. Marggraf, R. Mandelbaum, R. Massey, J. Rhodes, and A. Taylor, "Validation of PSF models for HST and other space-based observations," *MNRAS*, vol. 496, pp. 5017–5038, June 2020.

[106] J. E. Krist and C. J. Burrows, "Phase-retrieval analysis of pre-and post-repair Hubble Space Telescope images," *Appl. Opt.*, vol. 34, pp. 4951–4964, Aug. 1995.

[107] R. A. Gonsalves, "Phase Retrieval And Diversity In Adaptive Optics," *Optical Engineering*, vol. 21, p. 829, Oct. 1982.

[108] A. Roodman, K. Reil, and C. Davis, "Wavefront sensing and the active optics system of the dark energy camera," in *Ground-based and Airborne Telescopes V* (L. M. Stepp, R. Gilmozzi, and H. J. Hall, eds.), vol. 9145, pp. 421 – 438, International Society for Optics and Photonics, SPIE, 2014.

[109] B. Xin, A. Roodman, G. Angeli, C. Claver, and S. Thomas, "Comparison of LSST and DECam wavefront recovery algorithms," in *Ground-based and Airborne Telescopes VI* (H. J. Hall, R. Gilmozzi, and H. K. Marshall, eds.), vol. 9906, pp. 1577 – 1586, International Society for Optics and Photonics, SPIE, 2016.

[110] J. Bosch, R. Armstrong, S. Bickerton, H. Furusawa, H. Ikeda, M. Koike, R. Lupton, S. Mineo, P. Price, T. Takata, M. Tanaka, N. Yasuda, Y. AlSayyad, A. C. Becker, W. Coulton, J. Coupon, J. Garmilla, S. Huang, K. S. Krughoff, D. Lang, A. Leauthaud, K.-T. Lim, N. B. Lust, L. A. MacArthur, R. Mand elbaum, H. Miyatake, S. Miyazaki, R. Murata, S. More, Y. Okura, R. Owen, J. D. Swinbank, M. A. Strauss, Y. Yamada, and H. Yamanoi, "The Hyper Suprime-Cam software pipeline," *PASJ*, vol. 70, p. S5, Jan. 2018.

[111] J. Estrada, T. Abbott, B. Angstadt, L. Buckley-Geer, M. Brown, J. Campa, L. Cardiel, H. Cease, B. Flaugher, K. Dawson, G. Derylo, H. T. Diehl, S. Gruenendahl, I. Karliner, W. Merrit, P. Moore, T. C. Moore, N. Roe, V. Scarpine, R. Schmidt, M. Schubnel, T. Shaw, W. Stuermer, and J. Thaler, "CCD testing and characterization for dark energy survey," in *Ground-based and Airborne Instrumentation for Astronomy* (I. S. McLean and M. Iye, eds.), vol. 6269, pp. 1120 – 1134, International Society for Optics and Photonics, SPIE, 2006.

[112] A. Kannawadi, C. A. Shapiro, R. Mandelbaum, C. M. Hirata, J. W. Kruk, and J. D. Rhodes, "The Impact of Interpixel Capacitance in CMOS Detectors on PSF Shapes and Implications for WFIRST," *PASP*, vol. 128, p. 095001, Sept. 2016.

[113] R. Mandelbaum, C. M. Hirata, U. Seljak, J. Guzik, N. Padmanabhan, C. Blake, M. R. Blanton, R. Lupton, and J. Brinkmann, "Systematic errors in weak lensing: Application to SDSS galaxy-galaxy weak lensing," *Mon. Not. Roy. Astron. Soc.*, vol. 361, pp. 1287–1322, 2005.

[114] G. Bernstein and M. Jarvis, "Shapes and shears, stars and smears: optimal measurements for weak lensing," *Astron. J.*, vol. 123, pp. 583–618, 2002.

[115] N. Kaiser, G. Squires, and T. J. Broadhurst, "A Method for weak lensing observations," *Astrophys. J.*, vol. 449, pp. 460–475, 1995.

[116] R. Massey *et al.*, "The Shear TEsting Programme 2: Factors affecting high precision weak lensing analyses," *Mon. Not. Roy. Astron. Soc.*, vol. 376, pp. 13–38, 2007.

[117] P. R. Durrell, "Surface Photometry of Virgo Dwarf Ellipticals," *AJ*, vol. 113, pp. 531–539, Feb. 1997.

[118] J. L. Sérsic, "Influence of the atmospheric and instrumental dispersion on the brightness distribution in a galaxy," *Boletin de la Asociacion Argentina de Astronomia La Plata Argentina*, vol. 6, pp. 41–43, Feb. 1963.

[119] A. M. Koekemoer, H. Aussel, D. Calzetti, P. Capak, M. Giavalisco, J. P. Kneib, A. Leauthaud, O. Le Fèvre, H. J. McCracken, R. Massey, B. Mobasher, J. Rhodes, N. Scoville, and P. L. Shopbell, "The COSMOS Survey: Hubble Space Telescope Advanced Camera for Surveys Observations and Data Processing," *ApJS*, vol. 172, pp. 196–202, Sept. 2007.

[120] A. Kannawadi, R. Mandelbaum, and C. Lackner, "The impact of cosmic variance on simulating weak lensing surveys," *MNRAS*, vol. 449, pp. 3597–3612, June 2015.

[121] X. Li, N. Katayama, M. Oguri, and S. More, "Fourier Power Function Shapelets (FPFS) shear estimator: performance on image simulations," *MNRAS*, vol. 481, pp. 4445–4460, Dec. 2018.

[122] J. Zuntz, T. Kacprzak, L. Voigt, M. Hirsch, B. Rowe, and S. Bridle, "IM3SHAPE: A maximum-likelihood galaxy shear measurement code for cosmic gravitational lensing," *Mon. Not. Roy. Astron. Soc.*, vol. 434, p. 1604, 2013.

[123] M. Jurić, J. Kantor, K. T. Lim, R. H. Lupton, G. Dubois-Felsmann, T. Jenness, T. S. Axelrod, J. Aleksić, R. A. Allsman, Y. AlSayyad, J. Alt, R. Armstrong, J. Basney, A. C. Becker, J. Becla, R. Biswas, J. Bosch, D. Boutigny, M. C. Kind, D. R. Ciardi, A. J. Connolly, S. F. Daniel, G. E. Daues, F. Economou, H. F. Chiang, A. Fausti, M. Fisher-Levine, D. M. Freemon, P. Gris, F. Hernandez, J. Hoblitt, Z. Ivezić, F. Jammes, D. Jevremović, R. L. Jones, J. B. Kalmbach, V. P. Kasliwal, K. S. Krughoff, J. Lurie, N. B. Lust, L. A. MacArthur, P. Melchior, J. Moeyens, D. L. Nidever, R. Owen, J. K. Parejko, J. M. Peterson, D. Petravick, S. R. Pietrowicz, P. A. Price, D. J. Reiss, R. A. Shaw, J. Sick, C. T. Slater, M. A. Strauss, I. S. Sullivan, J. D. Swinbank, S. Van Dyk, V. Vujčić, A. Withers, and P. Yoachim, "The LSST Data Management System," in *Astronomical Data Analysis Software and Systems XXV* (N. P. F. Lorente, K. Shortridge, and R. Wayth, eds.), vol. 512 of *Astronomical Society of the Pacific Conference Series*, p. 279, Dec. 2017.

[124] R. Massey, H. Hoekstra, T. Kitching, J. Rhodes, M. Cropper, J. Amiaux, D. Harvey, Y. Mellier, M. Meneghetti, L. Miller, S. Paulin-Henriksson, S. r. Pires, R. Scaramella, and T. Schrabback, "Origins of weak lensing systematics, and requirements on future instrumentation (or knowledge of instrumentation)," *MNRAS*, vol. 429, pp. 661–678, Feb. 2013.

[125] Y. Zu and R. Mandelbaum, "Mapping stellar content to dark matter haloes using galaxy clustering and galaxy-galaxy lensing in the SDSS DR7," *MNRAS*, vol. 454, pp. 1161–1191, Dec. 2015.

[126] M. Asgari, C.-A. Lin, B. Joachimi, B. Giblin, C. Heymans, H. Hildebrandt, A. Kannawadi, B. Stölzner, T. Tröster, J. L. van den Busch, A. H. Wright, M. Bilicki, C. Blake, J. de Jong, A. Dvornik, T. Erben, F. Getman, H. Hoekstra, F. Köhlinger, K. Kuijken, L. Miller, M. Radovich, P. Schneider, H. Shan, and E. Valentijn, "KiDS-1000 cosmology: Cosmic shear constraints and comparison between two point statistics," *A&A*, vol. 645, p. A104, Jan. 2021.

[127] A. Amon, D. Gruen, M. A. Troxel, N. MacCrann, S. Dodelson, A. Choi, C. Doux, L. F. Secco, S. Samuroff, E. Krause, J. Cordero, J. Myles, J. DeRose, R. H. Wechsler, M. Gatti, A. Navarro-Alsina, G. M. Bernstein, B. Jain, J. Blazek, A. Alarcon, A. Ferté, M. Raveri, P. Lemos, A. Campos, J. Prat, C. Sánchez, M. Jarvis, O. Alves, F. Andrade-Oliveira, E. Baxter, K. Bechtol, M. R. Becker, S. L. Bridle, H. Camacho, A. Campos, A. Carnero Rosell, M. Carrasco Kind, R. Cawthon, C. Chang, R. Chen, P. Chintalapati, M. Crocce, C. Davis, H. T. Diehl, A. Drlica-Wagner, K. Eckert, T. F. Eifler, J. Elvin-Poole, S. Everett, X. Fang, P. Fosalba, O. Friedrich, G. Giannini, R. A. Gruendl, I. Harrison, W. G. Hartley, K. Herner, H. Huang, E. M. Huff, D. Huterer, N. Kuropatkin, P. F. Leget, A. R. Liddle, J. McCullough, J. Muir, S. Pandey, Y. Park, A. Porredon, A. Refregier, R. P. Rollins, A. Roodman, R. Rosenfeld, A. J. Ross, E. S. Rykoff, J. Sanchez, I. Sevilla-Noarbe, E. Sheldon, T. Shin, A. Troja, I. Tutusaus, T. N. Varga, N. Weaverdyck, B. Yanny, B. Yin, Y. Zhang, J. Zuntz, M. Aguena, S. Allam, J. Annis, D. Bacon, E. Bertin, S. Bhargava, D. Brooks, E. Buckley-Geer, D. L. Burke, J. Carretero, M. Costanzi, L. N. da Costa, M. E. S. Pereira, J. De Vicente, S. Desai, J. P. Dietrich, P. Doel, I. Ferrero, B. Flaugher, J. Frieman, J. García-Bellido, E. Gaztanaga, D. W. Gerdes, T. Giannantonio, J. Gschwend, G. Gutierrez, S. R. Hinton, D. L. Hollowood, K. Honscheid, B. Hoyle, D. J. James, R. Kron, K. Kuehn, O. Lahav, M. Lima, H. Lin, M. A. G. Maia, J. L. Marshall, P. Martini, P. Melchior, F. Menanteau, R. Miquel, J. J. Mohr, R. Morgan, R. L. C. Ogando, A. Palmese, F. Paz-Chinchón, D. Petravick, A. Pieres, A. A. Plazas Malagón, A. K. Romer, E. Sanchez, V. Scarpine, M. Schubnell, S. Serrano, M. Smith, M. Soares-Santos, E. Suchyta, G. Tarle, D. Thomas, C. To, and J. Weller, "Dark Energy Survey Year 3 Results: Cosmology from Cosmic Shear and Robustness to Data Calibration," *arXiv e-prints*, p. arXiv:2105.13543, May 2021.

[128] A. Albrecht, G. Bernstein, R. Cahn, W. L. Freedman, J. Hewitt, W. Hu, J. Huth, M. Kamionkowski, E. W. Kolb, L. Knox, J. C. Mather, S. Staggs, and N. B. Suntzeff, "Report of the Dark Energy Task Force," *arXiv e-prints*, pp. astro–ph/0609591, Sept. 2006.

[129] J. Anderson and I. R. King, "Toward High-Precision Astrometry with WFPC2. I. Deriving an Accurate Point-Spread Function," *PASP*, vol. 112, pp. 1360–1382, Oct. 2000.

[130] L. W. Piotrowski, T. Batsch, H. Czyrkowski, M. Cwiok, R. Dabrowski, G. Kasprowicz, A. Majcher, A. Majczyna, K. Malek, L. Mankiewicz, K. Nawrocki, R. Opiela, M. Siudek, M. Sokolowski, R. Wawrzaszek, G. Wrochna, M. Zaremba, and A. F. Żarnecki, "PSF modelling for very wide-field CCD astronomy," *A&A*, vol. 551, p. A119, Mar. 2013.

[131] J. Miralda-Escude, "The Correlation Function of Galaxy Ellipticities Produced by Gravitational Lensing," *ApJ*, vol. 380, p. 1, Oct. 1991.

[132] C. Heymans, L. Van Waerbeke, D. Bacon, J. Berge, G. Bernstein, E. Bertin, S. Bridle, M. L. Brown, D. Clowe, H. Dahle, T. Erben, M. Gray, M. Hetterscheidt, H. Hoekstra, P. Hudelot, M. Jarvis, K. Kuijken, V. Margoniner, R. Massey, Y. Mellier, R. Nakajima, A. Refregier, J. Rhodes, T. Schrabback, and D. Wittman, "The Shear Testing Programme - I. Weak lensing analysis of simulated ground-based observations," *MNRAS*, vol. 368, pp. 1323–1339, May 2006.

[133] R. Massey and A. Refregier, "Polar shapelets," *MNRAS*, vol. 363, pp. 197–210, Oct. 2005.

[134] R. Massey, B. Rowe, A. Refregier, D. J. Bacon, and J. Bergé, "Weak gravitational shear and flexion with polar shapelets," *MNRAS*, vol. 380, pp. 229–245, Sept. 2007.

[135] H. Aihara, Y. AlSayyad, M. Ando, R. Armstrong, J. Bosch, E. Egami, H. Furusawa, J. Furusawa, S. Harasawa, Y. Harikane, B.-C. Hsieh, H. Ikeda, K. Ito, I. Iwata, T. Kodama, M. Koike, M. Kokubo, Y. Komiyama, X. Li, Y. Liang, Y.-T. Lin, R. H. Lupton, N. B. Lust, L. A. MacArthur, K. Mawatari, S. Mineo, H. Miyatake, S. Miyazaki, S. More, T. Morishima, H. Murayama, K. Nakajima, F. Nakata,

A. J. Nishizawa, M. Oguri, N. Okabe, Y. Okura, Y. Ono, K. Osato, M. Ouchi, Y.-C. Pan, A. A. Plazas Malagón, P. A. Price, S. L. Reed, E. S. Rykoff, T. Shibuya, M. Simunovic, M. A. Strauss, K. Sugimori, Y. Suto, N. Suzuki, M. Takada, Y. Takagi, T. Takata, S. Takita, M. Tanaka, S. Tang, D. S. Taranu, T. Terai, Y. Toba, E. L. Turner, H. Uchiyama, B. Vijarnwannaluk, C. Z. Waters, Y. Yamada, N. Yamamoto, and T. Yamashita, "Third data release of the Hyper Suprime-Cam Subaru Strategic Program," *PASJ*, vol. 74, pp. 247–272, Apr. 2022.

[136] X. Li, H. Miyatake, W. Luo, S. More, M. Oguri, T. Hamana, R. Mandelbaum, M. Shirasaki, M. Takada, R. Armstrong, A. Kannawadi, S. Takita, S. Miyazaki, A. J. Nishizawa, A. A. Plazas Malagon, M. A. Strauss, M. Tanaka, and N. Yoshida, "The three-year shear catalog of the Subaru Hyper Suprime-Cam SSP Survey," *PASJ*, vol. 74, pp. 421–459, Apr. 2022.

[137] D. Korytov, A. Hearin, E. Kovacs, P. Larsen, E. Rangel, J. Hollowed, A. J. Benson, K. Heitmann, Y.-Y. Mao, A. Bahmanyar, C. Chang, D. Campbell, J. DeRose, H. Finkel, N. Frontiere, E. Gawiser, S. Habib, B. Joachimi, F. Lanusse, N. Li, R. Mandelbaum, C. Morrison, J. A. Newman, A. Pope, E. Rykoff, M. Simet, C.-H. To, V. Vikraman, R. H. Wechsler, M. White, and (The LSST Dark Energy Science Collaboration, "CosmoDC2: A Synthetic Sky Catalog for Dark Energy Science with LSST," *ApJS*, vol. 245, p. 26, Dec. 2019.

[138] P. D. Allen, S. P. Driver, A. W. Graham, E. Cameron, J. Liske, and R. de Propris, "The Millennium Galaxy Catalogue: bulge-disc decomposition of 10095 nearby galaxies," *MNRAS*, vol. 371, pp. 2–18, Sept. 2006.

[139] L. Simard, J. T. Mendel, D. R. Patton, S. L. Ellison, and A. W. McConnachie, "A Catalog of Bulge+disk Decompositions and Updated Photometry for 1.12 Million Galaxies in the Sloan Digital Sky Survey," *ApJS*, vol. 196, p. 11, Sept. 2011.

[140] G. de Vaucouleurs, "Recherches sur les Nebuleuses Extragalactiques," *Annales d'Astrophysique*, vol. 11, p. 247, Jan. 1948.

[141] D. Korytov *et al.*, "CosmoDC2: A Synthetic Sky Catalog for Dark Energy Science with LSST," *Astrophys. J. Suppl.*, vol. 245, no. 2, p. 26, 2019.

[142] T. D. Kitching, A. C. Deshpande, and P. L. Taylor, "Propagating residual biases in masked cosmic shear power spectra," *The Open Journal of Astrophysics*, vol. 3, p. 14, Dec. 2020.

[143] E. Kovacs, Y.-Y. Mao, M. Aguena, A. Bahmanyar, A. Broussard, J. Butler, D. Campbell, C. Chang, S. Fu, K. Heitmann, D. Korytov, F. Lanusse, P. Larsen, R. Mandelbaum, C. B. Morrison, C. Payerne, M. Ricci, E. Rykoff, F. J. Sánchez, I. Sevilla-Noarbe, M. Simet, C.-H. To, V. Vikraman, R. Zhou, C. Avestruz, C. Benoist, A. J. Benson, L. Bleem, A. Ćiprianović, C. Combet, E. Gawiser, S. He, R. Joseph, J. A. Newman, J. Prat, S. Schmidt, A. Slosar, J. Zuntz, and The LSST DESC Dark Energy Science Collaboration, "Validating Synthetic Galaxy Catalogs for Dark Energy Science in the LSST Era," *arXiv e-prints*, p. arXiv:2110.03769, Oct. 2021.

[144] Y.-Y. Mao, E. Kovacs, K. Heitmann, T. D. Uram, A. J. Benson, D. Campbell, S. A. Cora, J. DeRose, T. Di Matteo, S. Habib, A. P. Hearin, J. Bryce Kalmbach, K. S. Krughoff, F. Lanusse, Z. Lukić, R. Mandelbaum, J. A. Newman, N. Padilla, E. Paillas, A. Pope, P. M. Ricker, A. N. Ruiz, A. Tenneti, C. A. Vega-Martínez, R. H. Wechsler, R. Zhou, Y. Zu, and LSST Dark Energy Science Collaboration, "DESCQA: An Automated Validation Framework for Synthetic Sky Catalogs," *ApJS*, vol. 234, p. 36, Feb. 2018.

[145] S. Singh, "improved MASTER for the LSS: fast and accurate analysis of the two-point power spectra and correlation functions.," *MNRAS*, vol. 508, pp. 1632–1651, Jan. 2021.

[146] A. Zonca, L. Singer, D. Lenz, M. Reinecke, C. Rosset, E. Hivon, and K. Gorski, "healpy: equal area pixelization and spherical harmonics transforms for data on the sphere in python," *Journal of Open Source Software*, vol. 4, p. 1298, Mar. 2019.

[147] K. M. Górski, E. Hivon, A. J. Banday, B. D. Wandelt, F. K. Hansen, M. Reinecke, and M. Bartelmann, "HEALPix: A Framework for High-Resolution Discretization and Fast Analysis of Data Distributed on the Sphere," *ApJ*, vol. 622, pp. 759–771, Apr. 2005.

[148] E. Krause and T. Eifler, "cosmolike - cosmological likelihood analyses for photometric galaxy surveys," *MNRAS*, vol. 470, pp. 2100–2112, Sept. 2017.

[149] P. A. D'Errico and D. John, "numdifftools," 2018.

[150] N. Bhandari, C. D. Leonard, M. M. Rau, and R. Mandelbaum, "Fisher Matrix Stability," *arXiv e-prints*, p. arXiv:2101.00298, Jan. 2021.

[151] N. E. Chisari, D. Alonso, E. Krause, C. D. Leonard, P. Bull, J. Neveu, A. Villarreal, S. Singh, T. McClintock, J. Ellison, Z. Du, J. Zuntz, A. Mead, S. Joudaki, C. S. Lorenz, T. Tröster, J. Sanchez, F. Lanusse, M. Ishak, R. Hlozek, J. Blazek, J.-E. Campagne, H. Almoubayyed, T. Eifler, M. Kirby, D. Kirkby, S. Plaszczynski, A. Slosar, M. Vrastil, E. L. Wagoner, and LSST Dark Energy Science Collaboration, "Core Cosmology Library: Precision Cosmological Predictions for LSST," *ApJS*, vol. 242, p. 2, May 2019.

[152] D. Huterer, M. Takada, G. Bernstein, and B. Jain, "Systematic errors in future weak-lensing surveys: requirements and prospects for self-calibration," *Monthly Notices of the Royal Astronomical Society*, vol. 366, pp. 101–114, 02 2006.

[153] C. Hikage, M. Oguri, T. Hamana, S. More, R. Mandelbaum, M. Takada, F. Köhlinger, H. Miyatake, A. J. Nishizawa, H. Aihara, R. Armstrong, J. Bosch, J. Coupon, A. Ducout, P. Ho, B.-C. Hsieh, Y. Komiyama, F. Lanusse, A. Leauthaud, R. H. Lupton, E. Medezinski, S. Mineo, S. Miyama, S. Miyazaki, R. Murata, H. Murayama, M. Shirasaki, C. Sifón, M. Simet, J. Speagle, D. N. Spergel, M. A. Strauss, N. Sugiyama, M. Tanaka, Y. Utsumi, S.-Y. Wang, and Y. Yamada, "Cosmology from cosmic shear power spectra with Subaru Hyper Suprime-Cam first-year data," *PASJ*, vol. 71, p. 43, Apr. 2019.

[154] A. Amon, D. Gruen, M. A. Troxel, N. MacCrann, S. Dodelson, A. Choi, C. Doux, L. F. Secco, S. Samuroff, E. Krause, J. Cordero, J. Myles, J. DeRose, R. H. Wechsler, M. Gatti, A. Navarro-Alsina, G. M. Bernstein, B. Jain, J. Blazek, A. Alarcon, A. Ferté, P. Lemos, M. Raveri, A. Campos, J. Prat, C. Sánchez, M. Jarvis, O. Alves, F. Andrade-Oliveira, E. Baxter, K. Bechtol, M. R. Becker, S. L. Bridle, H. Camacho, A. Carnero Rosell, M. Carrasco Kind, R. Cawthon, C. Chang, R. Chen, P. Chintalapati, M. Crocce, C. Davis, H. T. Diehl, A. Drlica-Wagner, K. Eckert, T. F. Eifler, J. Elvin-Poole, S. Everett, X. Fang, P. Fosalba, O. Friedrich, E. Gaztanaga, G. Giannini, R. A. Gruendl, I. Harrison, W. G. Hartley, K. Herner, H. Huang, E. M. Huff, D. Huterer, N. Kuropatkin, P. Leget, A. R. Liddle, J. McCullough, J. Muir, S. Pandey, Y. Park, A. Porredon, A. Refregier, R. P. Rollins, A. Roodman, R. Rosenfeld, A. J. Ross, E. S. Rykoff, J. Sanchez, I. Sevilla-Noarbe, E. Sheldon, T. Shin, A. Troja, I. Tutusaus, I. Tutusaus, T. N. Varga, N. Weaverdyck, B. Yanny, B. Yin, Y. Zhang, J. Zuntz, M. Aguena, S. Allam, J. Annis, D. Bacon, E. Bertin, S. Bhargava, D. Brooks, E. Buckley-Geer, D. L. Burke, J. Carretero, M. Costanzi, L. N. da Costa, M. E. S. Pereira, J. De Vicente, S. Desai, J. P. Dietrich, P. Doel, I. Ferrero, B. Flaugher, J. Frieman, J. García-Bellido, E. Gaztanaga, D. W. Gerdes, T. Giannantonio, J. Gschwend, G. Gutierrez, S. R. Hinton, D. L. Hollowood, K. Honscheid, B. Hoyle, D. J. James, R. Kron, K. Kuehn, O. Lahav, M. Lima, H. Lin, M. A. G. Maia, J. L. Marshall, P. Martini, P. Melchior, F. Menanteau, R. Miquel, J. J. Mohr, R. Morgan, R. L. C. Ogando, A. Palmese, F. Paz-Chinchón, D. Petravick, A. Pieres, A. K. Romer, E. Sanchez, V. Scarpine, M. Schubnell, S. Serrano,

M. Smith, M. Soares-Santos, G. Tarle, D. Thomas, C. To, J. Weller, and DES Collaboration, "Dark Energy Survey Year 3 results: Cosmology from cosmic shear and robustness to data calibration," *Phys. Rev. E*, vol. 105, p. 023514, Jan. 2022.

[155] L. F. Secco, S. Samuroff, E. Krause, B. Jain, J. Blazek, M. Raveri, A. Campos, A. Amon, A. Chen, C. Doux, A. Choi, D. Gruen, G. M. Bernstein, C. Chang, J. DeRose, J. Myles, A. Ferté, P. Lemos, D. Huterer, J. Prat, M. A. Troxel, N. MacCrann, A. R. Liddle, T. Kacprzak, X. Fang, C. Sánchez, S. Pandey, S. Dodelson, P. Chintalapati, K. Hoffmann, A. Alarcon, O. Alves, F. Andrade-Oliveira, E. J. Baxter, K. Bechtol, M. R. Becker, A. Brandao-Souza, H. Camacho, A. Carnero Rosell, M. Carrasco Kind, R. Cawthon, J. P. Cordero, M. Crocce, C. Davis, E. Di Valentino, A. Drlica-Wagner, K. Eckert, T. F. Eifler, M. Elidaiana, F. Elsner, J. Elvin-Poole, S. Everett, P. Fosalba, O. Friedrich, M. Gatti, G. Giannini, R. A. Gruendl, I. Harrison, W. G. Hartley, K. Herner, H. Huang, E. M. Huff, M. Jarvis, N. Jeffrey, N. Kuropatkin, P. F. Leget, J. Muir, J. Mccullough, A. Navarro Alsina, Y. Omori, Y. Park, A. Porredon, R. Rollins, A. Roodman, R. Rosenfeld, A. J. Ross, E. S. Rykoff, J. Sanchez, I. Sevilla-Noarbe, E. S. Sheldon, T. Shin, A. Troja, I. Tutusaus, T. N. Varga, N. Weaverdyck, R. H. Wechsler, B. Yanny, B. Yin, Y. Zhang, J. Zuntz, T. M. C. Abbott, M. Aguena, S. Allam, J. Annis, D. Bacon, E. Bertin, S. Bhargava, S. L. Bridle, D. Brooks, E. Buckley-Geer, D. L. Burke, J. Carretero, M. Costanzi, L. N. da Costa, J. De Vicente, H. T. Diehl, J. P. Dietrich, P. Doel, I. Ferrero, B. Flaugher, J. Frieman, J. García-Bellido, E. Gaztanaga, D. W. Gerdes, T. Giannantonio, J. Gschwend, G. Gutierrez, S. R. Hinton, D. L. Hollowood, K. Honscheid, B. Hoyle, D. J. James, T. Jeltema, K. Kuehn, O. Lahav, M. Lima, H. Lin, M. A. G. Maia, J. L. Marshall, P. Martini, P. Melchior, F. Menanteau, R. Miquel, J. J. Mohr, R. Morgan, R. L. C. Ogando, A. Palmese, F. Paz-Chinchón, D. Petravick, A. Pieres, A. A. Plazas Malagón, M. Rodriguez-Monroy, A. K. Romer, E. Sanchez, V. Scarpine, M. Schubnell, D. Scolnic, S. Serrano, M. Smith, M. Soares-Santos, E. Suchyta, M. E. C. Swanson, G. Tarle, D. Thomas, C. To, and DES Collaboration, "Dark Energy Survey Year 3 results: Cosmology from cosmic shear and robustness to modeling uncertainty," *Phys. Rev. E*, vol. 105, p. 023515, Jan. 2022.

[156] E. Di Valentino, L. A. Anchordoqui, Ö. Akarsu, Y. Ali-Haimoud, L. Amendola, N. Arendse, M. Asgari, M. Ballardini, S. Basilakos, E. Battistelli, M. Benetti, S. Birrer, F. R. Bouchet, M. Bruni, E. Calabrese, D. Camarena, S. Capozziello, A. Chen, J. Chluba, A. Chudaykin, E. Ó. Colgáin, F.-Y. Cyr-Racine, P. de Bernardis, J. de Cruz Pérez, J. Delabrouille, J. Dunkley, C. Escamilla-Rivera, A. Ferté, F. Finelli, W. Freedman, N. Frusciante, E. Giusarma, A. Gómez-Valent, W. Handley, I. Harrison, L. Hart, A. Heavens, H. Hildebrandt, D. Holz, D. Huterer, M. M. Ivanov, S. Joudaki, M. Kamionkowski, T. Karwal, L. Knox, S. Kumar, L. Lamagna, J. Lesgourgues, M. Lucca, V. Marra, S. Masi, S. Matarrese, A. Mazumdar, A. Melchiorri, O. Mena, L. Mersini-Houghton, V. Miranda, C. Moreno-Pulido, D. F. Mota, J. Muir, A. Mukherjee, F. Niedermann, A. Notari, R. C. Nunes, F. Pace, A. Paliathanasis, A. Palmese, S. Pan, D. Paoletti, V. Pettorino, F. Piacentini, V. Poulin, M. Raveri, A. G. Riess, V. Salzano, E. N. Saridakis, A. A. Sen, A. Shafieloo, A. J. Shajib, J. Silk, A. Silvestri, M. S. Sloth, T. L. Smith, J. Solà Peracaula, C. van de Bruck, L. Verde, L. Visinelli, B. D. Wandelt, D. Wang, J.-M. Wang, A. K. Yadav, and W. Yang, "Cosmology Intertwined III: fσ_8 and S$_8$," *Astroparticle Physics*, vol. 131, p. 102604, Sept. 2021.

[157] S. Paulin-Henriksson, A. Amara, L. Voigt, A. Refregier, and S. L. Bridle, "Point spread function calibration requirements for dark energy from cosmic shear," *A&A*, vol. 484, pp. 67–77, June 2008.

[158] E. S. Sheldon, M. R. Becker, N. MacCrann, and M. Jarvis, "Mitigating Shear-dependent Object Detection Biases with Metacalibration," *ApJ*, vol. 902, p. 138, Oct. 2020.

[159] X. Li and R. Mandelbaum, "Analytical Weak-lensing Shear Responses of Galaxy Properties and Galaxy Detection," *arXiv e-prints*, p. arXiv:2208.10522, Aug. 2022.

[160] X. Li, H. Miyatake, W. Luo, S. More, M. Oguri, T. Hamana, R. Mandelbaum, M. Shirasaki, M. Takada, R. Armstrong, A. Kannawadi, S. Takita, S. Miyazaki, A. J. Nishizawa, A. A. Plazas Malagon, M. A. Strauss, M. Tanaka, and N. Yoshida, "The three-year shear catalog of the Subaru Hyper Suprime-Cam SSP Survey," *PASJ*, vol. 74, pp. 421–459, Apr. 2022.

[161] N. Kaiser, G. Wilson, and G. A. Luppino, "Large-Scale Cosmic Shear Measurements," *arXiv e-prints*, pp. astro–ph/0003338, Mar. 2000.

[162] L. Van Waerbeke, Y. Mellier, M. Radovich, E. Bertin, M. Dantel-Fort, H. J. McCracken, O. Le Fèvre, S. Foucaud, J. C. Cuillandre, T. Erben, B. Jain, P. Schneider, F. Bernardeau, and B. Fort, "Cosmic shear statistics and cosmology," *A&A*, vol. 374, pp. 757–769, Aug. 2001.

[163] J. Rhodes, A. Refregier, N. R. Collins, J. P. Gardner, E. J. Groth, and R. S. Hill, "Measurement of Cosmic Shear with the Space Telescope Imaging Spectrograph," *ApJ*, vol. 605, pp. 29–36, Apr. 2004.

[164] C. Heymans, L. Van Waerbeke, L. Miller, T. Erben, H. Hildebrandt, H. Hoekstra, T. D. Kitching, Y. Mellier, P. Simon, C. Bonnett, J. Coupon, L. Fu, J. Harnois Déraps, M. J. Hudson, M. Kilbinger, K. Kuijken, B. Rowe, T. Schrabback, E. Semboloni, E. van Uitert, S. Vafaei, and M. Velander, "CFHTLenS: the Canada-France-Hawaii Telescope Lensing Survey," *MNRAS*, vol. 427, pp. 146–166, Nov. 2012.

[165] R. Massey, J. Rhodes, A. Leauthaud, P. Capak, R. Ellis, A. Koekemoer, A. Réfrégier, N. Scoville, J. E. Taylor, J. Albert, J. Bergé, C. Heymans, D. Johnston, J.-P. Kneib, Y. Mellier, B. Mobasher, E. Semboloni, P. Shopbell, L. Tasca, and L. Van Waerbeke, "COSMOS: Three-dimensional Weak Lensing and the Growth of Structure," *ApJS*, vol. 172, pp. 239–253, Sept. 2007.

[166] T. Schrabback, J. Hartlap, B. Joachimi, M. Kilbinger, P. Simon, K. Benabed, M. Bradač, T. Eifler, T. Erben, C. D. Fassnacht, F. W. High, S. Hilbert, H. Hildebrandt, H. Hoekstra, K. Kuijken, P. J. Marshall, Y. Mellier, E. Morganson, P. Schneider, E. Semboloni, L. van Waerbeke, and M. Velander, "Evidence of the accelerated expansion of the Universe from weak lensing tomography with COSMOS," *A&A*, vol. 516, p. A63, June 2010.

[167] J. Zhang, "Measuring the cosmic shear in fourier space," *MNRAS*, vol. 383, no. 1, p. 113, 2008.

[168] G. M. Bernstein and R. Armstrong, "Bayesian lensing shear measurement," *MNRAS*, vol. 438, pp. 1880–1893, Feb. 2014.

[169] A. Refregier and D. Bacon, "Shapelets - II. A method for weak lensing measurements," *MNRAS*, vol. 338, pp. 48–56, Jan. 2003.

[170] J. Zuntz, T. Kacprzak, L. Voigt, M. Hirsch, B. Rowe, and S. Bridle, "IM3SHAPE: a maximum likelihood galaxy shear measurement code for cosmic gravitational lensing," *MNRAS*, vol. 434, pp. 1604–1618, Sept. 2013.

[171] I. Fenech Conti, R. Herbonnet, H. Hoekstra, J. Merten, L. Miller, and M. Viola, "Calibration of weak-lensing shear in the Kilo-Degree Survey," *MNRAS*, vol. 467, pp. 1627–1651, May 2017.

[172] N. Kaiser, G. Squires, and T. Broadhurst, "A Method for Weak Lensing Observations," *ApJ*, vol. 449, p. 460, Aug. 1995.

[173] G. M. Bernstein and M. Jarvis, "Shapes and Shears, Stars and Smears: Optimal Measurements for Weak Lensing," *AJ*, vol. 123, pp. 583–618, Feb. 2002.

[174] N. Kaiser, "A new shear estimator for weak-lensing observations," *The Astrophysical Journal*, vol. 537, pp. 555–577, jul 2000.

[175] A. Refregier, T. Kacprzak, A. Amara, S. Bridle, and B. Rowe, "Noise bias in weak lensing shape measurements," *MNRAS*, vol. 425, pp. 1951–1957, Sept. 2012.

[176] E. Huff and R. Mandelbaum, "Metacalibration: Direct Self-Calibration of Biases in Shear Measurement," *ArXiv e-prints*, Feb. 2017.

[177] E. S. Sheldon and E. M. Huff, "Practical Weak-lensing Shear Measurement with Metacalibration," *ApJ*, vol. 841, p. 24, May 2017.

[178] R. Mandelbaum, F. Lanusse, A. Leauthaud, R. Armstrong, M. Simet, H. Miyatake, J. E. Meyers, J. Bosch, R. Murata, and S. Miyazaki, "Weak lensing shear calibration with simulations of the HSC survey," *MNRAS*, vol. 481, pp. 3170–3195, Dec 2018.

[179] J. Zhang and E. Komatsu, "Cosmic shears should not be measured in conventional ways," *MNRAS*, vol. 414, pp. 1047–1058, June 2011.

[180] C. Hirata and U. Seljak, "Shear calibration biases in weak-lensing surveys," *MNRAS*, vol. 343, pp. 459–480, Aug. 2003.

[181] R. Massey and A. Refregier, "Polar shapelets," *MNRAS*, vol. 363, pp. 197–210, Oct. 2005.

[182] S. Joudaki *et al.*, "KiDS+VIKING-450 and DES-Y1 combined: Cosmology with cosmic shear," *Astron. Astrophys.*, vol. 638, p. L1, 2020.

[183] C. Doux, B. Jain, D. Zeurcher, J. Lee, X. Fang, R. Rosenfeld, A. Amon, H. Camacho, A. Choi, L. F. Secco, J. Blazek, C. Chang, M. Gatti, E. Gaztanaga, N. Jeffrey, M. Raveri, S. Samuroff, A. Alarcon, O. Alves, F. Andrade-Oliveira, E. Baxter, K. Bechtol, M. R. Becker, G. M. Bernstein, A. Campos, A. Carnero Rosell, M. Carrasco Kind, R. Cawthon, R. Chen, J. Cordero, M. Crocce, C. Davis, J. DeRose, S. Dodelson, A. Drlica-Wagner, K. Eckert, T. F. Eifler, F. Elsner, J. Elvin-Poole, S. Everett, A. Ferté, P. Fosalba, O. Friedrich, G. Giannini, D. Gruen, R. A. Gruendl, I. Harrison, W. G. Hartley, K. Herner, H. Huang, E. M. Huff, D. Huterer, M. Jarvis, E. Krause, N. Kuropatkin, P. F. Leget, P. Lemos, A. R. Liddle, N. MacCrann, J. McCullough, J. Muir, J. Myles, A. Navarro-Alsina, S. Pandey, Y. Park, A. Porredon, J. Prat, M. Rodriguez-Monroy, R. P. Rollins, A. Roodman, A. J. Ross, E. S. Rykoff, C. Sánchez, J. Sanchez, I. Sevilla-Noarbe, E. Sheldon, T. Shin, A. Troja, M. A. Troxel, I. Tutusaus, T. N. Varga, N. Weaverdyck, R. H. Wechsler, B. Yanny, B. Yin, Y. Zhang, J. Zuntz, T. M. C. Abbott, M. Aguena, S. Allam, J. Annis, D. Bacon, E. Bertin, S. Bocquet, D. Brooks, D. L. Burke, J. Carretero, M. Costanzi, L. N. da Costa, M. E. S. Pereira, J. De Vicente, S. Desai, H. T. Diehl, P. Doel, I. Ferrero, B. Flaugher, J. Frieman, J. García-Bellido, D. W. Gerdes, T. Giannantonio, J. Gschwend, G. Gutierrez, S. R. Hinton, D. L. Hollowood, K. Honscheid, D. J. James, A. G. Kim, K. Kuehn, O. Lahav, J. L. Marshall, F. Menanteau, R. Miquel, R. Morgan, R. L. C. Ogando, A. Palmese, F. Paz-Chinchón, A. Pieres, A. A. Plazas Malagón, K. Reil, E. Sanchez, V. Scarpine, S. Serrano, M. Smith, E. Suchyta, M. E. C. Swanson, G. Tarle, D. Thomas, C. To, J. Weller, and DES Collaboration, "Dark energy survey year 3 results: cosmological constraints from the analysis of cosmic shear in harmonic space," *MNRAS*, vol. 515, pp. 1942–1972, Sept. 2022.

[184] A. Loureiro, L. Whittaker, A. Spurio Mancini, B. Joachimi, A. Cuceu, M. Asgari, B. Stölzner, T. Tröster, A. H. Wright, M. Bilicki, A. Dvornik, B. Giblin, C. Heymans, H. Hildebrandt, H. Shan, A. Amara, N. Auricchio, C. Bodendorf, D. Bonino, E. Branchini, M. Brescia, V. Capobianco, C. Carbone, J. Carretero, M. Castellano, S. Cavuoti, A. Cimatti, R. Cledassou, G. Congedo, L. Conversi, Y. Copin, L. Corcione, M. Cropper, A. Da Silva, M. Douspis, F. Dubath, C. A. J. Duncan, X. Dupac,

S. Dusini, S. Farrens, S. Ferriol, P. Fosalba, M. Frailis, E. Franceschi, M. Fumana, B. Garilli, B. Gillis, C. Giocoli, A. Grazian, F. Grupp, S. V. H. Haugan, W. Holmes, F. Hormuth, K. Jahnke, M. Kümmel, S. Kermiche, A. Kiessling, M. Kilbinger, T. Kitching, K. Kuijken, M. Kunz, H. Kurki-Suonio, S. Ligori, P. B. Lilje, I. Lloro, O. Mansutti, O. Marggraf, K. Markovic, F. Marulli, R. Massey, M. Meneghetti, G. Meylan, M. Moresco, B. Morin, L. Moscardini, E. Munari, S. M. Niemi, C. Padilla, S. Paltani, F. Pasian, K. Pedersen, V. Pettorino, S. Pires, M. Poncet, L. Popa, F. Raison, J. Rhodes, H. Rix, M. Roncarelli, R. Saglia, P. Schneider, A. Secroun, S. Serrano, C. Sirignano, G. Sirri, L. Stanco, J. L. Starck, P. Tallada-Crespí, A. N. Taylor, I. Tereno, R. Toledo-Moreo, F. Torradeflot, E. A. Valentijn, Y. Wang, N. Welikala, J. Weller, G. Zamorani, J. Zoubian, S. Andreon, M. Baldi, S. Camera, R. Farinelli, G. Polenta, and N. Tessore, "KiDS and Euclid: Cosmological implications of a pseudo angular power spectrum analysis of KiDS-1000 cosmic shear tomography," *A&A*, vol. 665, p. A56, Sept. 2022.

[185] E. Krause, T. F. Eifler, J. Zuntz, O. Friedrich, M. A. Troxel, S. Dodelson, J. Blazek, L. F. Secco, N. MacCrann, E. Baxter, C. Chang, N. Chen, M. Crocce, J. DeRose, A. Ferte, N. Kokron, F. Lacasa, V. Miranda, Y. Omori, A. Porredon, R. Rosenfeld, S. Samuroff, M. Wang, R. H. Wechsler, T. M. C. Abbott, F. B. Abdalla, S. Allam, J. Annis, K. Bechtol, A. Benoit-Levy, G. M. Bernstein, D. Brooks, D. L. Burke, D. Capozzi, M. Carrasco Kind, J. Carretero, C. B. D'Andrea, L. N. da Costa, C. Davis, D. L. DePoy, S. Desai, H. T. Diehl, J. P. Dietrich, A. E. Evrard, B. Flaugher, P. Fosalba, J. Frieman, J. Garcia-Bellido, E. Gaztanaga, T. Giannantonio, D. Gruen, R. A. Gruendl, J. Gschwend, G. Gutierrez, K. Honscheid, D. J. James, T. Jeltema, K. Kuehn, S. Kuhlmann, O. Lahav, M. Lima, M. A. G. Maia, M. March, J. L. Marshall, P. Martini, F. Menanteau, R. Miquel, R. C. Nichol, A. A. Plazas, A. K. Romer, E. S. Rykoff, E. Sanchez, V. Scarpine, R. Schindler, M. Schubnell, I. Sevilla-Noarbe, M. Smith, M. Soares-Santos, F. Sobreira, E. Suchyta, M. E. C. Swanson, G. Tarle, D. L. Tucker, V. Vikram, A. R. Walker, and J. Weller, "Dark Energy Survey Year 1 Results: Multi-Probe Methodology and Simulated Likelihood Analyses," *arXiv e-prints*, p. arXiv:1706.09359, June 2017.

[186] D. Foreman-Mackey, D. W. Hogg, D. Lang, and J. Goodman, "emcee: The MCMC Hammer," *PASP*, vol. 125, p. 306, Mar. 2013.

[187] F. Feroz and M. P. Hobson, "Multimodal nested sampling: an efficient and robust alternative to Markov Chain Monte Carlo methods for astronomical data analyses," *MNRAS*, vol. 384, pp. 449–463, 01 2008.

[188] F. Feroz, M. P. Hobson, and M. Bridges, "MULTINEST: an efficient and robust Bayesian inference tool for cosmology and particle physics," *MNRAS*, vol. 398, pp. 1601–1614, Oct. 2009.

[189] F. Feroz, M. P. Hobson, E. Cameron, and A. N. Pettitt, "Importance Nested Sampling and the MultiNest Algorithm," *OJAp*, vol. 2, p. 10, Nov. 2019.

[190] R. Mandelbaum, C. M. Hirata, U. Seljak, J. Guzik, N. Padmanabhan, C. Blake, M. R. Blanton, R. Lupton, and J. Brinkmann, "Systematic errors in weak lensing: application to SDSS galaxy-galaxy weak lensing," *MNRAS*, vol. 361, pp. 1287–1322, Aug. 2005.

[191] M. Gatti, E. Sheldon, A. Amon, M. Becker, M. Troxel, A. Choi, C. Doux, N. MacCrann, A. Navarro-Alsina, I. Harrison, D. Gruen, G. Bernstein, M. Jarvis, L. F. Secco, A. Ferté, T. Shin, J. McCullough, R. P. Rollins, R. Chen, C. Chang, S. Pandey, I. Tutusaus, J. Prat, J. Elvin-Poole, C. Sanchez, A. A. Plazas, A. Roodman, J. Zuntz, T. M. C. Abbott, M. Aguena, S. Allam, J. Annis, S. Avila, D. Bacon, E. Bertin, S. Bhargava, D. Brooks, D. L. Burke, A. Carnero Rosell, M. Carrasco Kind, J. Carretero, F. J. Castander, C. Conselice, M. Costanzi, M. Crocce, L. N. da Costa, T. M. Davis, J. De Vicente, S. Desai, H. T. Diehl, J. P. Dietrich, P. Doel, A. Drlica-Wagner, K. Eckert, S. Everett, I. Ferrero, J. Frieman, J. García-Bellido, D. W. Gerdes, T. Giannantonio, R. A. Gruendl, J. Gschwend, G. Gutierrez,

W. G. Hartley, S. R. Hinton, D. L. Hollowood, K. Honscheid, B. Hoyle, E. M. Huff, D. Huterer, B. Jain, D. J. James, T. Jeltema, E. Krause, R. Kron, N. Kuropatkin, M. Lima, M. A. G. Maia, J. L. Marshall, R. Miquel, R. Morgan, J. Myles, A. Palmese, F. Paz-Chinchón, E. S. Rykoff, S. Samuroff, E. Sanchez, V. Scarpine, M. Schubnell, S. Serrano, I. Sevilla-Noarbe, M. Smith, M. Soares-Santos, E. Suchyta, M. E. C. Swanson, G. Tarle, D. Thomas, C. To, D. L. Tucker, T. N. Varga, R. H. Wechsler, J. Weller, W. Wester, and R. D. Wilkinson, "Dark energy survey year 3 results: weak lensing shape catalogue," *MNRAS*, vol. 504, pp. 4312–4336, July 2021.

[192] B. Giblin, C. Heymans, M. Asgari, H. Hildebrandt, H. Hoekstra, B. Joachimi, A. Kannawadi, K. Kuijken, C.-A. Lin, L. Miller, T. Tröster, J. L. van den Busch, A. H. Wright, M. Bilicki, C. Blake, J. de Jong, A. Dvornik, T. Erben, F. Getman, N. R. Napolitano, P. Schneider, H. Shan, and E. Valentijn, "KiDS-1000 catalogue: Weak gravitational lensing shear measurements," *A&A*, vol. 645, p. A105, Jan. 2021.

[193] B. T. P. Rowe, M. Jarvis, R. Mandelbaum, G. M. Bernstein, J. Bosch, M. Simet, J. E. Meyers, T. Kacprzak, R. Nakajima, J. Zuntz, H. Miyatake, J. P. Dietrich, R. Armstrong, P. Melchior, and M. S. S. Gill, "GALSIM: The modular galaxy image simulation toolkit," *Astronomy and Computing*, vol. 10, pp. 121–150, Apr. 2015.

[194] C. Chang, M. Jarvis, B. Jain, S. M. Kahn, D. Kirkby, A. Connolly, S. Krughoff, E. H. Peng, and J. R. Peterson, "The effective number density of galaxies for weak lensing measurements in the LSST project," *MNRAS*, vol. 434, pp. 2121–2135, Sept. 2013.

[195] M. Tanaka, J. Coupon, B.-C. Hsieh, S. Mineo, A. J. Nishizawa, J. Speagle, H. Furusawa, S. Miyazaki, and H. Murayama, "Photometric redshifts for Hyper Suprime-Cam Subaru Strategic Program Data Release 1," *PASJ*, vol. 70, p. S9, Jan. 2018.

[196] M. Oguri, Y.-T. Lin, S.-C. Lin, A. J. Nishizawa, A. More, S. More, B.-C. Hsieh, E. Medezinski, H. Miyatake, H.-Y. Jian, L. Lin, M. Takada, N. Okabe, J. S. Speagle, J. Coupon, A. Leauthaud, R. H. Lupton, S. Miyazaki, P. A. Price, M. Tanaka, I.-N. Chiu, Y. Komiyama, Y. Okura, M. M. Tanaka, and T. Usuda, "An optically-selected cluster catalog at redshift $0.1 < z < 1.1$ from the hyper suprime-cam subaru strategic program s16a data," *Publications of the Astronomical Society of Japan*, vol. 70, no. SP1, p. S20, 2018.

[197] M. Shirasaki, T. Hamana, M. Takada, R. Takahashi, and H. Miyatake, "Mock galaxy shape catalogues in the Subaru Hyper Suprime-Cam Survey," *MNRAS*, vol. 486, pp. 52–69, June 2019.

[198] R. Takahashi, T. Hamana, M. Shirasaki, T. Namikawa, T. Nishimichi, K. Osato, and K. Shiroyama, "Full-sky gravitational lensing simulation for large-area galaxy surveys and cosmic microwave background experiments," *The Astrophysical Journal*, vol. 850, p. 24, nov 2017.

[199] N. MacCrann, J. Blazek, B. Jain, and E. Krause, "Controlling and leveraging small-scale information in tomographic galaxy-galaxy lensing," *MNRAS*, vol. 491, pp. 5498–5509, Feb. 2020.

[200] J. Zuntz, M. Paterno, E. Jennings, D. Rudd, A. Manzotti, S. Dodelson, S. Bridle, S. Sehrish, and J. Kowalkowski, "CosmoSIS: Modular cosmological parameter estimation," *Astronomy and Computing*, vol. 12, pp. 45–59, Sept. 2015.

[201] A. Lewis, A. Challinor, and A. Lasenby, "Efficient Computation of Cosmic Microwave Background Anisotropies in Closed Friedmann-Robertson-Walker Models," *ApJ*, vol. 538, pp. 473–476, Aug. 2000.

[202] A. Lewis and S. Bridle, "Cosmological parameters from cmb and other data: A monte carlo approach," *Phys. Rev. E*, vol. 66, p. 103511, Nov 2002.

[203] C. Howlett, A. Lewis, A. Hall, and A. Challinor, "CMB power spectrum parameter degeneracies in the era of precision cosmology," *J. Cosmology Astropart. Phys.*, vol. 2012, pp. 027–027, apr 2012.

[204] R. Takahashi, M. Sato, T. Nishimichi, A. Taruya, and M. Oguri, "Revising the Halofit Model for the Nonlinear Matter Power Spectrum," *ApJ*, vol. 761, p. 152, Dec. 2012.

[205] C. M. Hirata and U. Seljak, "Intrinsic alignment-lensing interference as a contaminant of cosmic shear," *Phys. Rev. E*, vol. 70, p. 063526, Sep 2004.

[206] S. Bridle and L. King, "Dark energy constraints from cosmic shear power spectra: impact of intrinsic alignments on photometric redshift requirements," *New Journal of Physics*, vol. 9, pp. 444–444, dec 2007.

[207] T. Hamana, M. Shirasaki, S. Miyazaki, C. Hikage, M. Oguri, S. More, R. Armstrong, A. Leauthaud, R. Mandelbaum, H. Miyatake, A. J. Nishizawa, M. Simet, M. Takada, H. Aihara, J. Bosch, Y. Komiyama, R. Lupton, H. Murayama, M. A. Strauss, and M. Tanaka, "Erratum: Cosmological constraints from cosmic shear two-point correlation functions with HSC survey first-year data," *PASJ*, vol. 74, pp. 488–491, Apr. 2022.

[208] M. Raveri and W. Hu, "Concordance and discordance in cosmology," *Phys. Rev. E*, vol. 99, p. 043506, Feb. 2019.

[209] T. Zhang, M. M. Rau, R. Mandelbaum, X. Li, and B. Moews, "Photometric Redshift Uncertainties in Weak Gravitational Lensing Shear Analysis: Models and Marginalization," *arXiv e-prints*, p. arXiv:2206.10169, June 2022.

[210] M. M. Rau, R. Dalal, T. Zhang, X. Li, A. J. Nishizawa, S. More, R. Mandelbaum, M. A. Strauss, and M. Takada, "Weak Lensing Tomographic Redshift Distribution Inference for the Hyper Suprime-Cam Subaru Strategic Program three-year shape catalogue," *arXiv e-prints*, p. arXiv:2211.16516, Nov. 2022.

[211] S. Pandey, E. Krause, J. DeRose, N. MacCrann, B. Jain, M. Crocce, J. Blazek, A. Choi, H. Huang, C. To, X. Fang, J. Elvin-Poole, J. Prat, A. Porredon, L. F. Secco, M. Rodriguez-Monroy, N. Weaverdyck, Y. Park, M. Raveri, E. Rozo, E. S. Rykoff, G. M. Bernstein, C. Sánchez, M. Jarvis, M. A. Troxel, G. Zacharegkas, C. Chang, A. Alarcon, O. Alves, A. Amon, F. Andrade-Oliveira, E. Baxter, K. Bechtol, M. R. Becker, H. Camacho, A. Campos, A. Carnero Rosell, M. Carrasco Kind, R. Cawthon, R. Chen, P. Chintalapati, C. Davis, E. Di Valentino, H. T. Diehl, S. Dodelson, C. Doux, A. Drlica-Wagner, K. Eckert, T. F. Eifler, F. Elsner, S. Everett, A. Farahi, A. Ferté, P. Fosalba, O. Friedrich, M. Gatti, G. Giannini, D. Gruen, R. A. Gruendl, I. Harrison, W. G. Hartley, E. M. Huff, D. Huterer, A. Kovacs, P. F. Leget, J. McCullough, J. Muir, J. Myles, A. Navarro-Alsina, Y. Omori, R. P. Rollins, A. Roodman, R. Rosenfeld, I. Sevilla-Noarbe, E. Sheldon, T. Shin, A. Troja, I. Tutusaus, T. N. Varga, R. H. Wechsler, B. Yanny, B. Yin, Y. Zhang, J. Zuntz, T. M. C. Abbott, M. Aguena, S. Allam, J. Annis, D. Bacon, E. Bertin, D. Brooks, D. L. Burke, J. Carretero, C. Conselice, M. Costanzi, L. N. da Costa, M. E. S. Pereira, J. De Vicente, J. P. Dietrich, P. Doel, A. E. Evrard, I. Ferrero, B. Flaugher, J. Frieman, J. García-Bellido, E. Gaztanaga, D. W. Gerdes, T. Giannantonio, J. Gschwend, G. Gutierrez, S. R. Hinton, D. L. Hollowood, K. Honscheid, D. J. James, T. Jeltema, K. Kuehn, N. Kuropatkin, O. Lahav, M. Lima, H. Lin, M. A. G. Maia, J. L. Marshall, P. Melchior, F. Menanteau, C. J. Miller, R. Miquel, J. J. Mohr, R. Morgan, A. Palmese, F. Paz-Chinchón, D. Petravick, A. Pieres, A. A. Plazas Malagón, E. Sanchez, V. Scarpine, S. Serrano, M. Smith, M. Soares-Santos, E. Suchyta, G. Tarle, D. Thomas, J. Weller, and DES Collaboration, "Dark Energy Survey year 3 results: Constraints on cosmological parameters and galaxy-bias models from galaxy clustering and galaxy-galaxy lensing using the redMaGiC sample," *Phys. Rev. E*, vol. 106, p. 043520, Aug. 2022.

[212] A. Nicola, C. García-García, D. Alonso, J. Dunkley, P. G. Ferreira, A. Slosar, and D. N. Spergel, "Cosmic shear power spectra in practice," *J. Cosmology Astropart. Phys.*, vol. 2021, p. 067, Mar. 2021.

[213] D. Alonso, J. Sanchez, A. Slosar, and LSST Dark Energy Science Collaboration, "A unified pseudo-C_ℓ framework," *MNRAS*, vol. 484, pp. 4127–4151, Apr. 2019.

[214] K.-W. Ng and G.-C. Liu, "Correlation Functions of CMB Anisotropy and Polarization," *International Journal of Modern Physics D*, vol. 8, pp. 61–83, Jan. 1999.

[215] H. Hildebrandt *et al.*, "KiDS+VIKING-450: Cosmic shear tomography with optical and infrared data," *Astron. Astrophys.*, vol. 633, p. A69, 2020.

[216] D. Huterer, M. Takada, G. Bernstein, and B. Jain, "Systematic errors in future weak-lensing surveys: requirements and prospects for self-calibration," *MNRAS*, vol. 366, pp. 101–114, Feb. 2006.

[217] M. Salvato, O. Ilbert, and B. Hoyle, "The many flavours of photometric redshifts," *Nature Astronomy*, vol. 3, pp. 212–222, June 2019.

[218] A. I. Malz, "How not to obtain the redshift distribution from probabilistic redshift estimates: Under what conditions is it not inappropriate to estimate the redshift distribution N (z) by stacking photo-z PDFs?," *Phys. Rev. E*, vol. 103, p. 083502, Apr. 2021.

[219] C. E. Cunha, M. Lima, H. Oyaizu, J. Frieman, and H. Lin, "Estimating the redshift distribution of photometric galaxy samples - II. Applications and tests of a new method," *MNRAS*, vol. 396, pp. 2379–2398, July 2009.

[220] J. A. Newman, "Calibrating Redshift Distributions beyond Spectroscopic Limits with Cross-Correlations," *ApJ*, vol. 684, pp. 88–101, Sept. 2008.

[221] C. Sánchez and G. M. Bernstein, "Redshift inference from the combination of galaxy colours and clustering in a hierarchical Bayesian model," *MNRAS*, vol. 483, pp. 2801–2813, Feb. 2019.

[222] M. M. Rau, S. Wilson, and R. Mandelbaum, "Estimating redshift distributions using hierarchical logistic Gaussian processes," *MNRAS*, vol. 491, pp. 4768–4782, Feb. 2020.

[223] M. Lima, C. E. Cunha, H. Oyaizu, J. Frieman, H. Lin, and E. S. Sheldon, "Estimating the redshift distribution of photometric galaxy samples," *ApJ*, vol. 390, pp. 118–130, 10 2008.

[224] A. I. Malz, P. J. Marshall, J. DeRose, M. L. Graham, S. J. Schmidt, and R. W. and, "Approximating photo-z pdfs for large surveys," *ApJ*, vol. 156, p. 35, jun 2018.

[225] B. Henghes, C. Pettitt, J. Thiyagalingam, T. Hey, and O. Lahav, "Benchmarking and scalability of machine-learning methods for photometric redshift estimation," *MNRAS*, vol. 505, pp. 4847–4856, 05 2021.

[226] M. M. Rau, C. B. Morrison, S. J. Schmidt, S. Wilson, R. Mandelbaum, Y. Y. Mao, Y. Y. Mao, and LSST Dark Energy Science Collaboration, "A composite likelihood approach for inference under photometric redshift uncertainty," *MNRAS*, vol. 509, pp. 4886–4907, Feb. 2022.

[227] H. Hildebrandt, M. Viola, C. Heymans, S. Joudaki, K. Kuijken, C. Blake, T. Erben, B. Joachimi, D. Klaes, L. Miller, C. B. Morrison, R. Nakajima, G. Verdoes Kleijn, A. Amon, A. Choi, G. Covone, J. T. A. de Jong, A. Dvornik, I. Fenech Conti, A. Grado, J. Harnois-Déraps, R. Herbonnet, H. Hoekstra, F. Köhlinger, J. McFarland, A. Mead, J. Merten, N. Napolitano, J. A. Peacock, M. Radovich, P. Schneider, P. Simon, E. A. Valentijn, J. L. van den Busch, E. van Uitert, and L. Van Waerbeke,

"KiDS-450: cosmological parameter constraints from tomographic weak gravitational lensing," *MNRAS*, vol. 465, pp. 1454–1498, Feb. 2017.

[228] B. Hadzhiyska, D. Alonso, A. Nicola, and A. Slosar, "Analytic marginalization of n(z) uncertainties in tomographic galaxy surveys," *J. Cosmology Astropart. Phys.*, vol. 2020, pp. 056–056, oct 2020.

[229] B. Stölzner, B. Joachimi, A. Korn, H. Hildebrandt, and A. H. Wright, "Self-calibration and robust propagation of photometric redshift distribution uncertainties in weak gravitational lensing," *A&A*, vol. 650, p. A148, June 2021.

[230] J. P. Cordero, I. Harrison, R. P. Rollins, G. M. Bernstein, S. L. Bridle, A. Alarcon, O. Alves, A. Amon, F. Andrade-Oliveira, H. Camacho, A. Campos, A. Choi, J. DeRose, S. Dodelson, K. Eckert, T. F. Eifler, S. Everett, X. Fang, O. Friedrich, D. Gruen, R. A. Gruendl, W. G. Hartley, E. M. Huff, E. Krause, N. Kuropatkin, N. MacCrann, J. McCullough, J. Myles, S. Pandey, M. Raveri, R. Rosenfeld, E. S. Rykoff, C. Sánchez, J. Sánchez, I. Sevilla-Noarbe, E. Sheldon, M. Troxel, R. Wechsler, B. Yanny, B. Yin, Y. Zhang, M. Aguena, S. Allam, E. Bertin, D. Brooks, D. L. Burke, A. Carnero Rosell, M. Carrasco Kind, J. Carretero, F. J. Castander, R. Cawthon, M. Costanzi, L. da Costa, M. E. da Silva Pereira, J. De Vicente, H. T. Diehl, J. Dietrich, P. Doel, J. Elvin-Poole, I. Ferrero, B. Flaugher, P. Fosalba, J. Frieman, J. Garcia-Bellido, D. Gerdes, J. Gschwend, G. Gutierrez, S. Hinton, D. L. Hollowood, K. Honscheid, B. Hoyle, D. James, K. Kuehn, O. Lahav, M. A. G. Maia, M. March, F. Menanteau, R. Miquel, R. Morgan, J. Muir, A. Palmese, F. Paz-Chinchon, A. Pieres, A. Plazas Malagón, E. Sánchez, V. Scarpine, S. Serrano, M. Smith, M. Soares-Santos, E. Suchyta, M. Swanson, G. Tarle, D. Thomas, C. To, T. N. Varga, and DES Collaboration, "Dark Energy Survey Year 3 results: marginalization over redshift distribution uncertainties using ranking of discrete realizations," *MNRAS*, vol. 511, pp. 2170–2185, Apr. 2022.

[231] X. Li, H. Miyatake, W. Luo, S. More, M. Oguri, T. Hamana, R. Mandelbaum, M. Shirasaki, M. Takada, R. Armstrong, A. Kannawadi, S. Takita, S. Miyazaki, A. J. Nishizawa, A. A. Plazas Malagon, M. A. Strauss, M. Tanaka, and N. Yoshida, "The three-year shear catalog of the Subaru Hyper Suprime-Cam SSP Survey," *PASJ*, vol. 74, pp. 421–459, Apr. 2022.

[232] P. J. E. Peebles, *The large-scale structure of the universe*. 1980.

[233] L. Fu, E. Semboloni, H. Hoekstra, M. Kilbinger, L. van Waerbeke, I. Tereno, Y. Mellier, C. Heymans, J. Coupon, K. Benabed, J. Benjamin, E. Bertin, O. Doré, M. J. Hudson, O. Ilbert, R. Maoli, C. Marmo, H. J. McCracken, and B. Ménard, "Very weak lensing in the CFHTLS wide: cosmology from cosmic shear in the linear regime," *A&A*, vol. 479, pp. 9–25, Feb. 2008.

[234] M. Kilbinger, "Cosmology with cosmic shear observations: a review," *Reports on Progress in Physics*, vol. 78, p. 086901, July 2015.

[235] M. Bartelmann and P. Schneider, "Weak gravitational lensing," *Phys. Rep.*, vol. 340, pp. 291–472, Jan. 2001.

[236] B. Joachimi and S. L. Bridle, "Simultaneous measurement of cosmology and intrinsic alignments using joint cosmic shear and galaxy number density correlations," *A&A*, vol. 523, p. A1, Nov. 2010.

[237] S. Ishikawa, T. Okumura, M. Oguri, and S.-C. Lin, "Halo-model Analysis of the Clustering of Photometric Luminous Red Galaxies at $0.10 \leq z \leq 1.05$ from the Subaru Hyper Suprime-Cam Survey," *ApJ*, vol. 922, p. 23, Nov. 2021.

[238] M. Oguri, "A cluster finding algorithm based on the multiband identification of red sequence galaxies," *MNRAS*, vol. 444, pp. 147–161, Oct. 2014.

[239] C. B. Morrison, H. Hildebrandt, S. J. Schmidt, I. K. Baldry, M. Bilicki, A. Choi, T. Erben, and P. Schneider, "the-wizz: clustering redshift estimation for everyone," *MNRAS*, vol. 467, pp. 3576–3589, May 2017.

[240] S. Ishikawa, T. Okumura, M. Oguri, and S.-C. Lin, "Halo-model Analysis of the Clustering of Photometric Luminous Red Galaxies at $0.10 \leq z \leq 1.05$ from the Subaru Hyper Suprime-Cam Survey," *ApJ*, vol. 922, p. 23, Nov. 2021.

[241] M. Gatti, G. Giannini, G. M. Bernstein, A. Alarcon, J. Myles, A. Amon, R. Cawthon, M. Troxel, J. DeRose, S. Everett, A. J. Ross, E. S. Rykoff, J. Elvin-Poole, J. Cordero, I. Harrison, C. Sanchez, J. Prat, D. Gruen, H. Lin, M. Crocce, E. Rozo, T. M. C. Abbott, M. Aguena, S. Allam, J. Annis, S. Avila, D. Bacon, E. Bertin, D. Brooks, D. L. Burke, A. C. Rosell, M. C. Kind, J. Carretero, F. J. Castander, A. Choi, C. Conselice, M. Costanzi, M. Crocce, L. N. da Costa, M. E. S. Pereira, K. Dawson, S. Desai, H. T. Diehl, K. Eckert, T. F. Eifler, A. E. Evrard, I. Ferrero, B. Flaugher, P. Fosalba, J. Frieman, J. García-Bellido, E. Gaztanaga, T. Giannantonio, R. A. Gruendl, J. Gschwend, S. R. Hinton, D. L. Hollowood, K. Honscheid, B. Hoyle, D. Huterer, D. J. James, K. Kuehn, N. Kuropatkin, O. Lahav, M. Lima, N. MacCrann, M. A. G. Maia, M. March, J. L. Marshall, P. Melchior, F. Menanteau, R. Miquel, J. J. Mohr, R. Morgan, R. L. C. Ogando, A. Palmese, F. Paz-Chinchón, W. J. Percival, A. A. Plazas, M. Rodriguez-Monroy, A. Roodman, G. Rossi, S. Samuroff, E. Sanchez, V. Scarpine, L. F. Secco, S. Serrano, I. Sevilla-Noarbe, M. Smith, M. Soares-Santos, E. Suchyta, M. E. C. Swanson, G. Tarle, D. Thomas, C. To, T. N. Varga, J. Weller, R. D. Wilkinson, and D. Collaboration), "Dark Energy Survey Year 3 Results: clustering redshifts – calibration of the weak lensing source redshift distributions with redMaGiC and BOSS/eBOSS," *MNRAS*, vol. 510, pp. 1223–1247, 11 2021.

[242] M. Tanaka, "Photometric Redshift with Bayesian Priors on Physical Properties of Galaxies," *ApJ*, vol. 801, p. 20, Mar. 2015.

[243] M. Carrasco Kind and R. J. Brunner, "TPZ: photometric redshift PDFs and ancillary information by using prediction trees and random forests," *MNRAS*, vol. 432, pp. 1483–1501, June 2013.

[244] J. S. Speagle, A. Leauthaud, S. Huang, C. P. Bradshaw, F. Ardila, P. L. Capak, D. J. Eisenstein, D. C. Masters, R. Mandelbaum, S. More, M. Simet, and C. Sifón, "Galaxy-Galaxy lensing in HSC: Validation tests and the impact of heterogeneous spectroscopic training sets," *MNRAS*, vol. 490, pp. 5658–5677, Dec. 2019.

[245] C. Laigle, H. J. McCracken, O. Ilbert, B. C. Hsieh, I. Davidzon, P. Capak, G. Hasinger, J. D. Silverman, C. Pichon, J. Coupon, H. Aussel, D. Le Borgne, K. Caputi, P. Cassata, Y. Y. Chang, F. Civano, J. Dunlop, J. Fynbo, J. S. Kartaltepe, A. Koekemoer, O. Le Fèvre, E. Le Floc'h, A. Leauthaud, S. Lilly, L. Lin, S. Marchesi, B. Milvang-Jensen, M. Salvato, D. B. Sanders, N. Scoville, V. Smolcic, M. Stockmann, Y. Taniguchi, L. Tasca, S. Toft, M. Vaccari, and J. Zabl, "The COSMOS2015 Catalog: Exploring the $1 < z < 6$ Universe with Half a Million Galaxies," *ApJS*, vol. 224, p. 24, June 2016.

[246] R. E. Smith, J. A. Peacock, A. Jenkins, S. D. M. White, C. S. Frenk, F. R. Pearce, P. A. Thomas, G. Efstathiou, and H. M. P. Couchman, "Stable clustering, the halo model and non-linear cosmological power spectra," *MNRAS*, vol. 341, pp. 1311–1332, June 2003.

[247] E. P. Longley, C. Chang, C. W. Walter, J. Zuntz, M. Ishak, R. Mandelbaum, H. Miyatake, A. Nicola, E. M. Pedersen, M. E. S. Pereira, J. Prat, J. Sánchez, T. Tröster, M. Troxel, A. Wright, and The LSST Dark Energy Science Collaboration, "A Unified Catalog-level Reanalysis of Stage-III Cosmic Shear Surveys," *arXiv e-prints*, p. arXiv:2208.07179, Aug. 2022.

[248] P. Lemos, N. Weaverdyck, R. P. Rollins, J. Muir, A. Ferté, A. R. Liddle, A. Campos, D. Huterer, M. Raveri, J. Zuntz, E. Di Valentino, X. Fang, W. G. Hartley, M. Aguena, S. Allam, J. Annis, E. Bertin, S. Bocquet, D. Brooks, D. L. Burke, A. Carnero Rosell, M. Carrasco Kind, J. Carretero, F. J. Castander, A. Choi, M. Costanzi, M. Crocce, L. N. da Costa, M. E. S. Pereira, J. P. Dietrich, S. Everett, I. Ferrero, J. Frieman, J. García-Bellido, M. Gatti, E. Gaztanaga, D. W. Gerdes, D. Gruen, R. A. Gruendl, J. Gschwend, G. Gutierrez, S. R. Hinton, D. L. Hollowood, K. Honscheid, D. J. James, K. Kuehn, N. Kuropatkin, M. Lima, M. March, P. Melchior, F. Menanteau, R. Miquel, R. Morgan, A. Palmese, F. Paz-Chinchón, A. Pieres, A. A. Plazas Malagón, A. Porredon, E. Sanchez, V. Scarpine, M. Schubnell, S. Serrano, I. Sevilla-Noarbe, M. Smith, E. Suchyta, M. E. C. Swanson, G. Tarle, D. Thomas, C. To, T. N. Varga, and J. Weller, "Robust sampling for weak lensing and clustering analyses with the Dark Energy Survey," *arXiv e-prints*, p. arXiv:2202.08233, Feb. 2022.

[249] W. J. Handley, M. P. Hobson, and A. N. Lasenby, "polychord: nested sampling for cosmology," *MNRAS Letters*, vol. 450, pp. L61–L65, 04 2015.

[250] W. J. Handley, M. P. Hobson, and A. N. Lasenby, "POLYCHORD: next-generation nested sampling," *MNRAS*, vol. 453, pp. 4384–4398, Nov. 2015.

[251] G. Casella, R. Berger, and B. P. Company, *Statistical Inference*. Duxbury advanced series in statistics and decision sciences, Thomson Learning, 2002.

[252] S. J. Schmidt, A. I. Malz, J. Y. H. Soo, I. A. Almosallam, M. Brescia, S. Cavuoti, J. Cohen-Tanugi, A. J. Connolly, J. DeRose, P. E. Freeman, M. L. Graham, K. G. Iyer, M. J. Jarvis, J. B. Kalmbach, E. Kovacs, A. B. Lee, G. Longo, C. B. Morrison, J. A. Newman, E. Nourbakhsh, E. Nuss, T. Pospisil, H. Tranin, R. H. Wechsler, R. Zhou, R. Izbicki, and LSST Dark Energy Science Collaboration, "Evaluation of probabilistic photometric redshift estimation approaches for The Rubin Observatory Legacy Survey of Space and Time (LSST)," *MNRAS*, vol. 499, pp. 1587–1606, Dec. 2020.

[253] R. Bordoloi, S. J. Lilly, and A. Amara, "Photo-z performance for precision cosmology," *MNRAS*, vol. 406, pp. 881–895, Aug. 2010.

[254] A. H. Wright, H. Hildebrandt, J. L. van den Busch, C. Heymans, B. Joachimi, A. Kannawadi, and K. Kuijken, "KiDS+VIKING-450: Improved cosmological parameter constraints from redshift calibration with self-organising maps," *A&A*, vol. 640, p. L14, Aug. 2020.